

ANAL

CRISIS

ABDULRAHIM MOUMEN





TR 3657 S

Stellingen behorende bij het proefschrift

**ANALYSIS AND SYNTHESIS OF COMPACT FEEDS  
FOR LARGE MULTIPLE-BEAM REFLECTOR ANTENNAS**



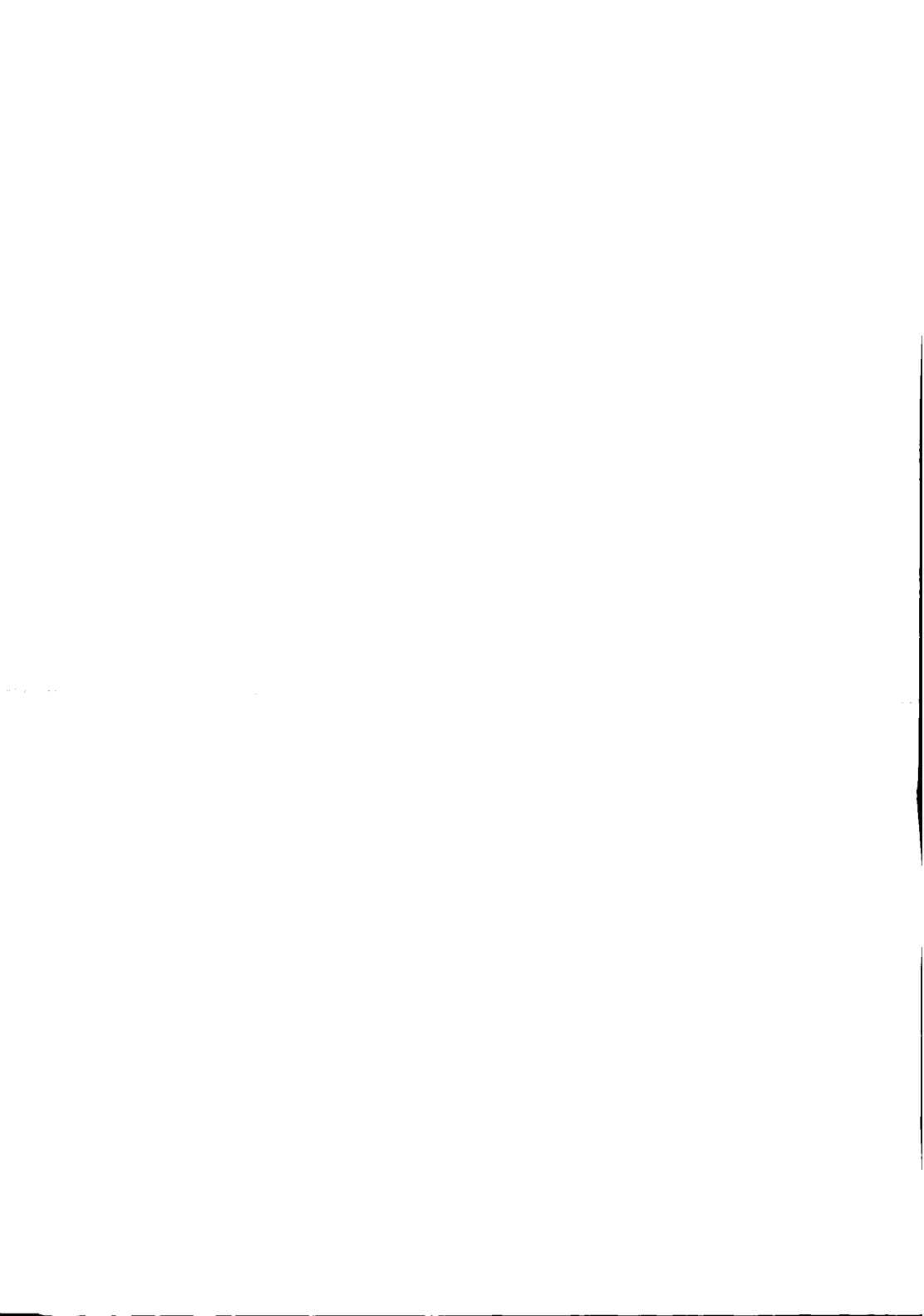
door

**Abderrahim Moumen**

Delft, 6 maart 2001

1. *The miniaturized dielectric rod antenna is a good reflector feed-array element because of its compact size. Feed elements can be placed closely together, as a result of which, less aperture blockage and better beam resolution are achieved. (See Chapter 4 in this thesis)*
2. *Despite the strong mutual coupling between two dielectric rod antennas located closely together leading to pattern degradation, the inter-port coupling remained very small. (See Chapter 5 in this thesis)*
3. *In the design of feed arrays for reflector antennas, the blockage caused by the struts and the feed housing is very crucial. It is possible to design supporting structures which are both mechanically stable and at the same time electrically "invisible" in some angular regions. (See Chapter 6 in this thesis)*
4. *Designing a good experiment is as difficult as solving a theoretical problem. Both require careful preparation, logical thinking and patience.*
5. *Minds are like parachutes. They only function when they are open. (Sir James Dewar)*
6. *The important thing is never to stop questioning. (Albert Einstein)*
7. *It is surprising that antenna designs originating from commercially available software nearly always require experimental tuning.*
8. *For an ordinary person to buy a house in future, the abolition of the tax-deductible mortgage must be accompanied by a significant decrease of income tax.*
9. *The recent visit of a member of the Dutch royal family to Morocco is a second step in the process of reviving the relations between both countries. The discovery of a significant amount of oil in the southern part of Morocco seems to be a first step.*
10. *As far as the laws of physics refer to reality, they are uncertain. As far as they are certain, they do not refer to reality. (Albert Einstein)*

1. *Vanwege hun kleine doorsnede zijn diëlectrisch gevulde staafantennes een goede keus als element in belichter-arrays voor reflectorantennes. De elementen kunnen op korte afstand van elkaar geplaatst worden, waardoor er weinig blokkering optreedt en een betere kwaliteit van de bundel gerealiseerd kan worden. (Zie hoofdstuk 4 van dit proefschrift)*
2. *Ondanks de sterke mutuele koppeling tussen twee dicht bij elkaar geplaatste diëlectrisch gevulde staafantennes met als gevolg een degradatie van het antennepatroon blijft de koppeling tussen de twee ingangspoorten zeer laag. (Zie hoofdstuk 5 van dit proefschrift)*
3. *De blokkeringseffecten veroorzaakt door "uithouders" en "belichterhuis" spelen een belangrijke rol bij het ontwerpen van belichters voor reflectorantennes. Het is mogelijk het ontwerp van de uithouders zo te maken dat ze tegelijkertijd mechanisch sterk en, in bepaalde richtingen, elektrisch onzichtbaar zijn. (Zie hoofdstuk 6 van dit proefschrift)*
4. *Het ontwerpen van een goed experiment is even moeilijk als het oplossen van een theoretisch probleem. Beiden vereisen een gedegen voorbereiding, logisch denken en geduld.*
5. *Het verstand is als een parachute. Zij functioneren alleen als zij open staan. (Sir James Dewar)*
6. *Het belangrijkste is altijd te blijven vragen. (Albert Einstein)*
7. *Het is verbazingwekkend dat een antenneontwerp gebaseerd op commercieel verkrijgbare software haast altijd experimenteel bijgesteld moet worden.*
8. *Om te zorgen dat de gemiddelde persoon in de toekomst nog steeds een huis kan kopen, moet de afschaffing van de hypotheekrenteaftrek samenvallen met een significante reductie van de inkomstenbelasting.*
9. *Het recente bezoek van een lid van het koninklijk huis aan Marokko is een tweede stap in het opleven van de betrekkingen tussen Nederland en Marokko. Het ontdekken van een substantiële hoeveelheid olie in het zuidelijke deel van Marokko lijkt een eerste stap te zijn.*
10. *In zoverre de wetten der natuurkunde betrekking hebben op de realiteit zijn zij onzeker. Die wetten die zeker zijn verwijzen niet naar de realiteit. (Albert Einstein)*



TR 3657

3657  
752917  
3000

ANALYSIS AND SYNTHESIS OF COMPACT FEEDS  
FOR LARGE MULTIPLE-BEAM REFLECTOR  
ANTENNAS







ANALYSIS AND SYNTHESIS OF COMPACT FEEDS  
FOR LARGE MULTIPLE-BEAM REFLECTOR  
ANTENNAS

PROEFSCHRIFT



ter verkrijging van de graad van doctor  
aan de Technische Universiteit Delft,  
op gezag van de Rector Magnificus Prof. ir. K.F. Wakker,  
voorzitter van het College voor Promoties,  
in het openbaar te verdedigen op dinsdag 06 maart 2001 om 10.30 uur

door

**Abderrahim MOUMEN**

elektrotechnische ingenieur,  
geboren te Oujda, Marokko.

Dit proefschrift is goedgekeurd door de promotoren:

Prof. dr. ir. L.P. Ligthart

Prof. dr. T. Birand

Samenstelling promotiecommissie:

Rector Magnificus (Voorzitter)

Prof. dr. ir. L.P. Ligthart Technische Universiteit Delft, (promotor)

Prof. dr. T. Birand Middle East Technical University Ankara, Turkey  
(promotor)

Prof. ir. P. van Genderen Technische Universiteit Delft

Prof. dr. ir. H. Blok Technische Universiteit Delft

Dr. ir. G. Mur Technische Universiteit Delft

Prof. dr. A.G. Tjhuis Technische Universiteit Eindhoven

**CIP-DATA KONINKLIJKE BIBLIOTHEEK, DEH HAAG**

**Abderrahim Moumen**

Analysis and synthesis of compact feeds for large multiple-beam reflector antennas

Abderrahim Moumen.- IRCTR-ITS, Delft University of Technology

Thesis Delft University of Technology. - With ref. - With summary in Dutch

ISBN 90-76928-01-0

Subject headings: dielectric rod/ array antennas/ beam switching/ reflector antennas  
/ integral equations/ MoM/ antenna miniaturization

Copyright © 2000 by Abderrahim Moumen

All rights reserved. No part of the material protected by this copyright notice may be reproduced or utilized in any form or by any means, electronic or mechanical, including photocopying, recording or by any information storage and retrieval system, without permission from the author Abderrahim Moumen.

*To my mother and my father*

*To my wife*



# Summary

In this dissertation, a complete and accurate design and analysis procedure is provided for multiple-beam reflector antennas using finite arrays of miniaturized dielectric rod antennas. It is demonstrated that the miniaturized dielectric rod antenna is a good reflector feed-array element because despite its compact size, it can produce a relatively high gain. Due to its compact size, feed elements can be placed closely together, as a result of which the feed-array is compact (less blockage) and the scanned beam is improved (better resolution). Aspects related to the miniaturization process, the radiation mechanism and the electromagnetic model of a single dielectric rod antenna and the analysis of the mutual coupling for arrays with small inter-element spacing are all addressed in this work. A miniaturized dielectric rod antenna design with exceptionally good low input loss, high gain and low mutual coupling levels has been realized. The feed-array synthesis method adapted in this research takes into account the mutual coupling between the dielectric rods, the losses in the beam-forming network and the blockage due to the metallic feed housing and the struts that are required for mechanical stability and mounting purposes. The electromagnetic models and the array synthesis method presented in this dissertation were applied with success; not only was the novel feed system of the transportable atmospheric radar (TARA) designed and analyzed, a full-scale version has also been realized at the Delft University of Technology, which is now fully operational.



# Contents

Summary	i
<b>1 Introduction</b>	<b>1</b>
1.1 Background of research . . . . .	1
1.2 Reflector antennas . . . . .	2
1.3 Dielectric rod antennas . . . . .	4
1.4 Problems addressed in this dissertation . . . . .	5
1.5 Organization of the thesis . . . . .	6
<b>2 Dielectric filled open-ended waveguides</b>	<b>9</b>
2.1 Introduction . . . . .	9
2.2 Modal analysis of discontinuities in rectangular waveguides . . . . .	12
2.2.1 Modes in rectangular waveguides . . . . .	12
2.2.2 Scattering matrix of step discontinuities . . . . .	15
2.2.3 Scattering matrix of multiple step discontinuities . . . . .	21
2.3 Characterization of the radiating aperture . . . . .	23
2.3.1 Aperture admittance . . . . .	23
2.3.2 Spectral representation of fields . . . . .	26
2.3.3 Radiated far fields . . . . .	30
2.4 Discussion of numerical results and experimental validation . . . . .	34

---

2.5	Conclusions . . . . .	52
	References . . . . .	55
<b>3</b>	<b>Radiation from an aperture on a 3-D metallic body</b>	<b>59</b>
3.1	Introduction . . . . .	59
3.2	Problem formulation and integral equation . . . . .	61
3.2.1	Field in the waveguide region . . . . .	64
3.2.2	Integral representation for the field in free-space . . . . .	65
3.2.3	Weak formulation and MoM solution . . . . .	69
3.2.4	Expansion functions and MOM matrix . . . . .	70
3.2.5	Far-field numerical computation . . . . .	75
3.3	Iterative solution of the MoM linear system . . . . .	76
3.4	Numerical results and experimental validation . . . . .	77
3.4.1	Numerical examples . . . . .	77
3.4.2	Computational aspects . . . . .	80
3.5	Conclusions . . . . .	81
	References . . . . .	89
<b>4</b>	<b>Rigorous analysis of dielectric rod antennas with arbitrary shape</b>	<b>93</b>
4.1	Introduction . . . . .	93
4.2	Problem formulation and derivation of the integral equation . . . . .	95
4.2.1	Field scattered by a dielectric body of arbitrary 3-D shape . . . . .	97
4.2.2	Representation for the incident field . . . . .	98
4.2.3	Total field and boundary conditions . . . . .	99
4.3	Expansion functions and MoM solution . . . . .	100
4.3.1	Discretization of the computational domain and expansion functions . . . . .	101
4.3.2	Discretization of the current densities and integral equations . . . . .	103



---

4.3.3	Weak formulation and MoM system . . . . .	105
4.3.4	Iterative solution of the MoM system . . . . .	106
4.3.5	Far-field computations . . . . .	108
4.4	Numerical results and experimental validation . . . . .	109
4.4.1	General design procedure . . . . .	109
4.4.2	Numerical examples . . . . .	112
4.4.3	Discussion of the numerical results . . . . .	115
4.5	Conclusions . . . . .	117
	References . . . . .	127
<b>5</b>	<b>Mutual coupling between two separate dielectric rod antennas</b>	<b>131</b>
5.1	Introduction . . . . .	131
5.2	Review of the theory on MSAs . . . . .	133
5.2.1	General scattering matrix representation . . . . .	134
5.2.2	Minimum scattering antennas . . . . .	135
5.2.3	Mutual coupling between two minimum scattering antennas . . . . .	137
5.3	Application to an array of two dielectric rod antennas . . . . .	139
5.3.1	General network representation of a single rod antenna . . . . .	140
5.3.2	General network representation of an array of two rod antennas . . . . .	141
5.3.3	The embedded patterns of an array of two dielectric rod antennas . . . . .	145
5.4	Experimental and numerical results . . . . .	147
5.5	Conclusions . . . . .	149
	References . . . . .	159
<b>6</b>	<b>Multiple-beam reflector antenna using a dielectric rod array</b>	<b>161</b>
6.1	Introduction . . . . .	161
6.2	Reflector antenna in receive case: Focal plane analysis . . . . .	163
6.2.1	Computation of the focal fields . . . . .	164

6.2.2	Near-field matching condition . . . . .	166
6.3	Reflector antenna in transmit case: Array synthesis . . . . .	167
6.3.1	Secondary pattern of reflectors fed by a dielectric rod array . . . . .	167
6.3.2	Far-field conjugate matching including mutual coupling . . . . .	170
6.4	Analysis of feeds and struts blockage in reflector antennas . . . . .	172
6.4.1	Introduction . . . . .	172
6.4.2	Problem description and method of solution . . . . .	173
6.5	The design procedure applied to the feed system of TARA . . . . .	175
6.5.1	Introduction . . . . .	175
6.5.2	TARA antenna requirements . . . . .	176
6.5.3	Central feed design . . . . .	177
6.5.4	Dielectric rod array design for the $15^\circ$ pointing angle . . . . .	178
6.5.5	Analysis of struts and housing blockage in TARA . . . . .	180
6.6	Conclusions . . . . .	181
	References . . . . .	193
<b>7</b>	<b>Conclusions and discussion</b>	<b>195</b>
7.1	Discussion of research . . . . .	195
7.2	Main conclusions . . . . .	199
7.3	Implications of research . . . . .	200
<b>A</b>	<b>Expressions for admittance integral and matching condition</b>	<b>201</b>
A.1	Derivation of scattering matrix of general step . . . . .	201
A.2	Evaluation of the mutual admittance integral . . . . .	202
A.3	Aperture matching condition . . . . .	204
<b>B</b>	<b>Derivation of the MOM matrix for aperture on 3-D metallic body</b>	<b>207</b>
B.1	Entries of the sub-matrix $Z^{c-c}$ . . . . .	207

---

B.2	Entries of the sub-matrix $Z^{c-a}$ . . . . .	209
B.3	Entries of the sub-matrix $Z^{a-a}$ . . . . .	210
B.4	Entries of the sub-matrix $Z^{a-c}$ . . . . .	211
<b>C</b>	<b>Derivation of MoM matrix for dielectric rod antenna problem</b>	<b>213</b>
C.1	The discretized form of the integral equations . . . . .	214
C.2	Entries of the sub-matrix $Z^{d-d}$ . . . . .	216
C.3	Entries of the sub-matrix $Z^{d-f}$ . . . . .	218
C.4	Entries of the sub-matrix $Z^{d-g}$ . . . . .	218
C.5	Entries of the sub-matrix $Z^{f-d}$ . . . . .	219
<b>D</b>	<b>Numerical evaluation of the mutual impedance</b>	<b>221</b>
<b>E</b>	<b>List of symbols and acronyms</b>	<b>223</b>
	<b>Acknowledgments</b>	<b>227</b>
	<b>Samenvatting (Summary in Dutch)</b>	<b>229</b>
	<b>Author publications</b>	<b>231</b>
	<b>Curriculum vitae</b>	<b>233</b>



# Chapter 1

## Introduction

### 1.1 Background of research

In recent years, issues related to the monitoring of global climate changes, water management, air safety around airports and effects of the atmosphere on communication links have become the driving forces behind the development of advanced electromagnetic observation techniques. Radar plays an important role in all the applications mentioned above. The International Research Centre for Telecommunications-transmission and Radar (IRCTR) at the Delft University of Technology (DUT) has gained a lot of experience in the fields of radar technology and remote sensing of the atmosphere. This has led to the development of a number of different radar systems working at different frequency bands.

One of the largest radar systems located at the DUT campus is the S-band Delft Atmospheric Research Radar (DARR). DARR is a mechanically steerable FM-CW radar operating at S-band and possessing polarimetric capabilities. The immobility of this system has limited the investigations for which it could be used to investigations of the sea-coast-urban environment. The necessity to study atmospheric phenomena at different locations has led to the design and realization of a new transportable

(mobile) atmospheric radar system called TARA.

The TARA radar is an international measurement facility financed by the Netherlands Technology Foundation (STW). It incorporates the latest developments in antenna and FM-CW technology.

The TARA antenna system consists of two separate reflector antennas with a parabolic shape, one used for transmitting and the other for receiving. Each antenna system has multiple beams pointing at different directions (i.e.  $0^\circ$ ,  $15^\circ$  in both the horizontal and the vertical plane). The beams are switched electronically so that three-dimensional wind fields can be measured. This dissertation is devoted to the development of tools and techniques for the analysis and design of such high-gain reflector antennas with beam-switching capabilities.

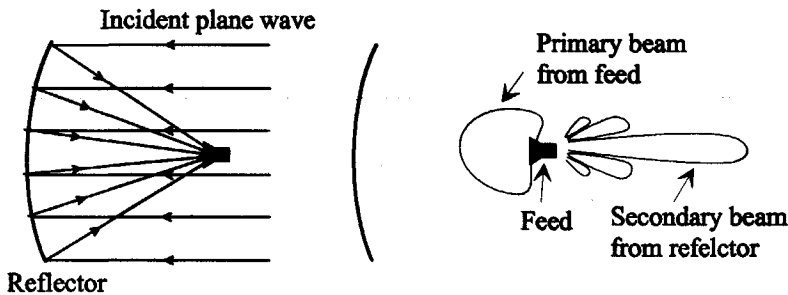


Figure 1.1: Reflector antenna with feed at focus. Left: reflector antenna in receive mode. Right: Reflector antenna in transmit mode.

## 1.2 Reflector antennas

Reflector antennas are widely used in radio astronomy, microwave communications, satellite communications and remote sensing because of their low cost, low weight, and high reliability compared to lens or phased-array systems. Reflector antennas may take many configurations (plane, corner, curved,...etc.). They can be classified according to

reflector shape, pattern type (pencil/shaped, fixed/scanned, single/multiple) and feed type. Most reflectors are parabolic, with a single focal point, the focus. A plane wave received from the bore sight direction is reflected by the parabolic surface and focused at the focal point, see Fig. 1.1. By reciprocity, a transmitted wave emanating from a feed located at the focus will be collimated by the reflector into a highly directive beam.

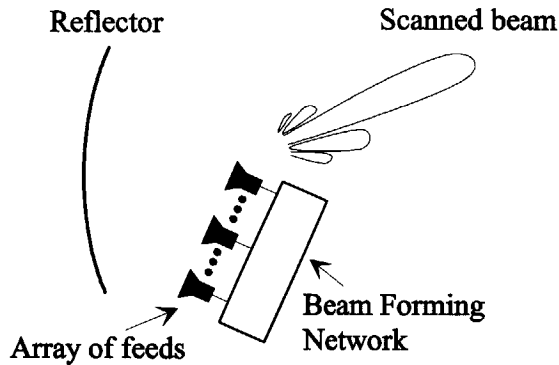


Figure 1.2: Concept of a reflector antenna with beam-switching capabilities.

In a reflector antenna system, beam-switching can be achieved by using a feed positioned at a distance out of the focus (off-axis). However, the beam generated by a reflector antenna whose source is located off-focus is relatively broad (lower gain) and has stronger side lobes. Thus, the beam obtained is not of practical use. Many applications demand reflector antennas with good off-axis beam characteristics. This may be achieved if more feed elements are employed, see Fig. 2.1. In this antenna concept an important consideration is the complexity of the feed system in terms of the number of elements used, the geometry of the feed array and inter-element spacing. The proximity of feed elements necessitates a good understanding of the mutual coupling and overcoming the difficulties in dimensioning an acceptable beam-forming network. Another important aspect is the minimization of unwanted blockage caused by the struts and feed housing that are required for mechanical stability and

mounting purposes. It are these factors that really determine the overall performance of the antenna system.

### 1.3 Dielectric rod antennas

Antenna feeds play an important role in the efficient operation of any reflector system. Ideally they must have a symmetrical pattern, unique phase centre and low cross polarization. Furthermore, they must provide a uniform illumination of the reflector surface.

Dielectric rod antennas are among the earliest radiating structures used in radar applications. They were first used as primary sources illuminating reflectors and as elements in phased arrays in World War II. Recently, dielectric rod antennas have been receiving greater attention with the advance of millimeter-wave technology. Low production costs, high reliability, small size and the availability of high-performance low-loss dielectric materials make dielectric antennas good candidates for a wide range of applications, especially at higher frequencies where metallic antennas are costly and inefficient due to the significant increase of resistive losses.

It is well known that when waveguide antennas are filled with a dielectric material they can be miniaturized while retaining the same, scaled, modal field distribution. The higher the dielectric constant, the more the size can be reduced. By extending the dielectric medium over a distance outside the waveguide, we obtain very compact feeds with a relatively high gain. These feed elements are very attractive for reflector feed-array applications and due to their small size, they can be located closely together, which makes the feed-array compact (less blockage) and improves the scanned beam (better resolution).



## 1.4 Problems addressed in this dissertation

In this dissertation the following problems are analyzed.

1. *Miniaturized dielectric filled open-ended waveguide antennas:*
  - Electromagnetic model
  - Different means for increasing the radiation efficiency
  - Miniaturization process
2. *Open-ended waveguide antennas with arbitrary 3-D metallic body:*
  - Electromagnetic formulation and numerical solution
  - Radiation improvement by an external corrugation profile
  - Design and realization of an optimized waveguide launcher
3. *Dielectric rod antennas with arbitrary 3-D shape:*
  - Electromagnetic formulation and numerical solution
  - Antenna performance improvement by shaping the dielectric rod
  - Design and realization of an optimized dielectric rod antenna
4. *Array of two miniaturized dielectric rod antennas:*
  - Approximate model for the mutual coupling
  - Analysis of the mutual coupling for different inter-element spacing
  - Analysis of the mutual coupling for different array excitations
5. *Multiple-beam reflector antennas using arrays of miniaturized dielectric rods:*

- Focal plane analysis and array synthesis procedure
- Mutual coupling compensation
- Analysis of struts and feed-housing blockage
- Design of the TARA feed system

## 1.5 Organization of the thesis

In this thesis, an accurate design and analysis tool is provided for multiple-beam reflector antennas that use arrays of miniaturized dielectric rods. Aspects related to the miniaturization process, the radiation mechanism and the electromagnetic model of a single dielectric rod antenna and the analysis of the mutual coupling for finite arrays are all addressed in this research. In this section, an outline of this dissertation is given.

*In Chapter 2*, we analyze dielectric-filled open-ended waveguide antennas. For carrying out this analysis we use the generalized scattering matrix technique in conjunction with a variational technique. A novel expression for the aperture admittance is derived and new results are presented. The discontinuities inside the guiding structure are analyzed using a modal expansion of the field in the waveguide that includes both propagating and evanescent modes. Sequential scattering features are taken into account by means of a direct cascading process. The field in free space is expressed in terms of plane-wave spectra. Both fields are related to each other by using the reaction theorem and applying boundary and interface conditions. The problem is then numerically solved by using complete modal expansions and plane-wave spectra and their interactions at the aperture interface.

*Chapter 3* is devoted to the development of a diagnostic and design tool, based on a modified EFIE and MoM, for analyzing and improving the radiation from an aperture that incorporates dielectric material and is mounted on a metallic body.

The metallic body may consist of a combination of perfectly conducting structures with different sizes and shapes. The code obtained is used to study the effect of the incorporation of an external corrugation profile on the metallic body. Different examples are investigated and new results are presented. An optimum rectangular-waveguide feed design is presented.

*In Chapter 4*, a rigorous numerical technique based on a hybrid-iterative MoM is proposed for the accurate analysis and design of dielectric rod antennas with arbitrary 3-D shape. The proposed model contains a complete model of the rod launcher. A design procedure for the dielectric rod antenna is described and new theoretical and experimental results are presented.

*In Chapter 5*, the Minimum Scattering Antenna (MSA) theory is used for predicting the effect of the mutual coupling between two adjacent dielectric rod antennas on the performance of those rod antennas.

*In Chapter 6*, an analysis and synthesis tool is provided for reflector antennas that are fed by finite arrays of dielectric rod antennas. The method proposed makes use of the electromagnetic models developed in the previous chapters and takes into account mutual coupling between the dielectric rods. A hybrid Physical Optics-Moment Method is presented for analyzing the blockage caused by the feed housing and struts, which are required for mechanical stability and mounting purposes.

*In Chapter 7*, the main results of this research are summarized and conclusions are drawn. Furthermore, suggestions are given for future research related to the work presented here.



# Chapter 2

## Dielectric filled open-ended waveguides

### 2.1 Introduction

This chapter concentrates on the analysis of dielectric filled and open-ended waveguide antennas with miniaturized apertures. The waveguides are assumed to have a rectangular cross section (see Fig. 2.1); when used as an antenna they are terminated by an infinite metallic flange (see Fig. 2.6). These antennas are comparable to microstrip antennas. They may have a low weight, a relatively large bandwidth as compared to microstrip antennas, good polarization purity and can easily be integrated with a printed-circuit board (PCB) or flush-mounted conformal to curved surfaces. Therefore, they are good candidates for many practical applications.

It is well known that when waveguide antennas are filled with a dielectric material of relative permittivity  $\epsilon_r$ , they can be miniaturized. Each dimension (width  $a$ , height  $b$ , see Fig. 2.1) of the antennas' aperture can be reduced by a factor  $\sqrt{\epsilon_r}$  while retaining the same, scaled, modal field distribution. The higher the dielectric constant, the more the size can be reduced. For rectangular waveguides with a  $TE_{1,0}$  excitation, further

size reduction can be achieved by reducing the height  $b$ . The result is a miniaturized antenna. It turns out that the miniaturization is at the cost of a high aperture reflection and a poor radiation efficiency. In the transition from waveguide into free space, which causes the high aperture reflection, we recognize the following three aspects:

- The ending of the metallic guiding structure.
- The dielectric-air transition at the aperture plane.
- The small cross section of the miniaturized antenna.

Antennas with such a high aperture reflection are inefficient radiators and not of practical interest. Fortunately it is possible to add a matching device that is designed such that it eliminates the aperture reflection. Matching techniques are based either on the insertion of an air gap in the dielectric medium or on steps in the waveguide dimensions (see Fig. 2.2).

As stated above in this chapter, we will analyze the dielectric-filled open-ended waveguide antennas. For carrying out this analysis we use the generalized scattering matrix in conjunction with a variational technique. A novel expression for the aperture admittance is derived and new results are presented. The discontinuities inside the guiding structure are analyzed using a modal expansion of the field in the waveguide that includes both propagating and evanescent modes. Sequential scattering features are taken into account by a direct cascading process. The field in free space is expressed in terms of plane-wave spectra. Both fields are related to each other by using the reaction theorem and applying boundary and interface conditions. The problem is then numerically solved by using complete modal expansions and plane-wave spectra and their interactions at the aperture interface. Knowing the aperture field, we can find the radiated field using standard techniques.

This chapter is further organized as follows. First, for completeness, in section 2, the scattering matrix approach and its applicability to a general discontinuity problem in rectangular waveguides is described briefly. For multiple discontinuities in rectangular waveguides we discuss the cascading scheme. Subsequently, in section 3, the radiating aperture and the spectral field representation are characterized. The matching condition is then derived and the present formulation is validated against measurements and results available in published literature in section 4. Finally, we discuss some specific aspects of the design of miniaturized dielectric filled waveguide antennas and limitations of the present formulation.

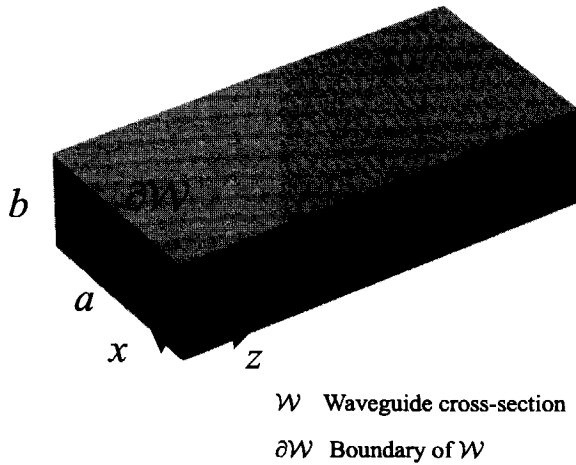


Figure 2.1: Waveguide dimensions and Cartesian coordinate system.

## 2.2 Modal analysis of discontinuities in rectangular waveguides

This section discusses the mathematical tool to be used for analyzing discontinuities in rectangular waveguides. Only two types of waveguide discontinuities will be considered, viz., a step in the waveguide dimensions and an air gap, which is a step in the material properties. The geometrical step discontinuity finds its application in waveguide transformers, iris couplers, and filters. The air gap is a very effective resonant matching device used mainly to improve the radiation efficiency of dielectric-filled waveguide antennas. Note that in a sense both types of waveguide discontinuities are of the same relatively simple type; they both allow the domain of computation to be subdivided into a number of sub-domains that are uniform waveguide sections in which we can use complete modal expansions. Because of this we can construct an algorithm with which multiple discontinuities in rectangular waveguides can be analyzed.

### 2.2.1 Modes in rectangular waveguides

Consider an infinite length metallic rectangular waveguide filled with a dielectric medium and of lateral dimensions  $a$  and  $b$ . The medium is assumed to be isotropic, linear and homogeneous. Fig. 2.1 shows the coordinate system that will be used throughout this section together with the waveguide dimensions. The fields in the waveguide can be decomposed into TE and TM modes. They are derivable from the axial  $z$ -components of the magnetic and electric Hertzian vector potentials  $\Pi^e$  and  $\Pi^h$  [1, p. 349]

$$\begin{aligned}\mathbf{E} &= -j\omega\mu\nabla \times \Pi^h + \nabla \times \nabla \times \Pi^e, \\ \mathbf{H} &= j\omega\epsilon\nabla \times \Pi^e + \nabla \times \nabla \times \Pi^h,\end{aligned}\tag{2.1}$$



where an  $\exp(j\omega t)$  time dependence of the fields is assumed, with angular frequency  $\omega$ .  $\epsilon$  denotes the permittivity of the medium and  $\mu$  denotes the permeability of the medium. The Hertzian potentials can be written as a sum of the products of the eigenfunctions  $\Psi^{h,e}(x, y)$  and the propagation factor  $\exp(\pm\gamma_{m,n}z)$  for each mode in the waveguide

$$\begin{aligned} \Pi_z^h &= \sum_{m=0}^{\infty} \sum_{n=0}^{\infty} A_{m,n}^{+,h} \Psi_{m,n}^h \exp(-\gamma_{m,n}z) + A_{m,n}^{-,h} \Psi_{m,n}^h \exp(+\gamma_{m,n}z), \\ \Pi_z^e &= \sum_{m=0}^{\infty} \sum_{n=0}^{\infty} A_{m,n}^{+,e} \Psi_{m,n}^e \exp(-\gamma_{m,n}z) + A_{m,n}^{-,e} \Psi_{m,n}^e \exp(+\gamma_{m,n}z). \end{aligned} \tag{2.2}$$

The prime in Eq. (2.2) indicates that the term  $m = n = 0$  is omitted from the summation.  $A_{m,n}^{+,e;h}$  represents the amplitude of a wave traveling in the  $+z$  direction while  $A_{m,n}^{-,e;h}$  designates the amplitude of a wave traveling in the  $-z$  direction. The TM and TE modes can be deduced from the solutions to the scalar Helmholtz equation on the waveguide cross section  $\mathcal{W}$  with Dirichlet and Neumann boundary conditions, respectively, on the boundary  $\partial\mathcal{W}$  (see Fig. 2.1). We find

$$\begin{aligned} \Psi_{m,n}^h(x, y) &= \sin\left(\frac{m\pi}{a}x\right) \sin\left(\frac{n\pi}{b}y\right), \quad m, n = 1, 2, \dots \\ \Psi_{m,n}^e(x, y) &= \cos\left(\frac{m\pi}{a}x\right) \cos\left(\frac{n\pi}{b}y\right), \quad m, n = 0, 1, 2, \dots \end{aligned} \tag{2.3}$$

where  $\gamma_{m,n} = j\sqrt{k^2 - \left(\frac{m\pi}{a}\right)^2 - \left(\frac{n\pi}{b}\right)^2}$  is the propagation constant and  $k = \omega\sqrt{\mu\epsilon}$  denotes the wave number in the medium filling the waveguide. If the medium in the waveguide is lossless then the cutoff frequency  $f_c$  of the  $\text{TE}_{m,n}$  or the  $\text{TM}_{m,n}$  mode is given by

$$f_c = \frac{1}{2\sqrt{\epsilon\mu}} \sqrt{\left(\frac{m}{a}\right)^2 + \left(\frac{n}{b}\right)^2}. \tag{2.4}$$

The propagation constants of the  $\text{TE}_{m,n}$  and the  $\text{TM}_{m,n}$  modes can be written as

$$\gamma_{m,n} = \begin{cases} jk\sqrt{1 - \left(\frac{f_c}{f}\right)^2} & \text{if } f > f_c, \\ k\sqrt{\left(\frac{f_c}{f}\right)^2 - 1} & \text{if } f < f_c, \end{cases} \tag{2.5}$$

where the frequency  $f$  is given by  $\frac{\omega}{2\pi}$ . The modal characteristic admittances are found to be  $Y_{m,n}^{\text{TE}} = -j\frac{\gamma_{m,n}}{\omega\mu}$  and  $Y_{m,n}^{\text{TM}} = j\frac{\omega\epsilon}{\gamma_{m,n}}$  for the TE and TM mode, respectively. Those

quantities are real and positive for frequencies above cutoff, and are purely imaginary, with a positive imaginary part, for frequencies below cutoff.

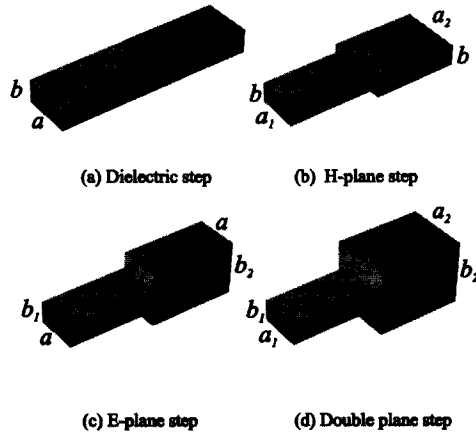


Figure 2.2: Examples of step discontinuities in rectangular waveguides.

### The $TE_{1,0}$ mode

Since the  $TE_{1,0}$  mode is the mode that is dominant and most commonly used in a rectangular waveguide, some expressions concerning its field distribution are repeated here. From the results given earlier, the nonzero field components of the  $TE_{1,0}$  mode are described by the following (propagation in the  $+z$  direction is assumed)

$$\begin{aligned}
 E_y &= E_0 \cos\left(\frac{\pi x}{a}\right) \exp(-j\beta_{1,0}z), \\
 H_x &= -E_0 Y_{1,0} \cos\left(\frac{\pi x}{a}\right) \exp(-j\beta_{1,0}z), \\
 H_z &= \frac{\pi E_0}{j\omega\mu a} \sin\left(\frac{\pi x}{a}\right) \exp(-j\beta_{1,0}z),
 \end{aligned} \tag{2.6}$$

where  $Y_{1,0} = \frac{\beta_{1,0}}{\omega\mu}$  is the wave admittance and  $\gamma_{1,0} = j\beta_{1,0} = j\sqrt{k^2 - \left(\frac{\pi}{a}\right)^2}$  the propagation constant of the  $TE_{1,0}$  mode.

### 2.2.2 Scattering matrix of step discontinuities

When the fundamental mode in a waveguide is excited, this is usually achieved by means of a coaxial line with its inner conductor extending a distance  $d$  into the waveguide [1, p. 471], it will propagate unperturbed inside the waveguide until some discontinuity is encountered. A discontinuity may be a change in the dielectric constant (i.e. dielectric step), the dimensions of the waveguide (i.e. E-plane, H-plane or double step), as pictured in Fig. 2.2, or simply the termination of the waveguide in a flange (i.e. aperture radiation). The presence of a discontinuity in a waveguide will cause a reflection of the fundamental mode and a storage of reactive energy in the vicinity of the discontinuity plane because of the excitation of higher-order waveguide modes which are evanescent, i.e. decay exponentially with distance from the discontinuity [2, p. 311]. Exact solution of Maxwell's equation for the field distribution existing near a discontinuity is a very difficult task [1, p. 547]. However, since we are interested only in the effect on the fundamental mode, the detailed nature of the diffraction field around the discontinuity is not required.

In this section we apply the modal analysis method to analyze the general step discontinuity problem of Fig. 2.3. The transversal electromagnetic field  $\{\mathbf{E}_t, \mathbf{H}_t\}$  in each waveguide region, 1 or 2 (see Fig. 2.3), is expanded in a complete set of waveguide modes, Eq. (2.2). In the region  $z < 0$  we can write the following

$$\mathbf{E}_t = \sum_{m,n}^{\infty'} \mathbf{e}_{m,n}^{(1),\text{TE}}(x,y) \left\{ a_{m,n}^{(1),\text{TE}} \exp(-\gamma_{m,n}^{(1)} z) + b_{m,n}^{(1),\text{TE}} \exp(\gamma_{m,n}^{(1)} z) \right\} / \sqrt{Y_{m,n}^{(1),\text{TE}}} \\ + \sum_{m,n}^{\infty'} \mathbf{e}_{m,n}^{(1),\text{TM}}(x,y) \left\{ a_{m,n}^{(1),\text{TM}} \exp(-\gamma_{m,n}^{(1)} z) + b_{m,n}^{(1),\text{TM}} \exp(\gamma_{m,n}^{(1)} z) \right\} / \sqrt{Y_{m,n}^{(1),\text{TM}}}, \quad (2.7)$$

$$\mathbf{H}_t = \sum_{m,n}^{\infty'} \mathbf{i}_z \times \mathbf{e}_{m,n}^{(1),\text{TE}}(x,y) \sqrt{Y_{m,n}^{(1),\text{TE}}} \left\{ a_{m,n}^{(1),\text{TE}} \exp(-\gamma_{m,n}^{(1)} z) - b_{m,n}^{(1),\text{TE}} \exp(\gamma_{m,n}^{(1)} z) \right\} \\ + \sum_{m,n}^{\infty'} \mathbf{i}_z \times \mathbf{e}_{m,n}^{(1),\text{TM}}(x,y) \sqrt{Y_{m,n}^{(1),\text{TM}}} \left\{ a_{m,n}^{(1),\text{TM}} \exp(-\gamma_{m,n}^{(1)} z) - b_{m,n}^{(1),\text{TM}} \exp(\gamma_{m,n}^{(1)} z) \right\}. \quad (2.8)$$

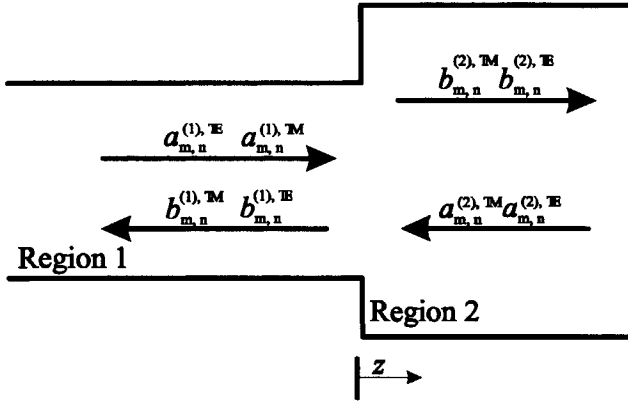


Figure 2.3: Different waves scattered at a waveguide step discontinuity.

The transversal field in the region  $z > 0$  can be written as

$$\mathbf{E}_t = \sum_{m,n}^{\infty'} \mathbf{e}_{m,n}^{(2),\text{TE}}(x, y) \left\{ a_{m,n}^{(2),\text{TE}} \exp(\gamma_{m,n}^{(2)} z) + b_{m,n}^{(2),\text{TE}} \exp(-\gamma_{m,n}^{(2)} z) \right\} / \sqrt{Y_{m,n}^{(2),\text{TE}}} \\ + \sum_{m,n}^{\infty'} \mathbf{e}_{m,n}^{(2),\text{TM}}(x, y) \left\{ a_{m,n}^{(2),\text{TM}} \exp(\gamma_{m,n}^{(2)} z) + b_{m,n}^{(2),\text{TM}} \exp(-\gamma_{m,n}^{(2)} z) \right\} / \sqrt{Y_{m,n}^{(2),\text{TM}}}, \quad (2.9)$$

$$\mathbf{H}_t = - \sum_{m,n}^{\infty'} \mathbf{i}_z \times \mathbf{e}_{m,n}^{(2),\text{TE}}(x, y) \sqrt{Y_{m,n}^{(2),\text{TE}}} \left\{ a_{m,n}^{(2),\text{TE}} \exp(\gamma_{m,n}^{(2)} z) - b_{m,n}^{(2),\text{TE}} \exp(-\gamma_{m,n}^{(2)} z) \right\} \\ - \sum_{m,n}^{\infty'} \mathbf{i}_z \times \mathbf{e}_{m,n}^{(2),\text{TM}}(x, y) \sqrt{Y_{m,n}^{(2),\text{TM}}} \left\{ a_{m,n}^{(2),\text{TM}} \exp(\gamma_{m,n}^{(2)} z) - b_{m,n}^{(2),\text{TM}} \exp(-\gamma_{m,n}^{(2)} z) \right\}, \quad (2.10)$$

where  $a_{m,n}^{(1),\text{TE};\text{TM}}$  and  $a_{m,n}^{(2),\text{TE};\text{TM}}$  represent the amplitudes of the waves incident upon the discontinuity plane,  $z = 0$ , from regions 1 and 2, respectively, while  $b_{m,n}^{(1),\text{TE};\text{TM}}$  and  $b_{m,n}^{(2),\text{TE};\text{TM}}$  are amplitudes of the waves reflected by the discontinuity plane in region 1 and 2, respectively. The functions  $\mathbf{e}_{m,n}^{\text{TE}}(x, y)$  and  $\mathbf{e}_{m,n}^{\text{TM}}(x, y)$  are the orthonormalized transverse field distributions of the  $(m, n)^{\text{th}}$  transverse electric and magnetic mode, respectively, in each waveguide section. As in [3], the transverse field distributions are

normalized. After a simple coordinate translation we obtain

$$\begin{aligned}
 \mathbf{e}_{m,n}^{\text{TE}} &= N_{m,n} \left\{ k_{y,n} \cos \left( k_{x,m} \left( x + \frac{a}{2} \right) \right) \sin \left( k_{y,n} \left( y + \frac{b}{2} \right) \right) \mathbf{i}_x \right. \\
 &\quad \left. - k_{x,m} \sin \left( k_{x,m} \left( x + \frac{a}{2} \right) \right) \cos \left( k_{y,n} \left( y + \frac{b}{2} \right) \right) \mathbf{i}_y \right\}, \\
 \mathbf{e}_{m,n}^{\text{TM}} &= N_{m,n} \left\{ k_{x,m} \cos \left( k_{x,m} \left( x + \frac{a}{2} \right) \right) \sin \left( k_{y,n} \left( y + \frac{b}{2} \right) \right) \mathbf{i}_x \right. \\
 &\quad \left. + k_{y,n} \sin \left( k_{x,m} \left( x + \frac{a}{2} \right) \right) \cos \left( k_{y,n} \left( y + \frac{b}{2} \right) \right) \mathbf{i}_y \right. \\
 &\quad \left. - \frac{(k_{x,m}^2 + k_{y,n}^2)}{\gamma_{m,n}} \sin \left( k_{x,m} \left( x + \frac{a}{2} \right) \right) \sin \left( k_{y,n} \left( y + \frac{b}{2} \right) \right) \mathbf{i}_z \right\},
 \end{aligned} \tag{2.11}$$

where  $N_{m,n} = \sqrt{\frac{\epsilon_m \epsilon_n}{ab}} \frac{1}{\sqrt{k_{x,m}^2 + k_{y,n}^2}}$  is the normalization factor, and  $\epsilon_p = \begin{cases} 1 & \text{if } (p = 0) \\ 2 & \text{if } (p \neq 0) \end{cases}$ .

At the interface  $z = 0$ , the transversal components of the electromagnetic field must be continuous. This leads to the following conditions

$$\begin{aligned}
 \lim_{z \downarrow 0} \mathbf{H}_t(x, y, z) &= \lim_{z \uparrow 0} \mathbf{H}_t(x, y, z), \text{ if } (x, y) \in \mathcal{S}_1 \\
 \lim_{z \downarrow 0} \mathbf{E}_t(x, y, z) &= \begin{cases} \lim_{z \uparrow 0} \mathbf{E}_t(x, y, z), & \text{if } (x, y) \in \mathcal{S}_1, \\ 0, & \text{if } (x, y) \in \mathcal{S}_2 \setminus \mathcal{S}_1, \end{cases}
 \end{aligned} \tag{2.12}$$

where  $\mathcal{S}_1$  and  $\mathcal{S}_2$  represent the waveguide cross sections at the step discontinuity; we have assumed  $\mathcal{S}_2 > \mathcal{S}_1$ . Substitution of Eqs. (2.7), (2.8), (2.9) and (2.10) by Eq. (2.12) gives rise to a linear system which cannot be solved since it must hold for an infinite number of points  $(x, y)$ . Hence, the problem as stated above results in a strong form and an additional weighting technique is needed to make the above equations numerically solvable. An appropriate weak form is obtained by testing Eq. (2.12) in its strong form with a sequence of transversal modal functions. In order to obtain such weak equivalents, we multiply the first part of Eq. (2.12) with the vectorial testing functions  $\mathbf{e}_{k,l}^{(1),\text{TE}}$  and  $\mathbf{e}_{k,l}^{(1),\text{TM}}$ , respectively, and integrate the result over the domain  $\mathcal{S}_1$ .

We obtain

$$\begin{aligned}
& \sum_{m,n}^{\infty} \sqrt{Y_{m,n}^{(2),\text{TE}}} \left\{ b_{m,n}^{(2),\text{TE}} - a_{m,n}^{(2),\text{TE}} \right\} \int_{S_1} \mathbf{e}_{m,n}^{(2),\text{TE}}(x,y) \cdot \mathbf{e}_{k,l}^{(1),\text{TE}}(x,y) dA \\
& + \sqrt{Y_{m,n}^{(2),\text{TM}}} \left\{ b_{m,n}^{(2),\text{TM}} - a_{m,n}^{(2),\text{TM}} \right\} \int_{S_1} \mathbf{e}_{m,n}^{(2),\text{TM}}(x,y) \cdot \mathbf{e}_{k,l}^{(1),\text{TE}}(x,y) dA = \\
& \sum_{m,n}^{\infty} \sqrt{Y_{m,n}^{(1),\text{TE}}} \left\{ a_{m,n}^{(1),\text{TE}} - b_{m,n}^{(1),\text{TE}} \right\} \int_{S_1} \mathbf{e}_{m,n}^{(1),\text{TE}}(x,y) \cdot \mathbf{e}_{k,l}^{(1),\text{TE}}(x,y) dA \\
& + \sqrt{Y_{m,n}^{(1),\text{TM}}} \left\{ a_{m,n}^{(1),\text{TM}} - b_{m,n}^{(1),\text{TM}} \right\} \int_{S_1} \mathbf{e}_{m,n}^{(1),\text{TM}}(x,y) \cdot \mathbf{e}_{k,l}^{(1),\text{TE}}(x,y) dA,
\end{aligned} \tag{2.13}$$

and

$$\begin{aligned}
& \sum_{m,n}^{\infty} \sqrt{Y_{m,n}^{(2),\text{TE}}} \left\{ b_{m,n}^{(2),\text{TE}} - a_{m,n}^{(2),\text{TE}} \right\} \int_{S_1} \mathbf{e}_{m,n}^{(2),\text{TE}}(x,y) \cdot \mathbf{e}_{k,l}^{(1),\text{TM}}(x,y) dA \\
& + \sqrt{Y_{m,n}^{(2),\text{TM}}} \left\{ b_{m,n}^{(2),\text{TM}} - a_{m,n}^{(2),\text{TM}} \right\} \int_{S_1} \mathbf{e}_{m,n}^{(2),\text{TM}}(x,y) \cdot \mathbf{e}_{k,l}^{(1),\text{TM}}(x,y) dA = \\
& \sum_{m,n}^{\infty} \sqrt{Y_{m,n}^{(1),\text{TE}}} \left\{ a_{m,n}^{(1),\text{TE}} - b_{m,n}^{(1),\text{TE}} \right\} \int_{S_1} \mathbf{e}_{m,n}^{(1),\text{TE}}(x,y) \cdot \mathbf{e}_{k,l}^{(1),\text{TM}}(x,y) dA \\
& + \sqrt{Y_{m,n}^{(1),\text{TM}}} \left\{ a_{m,n}^{(1),\text{TM}} - b_{m,n}^{(1),\text{TM}} \right\} \int_{S_1} \mathbf{e}_{m,n}^{(1),\text{TM}}(x,y) \cdot \mathbf{e}_{k,l}^{(1),\text{TM}}(x,y) dA.
\end{aligned} \tag{2.14}$$

Subsequently, we multiply the second part of Eq. (2.12) with the vectorial testing functions  $\mathbf{e}_{k,l}^{(2),\text{TE}}$  and  $\mathbf{e}_{k,l}^{(2),\text{TM}}$ , respectively, and integrate the result over the domain  $S_2$ . We obtain

$$\begin{aligned}
& \sum_{m,n}^{\infty} \frac{1}{\sqrt{Y_{m,n}^{(2),\text{TE}}}} \left\{ a_{m,n}^{(2),\text{TE}} + b_{m,n}^{(2),\text{TE}} \right\} \int_{S_2} \mathbf{e}_{m,n}^{(2),\text{TE}}(x,y) \cdot \mathbf{e}_{k,l}^{(2),\text{TE}}(x,y) dA \\
& + \frac{1}{\sqrt{Y_{m,n}^{(2),\text{TM}}}} \left\{ a_{m,n}^{(2),\text{TM}} + b_{m,n}^{(2),\text{TM}} \right\} \int_{S_2} \mathbf{e}_{m,n}^{(2),\text{TM}}(x,y) \cdot \mathbf{e}_{k,l}^{(2),\text{TE}}(x,y) dA = \\
& \sum_{m,n}^{\infty} \frac{1}{\sqrt{Y_{m,n}^{(1),\text{TE}}}} \left\{ a_{m,n}^{(1),\text{TE}} + b_{m,n}^{(1),\text{TE}} \right\} \int_{S_1} \mathbf{e}_{m,n}^{(1),\text{TE}}(x,y) \cdot \mathbf{e}_{k,l}^{(2),\text{TE}}(x,y) dA \\
& + \frac{1}{\sqrt{Y_{m,n}^{(1),\text{TM}}}} \left\{ a_{m,n}^{(1),\text{TM}} + b_{m,n}^{(1),\text{TM}} \right\} \int_{S_1} \mathbf{e}_{m,n}^{(1),\text{TM}}(x,y) \cdot \mathbf{e}_{k,l}^{(2),\text{TE}}(x,y) dA,
\end{aligned} \tag{2.15}$$

and

$$\begin{aligned}
& \sum_{m,n}^{\infty} \frac{1}{\sqrt{Y_{m,n}^{(2),\text{TE}}}} \{a_{m,n}^{(2),\text{TE}} + b_{m,n}^{(2),\text{TE}}\} \int_{S_2} \mathbf{e}_{m,n}^{(2),\text{TE}}(x,y) \cdot \mathbf{e}_{k,l}^{(2),\text{TM}}(x,y) dA \\
& + \frac{1}{\sqrt{Y_{m,n}^{(2),\text{TM}}}} \{a_{m,n}^{(2),\text{TM}} + b_{m,n}^{(2),\text{TM}}\} \int_{S_2} \mathbf{e}_{m,n}^{(2),\text{TM}}(x,y) \cdot \mathbf{e}_{k,l}^{(2),\text{TM}}(x,y) dA = \\
& \sum_{m,n}^{\infty} \frac{1}{\sqrt{Y_{m,n}^{(1),\text{TE}}}} \{a_{m,n}^{(1),\text{TE}} + b_{m,n}^{(1),\text{TE}}\} \int_{S_1} \mathbf{e}_{m,n}^{(1),\text{TE}}(x,y) \cdot \mathbf{e}_{k,l}^{(2),\text{TM}}(x,y) dA \\
& + \frac{1}{\sqrt{Y_{m,n}^{(1),\text{TM}}}} \{a_{m,n}^{(1),\text{TM}} + b_{m,n}^{(1),\text{TM}}\} \int_{S_1} \mathbf{e}_{m,n}^{(1),\text{TM}}(x,y) \cdot \mathbf{e}_{k,l}^{(2),\text{TM}}(x,y) dA,
\end{aligned} \tag{2.16}$$

Applying the orthogonality property of the waveguide modal functions we obtain the following matrix equation

$$\begin{bmatrix} \mathbf{I} & \mathbf{V}^T \\ \mathbf{V} & -\mathbf{I} \end{bmatrix} \begin{bmatrix} \mathbf{a}^{(1),\text{TE}} \\ \mathbf{a}^{(1),\text{TM}} \\ \mathbf{a}^{(2),\text{TE}} \\ \mathbf{a}^{(2),\text{TM}} \end{bmatrix} = \begin{bmatrix} \mathbf{I} & \mathbf{V}^T \\ -\mathbf{V} & \mathbf{I} \end{bmatrix} \begin{bmatrix} \mathbf{b}^{(1),\text{TE}} \\ \mathbf{b}^{(1),\text{TM}} \\ \mathbf{b}^{(2),\text{TE}} \\ \mathbf{b}^{(2),\text{TM}} \end{bmatrix}. \tag{2.17}$$

In Eq. (2.17) the sub-matrix  $\mathbf{I}$  denotes a unity matrix and  $\mathbf{V}^T$  is the transpose of  $\mathbf{V}$ . The sub-matrix  $\mathbf{V}$  involves reaction integrals between the modes of the two adjacent sections to the discontinuity and is given by [4]

$$\mathbf{V} = \begin{bmatrix} \mathbf{V}^{\text{TE-TE}} & \mathbf{V}^{\text{TM-TE}} \\ \mathbf{V}^{\text{TE-TM}} & \mathbf{V}^{\text{TM-TM}} \end{bmatrix}, \tag{2.18}$$

where

$$\begin{aligned}
\mathbf{V}_{p,q}^{\text{TE-TE}} &= \sqrt{\frac{Y_p^{(2),\text{TE}}}{Y_q^{(1),\text{TE}}}} \int_{S_1} \mathbf{e}_q^{(1),\text{TE}}(x,y) \cdot \mathbf{e}_p^{(2),\text{TE}}(x,y) dA, \\
\mathbf{V}_{p,q}^{\text{TE-TM}} &= \sqrt{\frac{Y_p^{(2),\text{TM}}}{Y_q^{(1),\text{TE}}}} \int_{S_1} \mathbf{e}_q^{(1),\text{TE}}(x,y) \cdot \mathbf{e}_p^{(2),\text{TM}}(x,y) dA, \\
\mathbf{V}_{p,q}^{\text{TM-TE}} &= \sqrt{\frac{Y_p^{(2),\text{TE}}}{Y_q^{(1),\text{TM}}}} \int_{S_1} \mathbf{e}_q^{(1),\text{TM}}(x,y) \cdot \mathbf{e}_p^{(2),\text{TE}}(x,y) dA, \\
\mathbf{V}_{p,q}^{\text{TM-TM}} &= \sqrt{\frac{Y_p^{(2),\text{TM}}}{Y_q^{(1),\text{TM}}}} \int_{S_1} \mathbf{e}_q^{(1),\text{TM}}(x,y) \cdot \mathbf{e}_p^{(2),\text{TM}}(x,y) dA,
\end{aligned} \tag{2.19}$$

$q = (m, n)$  and  $p = (k, l)$  are mode indices. Finally, the scattering matrix  $S$  of the step discontinuity can be found from Eq. (2.17) if the linear system has been solved and is given by (see Appendix A)

$$\begin{aligned}
 S &= \begin{bmatrix} S_{11} & S_{12} \\ S_{21} & S_{22} \end{bmatrix}, \\
 S_{11} &= [V^T V + I]^{-1} [I - V^T V], \\
 S_{21} &= V [I + S_{11}], \\
 S_{12} &= S_{21}^T, \\
 S_{22} &= V S_{12} - I.
 \end{aligned} \tag{2.20}$$

When all modes are included,  $S_{ij}$  are sub-matrices of infinite rank. The matrices may be truncated at a given finite number of modes  $N$  consistent with a required numerical accuracy.

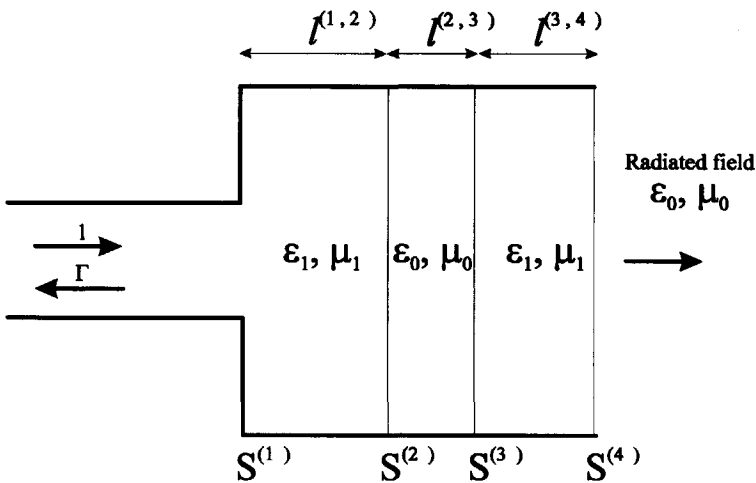


Figure 2.4: Example of a radiating aperture and its feeding section consisting of different discontinuities.



### 2.2.3 Scattering matrix of multiple step discontinuities

In this section a direct iterative algorithm is described for the analysis of multiple discontinuities in rectangular waveguides. Let us consider a microwave network representing the feeding section of a radiating aperture as shown in Fig. 2.4. This network is made by several elementary discontinuities and a number of uniform waveguide sections. Each discontinuity is represented by a scattering matrix (see Fig. 2.5). The relationship between incoming and outgoing waves for the  $i^{\text{th}}$  discontinuity is given by

$$\begin{bmatrix} b_1^{(i)} \\ b_2^{(i)} \end{bmatrix} = [S^{(i)}] \begin{bmatrix} a_1^{(i)} \\ a_2^{(i)} \end{bmatrix} \quad (2.21)$$

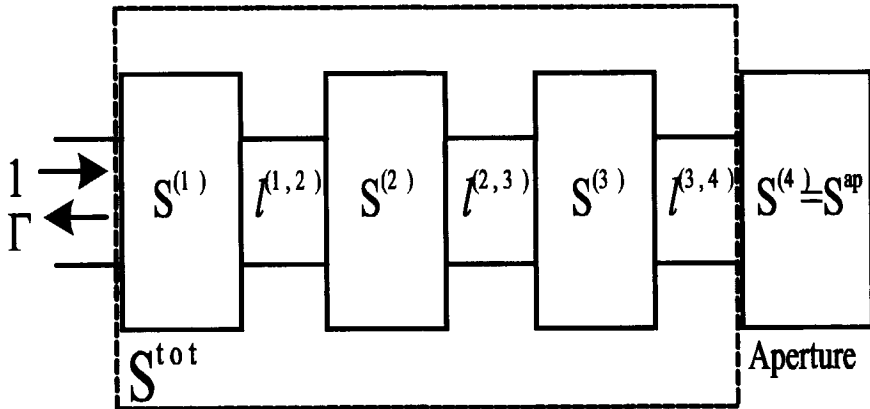


Figure 2.5: Equivalent transmission line model of an aperture antenna represented by a scattering matrix of each discontinuity and the overall scattering matrix of the feeding section.

Sequential waveguide discontinuities are commonly treated by transmission matrix parameters instead of scattering matrix parameters. However, this is not appropriate when higher-order modes are included which are excited below their cut-off frequency. For certain frequencies, the transmission matrix parameters will contain exponential

functions with a positive argument. This may lead to numerical instabilities. A direct combination of the involved scattering matrices is preferable. Although this procedure is quite complex, it guarantees numerical stability, since it involves only exponential functions with negative arguments [5]. Let  $S^{(i)}$  denote the scattering matrix of the  $i^{\text{th}}$  discontinuity and  $S^{(i+1)}$  the scattering matrix of the  $(i+1)^{\text{th}}$  discontinuity. Both discontinuities are adjacent and separated by a uniform waveguide section of length  $l^{(i,i+1)}$ . The combined scattering matrix  $S^{(i,i+1)}$ , representing the two discontinuities with index  $i$  and  $i+1$  and including the uniform waveguide section in between, can be obtained if the following scheme is used[3]

$$\begin{bmatrix} b_1^{(i)} \\ b_2^{(i+1)} \end{bmatrix} = \left( \begin{bmatrix} S_{11}^{(i)} & 0 \\ 0 & S_{22}^{(i+1)} \end{bmatrix} + \begin{bmatrix} S_{12}^{(i)}D & 0 \\ 0 & S_{21}^{(i+1)}D \end{bmatrix} \begin{bmatrix} ES_{11}^{(i+1)}D & E \\ F & FS_{22}^{(i)}D \end{bmatrix} \begin{bmatrix} S_{21}^{(i)} & 0 \\ 0 & S_{12}^{(i+1)} \end{bmatrix} \right) \begin{bmatrix} a_1^{(i)} \\ a_2^{(i+1)} \end{bmatrix}, \quad (2.22)$$

where  $E = [I - S_{11}^{(i+1)}DS_{22}^{(i)}D]^{-1}$ ,  $F = [I - S_{22}^{(i)}DS_{11}^{(i+1)}D]^{-1}$ , and  $I$  is the unit matrix.  $D$  is a diagonal matrix with entries  $D_{k,k} = \exp(-\gamma_{m,n}^{(i,i+1)}l^{(i,i+1)})$  due to the waveguide mode in the uniform waveguide section between the two discontinuities with index  $k = (m, n)$  and propagation constant  $\gamma_{m,n}^{(i,i+1)}$ . A series of more than two steps can be treated analogous to Eq. (2.22).

The scattering matrix representing the feeding section  $S^{\text{tot}}$ , when used together with the scattering matrix of the radiating aperture  $S^{\text{ap}}$ , will completely characterize the radiating aperture and its feeding part. The description of the aperture radiation model is the topic of the next section.

## 2.3 Characterization of the radiating aperture

This section discusses the radiation from miniaturized dielectric filled waveguide antennas terminated by a metallic flange of infinite size. The problem of radiating waveguide apertures may be formulated in terms of an integral equation having the tangential electric, and/or magnetic field in the aperture plane as the unknown function. One must first introduce suitable representations for the tangential fields in the regions both inside and outside the waveguide. The application of boundary conditions across the common aperture plane then leads to the solution of the problem. In this section we choose the variational approach introduced by Swift [6] and used in [7, p. 11] with a more general formulation that takes into account the higher-order modes and their mutual interactions. A novel expression for the aperture admittance is derived and new results are presented.

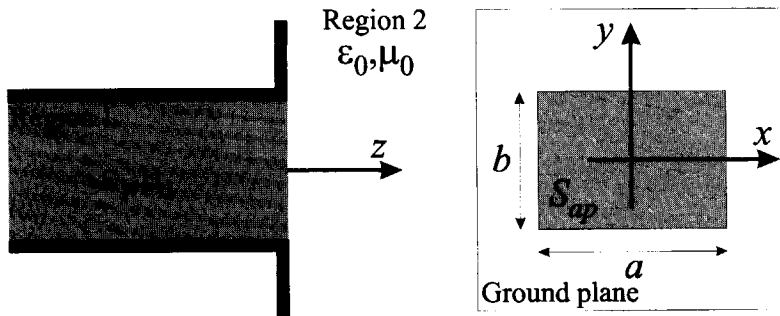


Figure 2.6: Waveguide antenna geometry.

### 2.3.1 Aperture admittance

The waveguide geometry and the coordinate system used throughout this section are shown in Fig. 2.6. The rectangular waveguide opens into a perfectly conducting flat flange of infinite size. The waveguide is filled with an isotropic, linearly reacting, homogeneous and lossless dielectric material. The face of the dielectric is flush-mounted

with the infinite ground plane. The dimensions of the dielectric material are assumed to be equal to the inner dimensions of the waveguide. The guide dimensions are such that only propagation of the dominant mode is allowed, namely propagation of the TE<sub>10</sub> mode. Over a cross section inside the guide sufficiently far from the aperture, any component of the fields is the vector sum of the components associated with incident and reflected waves of the dominant mode. In the vicinity of the aperture, however, additional higher-mode fields exist locally, excited by the aperture discontinuity. For an exact determination of the radiated fields it is necessary to know the exact field at the waveguide aperture, both in amplitude and phase. Hence, an accurate solution to the boundary problem has to include the contributions from the reflected dominant mode as well as contributions from the higher-order modes. We limit ourselves to the most practical case where the TE<sub>10</sub> mode is incident upon the aperture. We write the tangential field components as

$$\begin{aligned} \lim_{z \rightarrow 0} \mathbf{E}_y^{(1)} &= E_0(1 + \Gamma) \cos\left(\frac{\pi x}{a}\right) + \sum_{m=3,5,\dots}^{\infty} E_0 D_m (1 + \Gamma) \cos\left(\frac{m\pi x}{a}\right) \\ \lim_{z \rightarrow 0} \mathbf{H}_x^{(1)} &= -E_0 Y_{1,0} (1 - \Gamma) \cos\left(\frac{\pi x}{a}\right) + \sum_{m=3,5,\dots}^{\infty} E_0 Y_{m,0} D_m (1 + \Gamma) \cos\left(\frac{m\pi x}{a}\right), \end{aligned} \quad (2.23)$$

Eq.(2.23) is obtained from Eqs. (2.7) and (2.8) by letting

$$\begin{aligned} a_{m,n}^{\text{TM}} &= 0, \quad b_{m,n}^{\text{TM}} = 0, \quad \forall(m, n), \\ b_{m,n}^{\text{TE}} &= 0, \quad \text{if } m \text{ is even or } n \neq 0, \quad a_{m,n}^{\text{TE}} = 0, \quad \text{if } m \neq 1 \text{ or } n \neq 0, \\ a_{1,0}^{\text{TE}} &= 1, \quad b_{1,0}^{\text{TE}} = \Gamma, \quad E_0 = -\sqrt{\frac{\epsilon_m}{abY_{1,0}}}, \quad Y_{m,0} = Y_{m,0}^{\text{TE}}, \\ b_{m,0}^{\text{TE}} &= \sqrt{\frac{Y_{m,0}}{Y_{1,0}}} D_m (1 + \Gamma), \quad m = 3, 5, \dots, \\ \mathbf{e}_{m,0}^{\text{TE}}(x, y) &= -\sqrt{\frac{\epsilon_m}{ab}} \cos\left(\frac{m\pi x}{a}\right) \mathbf{i}_y, \end{aligned} \quad (2.24)$$

where  $\Gamma$  is the reflection coefficient of the fundamental mode,  $D_m$  is the excitation coefficient of the  $m^{\text{th}}$  mode and  $Y_{m,0}$  is the mode admittance. The remaining symbols were introduced in the previous sections. In Eq. (2.23) we assumed that only those modes which are symmetrical about the origin are excited and that the aperture

discontinuity induces a negligible  $E_x$  component. The first assumption is justified by the symmetry of the problem considered, while the second assumption is an approximation emanating from experimental observations. In order to solve the problem we need to find the unknown coefficients  $\Gamma$  and  $D_m$ . From the boundary conditions and Rumsey's reaction concept [8], we can deduce a variational formula for the aperture admittance. To do this we define the reaction integral [8] at the plane  $z = 0$  as follows

$$\langle 1, 1 \rangle = \lim_{z \uparrow 0} \iint_{S_{ap}} \mathbf{H}^{(1)}(x, y, z) \cdot (\mathbf{i}_z \times \mathbf{E}^{(1)}(x, y, z)) dA, \quad (2.25)$$

substituting Eq. (2.23) into Eq. (2.25) results

$$\langle 1, 1 \rangle = \iint_{S_{ap}} E_0^2 (1 + \Gamma) \left( \cos\left(\frac{\pi x}{a}\right) + \sum_{m=3,5,\dots}^{\infty} D_m \cos\left(\frac{m\pi x}{a}\right) \right) \left( Y_{1,0} (1 - \Gamma) \cos\left(\frac{\pi x}{a}\right) - \sum_{m=3,5,\dots}^{\infty} (1 + \Gamma) Y_{m,0} D_m \cos\left(\frac{m\pi x}{a}\right) \right) dx dy. \quad (2.26)$$

The orthogonality of the waveguide modal functions may be used in Eq. (2.26) to obtain

$$\langle 1, 1 \rangle = E_0^2 (1 + \Gamma)^2 \frac{ab}{2} \left( Y_{1,0} \frac{1 - \Gamma}{1 + \Gamma} - \sum_{m=3,5,\dots}^{\infty} D_m^2 Y_{m,0} \right). \quad (2.27)$$

The reflection coefficient  $\Gamma$  can be interpreted in terms of a normalized equivalent circuit admittance  $y_{ap}$  for the aperture by using the relation

$$y_{ap} = \frac{Y_{ap}}{Y_0} = \frac{1 - \Gamma}{1 + \Gamma}. \quad (2.28)$$

where  $Y_0 = \sqrt{\frac{\epsilon_0}{\mu_0}}$  the characteristic admittance of free-space. From Eq. (2.27) and Eq. (2.28), we can deduce the following stationary equation for the normalized aperture admittance

$$y_{ap} = \frac{\langle 1, 1 \rangle}{\frac{ab}{2} E_0^2 (1 + \Gamma)^2 Y_{1,0}} + \sum_{m=3,5,\dots}^{\infty} D_m^2 \frac{Y_{m,0}}{Y_{1,0}}. \quad (2.29)$$

The summation may be terminated at a given finite value of  $m$  consistent with the required numerical accuracy. Since the reaction is conserved across the aperture [8], we

can write the reaction integral in terms of the external fields radiated by the aperture

$$\langle 1, 1 \rangle = \langle 2, 2 \rangle = \lim_{z \downarrow 0} \iint_{S_{ap}} \mathbf{H}^{(2)}(x, y, z) \cdot (\mathbf{i}_z \times \mathbf{E}^{(2)}(x, y, z)) dA. \quad (2.30)$$

After applying the boundary conditions due to the presence of the metallic flange (i.e.  $E_y \neq 0$  only at the aperture) and Parseval's theorem, we obtain an expression for the reaction integral in the spectral domain

$$\langle 2, 2 \rangle = - \int_{-\infty}^{\infty} \int_{-\infty}^{\infty} E_y^{(2)}(x, y) H_x^{(2)}(x, y) dx dy = - \frac{1}{4\pi^2} \int_{-\infty}^{\infty} \int_{-\infty}^{\infty} \tilde{E}_y^{(2)}(k_x, k_y) \tilde{H}_x^{(2)}(k_x, k_y) dk_x dk_y, \quad (2.31)$$

where  $E_y^{(2)}(x, y)$ ,  $H_x^{(2)}(x, y)$ ,  $\tilde{E}_y^{(2)}(k_x, k_y)$ , and  $\tilde{H}_x^{(2)}(k_x, k_y)$  are the radiated electric and magnetic fields in the spatial and spectral domain, respectively, expressed at the plane  $z = 0$ . A thorough description of the spectral domain representation of the electromagnetic fields and the rest of the related formulation is provided in the following section.

### 2.3.2 Spectral representation of fields

The plane-wave spectra technique [9, p. 14] is based on the fact that any radiating field can be represented by a superposition of plane waves in different directions. The amplitude of the plane waves in the various directions, or the spectrum function, is determined from the tangential field in the aperture plane. This spectrum function represents the far-field radiation pattern of the aperture for real angles. The reactive aperture fields are represented by the complex directions of propagation in the spectrum function. For an aperture laying in the  $z = 0$  plane and radiating into  $z > 0$  half-space, the tangential electric and magnetic fields (in  $z > 0$ ) can be written in terms of the plane wave spectrum functions  $\tilde{f}(k_x, k_y)$  and  $\tilde{g}(k_x, k_y)$  of the electric potential  $\mathbf{F}$  and magnetic potentials  $\mathbf{A}$  [9, p. 10], respectively. After applying a spatial

Fourier transformation to the field quantities, we obtain

$$\begin{aligned}\tilde{E}_x^{(2)}(k_x, k_y, z) &= \left( \frac{ik_x k_z}{\omega \epsilon} \tilde{g}(k_x, k_y) + jk_y \tilde{f}(k_x, k_y) \right) \exp(-jk_z z), \\ \tilde{E}_y^{(2)}(k_x, k_y, z) &= \left( \frac{ik_y k_z}{\omega \epsilon} \tilde{g}(k_x, k_y) - jk_x \tilde{f}(k_x, k_y) \right) \exp(-jk_z z), \\ \tilde{E}_z^{(2)}(k_x, k_y, z) &= -j \frac{k_x^2 + k_y^2}{\omega \epsilon} \tilde{g}(k_x, k_y) \exp(-jk_z z),\end{aligned}\quad (2.32)$$

$$\begin{aligned}\tilde{H}_x^{(2)}(k_x, k_y, z) &= \left( -jk_y \tilde{g}(k_x, k_y) + \frac{ik_x k_z}{\omega \mu} \tilde{f}(k_x, k_y) \right) \exp(-jk_z z), \\ \tilde{H}_y^{(2)}(k_x, k_y, z) &= \left( jk_x \tilde{g}(k_x, k_y) + \frac{ik_y k_z}{\omega \mu} \tilde{f}(k_x, k_y) \right) \exp(-jk_z z), \\ \tilde{H}_z^{(2)}(k_x, k_y, z) &= \frac{j(k_x^2 - k_y^2)}{\omega \mu} \tilde{f}(k_x, k_y) \exp(-jk_z z).\end{aligned}\quad (2.33)$$

In order to express Eq. (2.31) only in terms of the tangential electric field, we first write the magnetic field component  $\tilde{H}_x^{(2)}$ , using Eq. (2.32) and Eq. (2.33), as

$$\tilde{H}_x^{(2)}(k_x, k_y, z) = \frac{-1}{\omega \mu k_z} \left( k_x k_y \tilde{E}_x^{(2)}(k_x, k_y, z) + (k^2 - k_x^2) \tilde{E}_y^{(2)}(k_x, k_y, z) \right), \quad (2.34)$$

According to the boundary conditions, the tangential components of the electric field are continuous at the common plane  $z = 0$

$$\begin{aligned}\lim_{z \downarrow 0} \tilde{E}_x^{(2)}(k_x, k_y, z) &= \lim_{z \uparrow 0} \tilde{E}_x^{(1)}(k_x, k_y, z), \\ \lim_{z \downarrow 0} \tilde{E}_y^{(2)}(k_x, k_y, z) &= \lim_{z \uparrow 0} \tilde{E}_y^{(1)}(k_x, k_y, z).\end{aligned}\quad (2.35)$$

Since we have assumed that  $E_x^{(1)}(x, y) = 0$ , it follows that  $\tilde{E}_x^{(1)}(k_x, k_y, 0) = 0$  and subsequently, with Eq. (2.34), equation (2.31) can be further simplified

$$\langle 2, 2 \rangle = \frac{1}{4\pi^2} \int_{-\infty}^{\infty} \int_{-\infty}^{\infty} \frac{k^2 - k_x^2}{\omega \mu k_z} \left( \tilde{E}_y^{(1)}(k_x, k_y, z=0) \right)^2 dk_x dk_y, \quad (2.36)$$

where

$$\tilde{E}_y^{(1)}(k_x, k_y, z=0) = \iint_{S_{\text{ap}}} E_y^{(1)}(x, y) \exp(jk_x x + jk_y y) dx dy. \quad (2.37)$$

Substituting  $E_y^{(1)}(x, y)$  from Eq. (2.23) into Eq. (2.36) and performing the integration yields the following

$$\tilde{E}_y^{(1)}(k_x, k_y) = E_0(1 + \Gamma)C_0(k_y) \left( C_1(k_x) + \sum_{m=3,5,\dots}^{\infty} D_m C_m(k_x) \right), \quad (2.38)$$

where

$$C_1(k_x) = \int_{-\frac{a}{2}}^{\frac{a}{2}} \cos\left(\frac{l\pi x}{a}\right) \exp(jk_x x) dx = \frac{2l\pi a j^{l-1} \cos\left(\frac{k_x a}{2}\right)}{(\pi l)^2 - (k_x a)^2}, \quad (2.39)$$

and

$$C_0(k_y) = \int_{-\frac{b}{2}}^{\frac{b}{2}} \exp(jk_y y) dy = \frac{b \sin\left(\frac{k_y b}{2}\right)}{k_y \frac{b}{2}}. \quad (2.40)$$

Squaring this expression we obtain

$$\begin{aligned} \left(\tilde{E}_y^{(1)}(k_x, k_y)\right)^2 &= E_0^2(1 + \Gamma)^2 C_0^2(k_y) \left( C_1^2(k_x) + 2 \sum_{m=3,5,\dots}^{\infty} C_1(k_x) C_m(k_x) D_m \right. \\ &\quad \left. + \sum_{m=3,5,\dots}^{\infty} \sum_{n=3,5,\dots}^{\infty} C_m(k_x) C_n(k_x) D_m D_n \right), \end{aligned} \quad (2.41)$$

The plane-wave spectrum functions  $\tilde{f}(k_x, k_y)$ , and  $\tilde{g}(k_x, k_y)$  can be evaluated directly from Eq. (2.32) and are found to be

$$\begin{bmatrix} \tilde{f}(k_x, k_y) \\ \tilde{g}(k_x, k_y) \end{bmatrix} = \frac{\omega \epsilon}{k_x(k_x^2 + k_y^2)} \tilde{E}_y^{(1)}(k_x, k_y) \begin{bmatrix} \frac{jk_x k_x}{\omega \epsilon} \\ -jk_y \end{bmatrix}. \quad (2.42)$$

Finally with substitution of Eq. (2.38) and Eq. (2.36) into Eq. (2.29) and after some mathematical manipulation we can write for the aperture admittance

$$y_{ap} = \frac{Y_{1,1}}{Y_{1,0}} + 2 \sum_{m=3,5,\dots}^{\infty} D_m \frac{Y_{1,m}}{Y_{1,0}} + \sum_{m=3,5,\dots}^{\infty} \sum_{n=3,5,\dots}^{\infty} D_m D_n \frac{Y_{m,n}}{Y_{1,0}} + \sum_{m=3,5,\dots}^{\infty} D_m^2 \frac{Y_{m,0}}{Y_{1,0}}, \quad (2.43)$$

or in matrix form

$$\begin{aligned} y_{ap} Y_{1,0} &= Y_{1,1} + 2 \begin{bmatrix} D_3 & \cdots & D_{\infty} \end{bmatrix} \cdot \begin{bmatrix} Y_{1,3} \\ \vdots \\ Y_{1,\infty} \end{bmatrix} \\ &+ \begin{bmatrix} D_3 & \cdots & D_{\infty} \end{bmatrix} \cdot \begin{bmatrix} Y_{3,3} + Y_{3,0} & Y_{3,5} & \cdots & Y_{3,\infty} \\ Y_{5,3} & Y_{5,5} + Y_{5,0} & \cdots & Y_{5,\infty} \\ \cdots & \cdots & \cdots & \cdots \\ Y_{\infty,3} & \cdots & \cdots & Y_{\infty,\infty} + Y_{\infty,0} \end{bmatrix} \cdot \begin{bmatrix} D_3 \\ \vdots \\ D_{\infty} \end{bmatrix} \end{aligned} \quad (2.44)$$



where  $Y_{m,n}$  ( $m, n = 1, 3, 5, \dots$ ) may be regarded as the mutual admittances between the  $TE_{n,0}$  and the  $TE_{m,0}$  modes respectively, and is given by

$$Y_{m,n} = -j^{m+n} nm \int_{-\infty}^{\infty} \int_{-\infty}^{\infty} \frac{2ab(k^2 - k_x^2) \sin^2(k_y \frac{b}{2}) \cos^2(k_x \frac{a}{2})}{\omega \mu k_z (k_y \frac{b}{2})^2 [(n\pi)^2 - (k_x a)^2] [(m\pi)^2 - (k_x a)^2]} dk_x dk_y. \quad (2.45)$$

We must now impose on Eq. (2.43) the condition that  $y_{ap}$  should be stationary for small arbitrary variations in the electric field distribution about its correct value. This condition is obtained by equating the partial derivatives of the unknown coefficients  $D_m$  to zero and gives the best possible solution to  $y_{ap}$  that can be obtained with the assumed field distribution. From Eq. (2.43) we obtain

$$\frac{\partial y_{ap}}{\partial D_m} = 0,$$

or in matrix form

$$\begin{bmatrix} Y_{3,3} + Y_{3,0} & Y_{3,5} & \cdots & Y_{3,\infty} \\ Y_{5,3} & Y_{5,5} + Y_{5,0} & \cdots & Y_{5,\infty} \\ \cdots & \cdots & \cdots & \cdots \\ Y_{\infty,3} & \cdots & \cdots & Y_{\infty,\infty} + Y_{\infty,0} \end{bmatrix} \begin{bmatrix} D_3 \\ D_5 \\ \vdots \\ D_{\infty} \end{bmatrix} = \begin{bmatrix} -Y_{1,3} \\ -Y_{1,5} \\ \vdots \\ -Y_{1,\infty} \end{bmatrix}. \quad (2.46)$$

This results in a novel expression for the aperture admittance of dielectric-filled waveguide antennas, namely

$$y_{ap} Y_{1,0} = Y_{1,1} + \begin{bmatrix} D_3 & \cdots & D_{\infty} \end{bmatrix} \begin{bmatrix} Y_{1,3} \\ \vdots \\ Y_{1,\infty} \end{bmatrix}. \quad (2.47)$$

In order to find the coefficient  $D_m$  a matrix inversion operation must be performed. The integrals in the expressions for  $Y_{m,n}$  ( $n, m = 3, 5, \dots$ ) are converted into forms suitable for numerical evaluation in Appendix A. Once the coefficients  $D_m$  are known, the aperture admittance  $y_{ap}$ , the reflection coefficient  $\Gamma$  and the aperture field distribution follow directly from Eqs. (2.47), (2.28) and (2.23), respectively.

### 2.3.3 Radiated far fields

Exact computation of the field in each point outside the opening is a difficult task. If the exact aperture field was known then the radiated field could be calculated exactly [10][11, p. 334][12, p. 460]. An exact formulation of the radiation from an open-ended waveguide can also be achieved by using the Wiener-Hopf method [13, p. 161], but this technique gives only asymptotic solutions for the far field, while in many cases both the near field and the far field are needed. Another limitation of this method is that it does not take into account the effect of the wall thickness and the metallic flange on which the aperture is mounted.

This section is devoted to the calculation of the radiated field in terms of the aperture field solution presented in the previous section. For an aperture mounted in an infinite plane the method gives an exact solution to the field radiated on one side of the aperture plane, the ( $z > 0$ ) half space. For an aperture in free space, approximate formulas based on the field equivalence principles [14, p. 106][15, p. 61][16] are presented.

#### **Aperture mounted on an infinite metallic flange: Exact solution**

For an aperture on an infinite metallic flange an exact solution can be achieved since the electric and magnetic fields in the aperture, Eq. (2.23), are known exactly, within numerical accuracy, after solution of the linear system in Eq. (2.46). The field in the half space ( $z > 0$ ) is uniquely determined by knowledge of either the tangential electric field or the tangential magnetic field in the aperture plane. Due to the fact that tangential component of the electric field is zero on the metallic flange, it is more convenient to determine the radiated field based on only the aperture electric field distribution. If we take the inverse Fourier transformation of the electric field

$\tilde{\mathbf{E}}^{(2)}(k_x, k_y, z)$ , represented by Eq. (2.32), with respect to  $k_x$  and  $k_y$  and let

$$\tilde{\Psi}(k_x, k_y) = \begin{bmatrix} \frac{jk_x k_z}{\omega\epsilon} \tilde{g}(k_x, k_y) + jk_y \tilde{f}(k_x, k_y) \\ \frac{jk_y k_z}{\omega\epsilon} \tilde{g}(k_x, k_y) - jk_x \tilde{f}(k_x, k_y) \\ -j \frac{k_x^2 + k_y^2}{\omega\epsilon} \tilde{g}(k_x, k_y) \end{bmatrix}, \quad (2.48)$$

we obtain

$$\mathbf{E}(\mathbf{r}) = \frac{1}{4\pi^2} \iint_{-\infty}^{\infty} \tilde{\Psi}(k_x, k_y) \exp(-j\mathbf{k} \cdot \mathbf{r}) dk_x dk_y. \quad (2.49)$$

In Eq. (2.49),  $\mathbf{r}$  denotes the position vector of a point in free space and  $\mathbf{k}$  represents the propagation vector. The far-zone radiated fields can be obtained by evaluating asymptotically Eq. (2.49) using the stationary-phase method. When  $r$ , the norm of the vector  $\mathbf{r}$ , tends to infinity the most significant contribution only comes from the stationary phase point. The dot product  $\mathbf{k} \cdot \mathbf{r}$  in Eq. (2.49) can be expressed in spherical coordinates as

$$\mathbf{k} \cdot \mathbf{r} = r \left( k_x \sin \theta \cos \phi + k_y \sin \theta \sin \phi + \sqrt{k_0^2 - k_x^2 - k_y^2} \cos \theta \right), \quad (2.50)$$

where we have used the expression of the vector  $\mathbf{r}$  in spherical coordinates, namely,  $\mathbf{r} = r(\sin \theta \cos \phi \mathbf{i}_x + \sin \theta \sin \phi \mathbf{i}_y + \cos \theta \mathbf{i}_z)$  and  $\mathbf{k} = k_x \mathbf{i}_x + k_y \mathbf{i}_y + \sqrt{k_0^2 - k_x^2 - k_y^2} \mathbf{i}_z$  with  $k_0 = \omega \sqrt{\mu_0 \epsilon_0}$ . The stationary phase points are found after solving the following equations

$$\frac{\partial \mathbf{k} \cdot \mathbf{r}}{\partial k_x} = 0 \quad \frac{\partial \mathbf{k} \cdot \mathbf{r}}{\partial k_y} = 0, \quad (2.51)$$

which gives  $k_x = k_0 \sin \theta \cos \phi$ , and  $k_y = k_0 \sin \theta \sin \phi$ . After some standard mathematical manipulations [15, pp. 61] we may write for the fields in the far zone

$$\mathbf{E}(\mathbf{r}) \sim j \frac{\exp(-jk_0 r)}{2\pi r} k_0 \cos \theta \tilde{\Psi}(k_0 \sin \theta \cos \phi, k_0 \sin \theta \sin \phi). \quad (2.52)$$

After evaluating the obtained expressions in spherical coordinates, we find

$$\begin{aligned} E_\theta(r, \theta, \phi) &\sim j \frac{\exp(-jk_0 r)}{2\pi r} k_0 \sin \phi \tilde{E}_y^{(1)}(k_0 \sin \theta \cos \phi, k_0 \sin \theta \sin \phi), \\ E_\phi(r, \theta, \phi) &\sim j \frac{\exp(-jk_0 r)}{2\pi r} k_0 \cos \theta \cos \phi \tilde{E}_y^{(1)}(k_0 \sin \theta \cos \phi, k_0 \sin \theta \sin \phi). \end{aligned} \quad (2.53)$$

where  $\tilde{E}_y^{(1)}$  is given by Eq. (2.38).

### Aperture in free space: Approximate solution

In this section we use the equivalence principles to derive an approximate expression for the field radiated from un-flanged dielectric-filled waveguide antennas. We first choose a closed surface with the opening as a part of it, and assume some values for the fields on this surface. For the aperture, these values may be assumed to be the field distribution obtained by using the method discussed in the previous section. Over the remainder of the surface, the field is assumed to be zero. Using the Green's representation of the electromagnetic fields [11, p. 80][12, p. 464], we can express the field in free space at any point lying outside the aperture as follows

$$\mathbf{E}(\mathbf{r}) = - \int_{\mathcal{S}_{ap}} \left\{ j\omega\mu_0 G(\mathbf{r}, \mathbf{r}') \mathbf{J}_S(\mathbf{r}') - \frac{1}{j\omega\epsilon_0} \nabla \cdot \mathbf{J}_S(\mathbf{r}') \nabla G(\mathbf{r}, \mathbf{r}') + (\nabla \times G(\mathbf{r}, \mathbf{r}') \mathbf{K}_S(\mathbf{r}')) \right\} dA', \quad (2.54)$$

$$\mathbf{H}(\mathbf{r}) = - \int_{\mathcal{S}_{ap}} \left\{ j\omega\epsilon_0 G(\mathbf{r}, \mathbf{r}') \mathbf{K}_S(\mathbf{r}') - \frac{1}{j\omega\mu_0} \nabla \cdot \mathbf{K}_S(\mathbf{r}') \nabla G(\mathbf{r}, \mathbf{r}') - (\nabla \times G(\mathbf{r}, \mathbf{r}') \mathbf{J}_S(\mathbf{r}')) \right\} dA', \quad (2.55)$$

where  $G(\mathbf{r}, \mathbf{r}')$  is the free-space Green's function given by  $G(\mathbf{r}, \mathbf{r}') = \frac{\exp(-jk_0|\mathbf{r}-\mathbf{r}'|)}{4\pi|\mathbf{r}-\mathbf{r}'|}$ ,  $\mathbf{r}$  represents the vector position of the point at which the field is computed while  $\mathbf{r}'$  is the vector position of the source element on the aperture. The above equations represent field solutions in terms of equivalent electric  $\mathbf{J}_S$  and magnetic  $\mathbf{K}_S$  sources lying on the aperture surface  $\mathcal{S}_{ap}$ . The nabla operator  $\nabla$  in Eqs. (2.54) and (2.55) operates only on the coordinate of the observation point  $\mathbf{r}$ . Applying the  $\nabla$ -operator within the field integrals results in the following expressions for the near fields

$$\mathbf{E}(\mathbf{r}) = \frac{-jk_0\eta_0}{4\pi} \int_{\mathcal{S}_{ap}} \left( [1 + p(1+p)] \mathbf{J}_S - (\mathbf{J}_S \cdot \hat{\mathbf{i}}_R) \hat{\mathbf{i}}_R [1 + 3p(1+p)] - \frac{1}{\eta_0} (\mathbf{K}_S \times \hat{\mathbf{i}}_R) (1+p) \right) G dA', \quad (2.56)$$

$$\mathbf{H}(\mathbf{r}) = \frac{-jk_0}{4\pi\eta_0} \int_{\mathcal{S}_{ap}} \left( [1 + p(1+p)] \mathbf{K}_S + (\mathbf{K}_S \cdot \hat{\mathbf{i}}_R) \hat{\mathbf{i}}_R [1 + 3p(1+p)] - \eta_0 (\mathbf{J}_S \times \hat{\mathbf{i}}_R) (1+p) \right) G dA', \quad (2.57)$$

where the following relations were used;  $R = |\mathbf{r} - \mathbf{r}'|$ ,  $\hat{\mathbf{i}}_R = \frac{\mathbf{r} - \mathbf{r}'}{R}$ ,  $\nabla \left( \frac{\exp(-jk_0 R)}{R} \right) = \left( jk_0 + \frac{1}{R} \right) \frac{\exp(-jk_0 R)}{R} \hat{\mathbf{i}}_R$  and  $p = 1/jk_0 R$ .  $\eta_0 = \sqrt{\frac{\mu_0}{\epsilon_0}}$  is the characteristic impedance of free space. The field in the far zone is found after using the well known far-field approximations [11, p. 87]. The result for the electric field is given by

$$\mathbf{E}(\mathbf{r}) \sim -\frac{j\omega\mu_0 \exp(-jk_0 r)}{4\pi r} \int_{S_{ap}} \left[ (\mathbf{J}_S - (\hat{\mathbf{i}}_r \cdot \mathbf{J}_S) \hat{\mathbf{i}}_r) + \sqrt{\frac{\epsilon_0}{\mu_0}} (\mathbf{K}_S \times \hat{\mathbf{i}}_r) \right] \exp(jk_0 \hat{\mathbf{i}}_r \cdot \mathbf{r}') dA'. \quad (2.58)$$

The equivalent electric and magnetic current distributions  $\mathbf{J}_S$  and  $\mathbf{K}_S$  on the aperture are related to the fields just inside the waveguide by application of the equivalence principle

$$\mathbf{J}_S(x, y) = \mathbf{i}_z \times \mathbf{H}^{(1)}(x, y, z = 0), \quad \mathbf{K}_S(x, y) = -\mathbf{i}_z \times \mathbf{E}^{(1)}(x, y, z = 0), \quad (2.59)$$

the aperture electric and magnetic fields used in (2.59) are those found in the previous section, given by Eq. (2.23). The evaluation of the radiated field can progress directly once the current, both electric and magnetic, distributions are known. Finally, after some straightforward computations, we find the following expression for the far field radiated by dielectric-filled waveguide antennas into free space

$$\begin{aligned} E_\theta(r, \theta, \phi) = \frac{jk_0 \exp(-jk_0 r)}{2r} E_0 ab \left\{ \left( \frac{1+\Gamma}{\pi^2 - (k_x a)^2} + \sum_{m=3,5,\dots}^{\infty} D_m \frac{m_j^{m-1}(1+\Gamma)}{(m\pi)^2 - (k_x a)^2} \right) + \eta_0 \cdot \right. \\ \left. \left( \frac{Y_{1,0}(1-\Gamma)}{\pi^2 - (k_x a)^2} - \sum_{m=3,5,\dots}^{\infty} D_m Y_{m,0} \frac{m_j^{m-1}(1+\Gamma)}{(m\pi)^2 - (k_x a)^2} \right) \cos \theta \right\} \cos \left( \frac{k_x a}{2} \right) \frac{\sin \left( \frac{k_y b}{2} \right)}{\frac{k_y b}{2}} \sin \phi, \end{aligned} \quad (2.60)$$

$$\begin{aligned} E_\phi(r, \theta, \phi) = \frac{jk_0 \exp(-jk_0 r)}{2r} E_0 ab \left\{ \left( \frac{1+\Gamma}{\pi^2 - (k_x a)^2} + \sum_{m=3,5,\dots}^{\infty} D_m \frac{m_j^{m-1}(1+\Gamma)}{(m\pi)^2 - (k_x a)^2} \right) \cos \theta \right. \\ \left. + \eta_0 \left( \frac{Y_{1,0}(1-\Gamma)}{\pi^2 - (k_x a)^2} - \sum_{m=3,5,\dots}^{\infty} D_m Y_{m,0} \frac{m_j^{m-1}(1+\Gamma)}{(m\pi)^2 - (k_x a)^2} \right) \right\} \cos \left( \frac{k_x a}{2} \right) \frac{\sin \left( \frac{k_y b}{2} \right)}{\frac{k_y b}{2}} \cos \phi, \end{aligned} \quad (2.61)$$

where  $k_x = k_0 \sin \theta \cos \phi$ ,  $k_y = k_0 \sin \theta \sin \phi$ , and  $k_z = k_0 \cos \theta$ .

## 2.4 Discussion of numerical results and experimental validation

To validate the analysis presented in the previous sections, we consider a number of numerical examples. First, three types of internal waveguide discontinuities are treated, namely, the E-plane step, the H-plane step, and the double-plane step. Since there are many examples related to this topic in open literature, the presented results are included for validation purposes only.

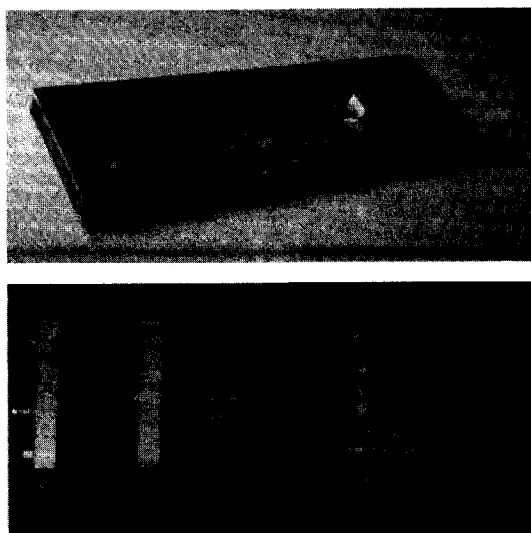


Figure 2.7: Example of two dielectric-filled waveguide antennas designed and constructed at IRCTR (L-band prototype: top, X-band prototype: bottom).

In the remainder of the section we will emphasise the aperture discontinuity problem, in particular the case of a dielectric filled waveguide with a very small cross section. Both the radiation mechanism and matching device (air gap) are discussed for a highly miniaturized antenna having a high aperture reflection coefficient. Key parameters like waveguide height and dielectric filling and their effect on the miniatur-

ization process are investigated thoroughly. The presented results include reflection coefficients for a different aperture geometry. Both E-field and H-field distributions are calculated for a better understanding of the radiation mechanism. The higher-order modes and their effect on the aperture admittance and far-field patterns are an important part of this study. The air-gap-matching network is investigated using the multi-mode analysis and design curves are presented in order to make the task of antenna matching easier even when having very high aperture reflections. Specific features useful as guidelines for implementation are presented. Solving for the mode coefficients at each discontinuity means solving the linear system of Eq. (2.17) in the case of a step discontinuity and Eq. (2.46) in the case of a radiating aperture. This is done iteratively by means of a conjugate-gradient scheme.

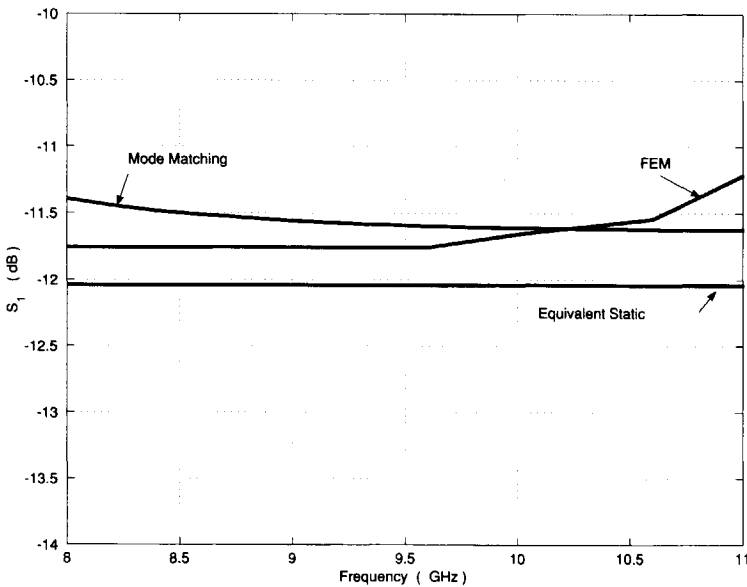


Figure 2.8: Input reflection coefficient of an E-plane step discontinuity in a rectangular waveguide with dimensions  $a_1 = a_2 = 2.286$  cm,  $b_1 = 0.6$  cm and  $b_2 = 1.0$  cm ( $\epsilon_r = 1$ ).

The Telecommunication and Teleobservation Technology group (TTT) at Delft University has been working on dielectric-filled waveguides for more than ten years [7, 17, 18]. A number of prototypes working at different frequency bands (S-, L-, and X-band) were already designed and constructed, see Fig. 2.7. The results obtained by the theory described in the previous sections were not only compared with measurements but also with results from different methods found in the open literature, like FEM [19] and Equivalent Static method [20].

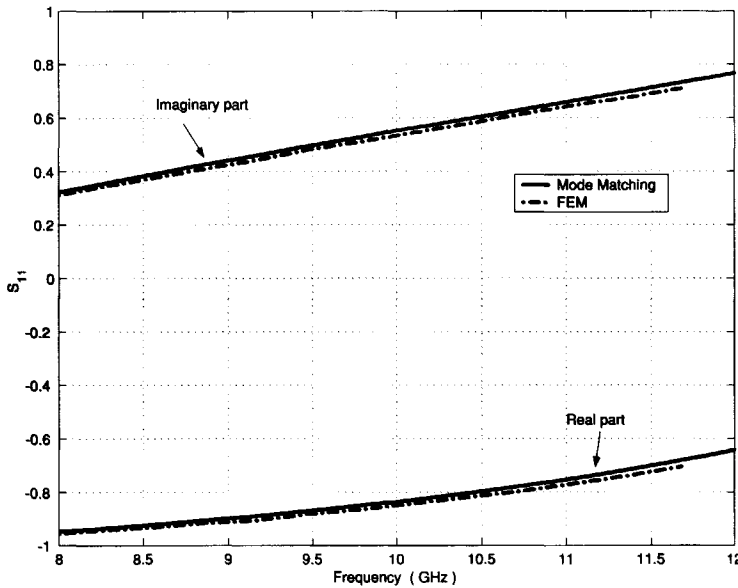


Figure 2.9: Input reflection coefficient of an H-Plane step discontinuity in rectangular waveguides with dimensions  $a_1 = 1.0\text{cm}$ ,  $a_2 = 2.286\text{cm}$  and  $b_1 = b_2 = 1.0\text{cm}$  ( $\epsilon_r = 1$ ).

### (a) Step in waveguide dimensions

To validate the developed code, we present numerical results of the reflection coefficient for three configurations, together with results obtained by FEM and the Equivalent Static method. The FEM results were taken from [19]. The analytical formulas



developed by Marcuvitz [20, p.296] were used to obtain the results for the Equivalent Static case. In all presented results the assumption was made that the dominant  $TE_{1,0}$  mode is incident on the discontinuity plane. The first result, Fig. 2.8, represents the reflection coefficient of an E-plane step discontinuity in rectangular waveguides with dimensions  $a_1 = a_2 = 2.286$  cm,  $b_1 = 0.6$  cm and  $b_2 = 1.0$  cm. Since the axes are concentric, only waves with mode indices  $m = 1, 3, 5, \dots$  and  $n = 0, 2, 4, \dots$  are excited. The number of modes required to represent the field components in the waveguide depends on the type of discontinuity that is analyzed and the waveguide dimensions. In this example 40 modes (both TE and TM) were used to represent the fields in both waveguide sections near the discontinuity plane. The second example is an H-plane step discontinuity in rectangular waveguide with dimensions  $a_1 = 1.0$  cm,  $a_2 = 2.286$  cm and  $b_1 = b_2 = 1.0$  cm. Both the real part and imaginary part of the reflection coefficient are shown in Fig. 2.9 versus frequency.

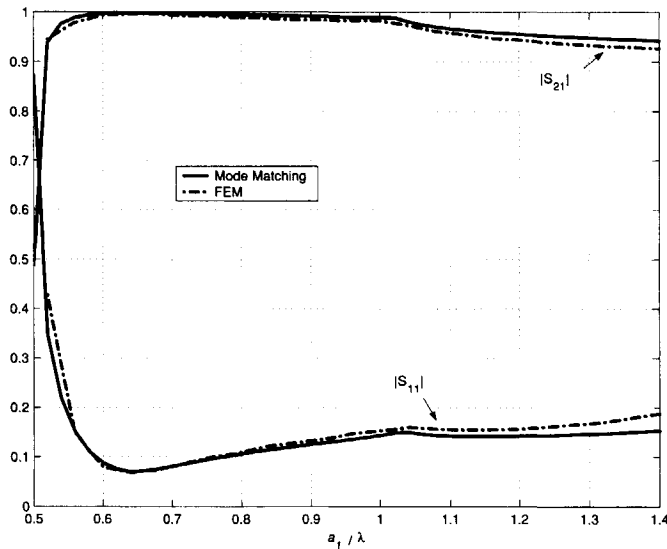


Figure 2.10: Scattering parameters of a double-step discontinuity with  $a_1 = 15.8$  mm,  $b_1 = 7.9$  mm,  $a_2 = 22.9$  mm, and  $b_2 = 10.2$  mm ( $\epsilon_r = 1$ ).

Finally the third example used for validation is a double-plane step waveguide discontinuity, Fig. 2.10, with dimensions  $a_1 = 15.8$  mm,  $b_1 = 7.9$  mm,  $a_2 = 22.9$  mm, and  $b_2 = 10.2$  mm. This problem was solved using 100 modes in both waveguide sections. The FEM results were obtained using 2700 tetrahedra, which cover the volume between two reference planes located 0.5 cm left and right of the discontinuity plane. A good agreement between the earlier published data and the numerical results obtained using the present code was observed.

Table 1: Reflection coefficient of the fundamental mode for a dielectric filled waveguide at 3.3 GHz (waveguide dimensions:  $a = b = 34.2$  mm,  $\epsilon_r = 2.53$ )

Number of Modes	Magnitude of $\Gamma$	Phase of $\Gamma$ in degrees
1	0.4247	38.90
3	0.4189	38.23
9	0.4254	38.07
11	0.4220	37.55
13	0.4216	37.60
15	0.4216	37.61

### (b) Aperture reflection coefficient

We now present numerical results for the aperture reflection coefficient obtained using the formulation given in section 2.3. The convergence of the algorithm is studied first. Although this was done for several apertures, only the results for a square aperture ( $a = b = 34.2$  mm at 3.3 GHz) and a flat aperture ( $a = 83$  mm,  $b = 10$  mm at 1.6 GHz) are given, see Tables 1 and 2. Both the magnitude and phase, versus the number of modes used to approximate the aperture field, are calculated. The results show a fast convergence. Measurements were performed on a waveguide with square cross section ( $a = b = 34.2$  mm) operating at the frequency of 3.3 GHz and filled with Rexolite ( $\epsilon_r = 2.53$ ).

Table 2: Reflection coefficient of the fundamental mode for a dielectric filled waveguide at 1.6 GHz (waveguide dimensions:  $a = 83$  mm,  $b = 10$  mm,  $\epsilon_r = 2.53$ )

Number of Modes	Magnitude of $\Gamma$	Phase of $\Gamma$ in degrees
1	0.8743	2.63
3	0.8737	2.50
9	0.8732	2.41
11	0.8734	2.40
13	0.8734	2.39
15	0.8733	2.39

First, the variation of the reflection coefficient  $\Gamma$  at the aperture versus frequency is considered. Fig. 2.11 shows the measurement results for two cases. Case (1), the aperture is radiating into free space and case (2) the aperture is loaded with an extended dielectric rod with relative permittivity  $\epsilon_r = 2.53$  and length  $l_{\text{rod}} = 90.6$  mm. In this figure, calculations are presented for an aperture radiating into free space and an aperture radiating into a dielectric filled half space ( $\epsilon_r = 2.53$ ). With the chosen configuration only the fundamental mode can propagate inside the dielectric filled waveguide. In Fig. 2.11 we see that by extending the dielectric outside of the waveguide the reflection coefficient at the aperture can be lowered. The lowest value one can achieve will always be higher than the value obtained when the antenna is radiating into a dielectric half-space filled with the same material. Other means of lowering the aperture reflection coefficient are the tapering of the outside of the metallic structure towards the aperture or the insertion of a matching network (i.e. irises, air gap, step,...) inside the waveguide. Note that the phase characteristic of the reflection coefficient is nearly flat. This is an advantage for an aperture matching design. During the measurements, we have found that a flat waveguide flange of standard dimensions is sufficient to approximate the infinite ground plane assumed in theory.

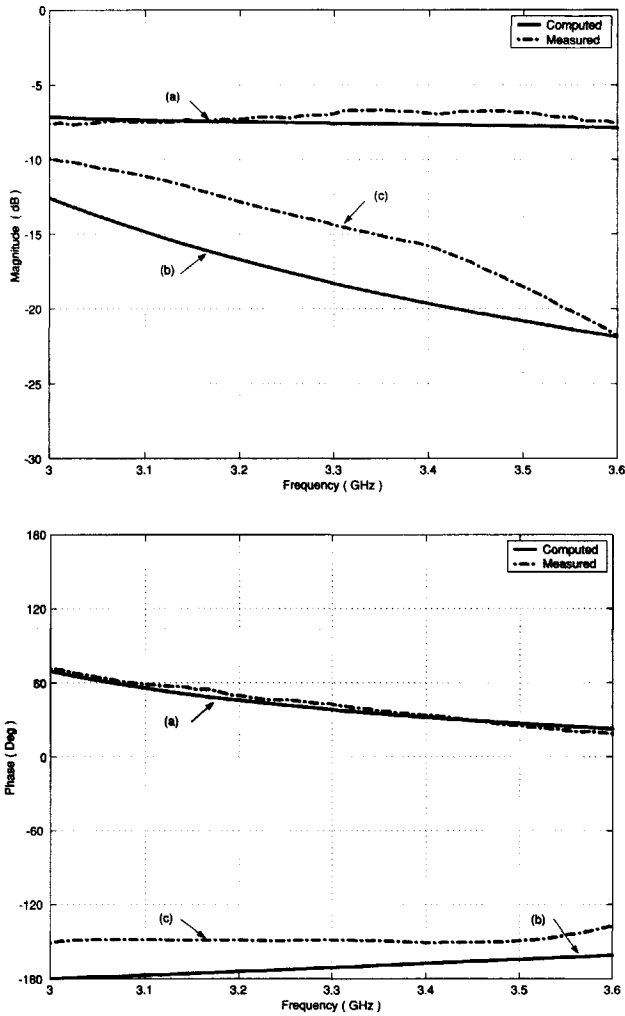


Figure 2.11: Computed and measured aperture reflection coefficient  $\Gamma$  of a dielectric filled waveguide with  $a = b = 34.2$  mm and  $\epsilon_r = 2.53$ . (a) Measured and computed for a waveguide radiating into free space. (b) Computed for a waveguide radiating into dielectric half-space ( $\epsilon_r = 2.53$ ). (c) Measured for a waveguide with a dielectric rod ( $\epsilon_r = 2.53$ ,  $l_{\text{rod}} = 90.6$  mm).

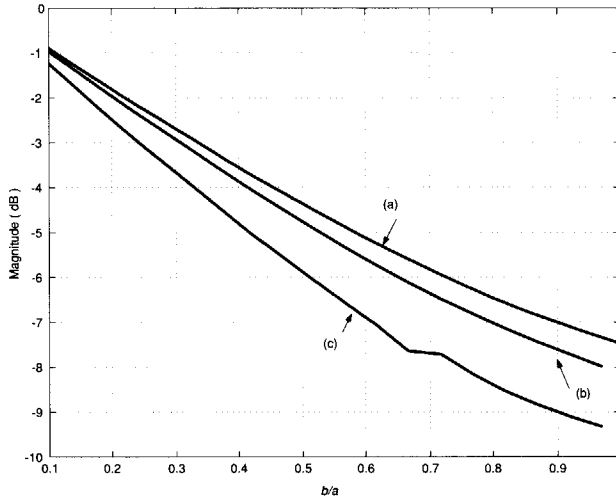


Figure 2.12: Effect of aperture height on the magnitude of  $\Gamma$  for different waveguide widths ( $\epsilon_r = 2.53$ ). (a)  $a = 0.37\lambda$ . (b)  $a = 0.44\lambda$ . (c)  $a = 0.55\lambda$ .

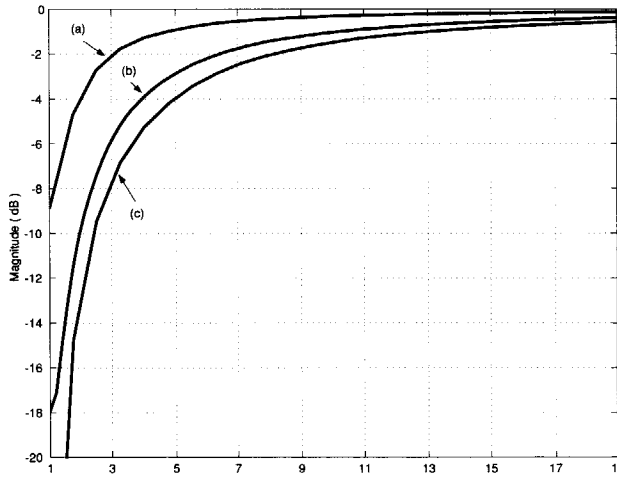


Figure 2.13: Magnitude of aperture reflection coefficient  $\Gamma$  versus relative dielectric permittivity  $\epsilon_r$  for different waveguide dimensions. (a)  $a = 0.6\lambda_d$ ,  $b/a = 0.3$ . (b)  $a = 0.88\lambda_d$ ,  $b/a = 0.6$ . (c)  $a = 0.88\lambda_d$ ,  $b/a = 1.0$ .

Hence, the reflection coefficient of waveguides with flanges of finite sizes agrees very well with the results obtained using the present formulation. Fig. 2.12 shows the effect of aperture height reduction on the magnitude of the reflection coefficient for different aperture widths. This figure clearly shows that the aperture height is an important factor in determining the aperture reflection. The effect of reducing the dielectric permittivity on the magnitude of the reflection coefficient is shown in Fig. 2.13. A similar behaviour was observed in the phase characteristic. During the calculations the dimensions of the waveguide were kept constant in relation the wavelength in the dielectric region  $\lambda_d = \lambda/\sqrt{\epsilon_r}$ . From this result it is clearly seen that the higher the dielectric constant, the higher the reflection coefficient. If the waveguide dimensions are kept constant while the dielectric constant is changed, one will observe a shift in the cut-off frequency. The cut-off frequency will decrease with increasing  $\epsilon_r$  and the aperture reflection phase will become more flat and nearly constant for higher values of  $\epsilon_r$ . When designing wideband aperture antennas, the aperture height ( $b$ ) and dielectric material used should be chosen carefully as they are the major parameters determining the magnitude of the reflections at the aperture. More results that show how to compensate for the high reflection at the aperture will be discussed next.

### (c) Aperture reflection cancellation with an air gap

An air gap of length  $l_a$  located at a distance  $l_d$  from the aperture plane is a simple, low-cost, and effective matching device. It was introduced and developed by the researchers of the Delft University [17, p. 101] in order to reduce the high aperture reflection, especially that of very flat aperture antennas ( $b/a \ll 1$ ). For a given aperture geometry one can compute the scattering matrix of an air gap by cascading the scattering matrices of two dielectric step discontinuities using the theory given in section 2.2. During the multi-modal analysis we noticed that when a  $TE_{1,0}$  mode is incident on the air gap, only a reflected and transmitted  $TE_{1,0}$  modes are excited.

Hence, the air gap does not excite any higher-order mode when it is inserted inside the waveguide. The reflected and transmitted modes are enough to satisfy the boundary conditions distorted by the presence of the air gap. However, the situation may change if the air gap is placed nearby the aperture where higher-order modes are excited. These modes can change the properties of the air gap by coupling energy into it. The air gap width  $l_a$  and position  $l_d$  must be appropriately adjusted such that they create a reflection with the same amplitude but with opposite phase to the reflection caused by the aperture discontinuity. If this condition is fulfilled the reflection at the aperture is canceled. Hence, in order to eliminate the aperture reflection completely at a certain frequency we must have (see Appendix A)

$$S_{22} = \Gamma^* \tag{2.62}$$

where the superscript \* denotes the complex conjugate.

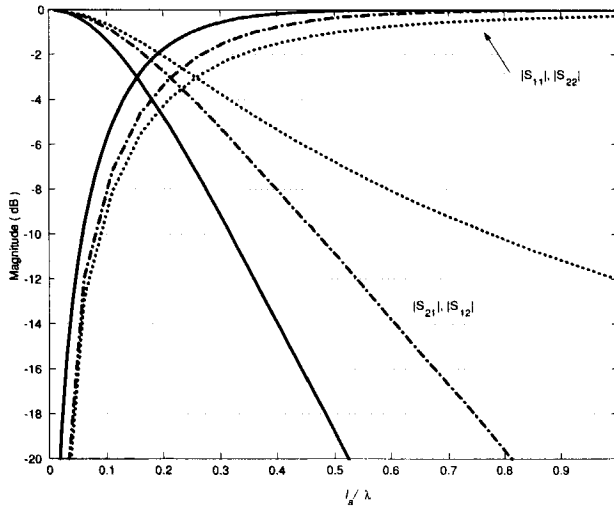


Figure 2.14: Magnitude of the air-gap scattering parameters versus normalized air-gap thickness for different aperture dimensions ( $\epsilon_r = 2.53$ ). — :  $a = 0.37\lambda$ ,  
 - - - :  $a = 0.44\lambda$ , ··· :  $a = 0.5\lambda$ .

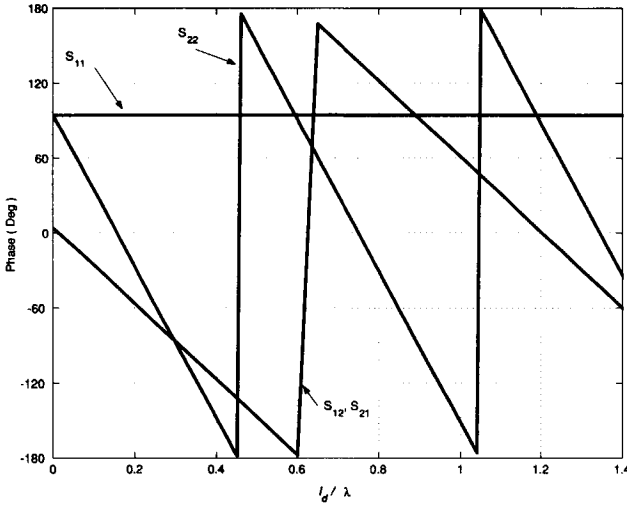


Figure 2.15: Phase of the air-gap scattering parameters versus normalized air-gap location ( $l_a = 0.37\lambda, \epsilon_r = 2.53$ ).

The fact that only two parameters have to be adjusted makes the matching process simple and fast. However, the aperture reflection cancellation can be obtained only at a single frequency, making the air gap a narrowband matching device. In order to achieve cancellation over a wider frequency band one has to synthesize a device in which  $S_{22}$  equals the complex conjugate of  $\Gamma$  over the entire desired frequency band. This device may consist of a number of air gaps, steps, irises, ...etc. If the number of parameters to be tuned is increased, a sophisticated optimization algorithm will be required.

A number of computations was carried out in order to investigate the effects of the air-gap width and position on the scattering parameters. Fig. 2.14 shows that the magnitude of the coefficient  $S_{22}$  can be simply tuned by adjusting the thickness of the air gap. The higher the aperture reflection coefficient, the thicker the air gap. The phase of  $S_{22}$  can be tuned by changing the air-gap position; this is demonstrated



in Fig. 2.15. These design curves can give a rapid indication on the required air-gap dimensions for a given magnitude and phase of the reflection at the aperture. They also indicate the type of fabrication tolerance one has to expect when designing such a device. Fig. 2.16 shows both the computed and the measured reflection coefficient for an L-band prototype with an integrated air gap previously designed at Delft University [18]. Good agreement is observed between simulation and experiment.

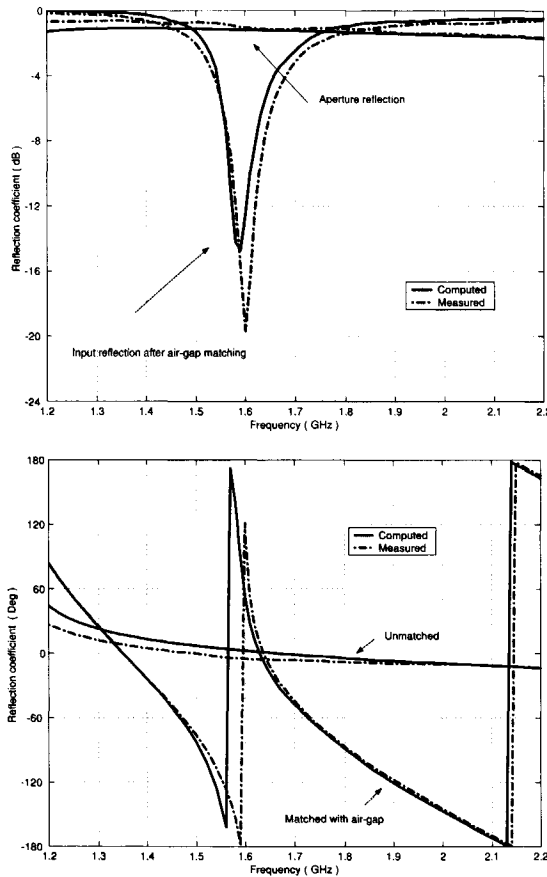


Figure 2.16: Matching the flat dielectric filled waveguide antenna at L-band with a single air gap ( $a = 83$  mm,  $b = 10$  mm,  $\epsilon_r = 2.53$ ,  $l_a = 60.5$  mm and  $l_d = 10.0$  mm)

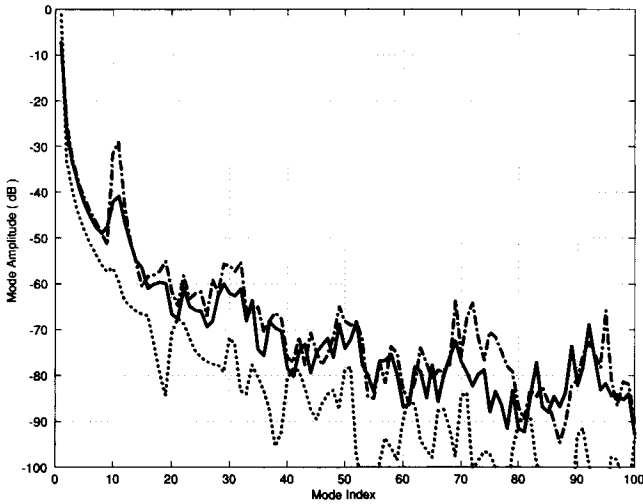


Figure 2.17: Higher-order excitations for different aperture dimensions ( $\epsilon_r = 2.53$ ).  
 - :  $a = 0.37\lambda$ ,  $b/a = 1.0$ . - · - :  $a = 0.55\lambda$ ,  $b/a = 0.65$ . · · :  $a = 0.44\lambda$ ,  $b/a = 0.12$ .

#### (d) Aperture fields and far-field patterns

The solution of the linear system of Eq. (2.46) together with the expression given in Eq. (2.47) determine the reflection coefficient and the amplitude of the higher-order modes. The obtained coefficients, when inserted in Eq. (2.23), directly give the electric and magnetic field distribution at the aperture. Fig. 2.17 shows the amplitude of the higher-order modes excitations relative to the amplitude of the  $TE_{1,0}$  mode for three different aperture dimensions. The three considered geometries allow only the fundamental mode  $TE_{1,0}$  to propagate. The amplitude of the higher-order modes decays when the mode index increases, becoming less than  $-30\text{dB}$  for modes with an index higher than five. Therefore, one may conclude that the contributions from modes having indices higher than five are negligible. Although this is true for the electric-field distribution, it will be shown that it is wrong for the magnetic-field distribution.

This is clearly seen in Fig. 2.18 where the electric-field distribution at the aperture is drawn for a different number of modes. The dominance of the well-known  $TE_{1,0}$  pattern is observed. This result was expected since if we inspect the first part of Eq. (2.23), we see that the ratio between the amplitude of the  $TE_{1,0}$  pattern and a higher-order pattern  $TE_{m,0}$  is simply the mode coefficient  $D_m$ . Note that the electric field at the aperture, when constructed according to Eq. (2.23), satisfies inherently the boundary conditions at the metallic flange. However, the singular behavior of the electric field at the aperture edges ( $x = \pm a/2$ ) and ( $y = \pm b/2$ ) is not covered by this modal field expansion. At the first boundary the electric field is parallel to the edges of the aperture and has to undergo a singularity of order  $r^{-1/3}$  [21], whereas at the second boundary the electric field is perpendicular to the aperture edges, resulting into a singularity of order  $r^{-2/3}$  [21]. These restrictions will not affect the far field but will certainly change the near-field behavior at the aperture plane. One example of such effect is the tapering of the electric field at the aperture along the  $y$ -direction.

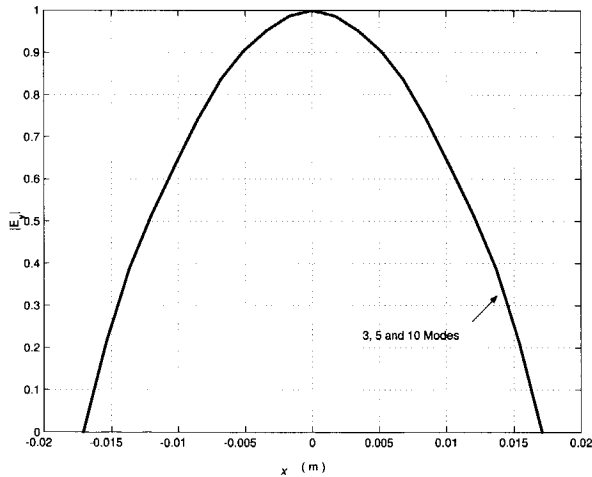


Figure 2.18: Electric-field distribution for a square aperture antenna ( $a = b = 34.2$  mm,  $\epsilon_r = 2.53$ , frequency = 3.3 GHz).

The effect of the higher-order modes on the aperture magnetic field is shown in Fig. 2.19 for a square aperture ( $a = b = 34.2$  mm) operating at a frequency of 3.3 GHz and in Fig. 2.20 for a flat aperture ( $a = 83$  mm,  $b = 10$  mm) operating at 1.6 GHz. We found that the higher-order modes strongly affect the magnetic-field distribution at the aperture. Especially the presence of relatively high peaks nearby the aperture edges ( $x = \pm a/2$ ) is noticeable. This can be checked by inspecting the second part of Eq. (2.23), which shows that the ratio between the  $TE_{1,0}$  and  $TE_{m,0}$  contributions to the aperture magnetic field is proportional to the factor  $Y_{m,0}D_m/Y_{1,0}y_{ap}$ , which is not negligible.

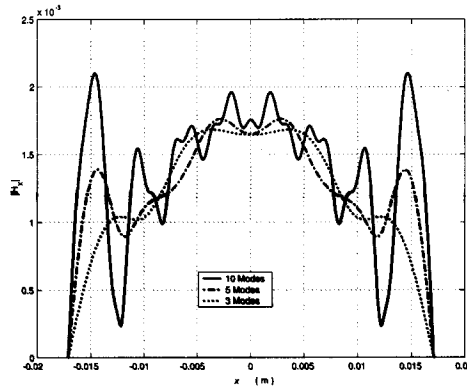


Figure 2.19: Magnetic-field distribution for a square aperture antenna ( $a = b = 34.2$  mm,  $\epsilon_r = 2.53$ , frequency = 3.3 GHz).

The  $TE_{1,0}$  pattern, in the magnetic field expression, is multiplied by the factor  $(1 - \Gamma)$ ; this means that in the case of apertures with very high reflection coefficients the contribution of the dominant mode becomes very low compared to that of the higher-order modes. This is confirmed by a comparison of Fig. 2.19 and Fig. 2.20. In Fig. 2.20 stronger peaks are present near the aperture edges. Note that in the latter case we are dealing with a much stronger reflecting aperture (very flat geometry  $b/a = 0.12$ ,  $\Gamma = -1.2$  dB at 1.6 GHz) than in the former case ( $b/a = 1$ ,  $\Gamma = -7.5$  dB

at 3.3 GHz).

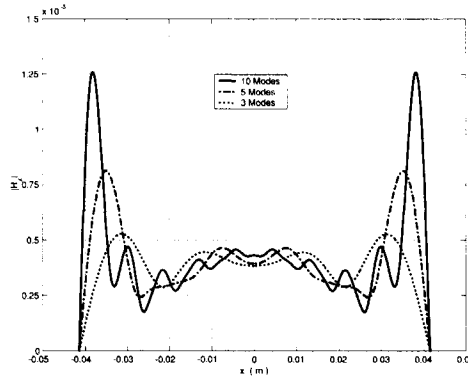


Figure 2.20: Magnetic field distribution for a flat aperture antenna ( $a = 83$  mm,  $b = 10$  mm,  $\epsilon_r = 2.53$ , frequency = 1.6 GHz).

For comparison we show calculated far-field patterns using the analysis described in section 2.3, and measured patterns in Fig. 2.21 and Fig. 2.22, for a square-aperture antenna ( $a = b = 34.2$  mm, frequency = 3.3 GHz) and a very flat-aperture antenna ( $a = 83$  mm,  $b = 10$  mm, Frequency = 1.6 GHz) respectively. A very good agreement is obtained in the region  $\pm 80^\circ$  in both E- and H-planes. The disagreement in the region nearby and above  $90^\circ$  is caused by the finite size of the metallic flange, which represents the main contribution to the far side lobes, the back lobe and the cross polarization, and is not included in the present formulation. During the measurements absorbers were used in order to reduce the parasitic effects caused by the metallic structure surrounding the aperture. The far-field patterns were not disturbed by the presence of the matching air gap since it was placed far enough from the aperture in both prototypes. Only a significant increase in radiating power was noticed, when comparing antennas with and without air gap.

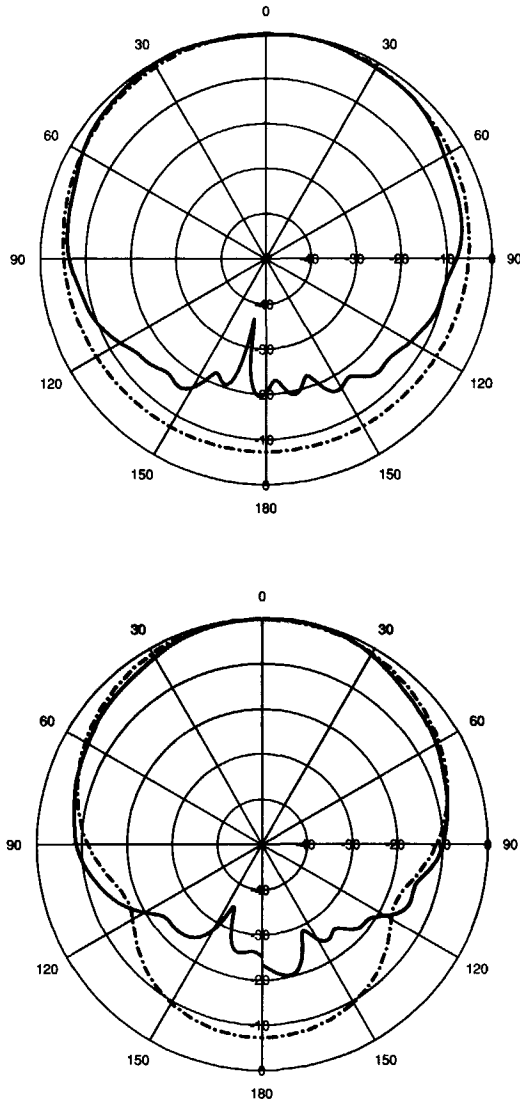


Figure 2.21: Far-field pattern in two orthogonal planes for a square aperture, top: E-plane, bottom: H-plane ( $a = b = 34.2$  mm,  $\epsilon_r = 2.53$ , frequency= 3.3 GHz). - : measured. -- : computed.

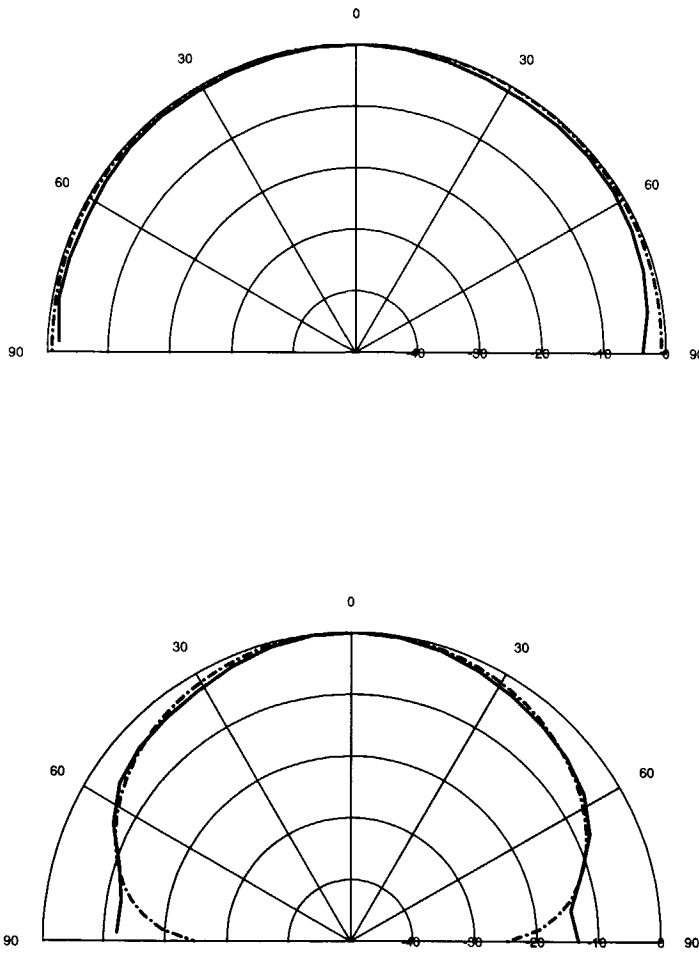


Figure 2.22: Far-field pattern in two orthogonal planes for a flat aperture, top: E-plane, bottom: H-plane ( $a = 83$  mm,  $b = 10$  mm,  $\epsilon_r = 2.53$ , frequency = 1.6 GHz).

- : measured. - - : computed.

## 2.5 Conclusions

A formulation has been presented for the aperture admittance and the far-field radiation pattern for highly miniaturized dielectric-filled waveguide antennas. The generalized scattering matrix technique was used to model the internal structure of the antenna (i.e. discontinuities and matching devices). In this approach, both propagating and evanescent modes were included. Sequential scattering mechanisms were taken into account by using a numerically stable direct cascading process, involving scattering matrices only. To solve the radiation problem, a variational expression for the aperture admittance has been developed using reaction integrals and spectral field representations. A novel expression for the aperture admittance, including higher-order excitations and their mutual interactions, was derived. The far-field patterns were obtained by applying the field equivalence principle to the obtained aperture field solution.

The radiation mechanism and matching device (air gap) of highly miniaturized apertures were studied thoroughly. In the miniaturization process, two parameters mainly control the antenna performance; the dielectric permittivity of the material used ( $\epsilon_r$ ) and the aperture height ( $b$ ). The dielectric filling determines the degree of miniaturization ( $\sim \sqrt{\epsilon_r}$ ), causes an increase of the aperture reflection coefficient, a shift in the cut-off frequency and affects the flatness of the phase characteristics. In  $TE_{1,0}$  waveguides, the aperture height reduction results in a strong increase of the aperture reflection. It makes the antenna inefficient unless a matching device can be synthesized for compensating this increase of reflection at the aperture.

Different means of lowering the aperture reflections were presented: extending the dielectric rod, tapering the metallic structure nearby the aperture, stepping the waveguide height and/or the insertion of an air gap.

The extension of the dielectric rod and the tapering of the metallic structure nearby



the aperture will reduce the aperture reflection, but they will also affect the radiation characteristics, see Chapter 3 and 4.

Insertion of an air gap with  $S_{22}$  having the same magnitude but the opposite phase as the aperture reflection coefficient will cause a complete reflection cancellation at a given frequency. To achieve this, two parameters must be set: the air-gap thickness ( $l_a$ ) and the air-gap position ( $l_d$ ). The air gap width controls the magnitude of the secondary reflection while the position, relative to the aperture plane, determines the phase shift that is needed. The fact that only two parameters have to be adjusted makes the air-gap matching device cheap, easy to use and effective.

The higher-order excitations decay rapidly for an increasing mode index. The dominance of the well-known  $TE_{1,0}$  pattern was observed in the aperture electric field distribution. The magnetic-field distribution shows the presence of relatively high peaks nearby the aperture edges, especially in case of highly miniaturized antennas. Higher-order excitations, if included, slightly affect the aperture admittance but they also permit a more accurate determination of the radiation fields. The results presented in this chapter were not only compared with measurements performed at different frequencies, but also with results taken from the open literature of different methods. During the measurements we found that, as far as the reflection coefficient is concerned, an aperture terminated into a flat flange of standard dimensions is of sufficient size to approximate the infinite ground plane assumed in the theoretical description. The models presented for the radiated fields represents the fields within  $\pm 80^\circ$  with reasonable accuracy. The failure of the present formulation in the region nearby and above  $90^\circ$  in the radiation pattern is due to the fact that the finite size of the metallic flange, which is the main contributing factor to the far side lobes, back lobe and cross polarization, was not taken into account.

With the present formulation, stable convergence of the numerical results and good agreement with experiments was achieved, even considering the involved ap-

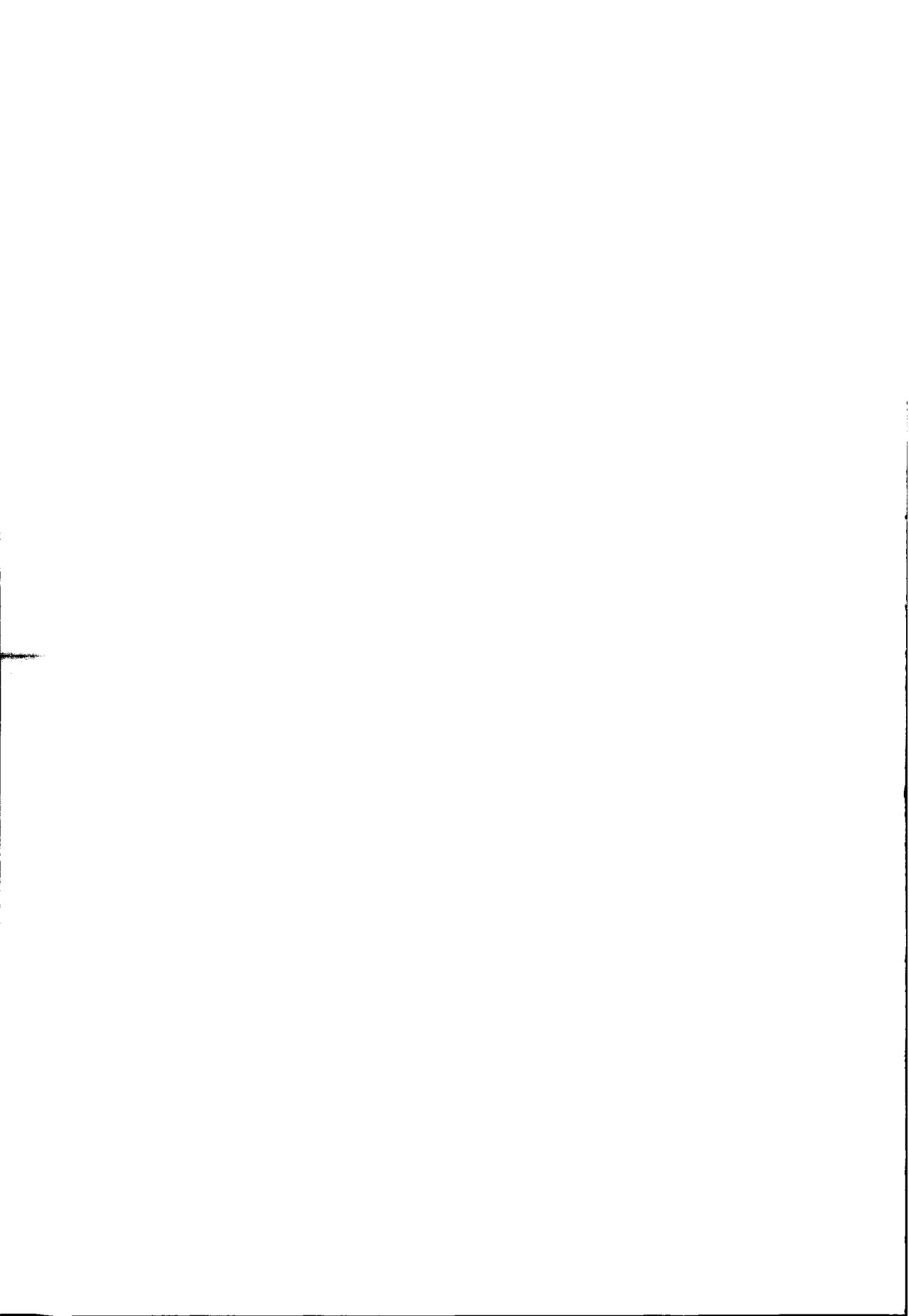
proximations. In the next chapter a different formulation will be derived which will be used to accurately determine the performances of aperture antennas mounted on finite metallic structures of arbitrary shape.

## References

- [1] R.E. Collin, "*Field Theory of Guided Waves*". New York: McGrawHill, 1960.
- [2] P.A. Rizzi, "*Microwave Engineering, Passive Circuits*", Prentice-Hall, Inc., 1988.
- [3] H. Patzelt and F. Arndt, "*Double-Plane Steps in Rectangular Waveguides and their Application for Transformer, Irises, and Filters*", IEEE Trans. Microwave Theory Tech., vol. MTT-30, pp. 771-776, May 1982.
- [4] G.V. Eleftheriades, W.Y. Ali-Ahmad, L.P.B. Katehi, and G.M. Rebeiz, "*Millimeter-Wave Integrated-Horn Antennas: Part I-Theory*", IEEE Trans. Antennas Propagat., vol. AP-39, pp. 1575-1581, November 1991.
- [5] T. Wriedt, K. Wolff, F. Arndt, and U. Tucholke, "*Rigorous Hybrid Field Theoretic Design of Stepped Rectangular Waveguide Mode Convertors Including the Horn Transition into Half-Space*", IEEE Trans. Antennas Propagat., vol. AP-37, pp. 780-790, June 1989.
- [6] C.T. Swift, "*Admittance of a Waveguide-Fed Aperture Loaded with a Dielectric Plug*", IEEE Trans. Antennas Propagat., vol. AP-17, pp. 356-359, May 1969.
- [7] M. Tian, "*Characterization of Miniature Dielectric Filled Waveguide Antennas*", Ph.D. dissertation, Delft university 1995.

- 
- [8] V.H. Rumsey, "*Reaction Concept in Electromagnetic Theory*", Phys. Rev. vol. 94 pp. 1483-1491, June 1954.
- [9] E.V. Jull, "*Aperture Antennas and Diffraction Theory*", IEE London and New York, Peter Peregrinus Ltd., Stevenage, UK, 1981.
- [10] A.Z. Fradin, "*Microwave Antennas*", Pergamon, New York 1961.
- [11] S. Silver, "*Microwave Antenna Theory and Design*", Boston Technical Publisher, INC. USA 1964.
- [12] J.A. Stratton, "*Electromagnetic Theory*", McGraw-Hill Book Company, New York 1941.
- [13] L. Weinstein, "*The theory of Diffraction and the Factorization Method*", Boulder CO Golem Press, USA 1969.
- [14] R.F. Harrington, "*Time Harmonic Electromagnetic Fields*", McGraw-Hill Book company, New York 1961.
- [15] R.E. Collin, "*Antenna Theory*", Part 1, McGraw-Hill Book Company, New York 1969.
- [16] L.J. Chu, "*Calculation of the Radiation Properties of Hollow Pipes and Horns*", J. Appl. Phys. vol. 11, pp. 603-610, USA 1940.
- [17] L.P. Ligthart, "*Antenna Design and Characterization Based on the Elementary Antenna Concept*", Ph.D. dissertation, Delft University, Dutch Efficiency Bureau, Pijnacker 1985.
- [18] D.P. Tran, M. Tian, and L.P. Ligthart, "*The E-Plane Stepped Microstrip-Like Antenna*", IEE 9<sup>th</sup> International Conference ICAP 95, vol. 1, pp.513-516.

- 
- [19] M. D. Deshpande, "*Analysis of Waveguide Junction Discontinuities Using Finite Element Method* ", NASA Report 201710, July 1997.
- [20] N. Marcuvitz, "*Waveguide Handbook* ", New York, McGraw-Hill, 1951.
- [21] J. Bladel, "*Singular Electromagnetic Fields and Sources* ", Oxford University Press, New York, 1991.



# Chapter 3

## Radiation from an aperture on a 3-D metallic body

### 3.1 Introduction

In the previous chapter we studied the basic radiating structure, namely the single rectangular waveguide that is terminated by an infinite metallic flange. For this end we used a variational technique. Since practical antennas involve a combination of metallic structures with finite sizes and different shapes, the formulation given in the previous chapter cannot be applied to solve the more practical radiation problem. When the shape of the metallic structure is arbitrary, an analytic solution cannot be obtained and a numerical method must be developed. Problems related to plane-wave scattering from conducting bodies have been studied extensively and numerous publications are available in the literature [1],[2], [3],[4]. On the other hand, problems arising from radiation from structures involving a combination of conductors and dielectric, which are considered in this chapter (see Fig. 3.1), have received limited attention and most available formulations are restricted to bodies of revolution [5],[6],[7] since this solution is easier to obtain.

Nowadays computers exist with high performance, so that it is possible to use general-purpose codes capable of handling problems with a wide variety of geometry. For this reason there has been a growing interest in the use and development of numerical techniques for treating scattering and radiation by arbitrary shaped bodies. The best known approach for treating such problems is the integral equation formulation in conjunction with the Method of Moments (MoM) [8],[9].

One of the useful formulations for accurately predicting the scattered field from arbitrary metallic objects is the Electric Field Integral Equation (EFIE), since it can be applied to both open and closed structures with sharp edges [3]. Implementation of MoM for EFIE involves solving for the induced surface electric current using vector and scalar potential solutions which satisfy the boundary condition that the tangential electric field at the boundary of the metallic structure is zero. This is done by using Galerkin's technique [8] to solve the related integral equations. In a sub-domain technique the metallic surface is generally modeled by means of planar triangular patches because they accurately conform to any geometrical surface. The integral equations are generated over the triangular sub-domains and combined to form a global matrix equation. Reaction-matching is applied to circumvent the difficulties associated with the singularities and the differentiation in the integral equation. This results in a dense complex matrix equation, which can be solved either by a direct (LU-decomposition) or by an iterative (conjugate gradient) technique. Generation of the matrix equation and its solution are the major computational operations in MoM.

This chapter is devoted to the development of an analysis and design tool based on a modified EFIE and MoM for analyzing and improving the radiation from an aperture incorporating dielectric material and mounted on a metallic body. The metallic body consists of a combination of perfectly conducting structures with different sizes and shapes (see Fig. 3.1). The obtained code is used to study the effect of the incorporation of an external corrugation profile on the metallic body. Different examples



are treated and new results are presented. An optimum rectangular-waveguide feed design is given. The chapter is organized as described below. First the problem is formulated and the integral equation is derived. Then the discretization of the domain of computation and the expansion functions are discussed. Next the accuracy of the method and validation of the design procedure are demonstrated by comparing computed and measured results for a few examples. Finally some concluding remarks on the advantages and disadvantages of the method are presented.

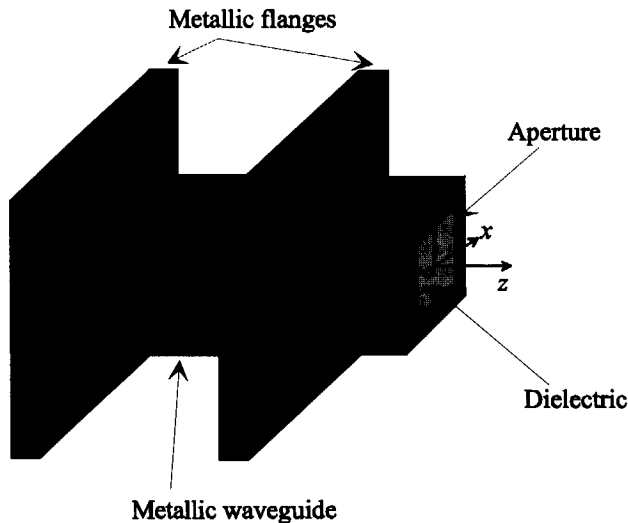
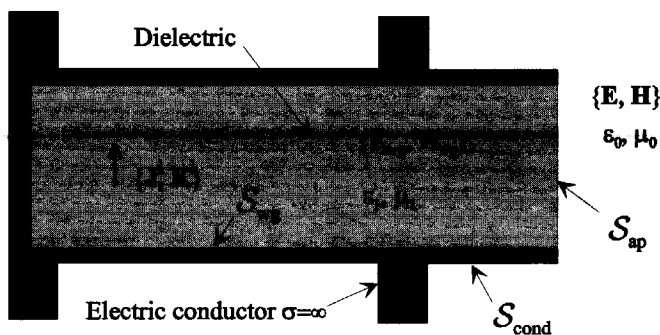


Figure 3.1: General problem of radiation from an aperture mounted on a metallic structure of arbitrary shape.

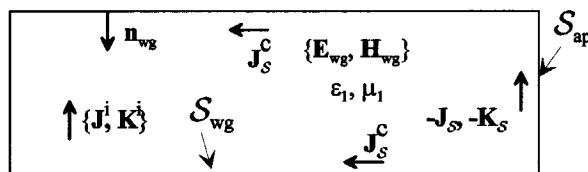
### 3.2 Problem formulation and integral equation

In this section the problem of a single waveguide-fed aperture mounted on a perfect conductor of arbitrary shape which radiates into free space is considered (see Fig. 3.1). The waveguide is uniformly filled with a non-dissipative, linear, isotropic and

homogeneous medium having dielectric constant  $\epsilon_1$  and magnetic permeability  $\mu_1$ . The aperture is rectangular with dimensions  $a$  and  $b$  in the  $x$ - and  $y$ -directions, respectively. The region outside the waveguide is assumed to be source free. The global coordinate system used throughout this chapter is shown in Fig. 3.1. The origin is located at the center of the aperture. The electromagnetic field inside the waveguide region is denoted by  $\mathbf{E}_{wg}$  and  $\mathbf{H}_{wg}$ , and the field in free space by  $\mathbf{E}$  and  $\mathbf{H}$ . The excitation of the waveguide is achieved by the impressed electric and magnetic sources  $\{\mathbf{J}^i, \mathbf{K}^i\}$ ; these produce the dominant mode  $TE_{10}$  traveling toward the aperture. The waveguide is assumed to be terminated in a matched load when viewed from the aperture. This means that we need not consider multiple reflections inside the waveguide here.



(a) Original problem



(b) Interior equivalent

Figure 3.2: The original problem and its interior equivalent representation.

The equivalence principle is used to divide the problem into two sub-problems, namely the interior sub-problem and the exterior sub-problem, as follows. The waveguide aperture is closed with an imaginary wall [10][11][12] and surface currents  $\mathbf{J}_S$  and  $\mathbf{K}_S$  of appropriate magnitude, see Fig. 3.2 and Fig. 3.3, are introduced on either side of the aperture. So the fields  $\mathbf{E}_{wg}$  and  $\mathbf{H}_{wg}$  inside the waveguide are due to the known impressed sources  $\{\mathbf{J}^i, \mathbf{K}^i\}$  and the unknown surface currents  $\mathbf{J}_S^c$ ,  $\mathbf{J}_S$  and  $\mathbf{K}_S$  radiating in the region bounded by  $\mathcal{S}_{wg}$  and  $\mathcal{S}_{ap}$  (see Fig. 3.2). The fields  $\mathbf{E}$  and  $\mathbf{H}$  exterior to the waveguide are due to the magnetic and electric current sources,  $\mathbf{J}_S$  and  $\mathbf{K}_S$ , radiating in front of the closed surface  $\mathcal{S} = \mathcal{S}_{coud} \cup \mathcal{S}_{ap}$  (see Fig. 3.3).

The condition that the equivalent magnetic current in the waveguide region must be  $-\mathbf{K}_S$  and in the exterior region  $+\mathbf{K}_S$  ensures that the tangential component of the electric field is continuous across the aperture. Hence, we have

$$\lim_{\mathbf{r} \downarrow \mathcal{S}_{ap}} \mathbf{n} \times \mathbf{E} = \lim_{\mathbf{r} \uparrow \mathcal{S}_{ap}} -\mathbf{n}_{wg} \times \mathbf{E}_{wg} = -\mathbf{K}_S, \quad (3.1)$$

where  $\mathbf{r}$  represents the vector position of an arbitrary point and  $\mathbf{n}_{wg}$  is the normal unit vector on the surface  $\mathcal{S}_{wg} \cup \mathcal{S}_{ap}$  directed into the waveguide region (see Fig. 3.2) while  $\mathbf{n}$  is the normal unit vector on the surface  $\mathcal{S}_{coud} \cup \mathcal{S}_{ap}$  directed into free space (see Fig. 3.3).

Similarly, the condition that the equivalent electric current in the waveguide region must be  $-\mathbf{J}_S$  and in the exterior region  $+\mathbf{J}_S$  guarantees the continuity of the tangential component of the magnetic field across the aperture. Hence, we have

$$\lim_{\mathbf{r} \downarrow \mathcal{S}_{ap}} \mathbf{n} \times \mathbf{H} = \lim_{\mathbf{r} \uparrow \mathcal{S}_{ap}} -\mathbf{n}_{wg} \times \mathbf{H}_{wg} = \mathbf{J}_S. \quad (3.2)$$

Eq.(3.1) and Eq.(3.2) insure the electromagnetic coupling, throughout the aperture, between the interior and the exterior sub-problem. Furthermore, the electromagnetic

field must satisfy the following conditions in the interior sub-problem

$$\begin{aligned} \lim_{r \uparrow S_{wg}} \mathbf{n}_{wg} \times \mathbf{E}_{wg} &= 0, \\ \lim_{r \uparrow S_{wg}} \mathbf{n}_{wg} \times \mathbf{H}_{wg} &= \mathbf{J}_S^c, \end{aligned} \quad (3.3)$$

and in the exterior sub-problem

$$\begin{aligned} \lim_{r \downarrow S_{cond}} \mathbf{n} \times \mathbf{E} &= 0, \\ \lim_{r \downarrow S_{cond}} \mathbf{n} \times \mathbf{H} &= \mathbf{J}_S. \end{aligned} \quad (3.4)$$

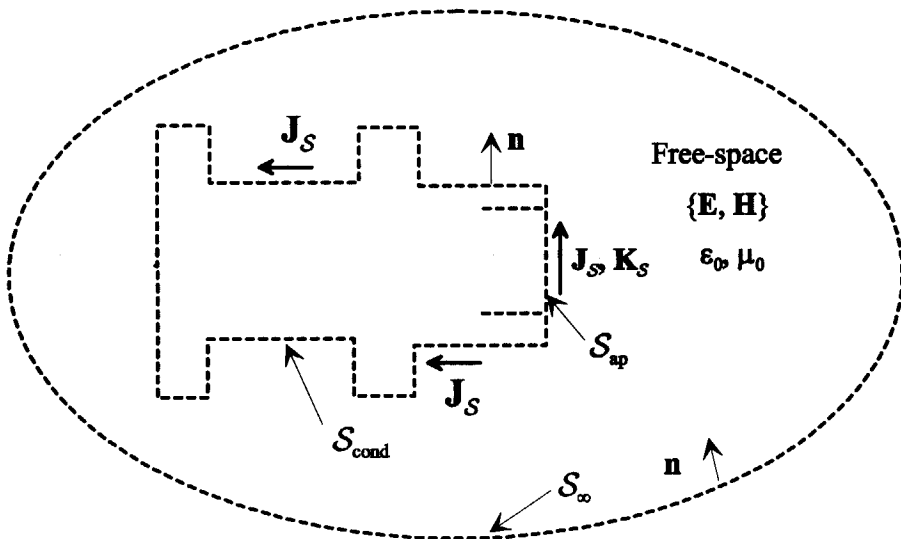


Figure 3.3: Equivalent representation for the exterior region.

### 3.2.1 Field in the waveguide region

The transverse electric field and magnetic field at any cross section inside a uniform waveguide can be expanded as a sum of modal fields. This is based on the completeness of the infinite set of modes inside a closed waveguide. From the results given in Chapter 2 we can write the transverse field components as (propagation in the  $z$ -direction is

assumed)

$$\begin{aligned} \mathbf{E}_{\text{wgt}} = & \sum_{m,n}^{\infty'} \left\{ a_{m,n}^{\text{TE}} \exp(-\gamma_{m,n}z) + b_{m,n}^{\text{TE}} \exp(\gamma_{m,n}z) \right\} \mathbf{e}_{m,n}^{\text{TE}}(x,y) / \sqrt{Y_{m,n}^{\text{TE}}} \\ & + \sum_{m,n}^{\infty'} \left\{ a_{m,n}^{\text{TM}} \exp(-\gamma_{m,n}z) + b_{m,n}^{\text{TM}} \exp(\gamma_{m,n}z) \right\} \mathbf{e}_{m,n}^{\text{TM}}(x,y) / \sqrt{Y_{m,n}^{\text{TM}}}, \end{aligned} \quad (3.5)$$

$$\begin{aligned} \mathbf{H}_{\text{wgt}} = & \sum_{m,n}^{\infty'} \left\{ a_{m,n}^{\text{TE}} \exp(-\gamma_{m,n}z) - b_{m,n}^{\text{TE}} \exp(\gamma_{m,n}z) \right\} \mathbf{i}_z \times \mathbf{e}_{m,n}^{\text{TE}}(x,y) \sqrt{Y_{m,n}^{\text{TE}}} \\ & + \sum_{m,n}^{\infty'} \left\{ a_{m,n}^{\text{TM}} \exp(-\gamma_{m,n}z) - b_{m,n}^{\text{TM}} \exp(\gamma_{m,n}z) \right\} \mathbf{i}_z \times \mathbf{e}_{m,n}^{\text{TM}}(x,y) \sqrt{Y_{m,n}^{\text{TM}}}. \end{aligned} \quad (3.6)$$

The symbols used in Eq. (3.5) and Eq. (3.6) were introduced in Chapter 2. The amplitude of the incident modes  $a_{m,n}^{\text{TE}}$  and  $a_{m,n}^{\text{TM}}$  are considered given. The impressed magnetic current density  $\mathbf{K}_S$  can be related to the field inside the waveguide using Eq.(3.1). In the vicinity of the aperture ( $z = 0$ ) we have

$$\begin{aligned} \mathbf{K}_S(\mathbf{r}) &= \mathbf{K}_S^{\text{inc}}(\mathbf{r}) + \mathbf{K}_S^{\text{ref}}(\mathbf{r}), \\ \mathbf{K}_S^{\text{inc}}(\mathbf{r}) &= -\mathbf{n} \times \sum_l a_l^{\text{TE}} \mathbf{e}_l^{\text{TE}}(\mathbf{r}) / \sqrt{Y_l^{\text{TE}}} + a_l^{\text{TM}} \mathbf{e}_l^{\text{TM}}(\mathbf{r}) / \sqrt{Y_l^{\text{TM}}}, \\ \mathbf{K}_S^{\text{ref}}(\mathbf{r}) &= -\mathbf{n} \times \sum_l b_l^{\text{TE}} \mathbf{e}_l^{\text{TE}}(\mathbf{r}) / \sqrt{Y_l^{\text{TE}}} + b_l^{\text{TM}} \mathbf{e}_l^{\text{TM}}(\mathbf{r}) / \sqrt{Y_l^{\text{TM}}}, \end{aligned} \quad (3.7)$$

where  $\mathbf{r} \in \mathcal{S}_{\text{ap}}$  and  $l = (m, n)$ . In Eq.(3.7) the magnetic current density  $\mathbf{K}_S$  is separated into two parts. The first part,  $\mathbf{K}_S^{\text{inc}}$ , represents contributions from the waveguide modes that are incident upon the aperture while the second part,  $\mathbf{K}_S^{\text{ref}}$ , represents contributions from the unknown waveguide modes which are excited at the aperture plane. Note that the first part of  $\mathbf{K}_S$  is considered known.

### 3.2.2 Integral representation for the field in free-space

In this section, we derive an integral equation for the electromagnetic field radiated by an aperture mounted on a metallic structure of arbitrary shape. The obtained integral equation relates the fields radiated into free space to equivalent sources (electric and magnetic) laying along a surface enclosing the antenna structure. The evaluation

of the fields can progress directly once the current distributions over the radiating structure are known.

The fields in the exterior region are due to the unknown surface electric and magnetic currents  $\mathbf{J}_S$  and  $\mathbf{K}_S$  radiating into free space. Hence, we can use the Green's function of free space. Summarizing: we are interested in finding a solution which satisfies Maxwell's equations in the region outside  $\mathcal{S} = \mathcal{S}_{\text{ap}} \cup \mathcal{S}_{\text{cond}}$ , the radiation condition [14, p. 464] at  $\mathcal{S}_{\infty}$  and which has a prescribed tangential electric and magnetic intensities on  $\mathcal{S}$  (see Fig. 3.3). We use the auxiliary vector potentials,  $\mathbf{A}$  and  $\mathbf{F}$  [15, p. 254], as aids in obtaining solutions for the electric and magnetic fields. This procedure requires two steps. In the first step, the vector potentials are found, once the boundary value problem is specified (i.e. radiating sources and Green's function). In the second step, the electromagnetic fields are determined from the computed vector potentials. In free space, any solution for the time-harmonic electric and magnetic fields must satisfy Maxwell's equations

$$\nabla \times \mathbf{E}(\mathbf{r}) = -j\omega\mu_0\mathbf{H}(\mathbf{r}) - \mathbf{K}(\mathbf{r}), \quad (3.8)$$

$$\nabla \times \mathbf{H}(\mathbf{r}) = j\omega\epsilon_0\mathbf{E}(\mathbf{r}) + \mathbf{J}(\mathbf{r}),$$

$$\nabla \cdot (\epsilon_0\mathbf{E}) = \rho_e, \quad \nabla \cdot (\mu_0\mathbf{H}) = \rho_m,$$

where an  $\exp(j\omega t)$  time dependence of the field is assumed. A solution to Eq. (3.8) in terms of electric and magnetic potentials is given by [15, p. 260]

$$\mathbf{E} = -j\omega\mathbf{A} - \nabla\phi_e - \frac{1}{\epsilon_0}\nabla \times \mathbf{F}, \quad (3.9)$$

$$\mathbf{H} = \frac{1}{\mu_0}\nabla \times \mathbf{A} - j\omega\mathbf{F} - \nabla\phi_m,$$

where

$$\phi_e = -\frac{1}{j\omega\epsilon_0\mu_0}\nabla \cdot \mathbf{A}, \quad \phi_m = -\frac{1}{j\omega\epsilon_0\mu_0}\nabla \cdot \mathbf{F}. \quad (3.10)$$

The vector potentials  $\mathbf{A}$  and  $\mathbf{F}$  are solutions to the following vector equations

$$\nabla^2\mathbf{A} + \omega^2\epsilon_0\mu_0\mathbf{A} = -\mu_0\mathbf{J}, \quad (3.11)$$

$$\nabla^2\mathbf{F} + \omega^2\epsilon_0\mu_0\mathbf{F} = -\epsilon_0\mathbf{K}.$$

The solutions are found to be

$$\mathbf{A} = \mu_0 \int_{\mathcal{V}} \mathbf{J}(\mathbf{r}') G(\mathbf{r}, \mathbf{r}') dV', \quad \mathbf{F} = \epsilon_0 \int_{\mathcal{V}} \mathbf{K}(\mathbf{r}') G(\mathbf{r}, \mathbf{r}') dV', \quad (3.12)$$

where  $\mathbf{r}'$  represents the vector position of a source element in  $\mathcal{V}$  while  $\mathbf{r}$  denotes the vector position of a point, outside  $\mathcal{V}$ , at which the field is being computed. The Green's function of free space,  $G(\mathbf{r}, \mathbf{r}')$ , is given by

$$G(\mathbf{r}, \mathbf{r}') = \frac{\exp(-jk_0 |\mathbf{r} - \mathbf{r}'|)}{4\pi |\mathbf{r} - \mathbf{r}'|}. \quad (3.13)$$

Note that since the Green's function of free space is used, the radiated field satisfies the radiation condition at  $S_\infty$ . When  $\mathbf{J}$  and  $\mathbf{K}$  represent linear densities ( $\text{m}^{-1}$ ), the integrals in Eq. (3.12) reduce to surface integrals

$$\mathbf{A} = \mu_0 \int_{\mathcal{S}} \mathbf{J}_{\mathcal{S}}(\mathbf{r}') G(\mathbf{r}, \mathbf{r}') dA', \quad \mathbf{F} = \epsilon_0 \int_{\mathcal{S}} \mathbf{K}_{\mathcal{S}}(\mathbf{r}') G(\mathbf{r}, \mathbf{r}') dA'. \quad (3.14)$$

Substitution of Eq. (3.14) into Eq. (3.9) results in the Green's representation of the electric field

$$\mathbf{E}(\mathbf{r}) = \mathbf{E}_{\text{cond}}(\mathbf{r}) + \mathbf{E}_{\text{ap}}(\mathbf{r}), \quad (3.15)$$

$$\mathbf{E}_{\text{cond}}(\mathbf{r}) = - \int_{\mathcal{S}} \left( j\omega\mu_0 G(\mathbf{r}, \mathbf{r}') \mathbf{J}_{\mathcal{S}}(\mathbf{r}') - \frac{1}{j\omega\epsilon_0} (\nabla'_{\mathcal{S}} \cdot \mathbf{J}_{\mathcal{S}}(\mathbf{r}')) \nabla G(\mathbf{r}, \mathbf{r}') \right) dA', \quad (3.16)$$

$$\mathbf{E}_{\text{ap}}(\mathbf{r}) = - \int_{\mathcal{S}_{\text{ap}}} \nabla \times (G(\mathbf{r}, \mathbf{r}') \mathbf{K}_{\mathcal{S}}(\mathbf{r}')) dA'. \quad (3.17)$$

where  $\nabla'_{\mathcal{S}}$  denotes a surface divergence with respect to the source coordinates  $\mathbf{r}'$ . The electric field expression, Eq. (3.15), consists of two parts  $\mathbf{E}_{\text{cond}}$  and  $\mathbf{E}_{\text{ap}}$ . The first part represents the field due to the electric current density  $\mathbf{J}_{\mathcal{S}}$  with support  $\mathcal{S}_{\text{cond}} \cup \mathcal{S}_{\text{ap}}$ , while the second part represents the field due to the impressed magnetic current density  $\mathbf{K}_{\mathcal{S}}$  with support  $\mathcal{S}_{\text{ap}}$ . Note that Eq. (3.15) is singular in the source region

where  $\mathbf{r} = \mathbf{r}'$ . To circumvent the singularity we write

$$\begin{aligned} \mathbf{E}_{\text{cond}}(\mathbf{r})|_{\mathbf{r} \in S} = & -j\omega\mu_0 \lim_{\delta \rightarrow 0} \left\{ \int_{S-S_\delta} G\mathbf{J}_S dA' \right\} + \frac{1}{j\omega\epsilon_0} \lim_{\delta \rightarrow 0} \left\{ \nabla \int_{S-S_\delta} \nabla'_S \cdot \mathbf{J}_S G dA' \right\} \\ & -j\omega\mu_0 \lim_{\delta \rightarrow 0} \left\{ \int_{S_\delta} G\mathbf{J}_S dA' \right\} + \frac{1}{j\omega\epsilon_0} \lim_{\delta \rightarrow 0} \left\{ \nabla \int_{S_\delta} \nabla'_S \cdot \mathbf{J}_S G dA' \right\}, \end{aligned} \quad (3.18)$$

and

$$\begin{aligned} \mathbf{E}_{\text{ap}}(\mathbf{r})|_{\mathbf{r} \in S} = & - \lim_{\delta \rightarrow 0} \left\{ \int_{S_{\text{ap}}-S_\delta} \nabla \times G\mathbf{K}_S dA' \right\} \\ & - \lim_{\delta \rightarrow 0} \left\{ \nabla \times \int_{S_\delta} G\mathbf{K}_S dA' \right\}, \end{aligned} \quad (3.19)$$

where  $S_\delta$  is a small circular disc that is part of  $S$ , with radius  $\delta$ , around the singularity point  $\mathbf{r} = \mathbf{r}'$ . The singularity is now contained within the second part of (3.18) and (3.19) respectively and has to be evaluated analytically. Note that the integral over the surface  $(S - S_\delta)$  and the integral over the surface  $(S_{\text{ap}} - S_\delta)$  cause no problems in their numerical evaluation ( $\mathbf{r} \neq \mathbf{r}'$ ). In the limit  $\delta \rightarrow 0$  they will lead to principal value integrals. The integrals over  $S_\delta$ , however, contain a singular integrand and have to be evaluated with care. For very small  $\delta$

$$\begin{aligned} \mathbf{I}_1^\delta(\mathbf{r}) &= -j\omega\mu_0 \int_{S_\delta} G(\mathbf{r}, \mathbf{r}') \mathbf{J}_S(\mathbf{r}') dA' \approx \frac{-j\omega\mu_0}{4\pi} \mathbf{J}_S(\mathbf{r}) \int_{S_\delta} \frac{1}{|\mathbf{r}-\mathbf{r}'|} dA', \\ \mathbf{I}_2^\delta(\mathbf{r}) &= \frac{1}{j\omega\epsilon_0} \nabla \int_{S_\delta} (\nabla'_S \cdot \mathbf{J}_S(\mathbf{r}')) G(\mathbf{r}, \mathbf{r}') dA' \approx \frac{1}{4\pi j\omega\epsilon_0} \int_{S_\delta} (\nabla'_S \cdot \mathbf{J}_S(\mathbf{r}')) \nabla \frac{1}{|\mathbf{r}-\mathbf{r}'|} dA', \\ \mathbf{I}_3^\delta(\mathbf{r}) &= -\nabla \times \int_{S_\delta} G(\mathbf{r}, \mathbf{r}') \mathbf{K}_S(\mathbf{r}') dA' \approx -\frac{1}{4\pi} \mathbf{K}_S(\mathbf{r}) \cdot \int_{S_\delta} \nabla \times \frac{\bar{\mathbf{I}}}{|\mathbf{r}-\mathbf{r}'|} dA', \end{aligned} \quad (3.20)$$

where the exponential factor in the Green's function is approximated by unity over the small disc  $S_\delta$  and  $\bar{\mathbf{I}}$  is a unitary dyadic. The surface  $S_\delta$  is considered so small that  $\mathbf{J}_S$  and  $\mathbf{J}_{S_m}$  can be considered to be constant on  $S_\delta$ . Following the same procedure as



in [16, p. 135], we obtain

$$\begin{aligned} \lim_{\delta \rightarrow 0} \mathbf{n} \times \mathbf{I}_1^\delta(\mathbf{r}) &= 0, & \lim_{\delta \rightarrow 0} \mathbf{n} \times \mathbf{I}_2^\delta(\mathbf{r}) &= 0, \\ \lim_{\delta \rightarrow 0} \mathbf{n} \times \mathbf{I}_3^\delta(\mathbf{r}) &= -\frac{1}{2} \mathbf{K}_S(\mathbf{r}) \end{aligned} \quad (3.21)$$

After substitution of Eq. (3.21) into Eqs. (3.18) and (3.19) and applying the boundary conditions we obtain the following set of coupled integral equations for the radiation from an aperture mounted on a perfectly conducting structure of arbitrary shape

$$\begin{aligned} -\mathbf{n} \times \text{PV} \int_S (j\omega\mu_0 G(\mathbf{r}, \mathbf{r}') \mathbf{J}_S(\mathbf{r}') - \frac{1}{j\omega\epsilon_0} (\nabla'_S \cdot \mathbf{J}_S(\mathbf{r}')) \nabla G(\mathbf{r}, \mathbf{r}')) dA' = \\ \mathbf{n} \times \text{PV} \int_{S_{\text{ap}}} \nabla \times (G(\mathbf{r}, \mathbf{r}') \mathbf{K}_S(\mathbf{r}')) dA' - \frac{1}{2} \mathbf{K}_S(\mathbf{r}) \mathcal{X}_{S_{\text{ap}}}(\mathbf{r}), \quad \mathbf{r} \in S \end{aligned} \quad (3.22)$$

$$\lim_{\mathbf{r}' \rightarrow \mathbf{r}} \mathbf{n} \times \mathbf{H}_{\text{wg}}(\mathbf{r}) = \mathbf{J}_S(\mathbf{r}), \quad \mathbf{r} \in S_{\text{ap}} \quad (3.23)$$

where the PV before the integral sign signifies a principal value and the shape function  $\mathcal{X}_{S_{\text{ap}}}(\mathbf{r})$  is unity for  $\mathbf{r} \in S_{\text{ap}}$  and zero otherwise.

### 3.2.3 Weak formulation and MoM solution

An approximate solution to the coupled integral equations (3.22) and (3.23) can be obtained by using the method of moments [8]. First we define a set of vectorial expansion functions  $\mathbf{f}_n(\mathbf{r})$  and  $\mathbf{g}_n(\mathbf{r})$  and let

$$\begin{aligned} \mathbf{J}_S(\mathbf{r}) &\approx \sum_n I_n \mathbf{f}_n(\mathbf{r}), \quad \mathbf{r} \in S \\ \mathbf{K}_S(\mathbf{r}) &\approx \sum_n V_n \mathbf{g}_n(\mathbf{r}), \quad \mathbf{r} \in S_{\text{ap}} \end{aligned} \quad (3.24)$$

where the complex coefficients  $I_n$  and  $V_n$  have to be determined numerically. Note that the basis functions  $\mathbf{f}_n(\mathbf{r})$  are defined over the computation domain  $S$  while the functions  $\mathbf{g}_n(\mathbf{r})$  are defined over the computation domain  $S_{\text{ap}}$ . Substitution of the expansions into the coupled integral equations results in an ill-defined system. Because of the approximate sign in Eq. (3.24), the left and right sides of Eqs. (3.22) and

(3.23) cannot be equal in the entire computational domain. Hence we are dealing with a strong statement and additional weighted measures are needed to resolve the unknown coefficients  $I_n$  and  $V_n$ . To accomplish that we define a set of testing functions  $\mathbf{f}_m^t(\mathbf{r})$  and  $\mathbf{g}_m^t(\mathbf{r})$ , over the domains of computation  $\mathcal{S}$  and  $\mathcal{S}_{ap}$  respectively and use the following product

$$\langle \mathbf{x}, \mathbf{y} \rangle_{\mathcal{A}} = \iint_{\mathcal{A}} \mathbf{x} \cdot \mathbf{y} dA \quad (3.25)$$

which is a scalar satisfying [17]

$$\begin{aligned} \langle \mathbf{x}, \mathbf{y} \rangle_{\mathcal{A}} &= \langle \mathbf{y}, \mathbf{x} \rangle_{\mathcal{A}} & (3.26) \\ \langle \mathbf{x}_1 + \mathbf{x}_2, \mathbf{y} \rangle_{\mathcal{A}} &= \langle \mathbf{x}_1, \mathbf{y} \rangle_{\mathcal{A}} + \langle \mathbf{x}_2, \mathbf{y} \rangle_{\mathcal{A}} \\ \langle \lambda \mathbf{x}, \mathbf{y} \rangle_{\mathcal{A}} &= \lambda \langle \mathbf{x}, \mathbf{y} \rangle_{\mathcal{A}} \\ \langle \mathbf{x}^*, \mathbf{x} \rangle_{\mathcal{A}} &> 0, \text{ if } \mathbf{x} \neq \mathbf{0} \\ \langle \mathbf{x}^*, \mathbf{x} \rangle_{\mathcal{A}} &= 0, \text{ if } \mathbf{x} = \mathbf{0} \end{aligned}$$

where  $\lambda$  is a scalar and the superscript \* denotes the complex conjugate. Applying the scalar product to the coupled integral equations results in the following weak equivalent for Eq. (3.22) and Eq. (3.23) respectively

$$j\omega \langle \mathbf{f}_m^t, \mathbf{A} \rangle_{\mathcal{S}} + \langle \mathbf{f}_m^t, \nabla \phi_e \rangle_{\mathcal{S}} = -\frac{1}{\epsilon_0} \langle \mathbf{f}_m^t, \nabla \times \mathbf{F} \rangle_{\mathcal{S}} - \frac{1}{2} \langle \mathbf{f}_m^t, \mathbf{n} \times \mathbf{K}_{\mathcal{S}} \rangle_{\mathcal{S}}, \quad \forall m \quad (3.27)$$

$$\langle \mathbf{g}_m^t, \mathbf{J}_{\mathcal{S}} \rangle_{\mathcal{S}_{ap}} = \langle \mathbf{g}_m^t, \mathbf{n} \times \mathbf{H}_{wg} \rangle_{\mathcal{S}_{ap}}, \quad \forall m \quad (3.28)$$

If the testing functions are chosen as  $\mathbf{f}_n^t = \mathbf{f}_n$  and  $\mathbf{g}_n^t = \mathbf{g}_n$  then the obtained formulation is known as Galerkin's method.

### 3.2.4 Expansion functions and MOM matrix

In this section a selection is made for the expansion functions  $\mathbf{f}_n(\mathbf{r})$  and  $\mathbf{g}_n(\mathbf{r})$ . We assume that a triangular discretization, defined in terms of a set of faces, edges and vertices, has been found to approximate the computational domain  $\mathcal{S}$  and  $\mathcal{S}_{ap}$  (see Fig. 3.4).

### Sub-domain expansion functions for the electric current density $\mathbf{J}_S$

The electric current density  $\mathbf{J}_S(\mathbf{r})$  is expanded in terms of basis functions  $\mathbf{f}_n(\mathbf{r})$  similar to those introduced by [3]. Such basis functions are defined on pairs of triangular patches  $\mathcal{TR}_n^+$  and  $\mathcal{TR}_n^- \in \mathcal{S}$ , and have a common interior edge with length  $l_n$  (see Fig. 3.5). Each non-boundary edge, i.e. edge belonging to a single triangle, is associated with a basis function. Hence, the number of basis functions is equal to the number of non-boundary edges. The vector basis function, associated with a common edge with index  $n$ , is defined as

$$\mathbf{f}_n(\mathbf{r}) = \begin{cases} \frac{l_n}{2S_n^+} \boldsymbol{\rho}_n^+, & \text{if } \mathbf{r} \in \mathcal{TR}_n^+ \\ \frac{l_n}{2S_n^-} \boldsymbol{\rho}_n^-, & \text{if } \mathbf{r} \in \mathcal{TR}_n^- \\ \mathbf{0}, & \text{otherwise,} \end{cases} \quad (3.29)$$

where  $l_n$  is the length of the common edge and  $S_n^\pm$  is the surface of triangle  $\mathcal{TR}_n^\pm$ . Points on triangle  $\mathcal{TR}_n^\pm$  can be designated either by the vector position  $\mathbf{r}$  defined with respect to the origin  $\mathcal{O}$ , or by the vector  $\boldsymbol{\rho}_n^\pm$  defined with respect to the vertex opposite to the common edge (free vertex). The direction of  $\boldsymbol{\rho}_n^+$  is chosen away from the free vertex while the direction of  $\boldsymbol{\rho}_n^-$  is toward the free vertex (see Fig. 3.5). This designation is chosen such that a positive current vector, associated with edge  $n$ , is directed from  $\mathcal{TR}_n^+$  to  $\mathcal{TR}_n^-$ .

The basis functions  $\mathbf{f}_n$ , when constructed according to Eq. (3.29), yield at least a piecewise constant approximation to the current density. Since each basis function varies linearly with distance inside the triangular pair associated with it, it can also model linear variations to some extent. Furthermore, the basis functions have the following properties

- $\mathbf{f}_n$  has no component normal to the outer boundary of the triangle pair  $\mathcal{TR}_n^+$  and  $\mathcal{TR}_n^-$ .
- The component of  $\mathbf{f}_n$  normal to the common edge of the triangle pair is constant

and continuous across the edge.

- The surface divergence of  $\mathbf{f}_n$ , used in the evaluation of the scalar electric potential, is simply

$$\nabla \cdot \mathbf{f}_n(\mathbf{r}) = \begin{cases} \frac{I_n}{S_n^+}, & \text{if } \mathbf{r} \in \mathcal{TR}_n^+ \\ -\frac{I_n}{S_n^-}, & \text{if } \mathbf{r} \in \mathcal{TR}_n^- \\ 0, & \text{otherwise,} \end{cases} \quad (3.30)$$



Figure 3.4: Example of discretization of the computational domain using triangular patches.

The first two properties imply that all edges of  $\mathcal{TR}_n^\pm$  are free of line charges while the third property means that the charge density is constant in each triangle and the total charge density associated with the triangle pair  $\mathcal{TR}_n^\pm$  equal zero [3]. Since the normal component of  $\mathbf{f}_n$  at each edge is unity, the coefficient  $I_n$  in the current expansion represents the normal component of the current density at the  $n^{\text{th}}$  edge.

**Global-domain basis functions for the magnetic current density  $\mathbf{K}_S$**

The magnetic current density is expanded using the orthonormal transversal waveguide modal functions, namely,  $\mathbf{e}_{m,n}^{\text{TE}}(\mathbf{r})$  and  $\mathbf{e}_{m,n}^{\text{TM}}(\mathbf{r})$  given by Eq. (2.11) in the previous chapter. The basis functions  $\mathbf{g}_l(\mathbf{r})$  are then defined as

$$\mathbf{g}_l(\mathbf{r}) = \begin{cases} -\mathbf{n} \times \mathbf{e}_{m,n}^{\text{TE}}(\mathbf{r}), & \mathbf{r} \in \mathcal{S}_{\text{ap}}, \text{ TE case,} \\ -\mathbf{n} \times \mathbf{e}_{m,n}^{\text{TM}}(\mathbf{r}), & \mathbf{r} \in \mathcal{S}_{\text{ap}}, \text{ TM case,} \\ \mathbf{0}, & \text{otherwise.} \end{cases} \quad (3.31)$$

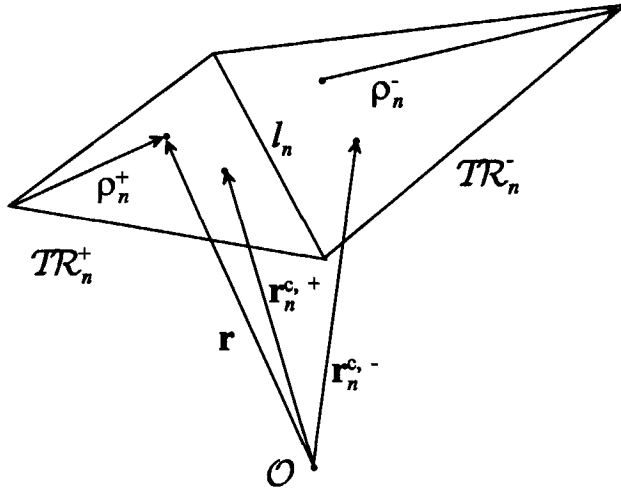


Figure 3.5: Geometry of a pair of triangular patches associated with basis function  $\mathbf{f}_n$ .

In Eq.(3.31), each value of the index  $l$  corresponds to a waveguide modal distribution with index  $(m, n)$ .

### Determination of the MOM matrix equation

In order to find the unknown coefficients  $I_n$  and  $V_n$  in Eq. (3.24) we need to have as many linearly independent equations as unknowns. Such a system can be obtained by taking the inner product of Eqs. (3.27) and (3.28) with a set of weighting functions  $\mathbf{f}_m^t = \mathbf{f}_m$  and  $\mathbf{g}_m^t = \mathbf{g}_m^{\text{TE;TM}}$ , respectively. The result obtained is

$$\begin{aligned} & j\omega \langle \mathbf{f}_m, \mathbf{A} \rangle_{TR_m^+ \cup TR_m^-} + \langle \mathbf{f}_m, \nabla \phi_e \rangle_{TR_m^+ \cup TR_m^-} = \\ & -\frac{1}{\epsilon_0} \langle \mathbf{f}_m, \nabla \times \mathbf{F} \rangle_{TR_m^+ \cup TR_m^-} - \frac{1}{2} \langle \mathbf{f}_m, \mathbf{n} \times \mathbf{K}_S \rangle_{TR_m^+ \cup TR_m^-}, \end{aligned} \quad (3.32)$$

$$\begin{aligned} \langle \mathbf{g}_m^{\text{TE}}, \mathbf{J}_S \rangle_{S_{\text{ap}}} &= \langle \mathbf{g}_m^{\text{TE}}, \mathbf{n} \times \mathbf{H}_{\text{wg}} \rangle_{S_{\text{ap}}}, \\ \langle \mathbf{g}_m^{\text{TM}}, \mathbf{J}_S \times \mathbf{n} \rangle_{S_{\text{ap}}} &= \langle \mathbf{g}_m^{\text{TM}}, \mathbf{H}_{\text{wg}} \rangle_{S_{\text{ap}}}. \end{aligned} \quad (3.33)$$

After substituting the basis functions by their expressions, Eqs. (3.29) and (3.31), we obtain the following linear system

$$\begin{aligned} \sum_{n=1}^N Z_{m,n}^{\text{c-c}} I_n &= \sum_{l=1}^{\text{NTE}} Z_{m,l}^{\text{c-a,TE}} (V_l^{\text{TE}} + V_l^{i,\text{TE}}) + \sum_{l=1}^{\text{NTM}} Z_{m,l}^{\text{c-a,TM}} (V_l^{\text{TM}} + V_l^{i,\text{TM}}), \\ & m = 1, \dots, N, \end{aligned} \quad (3.34)$$

$$\begin{aligned} \sum_{n=1}^N Z_{m,n}^{\text{a-c,TE}} I_n &= \sum_{l=1}^{\text{NTE}} Z_{m,l}^{\text{a-a,TE}} (V_l^{\text{TE}} - V_l^{i,\text{TE}}), \quad m = 1, \dots, \text{NTE}, \\ \sum_{n=1}^N Z_{m,n}^{\text{a-c,TM}} I_n &= \sum_{l=1}^{\text{NTM}} Z_{m,l}^{\text{a-a,TM}} (V_l^{\text{TM}} - V_l^{i,\text{TM}}), \quad m = 1, \dots, \text{NTM}, \end{aligned} \quad (3.35)$$

or in matrix notation

$$\begin{aligned} Z^{\text{c-c}} \mathbf{I} &= \begin{bmatrix} Z^{\text{c-a,TE}} & Z^{\text{c-a,TM}} \end{bmatrix} \begin{bmatrix} \mathbf{V}^{\text{TE}} \\ \mathbf{V}^{\text{TM}} \end{bmatrix} + \begin{bmatrix} Z^{\text{c-a,TE}} & Z^{\text{c-a,TM}} \end{bmatrix} \begin{bmatrix} \mathbf{V}^{i,\text{TE}} \\ \mathbf{V}^{i,\text{TM}} \end{bmatrix}, \\ \begin{bmatrix} Z^{\text{a-c,TE}} \\ Z^{\text{a-c,TM}} \end{bmatrix} \mathbf{I} &= \begin{bmatrix} Z^{\text{a-a,TE}} & 0 \\ 0 & Z^{\text{a-a,TM}} \end{bmatrix} \begin{bmatrix} \mathbf{V}^{\text{TE}} \\ \mathbf{V}^{\text{TM}} \end{bmatrix} - \begin{bmatrix} Z^{\text{a-a,TE}} & 0 \\ 0 & Z^{\text{a-a,TM}} \end{bmatrix} \begin{bmatrix} \mathbf{V}^{i,\text{TE}} \\ \mathbf{V}^{i,\text{TM}} \end{bmatrix}. \end{aligned} \quad (3.36)$$

Expressions for the entries of the different matrices are given in Appendix B. The linear system of Eq. (3.36) can be written in a more compact form

$$\begin{bmatrix} Z^{c-c} & -Z^{c-a} \\ Z^{a-c} & -Z^{a-a} \end{bmatrix} \begin{bmatrix} \mathbf{I} \\ \mathbf{V} \end{bmatrix} = \mathbf{V}^i, \quad (3.37)$$

where  $\mathbf{V} = \begin{bmatrix} \mathbf{V}^{\text{TE}} & \mathbf{V}^{\text{TM}} \end{bmatrix}^T$  and  $\mathbf{V}^i = \begin{bmatrix} \mathbf{V}_1^i & \mathbf{V}_2^i \end{bmatrix}^T$ . The known vectors  $\mathbf{V}_1^i$  and  $\mathbf{V}_2^i$  can be obtained directly after evaluation of the following expressions

$$\begin{aligned} \mathbf{V}_1^i &= \begin{bmatrix} Z^{c-a,\text{TE}} & Z^{c-a,\text{TM}} \end{bmatrix} \begin{bmatrix} \mathbf{V}^{i,\text{TE}} \\ \mathbf{V}^{i,\text{TM}} \end{bmatrix}, \\ \mathbf{V}_2^i &= - \begin{bmatrix} Z^{a-a,\text{TE}} & 0 \\ 0 & Z^{a-a,\text{TM}} \end{bmatrix} \begin{bmatrix} \mathbf{V}^{i,\text{TE}} \\ \mathbf{V}^{i,\text{TM}} \end{bmatrix}. \end{aligned} \quad (3.38)$$

The unknown coefficients  $\mathbf{I}$  and  $\mathbf{V}$  are found after solution of the linear system of Eq. (3.37).

### 3.2.5 Far-field numerical computation

The electric field strength in the far zone is found after using the well-known far-field approximations [18, p. 88] in Eq. (3.15). The result is given by

$$\begin{aligned} \mathbf{E}(\mathbf{r}) &= \mathbf{E}_{\text{cond}}(\mathbf{r}) + \mathbf{E}_{\text{ap}}(\mathbf{r}), \\ \mathbf{E}_{\text{cond}}(\mathbf{r}) &\approx -\frac{j\omega\mu_0 \exp(-jk_0 r)}{4\pi r} \int_S [\mathbf{J}_S - (\hat{\mathbf{i}}_r \cdot \mathbf{J}_S)\hat{\mathbf{i}}_r] \exp(jk_0 \hat{\mathbf{i}}_r \cdot \mathbf{r}') dA', \\ \mathbf{E}_{\text{ap}}(\mathbf{r}) &\approx -\frac{j\omega\mu_0 \exp(-jk_0 r)}{4\pi r} \sqrt{\frac{\epsilon_0}{\mu_0}} \int_{S_{\text{ap}}} (\mathbf{K}_S \times \hat{\mathbf{i}}_r) \exp(jk_0 \hat{\mathbf{i}}_r \cdot \mathbf{r}') dA', \end{aligned} \quad (3.39)$$

After putting the current expansions into Eq. (3.39), we obtain for the first part

$$\begin{aligned} \mathbf{E}_{\text{cond}}(\mathbf{r}) &\approx -\frac{j\omega\mu_0 \exp(-jk_0 r)}{4\pi r} \sum_i^{\text{NTR}} [\mathbf{J}_S(\mathbf{r}_i^c) - (\hat{\mathbf{i}}_r \cdot \mathbf{J}_S(\mathbf{r}_i^c))\hat{\mathbf{i}}_r] \exp(jk_0 \hat{\mathbf{i}}_r \cdot \mathbf{r}_i^c) S_i, \\ \mathbf{J}_S(\mathbf{r}_i^c) &= \sum_{n=1}^3 I_n \mathbf{f}_n(\mathbf{r}_i^c), \end{aligned} \quad (3.40)$$

where  $\mathbf{r}_i^c$  denotes the vector position of the centroid of the  $i^{\text{th}}$  triangle with surface  $\mathcal{S}_i$  and NTR is the total number of triangles used to approximate  $\mathcal{S}$ . In Eq. (3.40) the current density  $\mathbf{J}_S$  is assumed to be constant within each triangle and equal to its value at the triangle centroid. In a similar way, we found for the second part of Eq. (3.39)

$$\begin{aligned} \mathbf{E}_{\text{ap}}(\mathbf{r}) &\approx -\frac{jk_0 \exp(-jk_0 r)}{4\pi r} \sum_i^{\text{NTR}} \chi_{\mathcal{S}_{\text{ap}}}(\mathbf{r}_i^c) (\mathbf{K}_S(\mathbf{r}_i^c) \times \hat{\mathbf{r}}_r) \exp(jk_0 \hat{\mathbf{r}}_r \cdot \mathbf{r}_i^c) \mathcal{S}_i, \\ \mathbf{K}_S(\mathbf{r}_i^c) &= \sum_l^{\text{NTE}} \mathbf{g}_l^{\text{TE}}(\mathbf{r}_i^c) (V_l^{\text{TE}} + V_l^{i,\text{TE}}) + \sum_l^{\text{NTM}} \mathbf{g}_l^{\text{TM}}(\mathbf{r}_i^c) (V_l^{\text{TM}} + V_l^{i,\text{TM}}), \end{aligned}$$

$$\text{where } \chi_{\mathcal{S}_{\text{ap}}}(\mathbf{r}_i^c) = \begin{cases} 1, & \mathbf{r}_i^c \in \mathcal{S}_{\text{ap}} \\ 0, & \text{otherwise} \end{cases}.$$

### 3.3 Iterative solution of the MoM linear system

There are many techniques available in the literature for the numerical solution of the MoM linear system. A good survey can be found in [19] and [20]. In this section we solve Eq. (3.37) using the complex bi-conjugate gradient algorithm (BiCG) in the form proposed by Jacobs [21]. For completeness a brief description of the algorithm, for solving the system  $Ax = b$ , is given below [20]

$$\begin{aligned} x_{n+1} &= x_n + a_n p_n \\ r_{n+1} &= r_n - a_n A p_n, \quad q_{n+1} = q_n - a_n^* A^H w_n \\ p_{n+1} &= r_{n+1} + c_n p_n, \quad w_{n+1} = q_{n+1} + c_n^* w_n \\ a_n &= \frac{\langle r_n, q_n \rangle}{\langle A p_n, w_n \rangle}, \quad c_n = \frac{\langle r_{n+1}, q_{n+1} \rangle}{\langle r_n, q_n \rangle} \end{aligned} \quad (3.41)$$

The algorithm starts with initial values  $x_1 = 0$ ,  $r_1 = p_1 = y$ , and  $w_1 = q_1 = y^*$ , and stops when  $\|r_{n+1}\| \leq \text{tolerance} * \|y\|$ . The superscript \* denotes the complex conjugate, while the superscript  $^H$  denotes the adjoint (i.e. conjugate and transpose). In Eq.(3.41),  $\langle x, y \rangle = xy^H$  and  $\|x\| = \langle x, x \rangle^{\frac{1}{2}}$ . The bi-conjugate algorithm usually converges in nearly half the iterations of the conjugate gradient (CG) algorithm. However, the residual error of BiCG oscillates widely before convergence to a specified tolerance.



## 3.4 Numerical results and experimental validation

In this section, we present a number of new numerical results obtained using the formulation derived in the previous sections. Both the induced current distributions and far-field patterns are analyzed. The design and construction of a single antenna is described. The antenna is characterized by radiation pattern and reflection coefficient. Measurements were carried out and the data obtained were used to validate the numerical code. A comparison of theoretically predicted and measured results is presented and we discuss the code accuracy and validation of the design procedure. Some computational aspects related to parallel processing are also reviewed. All the presented results are normalized to their maximum value.

### 3.4.1 Numerical examples

#### (a) Antenna geometry 1

First consider a dielectric-filled waveguide terminated into a metallic flange with a complex 3-D geometry as shown in Fig. 3.6 and Fig. 3.7. The geometry of this example consists of a uniform waveguide section and three rectangular flanges intended for mounting purposes. The thickness of the waveguide metallic wall (2.0 mm) is gradually tapered toward the radiating aperture over a distance 39.6 mm, becoming 0.1 mm at the aperture plane. This reduces the reflections at the aperture plane, i.e. adaptation to free space. The waveguide is filled with dielectric medium rexolite ( $\epsilon_r = 2.53$ ) and designed to operate at the frequency of 3.3 GHz. The aperture dimensions,  $a = b = 34.2$  mm, are equal to the inner dimensions of the feeding waveguide and chosen to only allow the fundamental mode to propagate, namely the  $TE_{1,0}$ . The whole metallic structure, including the aperture, was approximated using a surface mesh with 582 nodes and 1160 triangles. This corresponds to a number of

unknowns of 1740 to represent the electric current density distribution. The number of modal functions we used to approximate the aperture field distribution was 20. The linear system associated with the problem considered involves 1760 unknowns in complex double precision.

The resulting impressed magnetic current density is shown in Fig. 3.6, while the obtained electric current distributions are presented in Fig. 3.7. From Fig. 3.6 we observe the dominance of the well-known  $TE_{1,0}$  pattern in the electric-field distribution at the aperture. The singular behavior of the current nearby the edges was predicted very well, as is demonstrated in Fig.3.7. A more accurate prediction of the field singular behaviour would require an increase of the mesh density in the vicinity of all the metallic edges and especially around the aperture where the field intensity fluctuates significantly. However, this comes at the cost of a significant increase in the computational efforts required for solving the problem. The computed reflection coefficient at the aperture is  $\Gamma = -14.0\text{dB}$  (measured value:  $-14.3\text{dB}$ ). The far-field patterns in the E- and H-plane are given in Fig. 3.8 and Fig. 3.9, respectively. Excellent agreement is observed between theory and experiment over a wide angular range.

### (b) Antenna geometry 2

The second example considered in this section is a rectangular waveguide antenna with finite dimensions ( $34.2 \times 34.2 \times 100\text{mm}$ , see Fig. 3.10) and filled with a dielectric material (rexolite,  $\epsilon_r = 2.53$ ). In this example 1326 triangles were used to approximate the structure, resulting in a total number of 2000 unknowns. The normalized magnitude of the induced electric current density along the outer waveguide metallic wall is shown in Fig. 3.10, while the far-field patterns in E-, H- and  $45^\circ$ -plane are given in Fig. 3.11 at 3.3GHz. The results indicate a high back-lobe level ( $-5.4\text{dB}$ ), a broad radiation pattern in different planes ( $\sim -10\text{dB}$  taper at  $90^\circ$ ) and a highly symmetric

pattern over  $40^\circ$ . The cross-polarization level, in the  $45^\circ$ -plane, is better than  $-20\text{dB}$  in the main beam region ( $0^\circ$ - $90^\circ$ ). In order to reduce the unwanted radiation in the region ( $90^\circ$  –  $180^\circ$ ), one can cover parts of the waveguide metallic wall with absorbing material. Such antenna configurations find application as probes in near field and far field antenna measurement systems.

### (c) Antenna geometry 3

A further design iteration considered was the insertion of three rectangular metallic plates with dimensions (plate 1 & 2:  $50 \times 50 \times 12\text{mm}$ , plate 3:  $50 \times 50 \times 6\text{mm}$ ) into the feeding waveguide of antenna geometry 2 (see Fig. 3.12). This procedure was carried out to examine whether it is possible to cancel back-lobe radiation by destructive interference. The resulting structure was modeled with 1940 triangles (number of unknowns: 2920). The magnitude of the computed electric-current density at 3.3 GHz is shown in Fig.3.12, while the resulting far-field patterns, in different planes, are given in Fig. 3.13. The introduction of the metallic plates did indeed result in a decrease of the back-lobe radiation level and an improvement of the cross-polarization level. A slight increase in the antenna gain was observed.

### (d) Antenna geometry 4

A final design example which follows naturally from the previous numerical experiment considers an external corrugation profile on the waveguide feed as shown in Fig. 3.14. The number of plates and their thicknesses was arrived at heuristically. This very complex structure was modeled with a mesh having 1305 nodes and 2606 triangles. The total number of unknowns is 3919. The normalized electric-current density is shown in Fig. 3.14 and the far-field patterns are given in Fig. 3.15. The results indicate a significant gain increase and back-lobe level reduction (better than  $30\text{dB}$ )

at the cost of an increase of the cross-polarization level ( $< -14\text{dB}$ ) in the  $45^\circ$ -plane.

Table 3.1: Summary of numerical results for the antenna designs presented.

Antenna Configuration of	Reflection Coefficient (dB)	Cross- Polarization (dB)	Back-lobe level (dB)	E-plane 3-dB beam width (deg)	H-plane 3-dB beam width (deg)
Fig. 3.6	-14	-18.0	-9.4	62	75
Fig. 3.10	-12.4	-20.3	-5.4	142	80
Fig. 3.12	-11.8	-21.6	-6.4	62	70
Fig. 3.14	-8	-14.2	-37	76	78

### 3.4.2 Computational aspects

Given the size of the electromagnetic problem encountered here it became both necessary and essential (because of memory and CPU time requirements) to migrate the code to a massive parallel computer system. To this end the code was ported to the CRAY J90se computer system available at the Centre for High Performance Applied Computing, Delft University of Technology. The J90se is a powerful, general-purpose multiprocessor machine. It contains ten 10-nanosecond central processing units for vector operations, a 5-nanosecond clock for scalar operations and 2.048 Gbytes of shared central memory. In the present code, two main types of parallelism were utilized: (1) the vector-syntax of FORTRAN-90 in the source code to represent all vector-, matrix-operations, and I/O accesses, and (2) parallel execution of independent modules of the code (pipelining). Other optimization of the code outside the scope of this work are possible, i.e. fully parallel implementation and optimization of the different code modules. The requirements of the present code are shown in Table 3.2.

Table 3.2: Summary of computational requirements for selected antenna examples.

Antenna Configuration of	Number of Unknowns	Memory Required (MB)	Matrix Fill Time (h)	Matrix Inversion Time (h)	Total CPU Time (h)
Fig. 3.6	1760	>25	0.51	0.73	1.25
Fig. 3.10	2000	>32	0.62	1.69	2.32
Fig. 3.12	2920	>68	1.89	3.83	5.72
Fig. 3.14	3919	>124	2.38	5.88	8.26

### 3.5 Conclusions

We presented an analysis and design tool for analyzing and improving the radiation from a dielectric-filled waveguide terminated by a metallic flange of finite size and arbitrary 3-D shape. Using the equivalence principle, we derived an equivalent problem and when the appropriate boundary and interface conditions are imposed a set of integral equations is obtained with surface currents as the unknowns. These coupled integral equations are solved by the MoM to yield the surface currents, from which the radiation pattern is calculated.

The electromagnetic field inside the waveguide is represented by means of waveguide modal decomposition, which takes into account both propagating and evanescent modes arising from the discontinuities at the transition from waveguide into free space. The electromagnetic field radiated into free space is due to equivalent electric and magnetic surface currents, located along a surface that encloses the whole structure. Both fields are related to each other by the application of the boundary and interface conditions. The whole structure, including the aperture, is approximated with a triangular discretization. The electric-current density is expanded in terms of vector rooftop

basis functions, and the unknown are the normal components of the electric current along each non-boundary edge of the triangular mesh. The magnetic current density on the aperture is expanded using transversal waveguide modal functions.

A number of numerical examples were presented and results in the form of induced currents distribution and far-field patterns were given. The code was implemented on a massively parallel computer system (CRAY J90se) supported by Delft University of Technology. Some computational aspects related to parallel processing of numerical problems have been discussed.

The presented results indicate that an antenna design that is improved in terms of gain, side lobes, cross polarization and back lobe can be obtained by optimizing the external corrugation profile on the metallic structure around the waveguide. The obtained optimum design may be very complex and the construction costs of both material and machinery become significantly high.

A single dielectric-filled waveguide antenna was built and tested. The excellent agreement between simulated and measured antenna performances demonstrate the accuracy of the present formulation.

The obtained code enabled the detailed design and further refinement to the waveguide antenna. This work resulted in a final design for a waveguide launcher, at 3.3 GHz, which will be used throughout the next chapters.

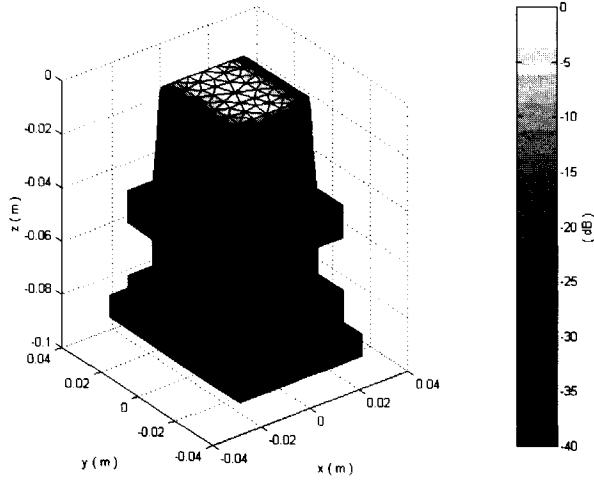


Figure 3.6: Normalized norm of surface magnetic current density at frequency 3.3 GHz (Aperture dimensions:  $a = b = 34.2$  mm,  $\epsilon_r = 2.53$ ).

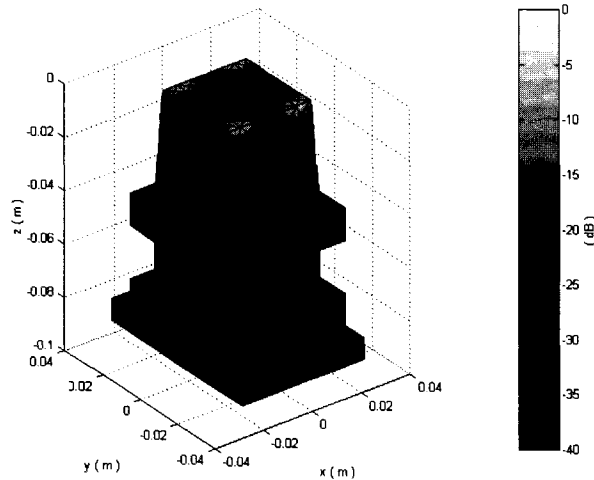


Figure 3.7: (a) Normalized magnitude of  $x$ -component of surface electric current density at frequency 3.3 GHz (Aperture dimensions:  $a = b = 34.2$  mm,  $\epsilon_r = 2.53$ ).

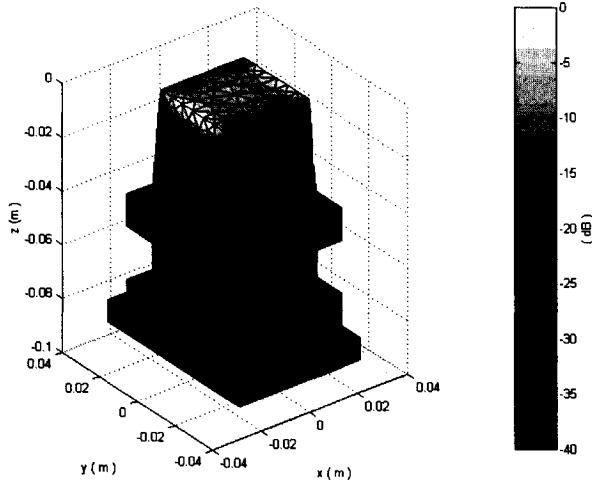


Figure 3.7: (b) Normalized magnitude of  $y$ -component of surface electric current density at frequency 3.3 GHz (Aperture dimensions:  $a = b = 34.2$  mm,  $\epsilon_r = 2.53$ ).

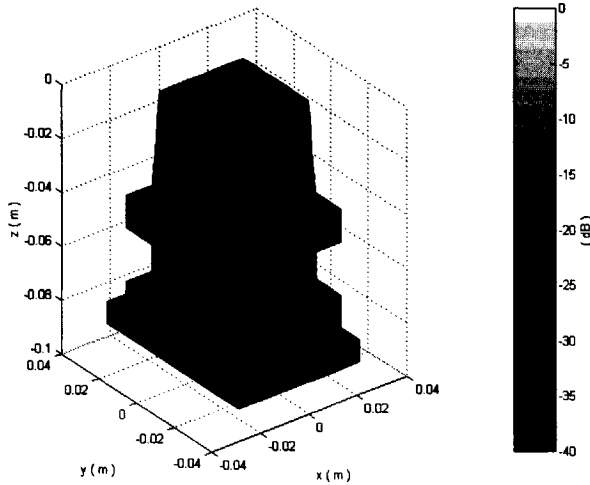


Figure 3.7: (c) Normalized magnitude of  $z$ -component of surface electric current density at frequency 3.3 GHz (Aperture dimensions:  $a = b = 34.2$  mm,  $\epsilon_r = 2.53$ ).



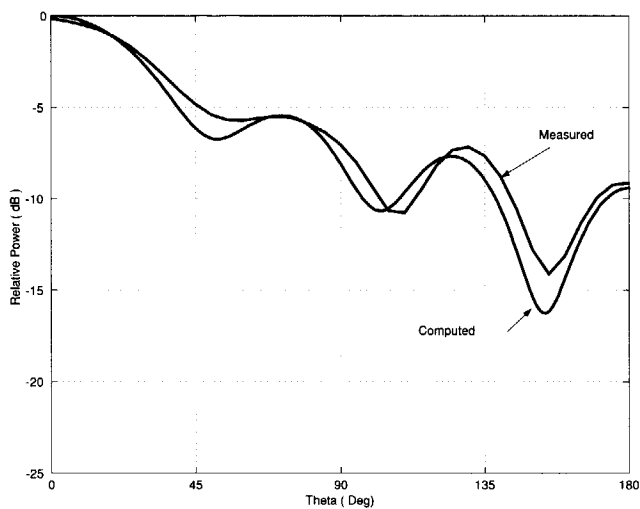


Figure 3.8: Computed and measured far-field E-plane patterns at frequency 3.3 GHz  
(Aperture dimensions:  $a = b = 34.2$  mm,  $\epsilon_r = 2.53$ )

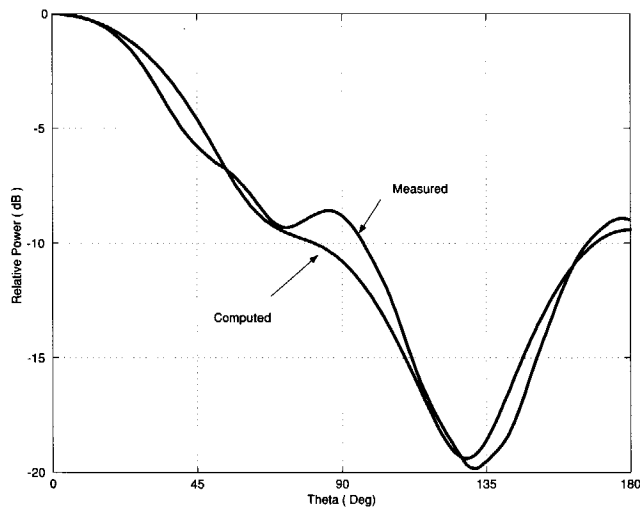


Figure 3.9: Computed and measured far-field H-plane patterns at frequency 3.3 GHz  
(Aperture dimensions:  $a = b = 34.2$  mm,  $\epsilon_r = 2.53$ )

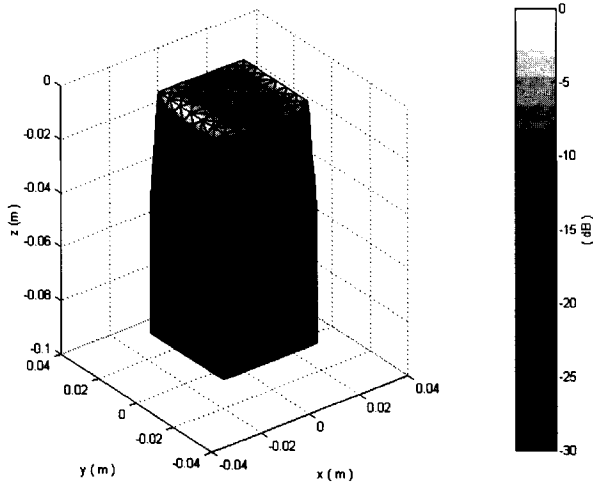


Figure 3.10: Normalized norm of surface electric current density at frequency 3.3 GHz (Aperture dimensions  $a = b = 34.2$  mm,  $\epsilon_r = 2.53$ ).

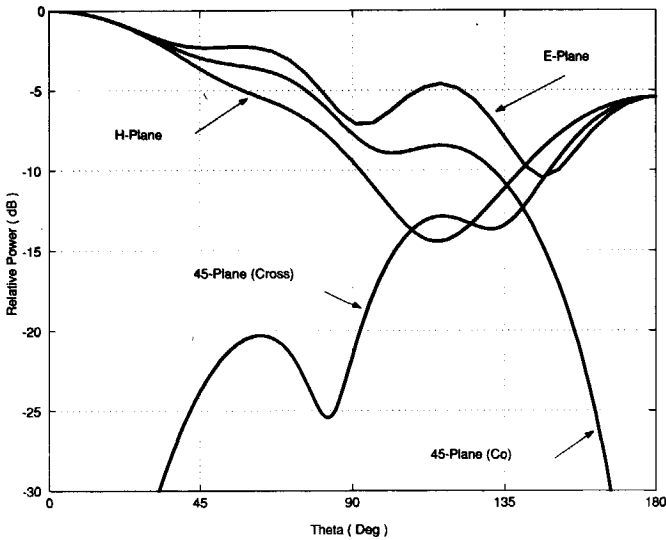


Figure 3.11: Computed far-field patterns in different planes for antenna geometry 2.

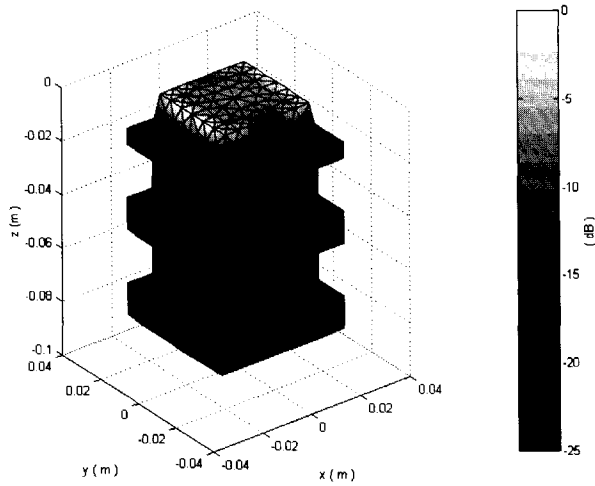


Figure 3.12: Normalized norm of surface electric current density at frequency 3.3 GHz (Aperture dimensions  $a = b = 34.2$  mm,  $\epsilon_r = 2.53$ ).

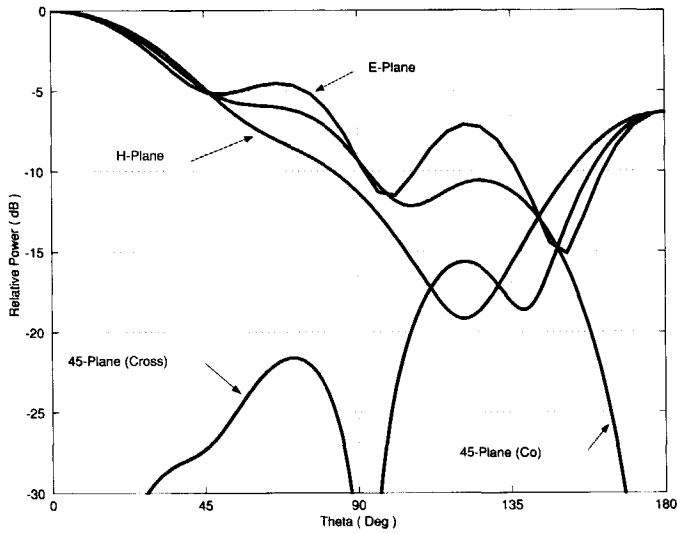


Figure 3.13: Computed far-field patterns in different planes for antenna geometry 3.

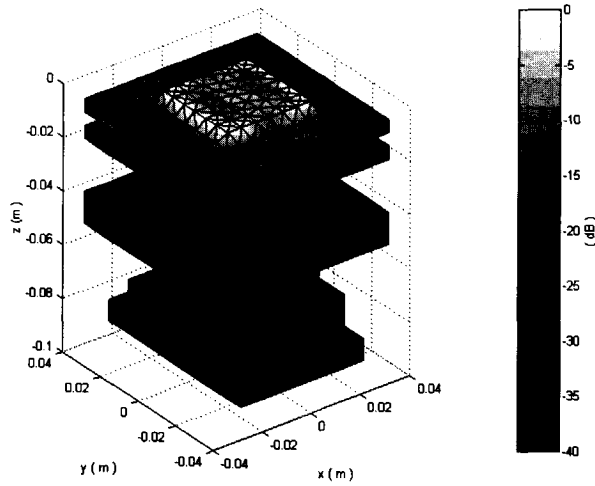


Figure 3.14: Normalized norm of surface electric current density at frequency 3.3 GHz (Aperture dimensions  $a = b = 34.2$  mm,  $\epsilon_r = 2.53$ ).

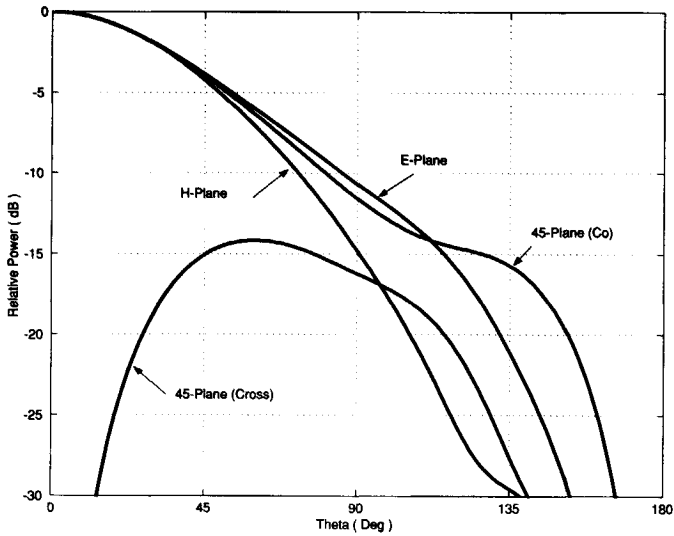


Figure 3.15: Computed far-field patterns in different planes for antenna geometry 4.

## References

- [1] N.N. Wang, J.H. Richmond, and M.C. Gilreath, "*Sinusoidal Reaction Formulation for Radiation and Scattering from Conducting Surfaces*", IEEE Trans. Antennas Propagat., vol. AP-23 No. 3, pp. 376-382, May 1975.
- [2] A.W. Glisson and D.R. Wilton, "*Simple and Efficient Numerical Methods for Problems of Electromagnetic Radiation and Scattering from Surfaces*", IEEE Trans. Antennas Propagat., vol. AP-28 No. 5, pp. 593-603, September 1980.
- [3] S.M. Rao, D.R. Wilton, and A.W. Glisson, "*Electromagnetic Scattering by Surfaces of Arbitrary Shape*", IEEE Trans. Antennas Propagat., vol. AP-30 No. 3, pp. 409-418, May 1982.
- [4] E. Arvas, R.F. Harrington, and J. Mautz, "*Radiation and Scattering from Electrically Small Conducting Bodies of Arbitrary Shape*", IEEE Trans. Antennas Propagat., vol. AP-34 No. 1, pp. 66-77, January 1986
- [5] A. Berthon, and R.P. Bills, "*Integral Equation Analysis of Radiating Structures of Revolution*", IEEE Trans. Antennas Propagat., vol. AP-37 No. 2, pp. 159-170, February 1989.
- [6] J.R. Mautz and R.F. Harrington, "*H-field, E-field, and Combined Field Solutions for Conducting Bodies of Revolution*", Arch. Elek. Ubertragung, vol. 32, pp. 157-164, 1978.

- 
- [7] A.A. Kishk and L. Shafai, "*Different Formulations for Numerical Solution of Single or Multibodies of Revolution with Mixed Boundary Conditions*", IEEE Trans. Antennas Propagat., vol. AP-34 No. 5, pp. 666-1673, May 1986.
- [8] R.F. Harrington, "*Field Computation by Moment Methods*", R.E. Krieger Publishing Company, Malabar, Florida, 1982.
- [9] J.H. Wang, "*Generalized Moment Methods In Electromagnetics*", John Wiley & Sons, INC., New York 1991.
- [10] R.F. Harrington and J.R. Mautz, "*A Generalized Network Formulation for Aperture Problems*", IEEE Trans. Antennas Propagat., AP-24 pp.870-873, November 1976.
- [11] R.F. Harrington and J.R. Mautz, "*Electromagnetic Transmission through an Aperture in a Conducting Plane*", Arch. Elek. Ubertragung, vol. 31, pp. 81-87, 1977.
- [12] R.F. Harrington and J.R. Mautz, "*Boundary Formulations for Aperture Coupling Problems*", Arch. Elek. Ubertragung, vol. 34, pp. 377-384, 1980.
- [13] R.F. Harrington, "*Time Harmonic Electromagnetic Fields*", McGraw-Hill Book, New York 1961.
- [14] D.S. Jones, "*Methods in Electromagnetic Wave Propagation*", Clarendon press, Oxford 1979.
- [15] C.A. Balanis, "*Advanced Engineering Electromagnetics*", John Wiley & Sons, Inc. 1989.
- [16] R.E. Collin, "*Field Theory of Guided Waves*", IEEE Press , 2nd ed. 1990.
- [17] J.J.H. Wang, "*Generalised Moment Methods in Electromagnetics*", IEE Proceedings, vol. 137, Pt. H, No. 2, April 1990.

- [18] S. Silver, "*Microwave Antenna Theory and Design*", Boston Technical Publisher, INC. USA 1964.
- [19] T.K. Sarkar, K.R. Siarkiewicz and R.F. Stratton, "*Survey of Numerical Methods for Solution of Large Systems of Linear Equations for Electromagnetic Field Problems*", IEEE Trans. Antennas Propagat., vol. AP-29 No. 6, pp. 435-444, November 1981.
- [20] J.L. Volakis, "*EM Programmer's Notebook*", IEEE Antennas Propagat. magazine, vol. 37, No. 6, December 1995.
- [21] C.F. Smith, A.F. Peterson and R. Mittra, "*The Biconjugate Gradient Method for Electromagnetic Scattering*", IEEE Trans. Antennas Propagat., vol. AP-38, No. 6, pp. 938-940, June 1990.
- [22] R. Kastner and N. Herscovici, "*A Concise Conjugate Gradient Computation of Plate Problems with Many Excitations*", IEEE Trans. Antennas Propagat., vol. AP-38, No. 8, pp. 1239-1243, August 1990.
- [23] T. Wang, R.F. Harrington and J.R. Mautz, "*Electromagnetic Scattering from and Transmission Through Arbitrary Apertures in Conducting Bodies*", IEEE Trans. Antennas Propagat., vol. AP-38, No. 11, pp. 1805-1814, November 1990.
- [24] M. Mongiardo and T. Rozzi, "*Singular Integral Equation Analysis of Flange-Mounted Rectangular Waveguide Radiators*", IEEE Trans. Antennas Propagat., vol. AP-41, No. 5, pp. 556-565, May 1993.
- [25] K.Y. Kabalan, A. El-Hajj and A. Rayes, "*3-D Analysis of Radiation from Apertures in Flange-Mounted rectangular Waveguides*", Int. J. Electron. Commun. (AEU), vol. 52, N. 2, pp. 49-56, 1998.

- [26] J.J. Ottusch, G.C. Valley and S. Wandzura, "*Integral Equations and Discretizations for Waveguide Apertures*", IEEE Trans. Antennas Propagat., vol. AP-46, No. 11, pp. 1727-1738, November 1998.
- [27] B.M. Kolundzija, "*Accurate Solution of Square Scatterer as Benchmark for Validation of Electromagnetic Modeling of Plate Structures*", IEEE Trans. Antennas Propagat., vol. AP-46, No. 7, pp. 1009-1014, July 1998.
- [28] P. Brachat, C. Dedebean, P. Ratajczak and T. Bousquet, "*Analyse de Structures Tridimensionnelles Inhomogenes Quelconques*", Ann. Telecommun., vol. 52, N. 9-10, pp. 489-502, 1997.



## Chapter 4

# Rigorous analysis of dielectric rod antennas with arbitrary shape

### 4.1 Introduction

Dielectric rod antennas are among the earliest radiating structures used in radar applications. They were first used as primary sources illuminating parabolic reflectors and as elements in phased-arrays in World War II. Recently, dielectric rod antennas have been receiving greater attention with the advance of millimeter-wave technology. Low production costs, high reliability, compact size and the availability of high performance low-loss dielectric materials make dielectric antennas a good candidate for a wide range of applications, especially those at higher frequencies where metallic antennas are costly and inefficient radiators due to the significant increase of resistive losses.

A dielectric antenna usually consists of two parts: the dielectric body and the feeding structure, known as the launcher (see Fig. 4.1.). The dielectric body is of finite length and may be solid or hollow. To improve the radiation pattern and impedance matching, the dielectric body is often tapered toward the end. The dielectric rod is

usually fed by an open-ended metallic waveguide with either a rectangular or a circular cross section.

In order to characterize the radiation from dielectric rod antennas, a variety of approximate methods and simple design equations have been used in the past. A good summary of the work on dielectric antennas has appeared in a recent monograph by Carlos Salema et al. [1]. Earlier reviews on dielectric and dielectric loaded antennas were carried out by Kiely [2] and Chatterjee [3]. In 1967, James reviewed four different methods for the analysis of dielectric antennas [4]. The first method [5] was based on the application of Schelkunoff's equivalence principle to the fictitious currents on a surface enclosing the dielectric medium. In the second method [6] the radiation from the end of a uniform rod carrying  $HE_{1,1}$  waves was neglected and only the field due to the radial surface was evaluated. In the third method [7], the volume equivalence principle is used to transform the uniform dielectric body into a volume of polarization current density. In the fourth method [8], the dielectric rod antenna was modeled as a structure carrying a surface wave to the end of the rod, where it is radiated. In 1972, Yaghjian and Kornhauser [9] used a hybrid modal technique to analyze a semi-infinite cylindrical rod excited by the  $HE_{1,1}$  mode. Later Dombek [10] obtained an approximate solution using Kirchoff integrals. A more rigorous formulation was presented by Kishk and Shafai [11]: they treated the radiation from a short cylindrical rod using a coupled surface integral formulation. All techniques mentioned above are full of assumptions or approximations normally made in the course of analytic studies. Moreover, these methods have been applied to rotational symmetric geometry since the solution is more easier to obtain.

In this chapter, I propose a more rigorous technique based on a hybrid-iterative MoM for the accurate analysis and design of dielectric rod antennas with arbitrary 3-D shape taking into account the launcher. This technique is applied to the dielectric rod configuration given in Fig. 4.1. A design procedure for the antenna is described

and new theoretical and experimental results are presented.

This chapter is organized as described below. First the problem is formulated and the integral equation is derived. Then the discretization of the domain of computation and the expansion functions are discussed. Next the accuracy of the new method and the validation of the design procedure are demonstrated by comparing computed and measured results for a few examples. Finally some concluding remarks on the advantages and disadvantages of the method are presented.

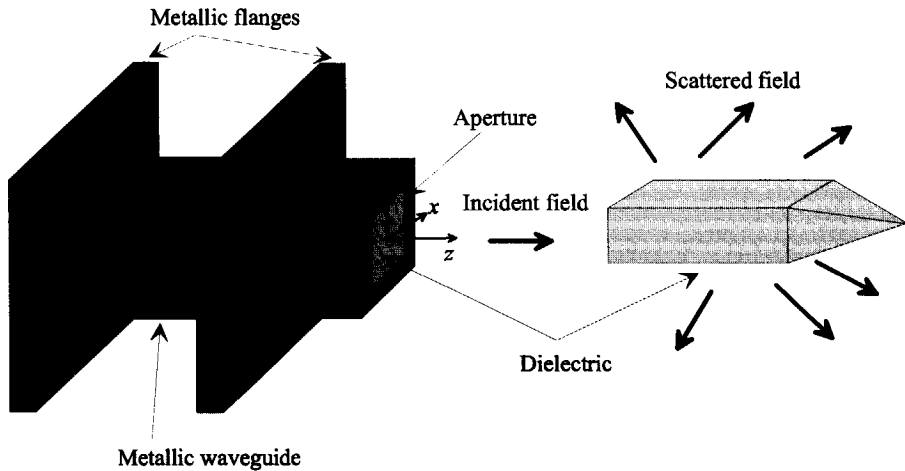


Figure 4.1: The dielectric rod antenna (left: launcher, right: dielectric scatterer); Problem geometry and coordinate system .

## 4.2 Problem formulation and derivation of the integral equation

If a dielectric body is placed in the vicinity of a radiating open-ended waveguide antenna, this will modify the antenna's radiation pattern. This suggests that the dielectric antenna can be treated as a scattering problem, where the incident field is

the field that is created by the open-ended waveguide (launcher). In the scattering formulation, the scatterers are usually supposed to be situated quite far away from the radiating source, so that the incident field is not perturbed by the scattered field. In the case that the scatterer, as in dielectric rod antennas, is situated in the near-field or touches directly the source, an accurate formulation must take into account the interactions between the scatterer (dielectric object) and the source (launcher). In this section, the electromagnetic radiation from a dielectric rod antenna, excited by an open-ended metallic waveguide with rectangular cross section, is formulated as a near-field scattering problem (see Fig. 4.1). The volume and surface equivalence are used to derive an integral representation for the electromagnetic field. Application of the boundary and interface conditions results in a set of coupled integral equations with the current density distributions (electric and magnetic) as the unknowns. Finally, the equations obtained are solved iteratively to yield the unknown current density distributions, from which the radiation pattern can be calculated. The geometry of the problem considered and the global coordinate system used throughout this chapter are depicted in Fig. 4.1.

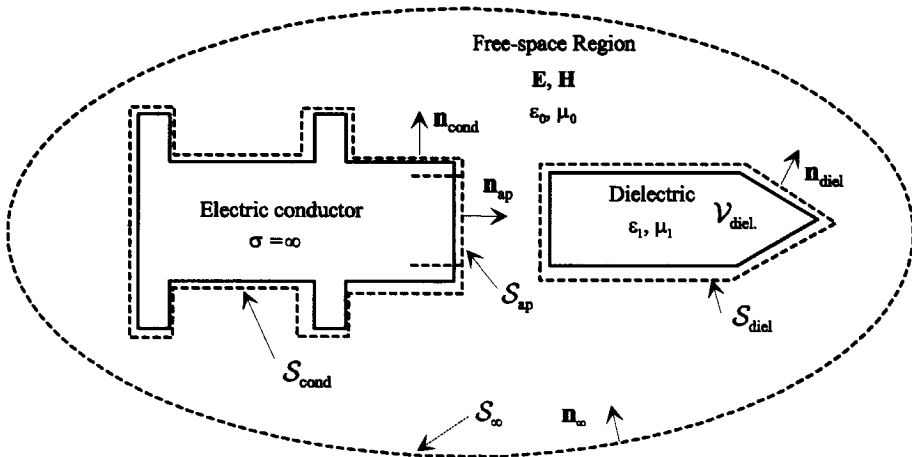


Figure 4.2: The dielectric rod antenna formulated as a near-field scattering problem.

### 4.2.1 Field scattered by a dielectric body of arbitrary 3-D shape

Consider an isotropic linear dielectric body of arbitrary shape, with magnetic permeability  $\mu_1 = \mu_0$  and complex permittivity

$$\hat{\epsilon}(\mathbf{r}) = \epsilon_1(\mathbf{r}) - j\sigma_1(\mathbf{r})/\omega \tag{4.1}$$

where  $\epsilon_1(\mathbf{r})$  denotes the permittivity of the dielectric body and  $\sigma_1(\mathbf{r})$  represents its conductivity. The dielectric object occupies a finite volume  $\mathcal{V}_{\text{diel}}$  and is enclosed by a surface  $\mathcal{S}_{\text{diel}}$  (see Fig. 4.2). The electromagnetic field  $\{\mathbf{E}, \mathbf{H}\}$  radiated by the dielectric rod antenna can be decomposed into a launcher field  $\{\mathbf{E}_{\text{laun}}, \mathbf{H}_{\text{laun}}\}$  and a rod field  $\{\mathbf{E}_{\text{rod}}, \mathbf{H}_{\text{rod}}\}$ . The rod-field is the field generated by an equivalent free-space volume electric current density  $\mathbf{J}_{\mathcal{V}}$ , given by [12, p. 328]

$$\mathbf{J}_{\mathcal{V}}(\mathbf{r}) = [\sigma_1(\mathbf{r}) + j\omega(\epsilon_1(\mathbf{r}) - \epsilon_0)] \mathbf{E}(\mathbf{r}) \chi_{\mathcal{V}}, \tag{4.2}$$

where the shape function  $\chi_{\mathcal{V}}(\mathbf{r}) = 1$  if  $\mathbf{r} \in \mathcal{V}_{\text{diel}}$  and zero otherwise. The first term at the right of Eq. (4.2) represents the conduction current and the second term denotes the polarization current density.  $\mathbf{E}(\mathbf{r})$  is the total electric field inside the dielectric medium.

The electric field  $\mathbf{E}_{\text{rod}}$  produced by  $\mathbf{J}_{\mathcal{V}}$  can be expressed using the vector and scalar electric potentials for an unbounded region as in [12, p. 257]

$$\mathbf{E}_{\text{rod}}(\mathbf{r}) = -j\omega \mathbf{A} - \nabla \phi_e, \tag{4.3}$$

where

$$\mathbf{A}(\mathbf{r}) = \mu_0 \int_{\mathcal{V}_{\text{diel}}} \mathbf{J}_{\mathcal{V}}(\mathbf{r}') G(\mathbf{r}, \mathbf{r}') dV', \quad \phi_e(\mathbf{r}) = \frac{1}{\epsilon_0} \int_{\mathcal{V}_{\text{diel}}} \rho(\mathbf{r}') G(\mathbf{r}, \mathbf{r}') dV', \tag{4.4}$$

$$\rho(\mathbf{r}) = -\frac{\nabla \cdot \mathbf{J}_{\mathcal{V}}(\mathbf{r})}{j\omega}. \tag{4.5}$$

In Eq. (4.4),  $\mathbf{r}'$  represents the vector position of a source element in  $\mathcal{V}_{\text{diel}}$  while  $\mathbf{r}$  denotes the vector position of the point at which the field is computed (observation point). The three-dimensional Green's function of free space,  $G(\mathbf{r}, \mathbf{r}')$ , is given by

$$G(\mathbf{r}, \mathbf{r}') = \frac{\exp(-jk_0 |\mathbf{r} - \mathbf{r}'|)}{4\pi |\mathbf{r} - \mathbf{r}'|}. \quad (4.6)$$

where  $k_0 = \omega\sqrt{\epsilon_0\mu_0}$ . Substitution of Eq. (4.4) into Eq. (4.3) yields the following expression for the scattered field

$$\mathbf{E}_{\text{rod}}(\mathbf{r}) = -j\omega\mu_0 \int_{\mathcal{V}_{\text{diel}}} \mathbf{J}_V(\mathbf{r}')G(\mathbf{r}, \mathbf{r}')dV' + \frac{1}{j\omega\epsilon_0} \nabla \int_{\mathcal{V}_{\text{diel}}} \nabla' \cdot \mathbf{J}_V(\mathbf{r}')G(\mathbf{r}, \mathbf{r}')dV'. \quad (4.7)$$

### 4.2.2 Representation for the incident field

In this section we derive an expression for the incident field using the formulation described in the previous chapter. The incident field is considered as that is the field radiated by the launcher. The launcher consists of a single waveguide-fed aperture mounted on a perfectly conducting structure (see Fig. 4.1). The waveguide is uniformly filled with a non-dissipative, linear, isotropic and homogeneous medium with dielectric constant  $\epsilon_1$  and magnetic permeability  $\mu_0$ . The aperture is rectangular with width  $a$  and height  $b$ . The electromagnetic field radiated by the launcher is given by Eq. (3.14) and Eq. (3.15) as

$$\begin{aligned} \mathbf{E}_{\text{laun}}(\mathbf{r}) = & - \int_{\mathcal{S}} \left( j\omega\mu_0 G(\mathbf{r}, \mathbf{r}') \mathbf{J}_S(\mathbf{r}') - \frac{1}{j\omega\epsilon_0} (\nabla'_S \cdot \mathbf{J}_S(\mathbf{r}')) \nabla G(\mathbf{r}, \mathbf{r}') \right) dA' \\ & - \int_{\mathcal{S}_{\text{ap}}} \nabla \times G(\mathbf{r}, \mathbf{r}') \mathbf{K}_S(\mathbf{r}') dA', \end{aligned} \quad (4.8)$$

where  $\mathcal{S} = \mathcal{S}_{\text{ap}} \cup \mathcal{S}_{\text{cond}}$  (see Fig. 4.2),  $\mathbf{J}_S$  is the equivalent current density on the closed surface  $\mathcal{S}$ , and  $\mathbf{K}_S$  represents the magnetic current density along the aperture surface  $\mathcal{S}_{\text{ap}}$ . The equivalent sources are related to the total electromagnetic field  $\{\mathbf{E}, \mathbf{H}\}$  by the relations

$$\begin{aligned} \mathbf{J}_S(\mathbf{r}) &= \mathbf{n}(\mathbf{r}) \times \mathbf{H}(\mathbf{r}), \quad \mathbf{r} \in \mathcal{S} \\ \mathbf{K}_S(\mathbf{r}) &= \mathbf{E}(\mathbf{r}) \times \mathbf{n}(\mathbf{r}), \quad \mathbf{r} \in \mathcal{S}_{\text{ap}} \end{aligned} \quad (4.9)$$

where  $\mathbf{n}$  is the vector unit normal on  $\mathcal{S}$  and equals  $\mathbf{n}_{\text{cond}}$  on  $\mathcal{S}_{\text{cond}}$  and  $\mathbf{n}_{\text{ap}}$  on  $\mathcal{S}_{\text{ap}}$  (see Fig. 4.2). The electromagnetic field inside the metallic waveguide  $\{\mathbf{E}_{\text{wg}}, \mathbf{H}_{\text{wg}}\}$  is represented by the modal expansions given by Eq.(3.5) and Eq.(3.6) in Chapter 3.

### 4.2.3 Total field and boundary conditions

As stated above, the total electric field radiated by the dielectric rod antenna is given by

$$\mathbf{E}(\mathbf{r}) = \mathbf{E}_{\text{launch}}(\mathbf{r}) + \mathbf{E}_{\text{rod}}(\mathbf{r}), \quad (4.10)$$

where  $\mathbf{E}_{\text{rod}}$  and  $\mathbf{E}_{\text{launch}}$  are given by Eq. (4.7) and Eq. (4.8), respectively. Since there are three unknown current density distributions ( $\mathbf{J}_V$ ,  $\mathbf{J}_S$  and  $\mathbf{K}_S$ ), three equations are required to solve the problem. Each equation will be the result of imposing a certain condition on the total field.

The total field must satisfy the following condition inside the dielectric object:

$$[\sigma_1(\mathbf{r}) + j\omega(\epsilon_1(\mathbf{r}) - \epsilon_0)] \mathbf{E}(\mathbf{r}) = \mathbf{J}_V(\mathbf{r}), \quad \mathbf{r} \in \mathcal{V}_{\text{diel}} \quad (4.11)$$

on the outer metallic walls of the launcher

$$\mathbf{n}(\mathbf{r}) \times \mathbf{E}(\mathbf{r}) = 0, \quad \mathbf{r} \in \mathcal{S}_{\text{cond}} \quad (4.12)$$

and at the aperture

$$\mathbf{n}(\mathbf{r}) \times \mathbf{E}(\mathbf{r}) = -\mathbf{K}_S(\mathbf{r}), \quad \mathbf{r} \in \mathcal{S}_{\text{ap}} \quad (4.13)$$

$$\mathbf{n}(\mathbf{r}) \times \mathbf{H}(\mathbf{r}) = \mathbf{n}(\mathbf{r}) \times \mathbf{H}_{\text{wg}}(\mathbf{r}) = \mathbf{J}_S(\mathbf{r}), \quad \mathbf{r} \in \mathcal{S}_{\text{ap}} \quad (4.14)$$

Substitution of each field quantity, in Eq. (6.6), (5.8), (5.9) and (4.14), by its integral representation results in the following set of coupled integral equations

$$\begin{aligned} -j\omega\mu_0 \int_{\mathcal{V}_{\text{diel}}} \mathbf{J}_V G dV' + \frac{1}{j\omega\epsilon_0} \int_{\mathcal{V}_{\text{diel}}} \nabla' \cdot \mathbf{J}_V \nabla G dV' - \int_S \left( j\omega\mu_0 G \mathbf{J}_S - \frac{1}{j\omega\epsilon_0} \nabla'_S \cdot \mathbf{J}_S \nabla G \right) dA' \\ - \int_{\mathcal{S}_{\text{ap}}} \nabla \times G \mathbf{K}_S dA' = \mathbf{J}_V / (j\omega\kappa\epsilon), \quad \mathbf{r} \in \mathcal{V}_{\text{diel}} \end{aligned} \quad (4.15)$$

$$\begin{aligned}
 & -j\omega\mu_0\mathbf{n} \times \int_{V_{\text{diel}}} \mathbf{J}_V G dV' + \frac{1}{j\omega\epsilon_0} \mathbf{n} \times \int_{V_{\text{diel}}} \nabla' \cdot \mathbf{J}_V \nabla G dV' \\
 -\mathbf{n} \times \int_S & \left( j\omega\mu_0 G \mathbf{J}_S - \frac{1}{j\omega\epsilon_0} \nabla'_S \cdot \mathbf{J}_S \nabla G \right) dA' - \mathbf{n} \times \int_{S_{\text{ap}}} \nabla \times G \mathbf{K}_S dA' \quad (4.16)
 \end{aligned}$$

$$\begin{aligned}
 & = -\frac{1}{2} \mathbf{K}_S \chi_S, \mathbf{r} \in S \\
 & \mathbf{n} \times \mathbf{H}_{\text{wg}} = \mathbf{J}_S, \mathbf{r} \in S_{\text{ap}} \quad (4.17)
 \end{aligned}$$

where the shape function  $\chi_S(\mathbf{r}) = 1$  if  $\mathbf{r} \in S_{\text{ap}}$  and zero otherwise. Note that the integrals occurring in Eq. (4.15) and Eq. (4.16) are principle-value integrals. Solving the problem means finding the unknown current distributions  $\mathbf{J}_V$ ,  $\mathbf{J}_S$  and  $\mathbf{K}_S$ . This is done in the next section using the MoM.

### 4.3 Expansion functions and MoM solution

In this section, the geometry of the dielectric rod that is analyzed is approximated with a set of elementary sub-domains. A local description of the current densities in each sub-domain is given. Multiplication of the discretized coupled integral equations with testing functions and integration of the resulting products over the sub-domains results in a linear system of algebraic equations. Iterative solution of the linear system yields the current expansion coefficients from which the total radiated field can be computed.



Figure 4.3: Discretization of the computational domain.



### 4.3.1 Discretization of the computational domain and expansion functions

Two types of elementary sub-domains are used to model the complex geometry of Fig. 4.2. Triangles are used to approximate the closed surface  $\mathcal{S} = \mathcal{S}_{\text{cond}} \cup \mathcal{S}_{\text{ap}}$ , while tetrahedra are used to approximate the dielectric scatterer volume  $\mathcal{V}_{\text{diel}}$  (see Fig. 4.3). The dielectric properties are assumed constant within each tetrahedron. For the computations it is necessary to know which vertices, edges and faces belong to each individual triangle or tetrahedron. These data (nodes, topology and material properties within each tetrahedron) are generated by the mesh generator. A good survey on mesh generation methods and software can be found in [13].

To represent locally, in each triangular patch, the surface electric current  $\mathbf{J}_{\mathcal{S}}$  and the surface magnetic current  $\mathbf{K}_{\mathcal{S}}$  we use the vectorial expansion functions,  $\mathbf{f}_n(\mathbf{r})$  and  $\mathbf{g}_n(\mathbf{r})$ , given in the previous chapter by Eq. (3.27) and Eq. (3.29), respectively. For the volumetric electric-current density  $\mathbf{J}_{\mathcal{V}}$  we need to define a different set of basis functions. We chose basis functions defined over tetrahedral volume elements. Each single basis function  $\mathbf{d}_n(\mathbf{r})$  is associated with a face of the tetrahedral approximation of  $\mathcal{V}_{\text{diel}}$ . They are analogous to the rooftop functions used in the previous chapter and are constructed to guarantee a continuous flux density across the faces of the tetrahedral computational model. They are defined as [14]

$$\mathbf{d}_n(\mathbf{r}) = \begin{cases} \frac{S_n}{3V_n^+} \boldsymbol{\rho}_n^+, & \mathbf{r} \in \mathcal{T}_n^+ \\ \frac{S_n}{3V_n^-} \boldsymbol{\rho}_n^-, & \mathbf{r} \in \mathcal{T}_n^- \\ \mathbf{0}, & \text{otherwise} \end{cases} \quad (4.18)$$

where  $S_n$  is the surface of the face with index  $n$  and  $V_n^{\pm}$  is the volume of the tetrahedral  $\mathcal{T}_n^{\pm}$ . Fig. 4.4 shows a pair of tetrahedra,  $\mathcal{T}_n^+$  and  $\mathcal{T}_n^-$ , associated with the  $n^{\text{th}}$  face of the divided dielectric scatterer volume  $\mathcal{V}_{\text{diel}}$ . Points in  $\mathcal{T}_n^{\pm}$  can be designated either by the position vector  $\mathbf{r}$  defined with respect to the origin  $\mathcal{O}$  or by the vector  $\boldsymbol{\rho}_n^{\pm}$  defined

with respect to the free vertex opposite to the  $n^{\text{th}}$  face in  $\mathcal{T}_n^\pm$ . The vector  $\boldsymbol{\rho}_n^-$  is directed toward the free vertex while the direction of  $\boldsymbol{\rho}_n^+$  is chosen away from the free vertex. The positive flux reference direction is chosen to be directed from  $\mathcal{T}_n^+$  to  $\mathcal{T}_n^-$ . When a face is located on the boundary  $\mathcal{S}_{\text{diel}}$  of  $\mathcal{V}_{\text{diel}}$  then the basis function associated with that face is defined only over the tetrahedral interior to  $\mathcal{V}_{\text{diel}}$ . Hence, the total number of basis functions  $N_d$  equals the total number of faces in the tetrahedral model of  $\mathcal{V}_{\text{diel}}$ .

The basis functions  $\mathbf{d}_n$ , when constructed according to Eq. (4.18), can provide at least a piecewise constant approximation to the quantity being approximated. The fact that each basis function varies linearly with distance inside the tetrahedron pair related to it, makes it also capable of representing linear variations. However, since these functions are constant in the transverse direction, they can accurately model linear variations only if the variation is in the same direction of the basis function. Other properties of these basis functions are given below [14]

- A constant vector in any direction can be represented as the sum of four linearly independent basis functions within each tetrahedron.
- The basis function  $\mathbf{d}_n$  has no component normal to any face except at the common face of the tetrahedra pair  $\mathcal{T}_n^\pm$ .
- The component of  $\mathbf{d}_n$  normal to the  $n^{\text{th}}$  face is constant and continuous across the face.

A useful expression, which will be needed later, is the divergence of  $\mathbf{d}_n$  given by

$$\nabla \cdot \mathbf{d}_n(\mathbf{r}) = \begin{cases} \frac{S_n}{V_n^+}, & \mathbf{r} \in \mathcal{T}_n^+ \\ -\frac{S_n}{V_n^-}, & \mathbf{r} \in \mathcal{T}_n^- \\ 0, & \text{otherwise} \end{cases} \quad (4.19)$$

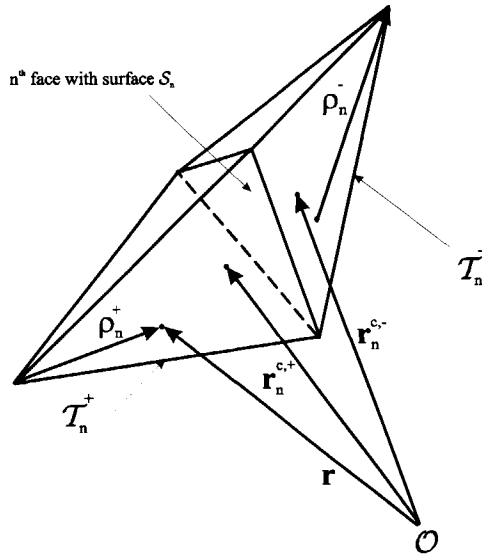


Figure 4.4: Geometry of a pair of tetrahedra associated with face  $S_n$ .

### 4.3.2 Discretization of the current densities and integral equations

In this subsection we discuss the discretization of the current densities,  $\mathbf{J}_V$ ,  $\mathbf{J}_S$  and  $\mathbf{K}_S$ , and the coupled integral equations (4.15), (4.16), and (4.17) using the linear expansions mentioned above. In the previous chapter we have given a discrete approximate to the surface current densities as follows

$$\mathbf{J}_S(\mathbf{r}) \approx \sum_n^{N_f} I_n \mathbf{f}_n(\mathbf{r}), \quad \mathbf{r} \in \mathcal{S} \quad (4.20)$$

$$\mathbf{K}_S(\mathbf{r}) \approx \sum_n^{N_k} (V_n + V_n^i) \mathbf{g}_n(\mathbf{r}), \quad \mathbf{r} \in \mathcal{S}_{\text{sp}} \quad (4.21)$$

where  $\mathbf{f}_n(\mathbf{r})$  and  $\mathbf{g}_n(\mathbf{r})$  are given by Eq. (3.27) and Eq. (3.29) in Chapter 3, respectively.  $I_n$  and  $V_n$  are the unknown expansion coefficients.  $V_n^i$  represents the known amplitude

of the  $n^{\text{th}}$  incident mode in the waveguide traveling toward the aperture. In order to find a discrete representation of the volume current density  $\mathbf{J}_V(\mathbf{r})$  we first approximate the unknown flux density  $\mathbf{D}(\mathbf{r}) = \hat{\epsilon}(\mathbf{r})\mathbf{E}(\mathbf{r})$  inside the dielectric volume  $\mathcal{V}_{\text{diel}}$  as follows

$$\mathbf{D}(\mathbf{r}) \approx \sum_n^{N_d} D_n \mathbf{d}_n(\mathbf{r}), \quad \mathbf{r} \in \mathcal{V}_{\text{diel}} \quad (4.22)$$

where  $\mathbf{d}_n(\mathbf{r})$  is given by Eq. (4.18) and  $D_n$  are the unknown electric flux coefficients. The summation is taken over all the faces in the tetrahedral model of  $\mathcal{V}_{\text{diel}}$ . The volume current density  $\mathbf{J}_V$  is related to the total electric flux density  $\mathbf{D}$  as follows

$$\mathbf{J}_V(\mathbf{r}) = [\sigma_1(\mathbf{r}) + j\omega(\epsilon_1(\mathbf{r}) - \epsilon_0)] \mathbf{D}(\mathbf{r}) / \hat{\epsilon}(\mathbf{r}) \chi_V = j\omega\kappa(\mathbf{r})\mathbf{D}(\mathbf{r}), \quad (4.23)$$

where the normalized contrast function  $\kappa(\mathbf{r})$  is defined as  $(\hat{\epsilon}(\mathbf{r}) - \epsilon_0) / \hat{\epsilon}(\mathbf{r})$ . Since the electric flux density  $\mathbf{D}$  has a continuous normal component at media interfaces, all discontinuities in the normal component of  $\mathbf{J}_V$  are contained within the normalized contrast function  $\kappa(\mathbf{r})$ . Substituting Eq. (4.22) into Eq. (4.23) results in a discrete form for the volumetric current density  $\mathbf{J}_V$

$$\mathbf{J}_V(\mathbf{r}) \approx j\omega\kappa(\mathbf{r}) \sum_n^{N_d} D_n \mathbf{d}_n(\mathbf{r}), \quad \mathbf{r} \in \mathcal{V}_{\text{diel}} \quad (4.24)$$

When we replace each current density in Eq. (4.15), (4.16) and (4.17) by its discretized form, we obtain the following set of linear equations

$$\sum_n^{N_d} D_n [\mathbf{E}_n^d(\mathbf{r}) - \mathbf{d}_n(\mathbf{r}) / \hat{\epsilon}] = \sum_n^{N_f} I_n \mathbf{E}_n^f(\mathbf{r}) + \sum_n^{N_g} (V_n + V_n^i) \mathbf{E}_n^g(\mathbf{r}), \quad \forall \mathbf{r} \in \mathcal{V}_{\text{diel}} \quad (4.25)$$

$$\mathbf{n} \times \sum_n^{N_d} D_n \mathbf{E}_n^d(\mathbf{r}) = \mathbf{n} \times \sum_n^{N_f} I_n \mathbf{E}_n^f(\mathbf{r}) + \sum_n^{N_k} (V_n + V_n^i) \left[ \mathbf{n} \times \mathbf{E}_n^g(\mathbf{r}) - \frac{1}{2} \mathbf{g}_n(\mathbf{r}) \right], \quad \forall \mathbf{r} \in \mathcal{S} \quad (4.26)$$

$$\mathbf{n} \times \sum_n^{N_k} (V_n - V_n^i) Y_n \mathbf{g}_n(\mathbf{r}) = \sum_n^{N_f} I_n \mathbf{f}_n(\mathbf{r}), \quad \forall \mathbf{r} \in \mathcal{S}_{\text{ap}} \quad (4.27)$$

where

$$\mathbf{E}_n^d(\mathbf{r}) = \omega^2 \mu_0 \int_{\mathcal{V}_{\text{diel}}} \kappa(\mathbf{r}') \mathbf{d}_n(\mathbf{r}') G dV' + \frac{1}{\epsilon_0} \int_{\mathcal{V}_{\text{diel}}} \nabla' \cdot [\kappa(\mathbf{r}') \mathbf{d}_n(\mathbf{r}')] \nabla G dV', \quad (4.28)$$

$$\mathbf{E}_n^f(\mathbf{r}) = \int_S \left( j\omega\mu_0 G \mathbf{f}_n(\mathbf{r}') - \frac{1}{j\omega\epsilon_0} \nabla'_S \cdot \mathbf{f}_n(\mathbf{r}') \nabla G \right) dA', \quad (4.29)$$

$$\mathbf{E}_n^g(\mathbf{r}) = \int_{S_{np}} \nabla \times G \mathbf{g}_n(\mathbf{r}') dA'. \quad (4.30)$$

### 4.3.3 Weak formulation and MoM system

The problem as stated in Eq. (4.25), Eq. (4.26) and Eq. (4.27) results in an ill-defined system since it cannot hold in the entire computational domain. Hence, we are dealing with a strong form. To resolve the unknown coefficients one has to solve the problem in a weighed form. Let's define two products between the vectors  $\mathbf{x}$  and  $\mathbf{y}$  as follows

$$\langle \mathbf{x}, \mathbf{y} \rangle_S = \iint_S \mathbf{x} \cdot \mathbf{y} dA, \quad (4.31)$$

$$\langle \mathbf{x}, \mathbf{y} \rangle_V = \iiint_V \mathbf{x} \cdot \mathbf{y} dV, \quad (4.32)$$

which are scalars satisfying the properties given by Eq. (3.24) in Chapter 3. Next, we define a set of testing functions  $\mathbf{f}_n^t = \mathbf{f}_n$ ,  $\mathbf{g}_n^t = \mathbf{g}_n$ , and  $\mathbf{d}_n^t = \mathbf{d}_n$  over the domains of computation  $\mathcal{S}$ ,  $\mathcal{S}_{ap}$ , and  $\mathcal{V}_{diel}$ , respectively. Applying the scalar products to the discretized integral equations results in the following weak equivalent for Eq.(4.25), Eq.(4.26) and Eq.(4.27), respectively

$$\sum_n^{N_d} D_n \langle \mathbf{d}_m, \mathbf{E}_n^d - \mathbf{d}_n / \hat{\epsilon} \rangle_{\mathcal{V}_{diel}} = \sum_n^{N_f} I_n \langle \mathbf{d}_m, \mathbf{E}_n^f \rangle_{\mathcal{V}_{diel}} + \sum_n^{N_g} (V_n + V_n^i) \langle \mathbf{d}_m, \mathbf{E}_n^g \rangle_{\mathcal{V}_{diel}}, \quad \forall m = 1, \dots, N_d \quad (4.33)$$

$$\sum_n^{N_d} D_n \langle \mathbf{f}_m, \mathbf{E}_n^d \rangle_S = \sum_n^{N_f} I_n \langle \mathbf{f}_m, \mathbf{E}_n^f \rangle_S + \sum_n^{N_g} (V_n + V_n^i) \langle \mathbf{f}_m, \mathbf{E}_n^g + \frac{1}{2} \mathbf{n} \times \mathbf{g}_n \rangle_S, \quad \forall m = 1, \dots, N_f \quad (4.34)$$

$$\sum_n^{N_g} (V_n - V_n^i) Y_n \langle \mathbf{g}_m, \mathbf{g}_n \rangle_{S_{np}} = \sum_n^{N_f} I_n \langle \mathbf{g}_m, \mathbf{f}_n \times \mathbf{n} \rangle_{S_{np}}, \quad \forall m = 1, \dots, N_g \quad (4.35)$$

or in matrix form

$$\begin{bmatrix} Z^{d-d} & Z^{d-f} & Z^{d-g} \\ Z^{f-d} & Z^{f-f} & Z^{f-g} \\ 0 & Z^{g-f} & Z^{g-g} \end{bmatrix} \begin{bmatrix} D \\ I \\ V \end{bmatrix} = \begin{bmatrix} -Z^{d-g} \\ -Z^{f-g} \\ Z^{g-g} \end{bmatrix} V^i, \quad (4.36)$$

$$\begin{aligned} D &= \begin{bmatrix} D_1 & \cdots & D_{N^d} \end{bmatrix}^T, \quad I = \begin{bmatrix} I_1 & \cdots & I_{N^f} \end{bmatrix}^T, \\ V &= \begin{bmatrix} V_1 & \cdots & V_{N^g} \end{bmatrix}^T, \quad V^i = \begin{bmatrix} V_1^i & \cdots & V_{N^g}^i \end{bmatrix}^T. \end{aligned} \quad (4.37)$$

The remaining expressions are defined in appendix C. Note that the matrices  $Z^{f-f}$ ,  $Z^{f-g}$ ,  $Z^{g-f}$ , and  $Z^{g-g}$  are equal to the matrices  $Z^{c-c}$ ,  $-Z^{c-a}$ ,  $Z^{a-c}$ , and  $-Z^{a-a}$  in Chapter 3, respectively. The linear system of Eq. (4.36) can be written in a more compact form as

$$\begin{bmatrix} Z^{d-d} & Z^{d-l} \\ Z^{l-d} & Z^{l-l} \end{bmatrix} \begin{bmatrix} D \\ L \end{bmatrix} = \begin{bmatrix} D^i \\ L^i \end{bmatrix}, \quad (4.38)$$

where

$$\begin{aligned} Z^{l-l} &= \begin{bmatrix} Z^{f-f} & Z^{f-g} \\ Z^{g-f} & Z^{g-g} \end{bmatrix}, \\ Z^{d-l} &= \begin{bmatrix} Z^{d-f} & Z^{d-g} \end{bmatrix}, \quad Z^{l-d} = \begin{bmatrix} Z^{f-d} & 0 \end{bmatrix}^T, \\ L &= \begin{bmatrix} I & V \end{bmatrix}^T, \quad L^i = \begin{bmatrix} -Z^{f-g} & Z^{g-g} \end{bmatrix}^T V^i, \quad D^i = -Z^{d-g} V^i. \end{aligned} \quad (4.39)$$

In Eq.(4.38), the vectors  $D$  and  $L$  contain the unknown expansion coefficients while the vectors  $D^i$  and  $L^i$  contain contributions from known sources. Note that in order to compute the matrix  $Z^{d-l}$  only knowledge of the dielectric scatterer geometry is required. Similar, for the evaluation of the matrix  $Z^{l-l}$  only the geometrical description of the launcher is needed.

#### 4.3.4 Iterative solution of the MoM system

The linear system of Eq. (4.38) can be solved using the bi-conjugate algorithm described in Chapter 3. However, due to the size of the numerical problem this procedure

may require a large evaluation time before convergence. In this section we propose a relatively simple iterative scheme based on solving one part of the problem, at each iteration, (i.e. the vector  $L$  or  $D$ ); we use the obtained result to update the other part. The main advantages of the proposed iterative scheme are the fast convergence and the high flexibility for integration within an optimizer. The algorithm works as follows. First, we compute the vector  $L$  (Launcher) in the absence of the dielectric body ( $D=0$ ). This is given by

$$L(0) = (Z^{l-1})^{-1} L^i. \quad (4.40)$$

Next, the vector  $L$  in Eq. (4.38) is replaced by the obtained vector  $L(0)$ , resulting into the following approximation for the vector  $D$

$$D(0) = (Z^{d-d})^{-1} (D^i - Z^{d-l}L(0)). \quad (4.41)$$

Similarly, by replacing  $D$  in Eq. (4.38) by its approximate value  $D(0)$  we can solve for the vector  $L$  at iteration 1. The same procedure must be repeated until convergence is achieved. In general, the algorithm can be represented as follows

$$\begin{aligned} L(n) &= L_1 + Z_1 L(n-1), \\ D(n) &= D_1 - Z_2 L(n), \end{aligned} \quad (4.42)$$

where

$$\begin{aligned} L_1 &= (Z^{l-1})^{-1} (L^i - Z^{l-d}D_1), \\ Z_1 &= (Z^{l-1})^{-1} Z^{l-d}Z_2, \\ D_1 &= (Z^{d-d})^{-1} D^i, \\ Z_2 &= (Z^{d-d})^{-1} Z^{d-l}. \end{aligned} \quad (4.43)$$

A numerical convergence test can be defined as

$$\|L(n) - L(n-1)\| < tolerance \quad (4.44)$$

After some forward mathematical manipulations one can prove that, when  $n \rightarrow \infty$ ,  $L(n)$  will approaches its exact value  $L$ . This is only true if all eigenvalues of the matrix

$Z_1$  are inside the unit circle. We obtain

$$\lim_{n \rightarrow \infty} L(n) = \lim_{n \rightarrow \infty} \sum_{i=0}^n (Z_1)^i L(0) + \sum_{i=0}^{n-1} (Z_1)^i [L_1 - L(0)] = (I - Z_1)^{-1} L_1 = L \quad (4.45)$$

where  $I$  is a unity matrix. In the presented algorithm, two matrix inversion operations are required (only once) and all the other operations are mainly vector summations and matrix-vector multiplications.

### 4.3.5 Far-field computations

The field in the far zone can be calculated directly after the linear system of Eq. (4.39) has being solved, for which the far-field approximation of Eq. (4.7) and Eq. (4.8) must be used. We obtain for the incident electric field

$$\begin{aligned} \mathbf{E}_{\text{Iaun}}(\mathbf{r}) \approx & -\frac{j\omega\mu_0 \exp(-jk_0 r)}{4\pi r} \sum_i^{\text{NTR}} [\mathbf{J}_S(\mathbf{r}_i^c) - (\hat{\mathbf{i}}_r \cdot \mathbf{J}_S(\mathbf{r}_i^c))\hat{\mathbf{i}}_r] \exp(jk_0 \hat{\mathbf{i}}_r \cdot \mathbf{r}_i^c) \mathcal{S}_i, \\ & -\frac{jk_0 \exp(-jk_0 r)}{4\pi r} \sum_i^{\text{NTR}} (\mathbf{K}_S(\mathbf{r}_i^c) \times \hat{\mathbf{i}}_r) \exp(jk_0 \hat{\mathbf{i}}_r \cdot \mathbf{r}_i^c) \mathcal{S}_i, \end{aligned} \quad (4.46)$$

where

$$\mathbf{J}_S(\mathbf{r}_i^c) = \sum_{n=1}^3 I_n \mathbf{f}_n(\mathbf{r}_i^c), \quad \mathbf{K}_S(\mathbf{r}_i^c) = \sum_n^{N_g} \mathbf{g}_n(\mathbf{r}_i^c) (V_n + V_n^i) \quad (4.47)$$

and for the scattered electric field

$$\mathbf{E}_{\text{rod}}(\mathbf{r}) \approx -\frac{j\omega\mu_0 \exp(-jk_0 r)}{4\pi r} \sum_i^{\text{NTE}} [\mathbf{J}_V(\mathbf{r}_i^c) - (\hat{\mathbf{i}}_r \cdot \mathbf{J}_V(\mathbf{r}_i^c))\hat{\mathbf{i}}_r] \exp(jk_0 \hat{\mathbf{i}}_r \cdot \mathbf{r}_i^c) \mathcal{V}_i, \quad (4.48)$$

where

$$\mathbf{J}_V(\mathbf{r}_i^c) = j\omega\kappa(\mathbf{r}_i^c) \sum_{n=1}^4 D_n \mathbf{d}_n(\mathbf{r}_i^c) \quad (4.49)$$

and  $\mathbf{r} = r(\sin\theta \cos\phi \mathbf{i}_x + \sin\theta \sin\phi \mathbf{i}_y + \cos\theta \mathbf{i}_z)$ .  $\theta$  and  $\phi$  are spherical coordinates. In the above expressions  $\mathbf{r}_i^c$  denotes the position vector of the centroid of the  $i^{\text{th}}$  triangle or  $i^{\text{th}}$  tetrahedral. NTR is the total number of triangles while NTE is the total number of tetrahedra used in the geometrical model.



## 4.4 Numerical results and experimental validation

This section deals with a number of numerical examples obtained using the formulation described in the previous sections. A single dielectric rod antenna was designed and constructed (see Fig. 4.5). Measurements were performed and the results were used to validate the present computer code. In this section the design procedure for the rod antenna is presented and new results are given for alternative configurations.

### 4.4.1 General design procedure

Here we discuss the design and construction of a dielectric rod antenna at S-band (3.3GHz). The design of dielectric rod antennas usually starts with a gain requirement. The gain is determined by the dielectric rod length. Rod dimensions are usually found by experiment; one starts with a given dielectric cross section and incrementally adjusts the length of the dielectric material until the measured field pattern satisfies the requirements (see Fig. 4.6). The next stage is to match the impedance of the dielectric rod to the waveguide feed using an air gap and tuning the waveguide probe for maximum excitation power.

The basic antenna geometry of Fig. 4.5 consists of a dielectric waveguide of a rectangular cross section fed by a metallic waveguide with the same cross section. The geometry is shown schematically in Fig. 4.7. The transition from the metallic waveguide into the dielectric rod was made sufficiently continuous by tapering the metallic walls gradually toward the dielectric rod (see Fig. 4.7). This insures the excitation of a slow surface wave which will propagate, unperturbed, along the uniform section of the dielectric rod. The cross section of the dielectric body is maintained constant over a length ( $L-L_1$ , see Fig. 4.7) and then decreased monotonically in the forward direction. By doing so, one reduces the reflections caused by an abrupt ending of the rod and thus improves the radiation efficiency (see Fig. 4.8). A matching network based on a

single air gap and the design steps described in Chapter 2 was constructed in order to cancel unwanted reflections from the waveguide-rod transition. Any reflections caused by the coax-waveguide transition are reduced by carefully tuning the probe (pin) thickness and length ( $L_p$ , see Fig. 4.7). The antenna dimensions for the final optimized design are summarized in Table 4.1 and related measurements results are given in Fig. 4.9-4.13.

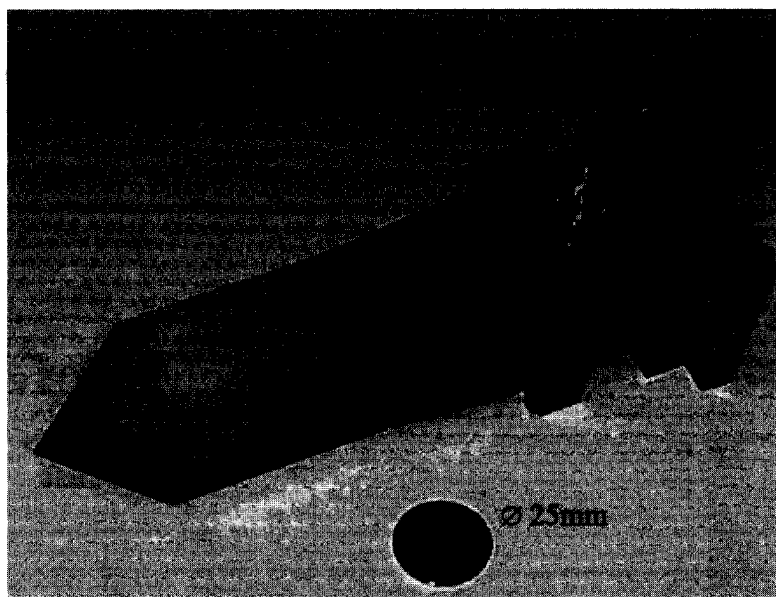


Figure 4.5: Example of a dielectric rod antenna designed to operate at S-band.

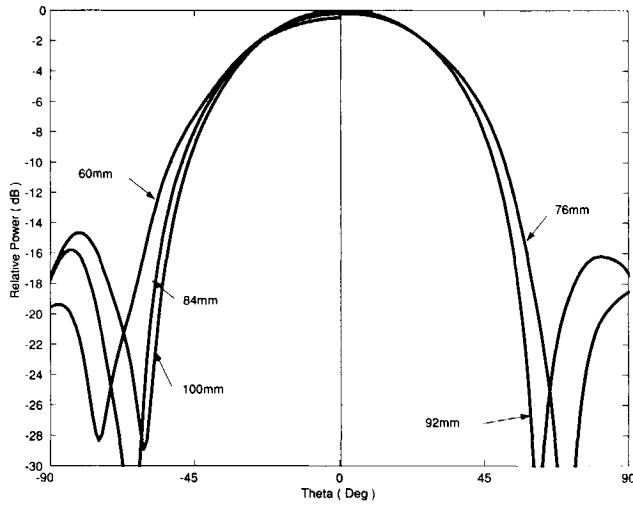


Figure 4.6: Measured H-plane patterns showing the effect of different dielectric slab lengths on the radiation pattern.

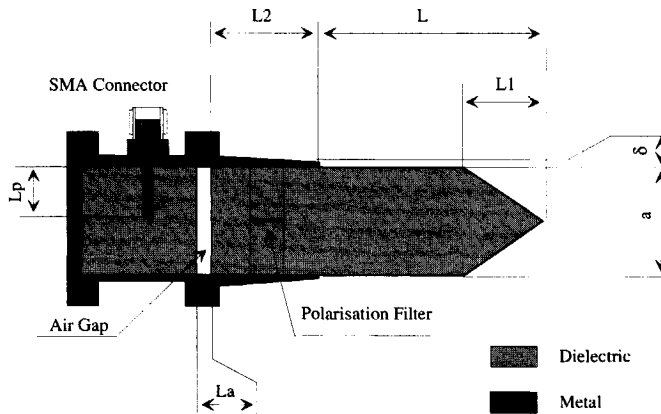


Figure 4.7: Geometry of a dielectric rod antenna optimized at 3.3GHz (Dimensions are given in Table 4.1).

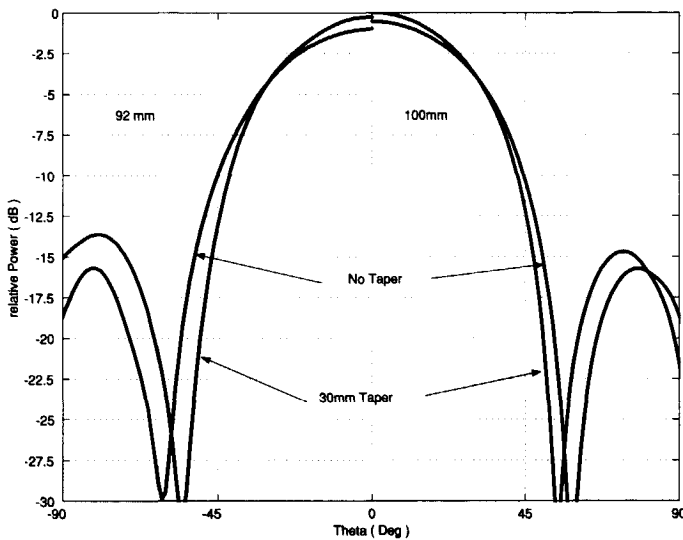


Figure 4.8: Measured H-plane patterns demonstrating the effect of terminal tapering on the radiation pattern for two different rod lengths ( $L-L_1=92\text{mm}$ ,  $100\text{mm}$ ).

Table 4.1: Rod dimensions in (mm).

L	L1	L2	La	Lp	a	$\delta$
90.1	30.0	43.6	3.3	12.3	34.2	0.1

#### 4.4.2 Numerical examples

In this section, three dielectric rod configurations are analyzed numerically using the formulation described above. All three antenna examples assume the same launcher, the same dielectric material, and operate at the same frequency. They differ only in the shape of the dielectric body. In order to validate the numerical code, we first consider the antenna configuration of Fig. 4.5. The antenna geometry was modeled using 1160 triangles and 701 tetrahedra, which is equivalent to 3280 ( $N_d=1530$ ,  $N_f=1740$  and  $N_g=10$ ) total number of unknowns. The computer code was migrated to the massively parallel computer system at Delft University of Technology (CRAY-J90se).

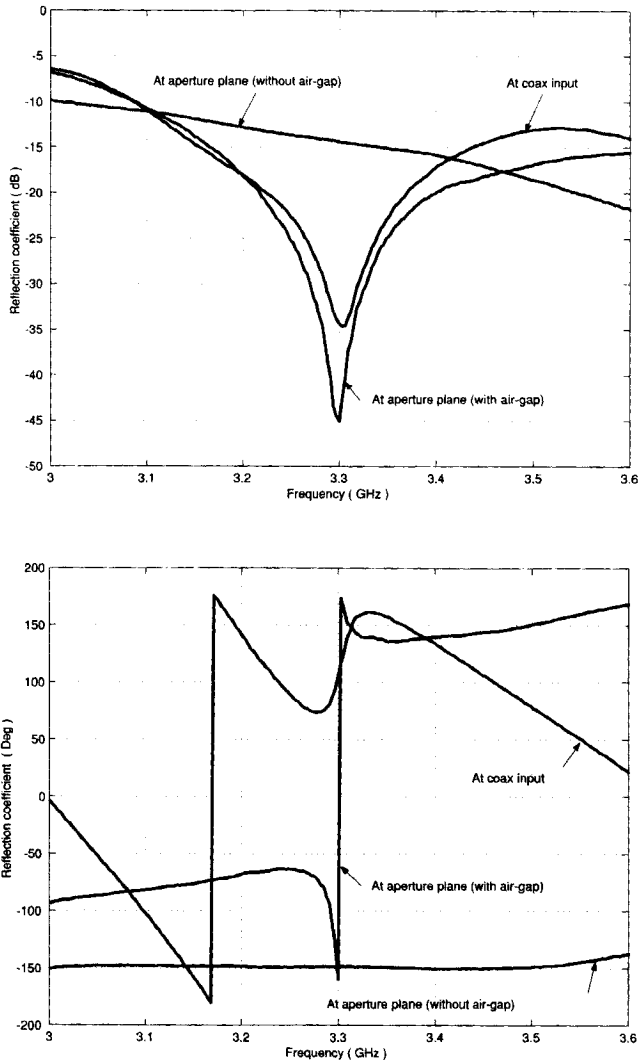
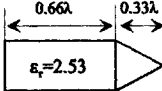
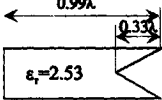
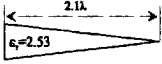


Figure 4.9: Measured magnitude and phase of the reflection coefficient at the waveguide-slab and coax-waveguide reference planes with and without matching network.

The computational aspects discussed in section 3.4.2 were also considered in the implementation of the present formulation. The most time-consuming operations in the present formulation are the filling of the matrix  $Z^{d-d}$ , since it involves volume integrations, and the solution of the linear system.

Table 4.2: Summary of numerical results for the antenna configurations considered.

Antenna configuration	First Side lobe level (dB)	Back lobe level (dB)	Cross-polarization level (dB)	E-plane 3-dB beam width (deg)	H-plane 3-dB beam width (deg)
	-17.3 @ (100°, 0°) -12.5 @ (126°, 90°)	-13.4	<-27 (main-beam)	58	64
	-17 @ (96°, 0°) -13 @ (126°, 90°)	-13.4	<-29.3 (main-beam)	57	63
	-11.5 @ (124°, 90°)	-13.15	<-28 (main-beam)	60	67

The measured and computed far-field patterns for the antenna geometry of Fig. 4.5 are given in Fig. 4.10-4.13 for the planes  $\phi = 0^\circ, 90^\circ,$  and  $45^\circ$ . A good agreement between theory and experiment is observed. Fig. 4.14 shows the first three individual contributions to the far-field pattern in the E-plane while Fig. 4.15 shows the individual contributions to the far-field pattern in the H-plane.

The individual contributions are fields due to (1) the Launcher, (2) the dielectric

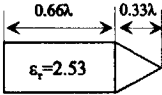
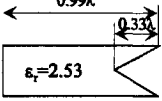
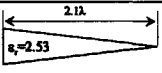
body and (3) the second interaction (dielectric→ launcher). Although the obtained results are approximate, they provide the antenna designer with a lot of insight into the physics of dielectric rod antennas. One can clearly identify and quantify which parts of the geometry contribute to the radiation in a certain region. From the phase information one can also see which parts interfere constructively or destructively. This information helps in improving the antenna design with respect to side lobes, back lobe and cross polarization by altering the geometry of the launcher and shape of the dielectric body in light of computed results. The second antenna geometry we analyzed is a dielectric rod antenna with the terminal part of the dielectric body shaped like a cut-wedge profile (see Table 4.2). The antenna geometry was discretized into 1160 triangles and 829 tetrahedra, resulting in 3584 total number of unknowns. The obtained far-field patterns in different planes are given in Fig. 4.16. The individual contribution to the far-field pattern are shown in Fig. 4.17 and Fig. 4.18 for the E-plane and H-plane respectively. The third antenna geometry we analyzed is a dielectric rod antenna with its dielectric body totally tapered in both planes (wedge profile, see Table 4.2). This geometry was discretized into 1160 triangles and 1765 tetrahedra. The total number of unknowns is 5580. The computed far-field patterns are shown in Fig. 4.19-21.

#### 4.4.3 Discussion of the numerical results

Table 4.2 gives a summary of the obtained results for the three different geometries treated in this section. Details of the computational requirements of the present code are shown in Table 4.3. All the selected antenna examples have a similar gain ( $9.5 \pm 0.5$  dBi). The purpose of the investigation carried out was to study the effect of the dielectric body shape on the radiation pattern. From the results it is clear that the launcher contributions are not negligible and in certain regions may even dominate the contributions from the dielectric body. The launcher radiation is responsible for

the high side-lobe levels occurring in short dielectric rod antennas, especially in the E-plane.

Table 4.3 Summary of computational requirements for selected antenna examples.

Antenna configuration	Number of unknowns	Memory required (MB)	Matrix fill time (h)	Matrix inversion time (h)	Total CPU time (h)
	3280	>90	5	3.2	8.2
	3584	>100	5	3.2	8.2
	5580	>125	12	6.3	18.3

The side-lobe level in the configurations studied were found to be around  $\approx -13$ dB in the E-plane and  $\approx -17$ dB in the H-plane. For the third example (wedge profile), the pattern in the H-plane is side-lobe free. The cut-wedge profile (second example) has resulted in the best configuration with respect to the cross-polar performance. Although the cut-wedge and wedge configurations, when optimized, indicate better performances with respect to either cross-polar or side-lobe level, they may result, at certain frequencies, in very fragile structures. This makes the fabrication process very costly and the manufactured structures will be very difficult to handle mechanically. A solution to this problem may be the combination of different dielectric materials having different dielectric properties.

An optimized design at 3.3 GHz has been presented. The antenna has a highly symmetrical pattern, very low return loss ( $< -30$  dB), low cross-polar ( $< -27$  dB) and high gain (9.5 dBi) at the frequency of interest. The whole metallic waveguide was



filled with dielectric material ( $\epsilon_r = 2.53$ ), resulting in an antenna size reduction factor of ( $\approx 1.6$ ). The overall dimensions of the final antenna design are ( $0.55\lambda \times 0.55\lambda \times 2\lambda$ ).

## 4.5 Conclusions

In this chapter, I proposed a rigorous technique based on a hybrid-iterative MoM for analyzing dielectric rod antennas with arbitrary 3-D shape. The method takes into account the launcher (waveguide feed) and can handle arbitrary shaped dielectric bodies. A number of numerical examples were treated and new results were presented. The general design procedure of dielectric rod antennas was reviewed and a detail description was given for an optimized prototype operating at S-band. The prototype was constructed and the experimental data used to validate the numerical code. A good agreement was observed between the proposed model and the experimental data.

Three different antenna geometries were investigated: (1) a uniform dielectric section with terminal tapering, (2) a cut-wedge configuration, and (3) a wedge configuration. The results indicate that by properly shaping the dielectric body, improvements can be achieved in side-lobe level and cross-polar performance. In dielectric rod antennas with moderate length, the launcher contributions are clearly visible and dominant in the side-lobe region. A good design first stresses the optimization of the launcher, and then that of the dielectric extended body.

When considering optimization of dielectric rod antennas, one need to take into account many control parameters, which often conflict. The present numerical code allows the investigation of their effects. In general any “geometry” can be numerically analyzed and optimized. However, it should be mentioned for completeness that the computational cost of the method is high for complex structures and with the present formulation it would be limited to very large computer platforms. Further work on techniques to speed up the computational scheme should be investigated.

The optimized S-band prototype presented herein has a highly symmetrical pattern, very low return losses ( $< -30$  dB), low cross-polar ( $< -27$  dB in  $45^\circ$  plane), and high gain (9.5 dBi) at 3.3GHz. A compact antenna resulted when a dielectric filling was used. An air-gap matching network was employed in the design. A number of identical antennas were constructed that demonstrated similar performances. From the results obtained, it is found that the design proposed can be used as a very efficient array element for various applications.

The integration of the proposed design in an array environment and aspects related to mutual coupling and array synthesis are addressed in the next chapters.

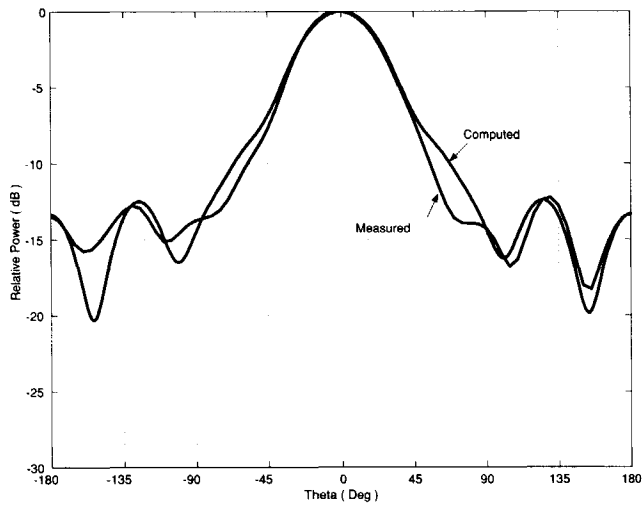


Figure 4.10: Computed and measured E-plane far-field patterns for the antenna geometry of Fig. 4.5 at frequency 3.3GHz.

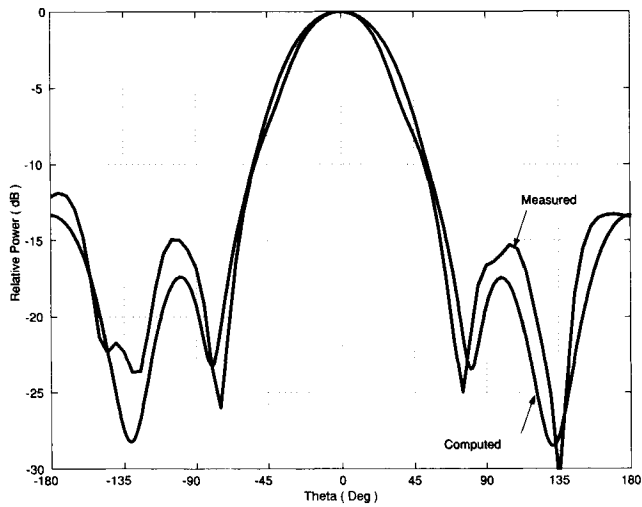


Figure 4.11: Computed and measured H-plane far-field patterns for the antenna geometry of Fig. 4.5 at frequency 3.3GHz.

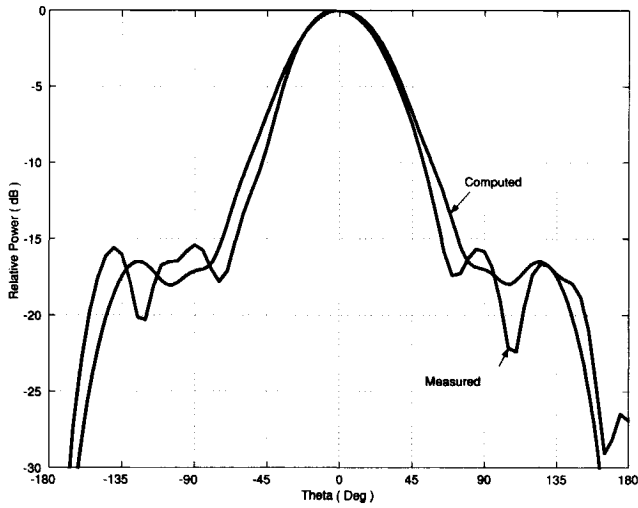


Figure 4.12: Computed and measured 45°-plane far-field patterns for the antenna geometry of Fig. 4.5 at frequency 3.3GHz.

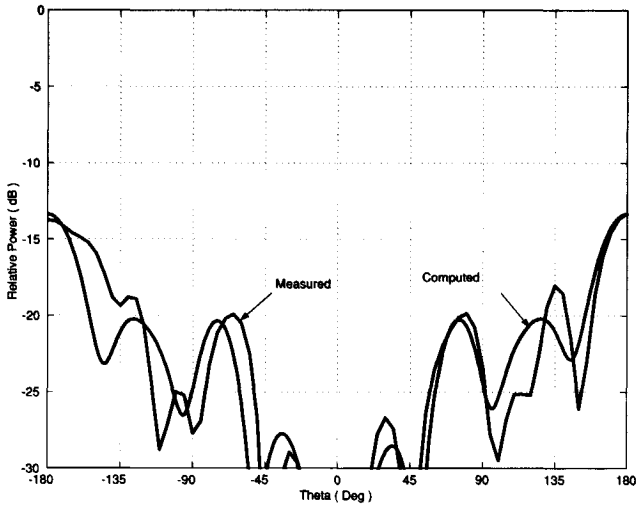


Figure 4.13: Computed and measured cross-polar patterns for the antenna geometry of Fig. 4.5 at frequency 3.3GHz.

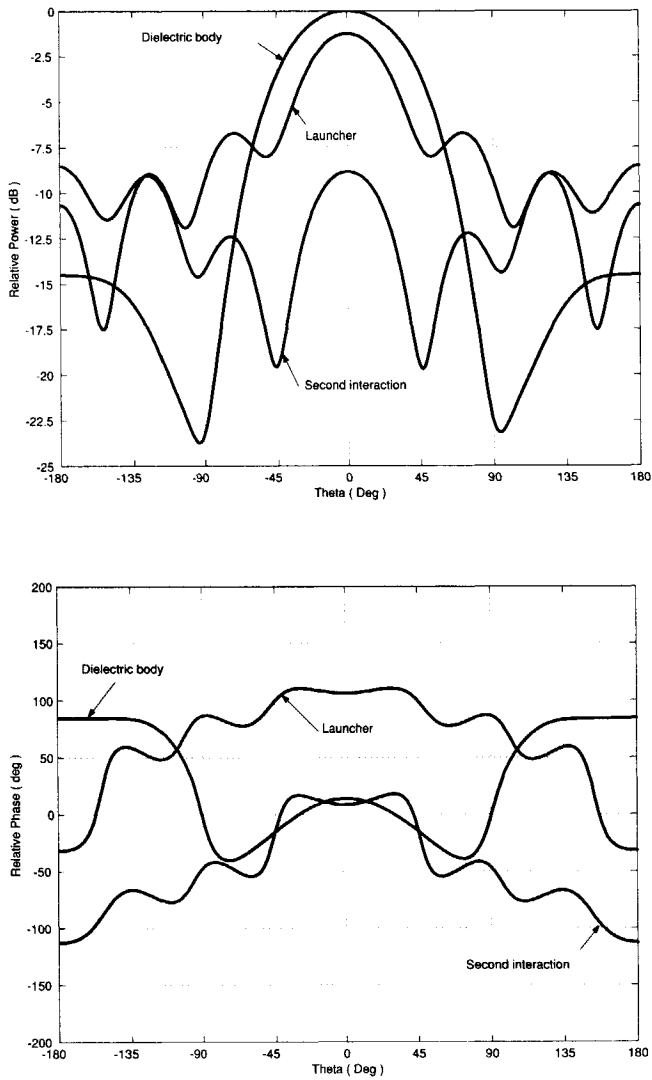


Figure 4.14: Three different contributions to the E-plane far-field pattern for the antenna geometry of Fig. 4.5 at frequency 3.3GHz.

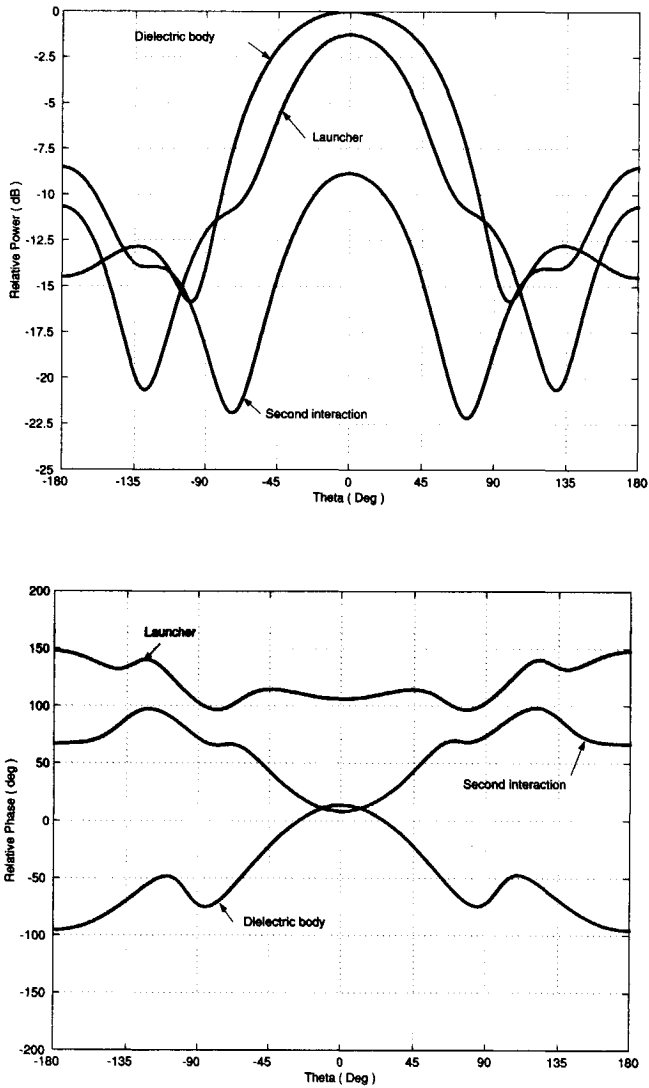


Figure 4.15: Three different contributions to the H-plane far-field pattern for the antenna geometry of Fig. 4.5 at frequency 3.3GHz.

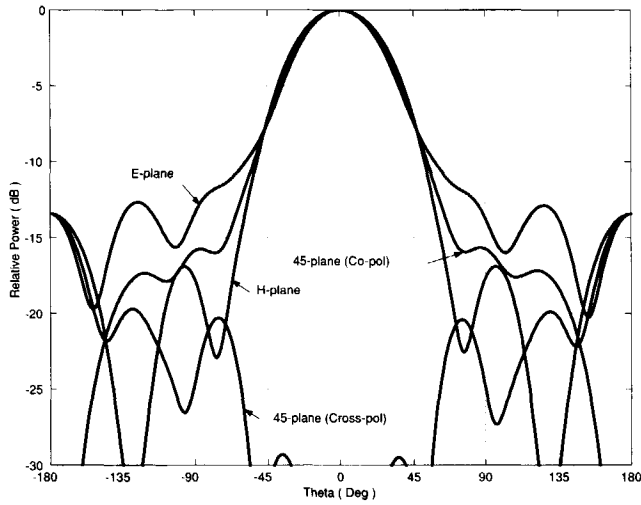


Figure 4.16: Computed far-field patterns in different planes for the cut-wedge profile antenna configuration.

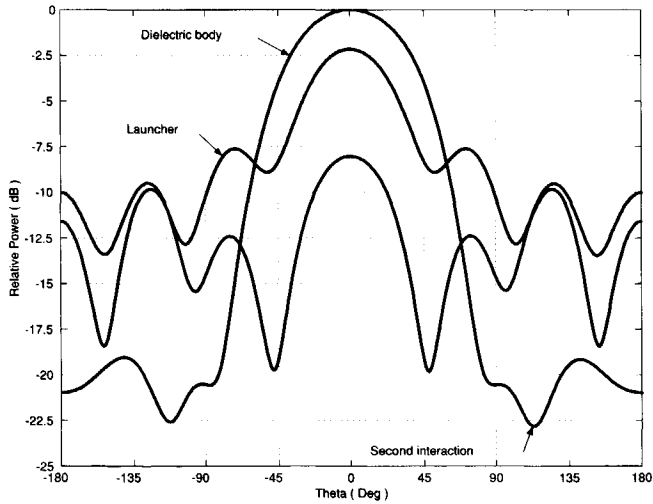


Figure 4.17: Individual contributions to the E-plane far-field pattern for the cut-wedge profile antenna configuration.

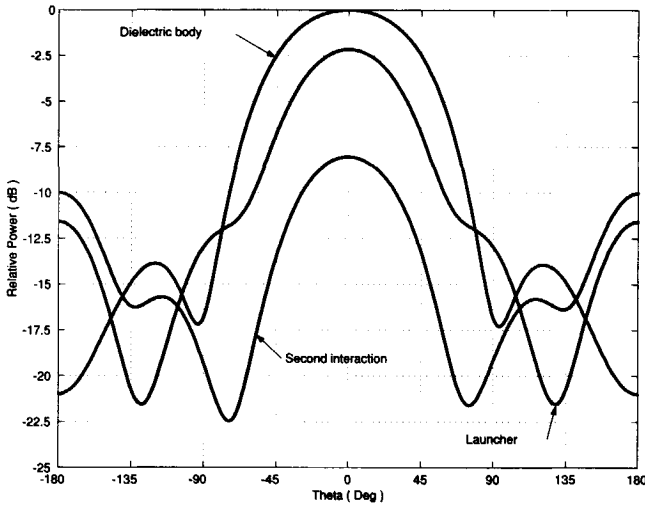


Figure 4.18: Individual contributions to the H-plane far-field pattern for the cut-wedge profile antenna configuration.

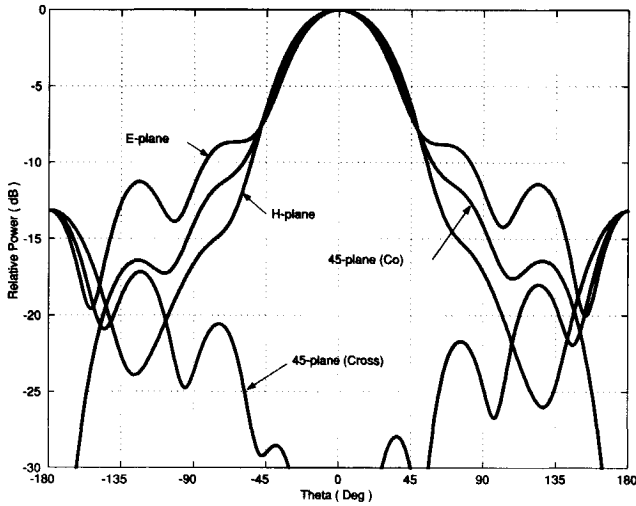


Figure 4.19: Computed far-field patterns in different planes for the wedge profile antenna configuration.



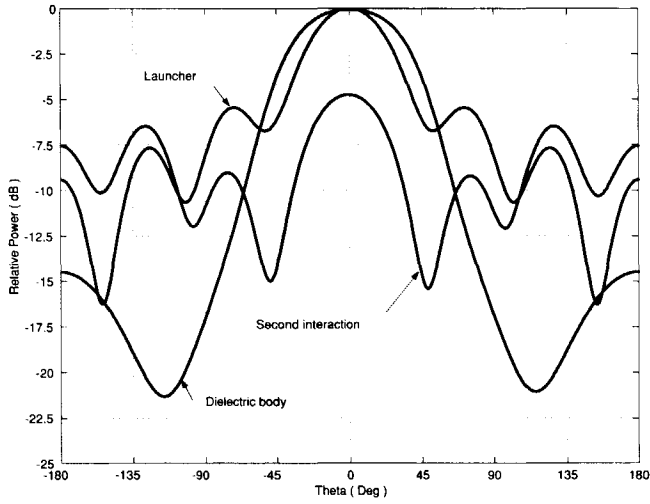


Figure 4.20: Individual contributions to the E-plane far-field pattern for the wedge profile antenna configuration.

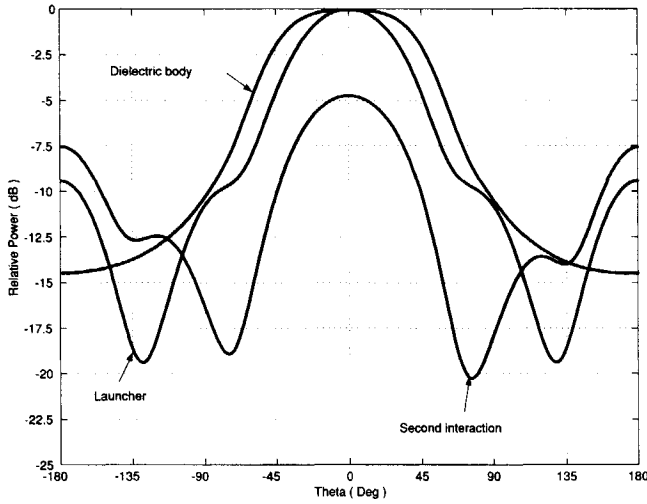


Figure 4.21: Individual contributions to the H-plane far-field pattern for the wedge profile antenna configuration.



## References

- [1] C. Salema, C. Fernandes and R.K. Jha, "*Solid Dielectric Horn Antennas*", Artech House, 1998.
- [2] D.G. Kiely, "*Dielectric Aerials*", Methuen Monograph, 1953.
- [3] R. Chatterjee, "*Dielectric and Dielectric Loaded Antennas*", Press Ltd., Letchworth, Hertfordshire, England 1985.
- [4] J.R. James, "*Theoretical Investigation of Cylindrical Dielectric-Rod Antennas*", Proc. Inst. Elec. Eng., vol. 114, pp.309-319, 1967.
- [5] R.B. Watson and C.W. Horton, "*The Radiation Pattern of Dielectric Rods, Experimental and Theory*", J. Appl. Phys., vol. 19, pp. 661-670, 1948.
- [6] M. Bouix, "*Contribution a l'Etude des Antenne Dielectrique*", dissertation, Universite de Paris, 1952.
- [7] A.Z. Fradin, "*Microwave Antennas*", Pergamon Press 1961.
- [8] J. Brown and J.O. Spector, "*The Radiation Properties of End-Fire Aerials*", Proc. Inst. Elec. Eng., vol 104 B, pp. 27-34, 1957.
- [9] A.D. Yaghjian and Kornhauser, "*A Modal Analysis of the Dielectric Rod Antenna Excited by the  $HE_{11}$  Mode*", IEEE Trans. Antennas Propagat., vol. AP-20, pp. 122-128, 1972.

- [10] P.K. Dombek, "*Dielektrische Antennen Geringer Querabmessungen als Erreger für Spiegellantennen*", Nachrichtent. Z., vol. 28, pp. 311-315, 1975.
- [11] A.A. Kishk and L. Shafai, "*Radiation Characteristics of the Short Dielectric Rod Antenna: a Numerical Solution*", IEEE Trans. Antennas Propagat., vol. AP-35, pp. 139-146, 1987.
- [12] C.A. Balanis, "*Advanced Engineering Electromagnetics*", John Wiley & Sons, Inc. 1989.
- [13] <http://www-users.informatik.rwth-aachen.de/~roberts/meshgeneration.html>
- [14] D.H. Schaubert, D.R. Wilton and A. W. Glisson, "*A Tetrahedral Modeling Method for Electromagnetic Scattering by Arbitrarily Shaped Inhomogeneous Dielectric Bodies*", IEEE Trans. Antennas Propagat., vol. AP-32, pp. 243-251, 1984.
- [15] D.H. Schaubert, and P.M. Meaney, "*Efficient Computation of Scattering by Inhomogeneous Dielectric Bodies*", IEEE Trans. Antennas Propagat., vol. AP-34, pp. 587-592, 1986.
- [16] T.K. Sarkar, E. Arvas, and S. Ponnappalli, "*Electromagnetic Scattering from Dielectric Bodies*", IEEE Trans. Antennas Propagat., vol. AP-37, pp. 673-676, 1989.
- [17] S.C. Ucak, G. Dural, T. Birand, S. Heijnen, and L.P. Ligthart, "*Analysis of Tapered Dielectric Rod Antennas using a Simple Model Based on the Method of Effective Dielectric Constants*", Conference CDROM, AP-2000, Davos, Switzerland.
- [18] P. Zwamborn and P.M. van den Berg, "*The Three-Dimensional Weak form of the Conjugate Gradient FFT Method for Solving Scattering Problems*", IEEE Trans. Microwave Theory and Techniques, vol. MTT-40, pp. 1757-1765, 1992.

- [19] M.A. Hamid, S.J. Towaij, and G.O. Martens, "A Dielectric-Loaded Circular Wave-Guide Antenna", IEEE Trans. Antennas Propagat., vol. AP-20, pp. 366-367, 1972.
- [20] Y. Shiau, "Dielectric Rod Antennas for Millimeter-Wave Integrated Circuits", IEEE Trans. Microwave Theory and Techniques, pp. 869-872, November 1976.
- [21] S. Kobayashi, R. Mittra, and R. Lampe, "Dielectric Tapered Rod Antennas for Millimeter-Wave Applications", IEEE Trans. Antennas Propagat., vol. AP-30, pp. 54-58, January 1982.
- [22] K. Mahdjoubi and C. Terret, "Analyse d'Antenne Dielectriques par une Method de Diffraction", Annale des Telecommunications, Tome 38, May-June 1983.
- [23] K. Mahdjoubi and C. Terret, "An Analysis of Piecewise Homogeneous Dielectric Rod Antennas", IEEE Trans. Antennas Propagat., vol. AP-34, pp. 598-601, 1986.
- [24] T. Milligan, "Design of Poly-Rod and Corrugated-Rod Antennas", IEEE Antennas and Propagation Magazine, vol. 42, No. 1, pp. 88-91, February 2000.
- [25] A.O. Boryssenko, "Dielectric-Core Conical-Horn Antennas with Rectangular Waveguide Feed for Point-to-Point Millimeter-Wave Communication", IEEE Antennas and Propagation Magazine, vol. 42, No. 2, pp. 129-136, April 2000.



# Chapter 5

## Mutual coupling between two separate dielectric rod antennas

### 5.1 Introduction

The radiation pattern of an array of identical antenna elements is usually obtained by taking the product of the element pattern and the array factor [1, p.11-5] [2, p. 249]. In this approach the assumption is made that all elements have the same radiation pattern (i.e. the isolated pattern). In practical arrays, however, the presence of nearby elements has a distorting effect on the pattern of the single antenna, causing pattern degradation and mismatches. The degree of distortion depends on the element type, its physical size and on the array geometry, i.e. inter-element spacing and array lattice. In general, the smaller the inter-element spacing, the larger the distortions. Hence, the mutual coupling causes the element pattern to vary within the array. The element pattern which embraces the mutual coupling effects is characterized by the active or embedded pattern [3].

An understanding of the mutual coupling requires a rigorous solution of the electromagnetic problem. Since the mutual coupling is typically a near-field phenomenon,

a numerical technique will usually involve complex computations resulting in significant computational requirements (time and memory). To avoid this one has to rely on measurements (far-field pattern and S-parameters) for obtaining a clear picture of the effects caused by the mutual coupling. However, measurements of mutual coupling between all pairs of combinations within an array can become very laborious and cost a lot of money and time, even for small finite arrays.

Finite arrays are used in many applications, like radar, satellite antennas, and mobile communications, and especially as feeding devices for reflector or lens antennas. They have a number of important uses which include generating contour coverage patterns, correction for reflector distortions and improving wide-angle scan performances.

A dielectric rod antenna is an attractive candidate to be used as a feed-array element for reflector antennas since it can, due to its dielectric filling and extension, produce a relatively high gain with a small cross section. Because of this the feed elements can be packed closely together. Consequently it is possible to design arrays with a relative spacing in the order of  $0.5 < d/\lambda < 1.0$ , where  $\lambda$  stands for the wavelength. Due to the small spacing, mismatches due to mutual coupling can become a serious problem and should be investigated carefully. However, because dielectric antennas involve a combination of metal and dielectric, solution of the field problem is complex, even for a single antenna, as was demonstrated in Chapter 4. Approximate techniques are then required.

In this chapter, the Minimum Scattering Antenna (MSA) theory is used for predicting the effect of the coupling between two adjacent dielectric rod antennas. Earlier work on coupling theory between MSA antennas has been published by Wasylkiwskyj and Khan [4][5]. Andersen [6] later applied the same theory with success for predicting the coupling between crossed dipoles and helices. Although dielectric rod antennas do not belong to the class of MSAs, it will be shown that under certain conditions one can still model the free-space mutual coupling between dielectric rod antennas



in terms of a coupling between the radiation modes of MSAs. By doing so one can represent the mutual impedance by an integral which involves only the far-field power pattern of a single rod antenna. Once the mutual impedance is calculated for a given spacing and a given power pattern, the excitations and the embedded pattern of each element in the array are found by simple array calculations.

This chapter is organized further as follows. For completeness, we begin with a brief review of the theory of MSAs in section 2. In section 3, we examine to what extent the necessary assumptions and approximations of the MSA theory allow us to characterize the dielectric rod antenna. In section 4, computations of the mutual impedance and embedded patterns for an array of two dielectric rod antennas are given. The calculations are then verified with measurement results for different inter-element spacing. Finally, some concluding remarks on the limitations of the present method are discussed.

## 5.2 Review of the theory on MSAs

Work has been published in [4][5] on the mutual coupling among a class of idealized antennas, the electromagnetic properties of which are determined in terms of their radiation patterns only. Such antennas are called Minimum Scattering Antennas (MSAs). They have the following properties:

1. They become “invisible” when their local ports are open circuited.
2. They receive as much power as they scatter.
3. Their electromagnetic properties are completely and uniquely defined by their transmitting (receiving ) patterns.

In this section, the scattering matrix representation of a single MSA is discussed followed by a physical interpretation of the properties mentioned above. Next, a

system of two coupled MSAs is treated and an expression is given for their mutual impedance in terms of the radiation pattern of a single MSA.

### 5.2.1 General scattering matrix representation

The general scattering matrix representation of an antenna may be written as

$$\mathbf{b} = \mathbf{S}\mathbf{a} = \begin{bmatrix} \mathbf{b}_\alpha \\ \mathbf{b}_\beta \end{bmatrix} = \begin{bmatrix} S_{\alpha,\alpha} & S_{\alpha,\beta} \\ S_{\beta,\alpha} & S_{\beta,\beta} \end{bmatrix} \begin{bmatrix} \mathbf{a}_\alpha \\ \mathbf{a}_\beta \end{bmatrix}, \quad (5.1)$$

where  $\mathbf{a}_\alpha$  and  $\mathbf{b}_\alpha$  are vectors of finite length containing incident and reflected wave amplitudes at the antenna local ports, respectively.  $\mathbf{a}_\beta$  and  $\mathbf{b}_\beta$  are vectors of infinite length denoting incident and reflected wave amplitudes of the radiated modes (i.e. spherical, plane-wave,...,etc.) defined at a surface enclosing the antenna. Note, that in the transmit case, an input wave  $\mathbf{a}_\alpha$  at the antenna ports produces a wave  $\mathbf{b}_\beta$  radiated into free space and a wave  $\mathbf{b}_\alpha$  reflected back into the antenna terminals. In receive mode, an incident wave  $\mathbf{a}_\beta$  from free space gives rise to a wave  $\mathbf{b}_\alpha$  at the antenna terminal ports and a wave  $\mathbf{b}_\beta$  scattered back into free-space. The sub-matrix  $S_{\alpha,\alpha}$  describes the mutual and self coupling among the antenna ports while the sub-matrices  $S_{\alpha,\beta}$ ,  $S_{\beta,\alpha}$  and  $S_{\beta,\beta}$  represent the receiving, transmitting and scattering properties of the antenna being considered, respectively. If the antenna is lossless then power must be conserved and the matrix  $\mathbf{S}$  is unitary

$$\mathbf{S}^+\mathbf{S} = \mathbf{I}, \quad (5.2)$$

where the superscript  $+$  denotes the transpose complex conjugate of the matrix. If the antenna is matched to free space we have no reflections on the local ports, hence

$$S_{\alpha,\alpha} = 0. \quad (5.3)$$

The lossless and matching constraints result in the following equations

$$\begin{aligned} S_{\beta,\alpha}^+ S_{\beta,\alpha} &= I_{\alpha,\alpha}, \\ S_{\beta,\alpha}^+ S_{\beta,\beta} &= 0, \\ S_{\alpha,\beta}^+ S_{\alpha,\beta} + S_{\beta,\beta}^+ S_{\beta,\beta} &= I_{\beta,\beta}, \end{aligned} \quad (5.4)$$

where  $I_{\alpha,\alpha}$  is an  $N$  ( $N$ = number of antenna ports) dimensional and  $I_{\beta,\beta}$  is an infinite (number of radiating modes) dimensional unit matrix.

### 5.2.2 Minimum scattering antennas

The scattering matrix representation of free space is

$$\mathbf{b} = S_0 \mathbf{a} = \begin{bmatrix} \mathbf{b}_\alpha \\ \mathbf{b}_\beta \end{bmatrix} = \begin{bmatrix} - & - \\ - & I_{\beta,\beta} \end{bmatrix} \begin{bmatrix} \mathbf{a}_\alpha \\ \mathbf{a}_\beta \end{bmatrix}. \quad (5.5)$$

The “-” sign in Eq.(5.5) means that the corresponding quantities are omitted since in the absence of any antenna they are meaningless. The matrix  $I_{\beta,\beta}$  represents the reflection coefficients of the radiating modes. In the absence of any antenna the incident modes must be totally reflected since they cannot be absorbed.

In order to derive the scattering matrix representation of an MSA we first enforce property 1. From this property it follows that when the antenna ports are open-circuited (i.e. reflection coefficient is one),

$$\mathbf{b}_\alpha = \mathbf{a}_\alpha. \quad (5.6)$$

After substitution of Eq.(5.6) into Eq.(5.1) we obtain

$$\mathbf{b}_\beta = (S_{\beta,\alpha} S_{\alpha,\beta} + S_{\beta,\beta}) \mathbf{a}_\beta. \quad (5.7)$$

According to property 1 the MSA must be invisible, meaning that the scattering matrix in Eq.(5.1) must be identical to the one for free space, see Eq.(5.5). Thus we obtain

$$S_{\beta,\alpha} S_{\alpha,\beta} + S_{\beta,\beta} = I_{\beta,\beta}. \quad (5.8)$$

Multiplying Eq.(5.8) by the matrix  $S_{\beta,\alpha}^+$  and using Eq.(5.4) yields

$$S_{\alpha,\beta} = S_{\beta,\alpha}^+. \quad (5.9)$$

The scattered field due to an antenna is defined as the difference between the reflected fields when an antenna ( $S_{\beta,\beta}\mathbf{a}_\beta$ ) is present and when the antenna is removed ( $\mathbf{a}_\beta$ ). Kahn [4] then introduced the following expression for the scattered field

$$\mathbf{f}_\beta = S_{\beta,\beta}\mathbf{a}_\beta - \mathbf{a}_\beta = -S_{\beta,\alpha}S_{\beta,\alpha}^+\mathbf{a}_\beta, \quad (5.10)$$

where we have used Eq. (5.8) and Eq. (5.9). The scattered power is defined as

$$\begin{aligned} P_{\text{scat}} &= \mathbf{f}_\beta^+ \mathbf{f}_\beta, \\ &= (S_{\beta,\alpha}S_{\beta,\alpha}^+\mathbf{a}_\beta)^+ (S_{\beta,\alpha}S_{\beta,\alpha}^+\mathbf{a}_\beta), \\ &= \mathbf{a}_\beta^+ S_{\beta,\alpha} S_{\beta,\alpha}^+ S_{\beta,\alpha} S_{\beta,\alpha}^+ \mathbf{a}_\beta, \\ &= \mathbf{a}_\beta^+ S_{\beta,\alpha} S_{\beta,\alpha}^+ \mathbf{a}_\beta = |S_{\beta,\alpha}^+ \mathbf{a}_\beta|^2. \end{aligned} \quad (5.11)$$

The power received by the antenna is given by ( $\mathbf{a}_\alpha = \mathbf{0}$ )

$$P_{\text{rec}} = |\mathbf{b}_\alpha|^2 = |S_{\alpha,\beta}\mathbf{a}_\beta|^2 = |S_{\beta,\alpha}^+ \mathbf{a}_\beta|^2, \quad (5.12)$$

where we have used Eq. (5.9). From Eq. (5.11) and Eq. (5.12) follows that the power received equals the power scattered, which confirms the second property of the MSA. Eq. (5.10) implies that the scattered field is a linear combination of the columns of the matrix  $S_{\beta,\alpha}$ . Hence, the scattered pattern is a linear combination of the amplitudes of the radiation modes  $S_{\beta,\alpha}$  (Property 3). Finally, we obtain the scattering matrix representation of a Minimum Scattering Antenna cast in terms of radiation characteristics only as

$$S = \begin{bmatrix} 0 & S_{\beta,\alpha}^+ \\ S_{\beta,\alpha} & I_{\beta,\beta} - S_{\beta,\alpha}S_{\beta,\alpha}^+ \end{bmatrix}. \quad (5.13)$$

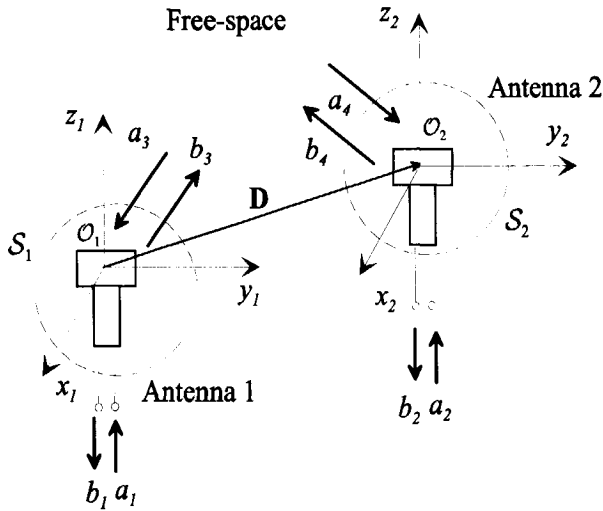


Figure 5.1: Scattering representation of two coupled antennas.

### 5.2.3 Mutual coupling between two minimum scattering antennas

Consider an array of two MSAs as shown in Fig. 5.1. The electromagnetic properties of each antenna, expressed in the antenna local coordinate system, can be represented by a scattering matrix similar to Eq. (5.13). We can write, respectively, for antenna (1) and antenna (2)

$$\begin{bmatrix} \mathbf{b}_1 \\ \mathbf{b}_3 \end{bmatrix} = \begin{bmatrix} 0 & S_{3,1}^+ \\ S_{3,1} & I - S_{3,1}S_{3,1}^+ \end{bmatrix} \begin{bmatrix} \mathbf{a}_1 \\ \mathbf{a}_3 \end{bmatrix}, \quad (5.14)$$

$$\begin{bmatrix} \mathbf{b}_2 \\ \mathbf{b}_4 \end{bmatrix} = \begin{bmatrix} 0 & S_{4,2}^+ \\ S_{4,2} & I - S_{4,2}S_{4,2}^+ \end{bmatrix} \begin{bmatrix} \mathbf{a}_2 \\ \mathbf{a}_4 \end{bmatrix}, \quad (5.15)$$

where  $\mathbf{a}_1$  and  $\mathbf{a}_2$  are vectors of amplitudes of incoming waves at the ports of antenna (1) and antenna (2), respectively.  $\mathbf{b}_1$  and  $\mathbf{b}_2$  are vectors of amplitudes of outgoing

waves at the ports of antenna (1) and antenna (2), respectively. The vectors  $\mathbf{b}_3$  and  $\mathbf{b}_4$  represent amplitudes of the transmitted waves, while the vectors  $\mathbf{a}_3$  and  $\mathbf{a}_4$  contain amplitudes of the received waves, defined with respect to the reference spheres  $\mathcal{S}_1$  and  $\mathcal{S}_2$  (see Fig. 5.1). Note that if the antennas are single-mode, the quantities in Eq. (5.14) and Eq. (5.15) become vectors with length one. The system of the two coupled antennas can be represented by a single scattering matrix  $S_{\alpha,\alpha}$

$$\mathbf{b} = S_{\alpha,\alpha}\mathbf{a} = \begin{bmatrix} b_1 \\ b_2 \end{bmatrix} = \begin{bmatrix} s_{1,1} & s_{1,2} \\ s_{2,1} & s_{2,2} \end{bmatrix} \begin{bmatrix} a_1 \\ a_2 \end{bmatrix}, \quad (5.16)$$

and a single impedance matrix  $Z$

$$\mathbf{v} = \mathbf{Z}\mathbf{i} = \begin{bmatrix} v_1 \\ v_2 \end{bmatrix} = \begin{bmatrix} Z_{1,1} & Z_{1,2} \\ Z_{2,1} & Z_{2,2} \end{bmatrix} \begin{bmatrix} i_1 \\ i_2 \end{bmatrix}, \quad (5.17)$$

where  $Z_{1,1}$ ,  $Z_{2,2}$ ,  $Z_{1,2}$  and  $Z_{2,1}$  are, respectively, the self and mutual impedances.  $v_1$ ,  $v_2$ ,  $i_1$  and  $i_2$  are total voltages and total currents at the ports of antenna (1) and antenna (2) respectively. The impedance and scattering matrices are related by the relation

$$\frac{1}{Z_0}\mathbf{Z} = \begin{bmatrix} z_{1,1} & z_{1,2} \\ z_{2,1} & z_{2,2} \end{bmatrix} = (\mathbf{I} + S_{\alpha,\alpha})(\mathbf{I} - S_{\alpha,\alpha})^{-1}, \quad (5.18)$$

where  $Z_0$  represents the characteristic impedance of the feeding line, while  $z_{1,1}$ ,  $z_{2,2}$ ,  $z_{1,2}$  and  $z_{2,1}$  are the normalized and dimensionless self and mutual impedances. For a system of two antennas which are identical, we have  $z_{1,2} = z_{2,1}$ . Wasyliwskyj derived the following expression, Eq. (73) in [5], for the normalized mutual impedance between two MSAs that radiate only in the half space  $z > 0$

$$z_{2,1} = \frac{Z_{2,1}}{Z_0} = 2 \int_{\varphi=0}^{2\pi} \int_{\Gamma} P(\theta, \varphi) \exp(-j\mathbf{k} \cdot \mathbf{D}) \sin \theta d\theta d\varphi, \quad (5.19)$$

where  $\mathbf{D}$  is the vector position of antenna (2) with respect to the coordinate system of antenna (1) and  $\mathbf{k} = k_0(\sin \theta \cos \varphi, \sin \theta \sin \varphi, \cos \theta)$ .  $\theta$  and  $\varphi$  are spherical coordinates.

$P(\theta, \varphi)$  is the radiation intensity in the far-field zone of an isolated antenna in free space and is defined as

$$P(\theta, \varphi) = \lim_{r \rightarrow \infty} \frac{r^2}{2\eta_0} \mathbf{E}(r, \theta, \varphi) \cdot \mathbf{E}^*(r, \theta, \varphi), \quad (5.20)$$

where  $\eta_0$  is the intrinsic impedance of free space and  $\mathbf{E}(r, \theta, \varphi)$  is the electric field of the antenna in the far-field zone. The  $\theta$  integration in Eq. (5.19) must be taken in the complex plane along the path  $\Gamma$  in the same way as in [6] (see Fig. 5.2).

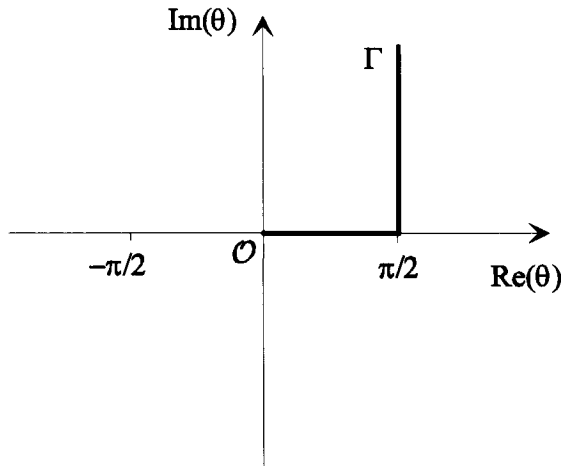


Figure 5.2: Integration contour in the  $\theta$  complex plane.

### 5.3 Application to an array of two dielectric rod antennas

In this section, we derive a general expression for the mutual impedance between two separate dielectric rod antennas using the general equivalent network representation of the antennas given in [7].

5.3.1 General network representation of a single rod antenna

Consider a model of a single dielectric rod antenna consisting of a single local port and  $M$  radiation modes representing the transmitting, receiving, and scattering properties of the antenna (see Fig. 5.3 (a)). A general network representation of this antenna can be obtained by considering an array of  $M$  single-mode, matched and de-coupled minimum scattering antennas. Each array element radiates a single mode (i.e. spherical mode). The  $M$  ports of the array are interconnected via a lossless network  $S$  as shown in Fig. 5.3 (b). The scattering matrix  $S$  ( $(M + 1) \times (M + 1)$ ) of the feeding network must be identical to the scattering matrix given by Eq. (5.1).

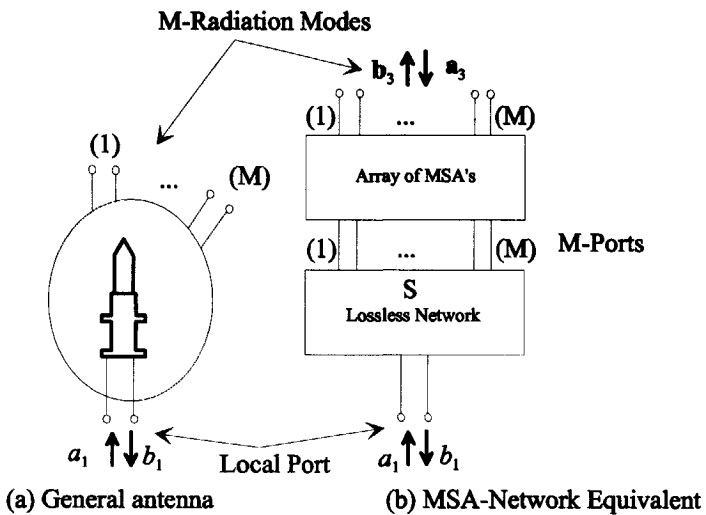


Figure 5.3: Network equivalent of a general antenna.



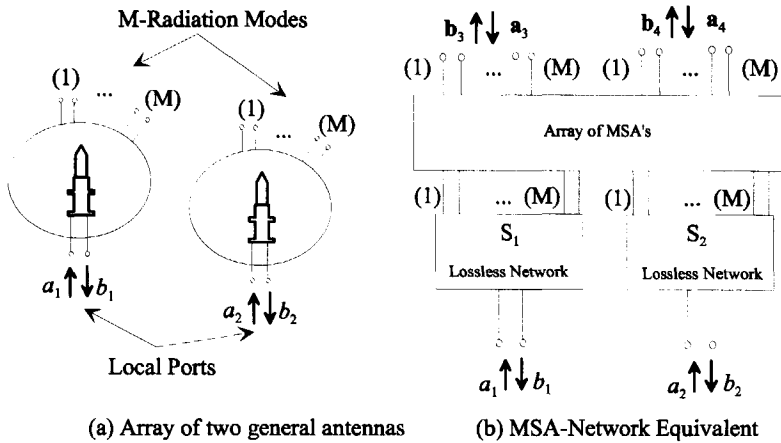


Figure 5.4: Network equivalent of an array of two coupled general antennas.

### 5.3.2 General network representation of an array of two rod antennas

Let us consider an array of two identical dielectric rod antennas. Each antenna, when isolated in free space, can be represented by a scattering matrix of the type in Eq. (5.1). Let  $S_1$  and  $S_2$  be the scattering matrices of antenna (1) and antenna (2), respectively. We have

$$\mathbf{b} = S_1 \mathbf{a} = \begin{bmatrix} b_1 \\ \mathbf{b}_3 \end{bmatrix} = \begin{bmatrix} s_{1,1} & s_{1,3} \\ s_{3,1} & s_{3,3} \end{bmatrix} \begin{bmatrix} a_1 \\ \mathbf{a}_3 \end{bmatrix}, \quad (5.21)$$

$$\mathbf{b} = S_2 \mathbf{a} = \begin{bmatrix} b_2 \\ \mathbf{b}_4 \end{bmatrix} = \begin{bmatrix} s_{2,2} & s_{2,4} \\ s_{4,2} & s_{4,4} \end{bmatrix} \begin{bmatrix} a_2 \\ \mathbf{a}_4 \end{bmatrix}, \quad (5.22)$$

where  $s_{1,1}$  and  $s_{2,2}$  are reflection coefficients at the antenna ports. The matrices  $s_{1,3}$ ,  $s_{3,1}$ ,  $s_{2,4}$  and  $s_{4,2}$  represent the receive and transmit properties of the two antennas, while the scattering properties are represented by the matrices  $s_{3,3}$  and  $s_{4,4}$ . All the quantities occurring in Eq. (5.21) and Eq. (5.22) apply to the case when the antennas

are isolated in free space and they are defined with respect to each antenna local coordinate system (see Fig. 5.1). A general network representation of the system of the two coupled rod antennas is shown in Fig. 5.4. The equivalent network consists of an array of two sub-arrays of MSAs. Each sub-array consists of  $M$  single port, single mode and matched MSAs. The two sub-arrays are individually excited using two lossless networks having scattering matrices  $S_1$  and  $S_2$ , respectively (see Fig. 5.4). In this equivalent model the free-space coupling between the two antennas is represented by the mutual coupling between the radiation modes of the two sub-arrays of the MSAs. We can write for the normalized mutual impedance between mode  $i$  of sub-array (1) and mode  $j$  of sub-array (2) [7]

$$z_{i,j} = \frac{1}{\eta_0} \lim_{r \rightarrow \infty} r^2 \int_{\varphi=0}^{2\pi} \int_{\Gamma} \mathbf{E}_i^{(1)}(r, \theta, \varphi) \cdot \mathbf{E}_j^{(2)*}(r, \theta, \varphi) \exp(-j\mathbf{k} \cdot \mathbf{D}) \sin \theta d\theta d\varphi, \quad (5.23)$$

where the superscript \* denotes the complex conjugate. In Eq. (5.23),  $\mathbf{E}_i^{(1)}(r, \theta, \varphi)$  and  $\mathbf{E}_j^{(2)}(r, \theta, \varphi)$  are the radiated electric field strength due to, respectively, mode  $i$  in sub-array (1) and mode  $j$  in sub-array (2).  $\mathbf{D}$  is the vector position of antenna (2) with respect to antenna (1). All the quantities are expressed in the coordinate system of antenna (1) (see Fig. 5.1). In order to determine the impedance matrix of the two coupled rod antennas, we first excite antenna (1) at its input local port with a current  $i_1$  and let antenna (2) be open circuited ( $i_2 = 0$ ) (see Fig. 5.5). Next, we write the network relation of the coupled MSAs as

$$\begin{bmatrix} \mathbf{v}_3 \\ \mathbf{v}_4 \end{bmatrix} = Z_0 \begin{bmatrix} \mathbf{I} & \mathbf{Z} \\ \mathbf{Z}^t & \mathbf{I} \end{bmatrix} \begin{bmatrix} -\mathbf{i}_3 \\ -\mathbf{i}_4 \end{bmatrix}, \quad (5.24)$$

where  $\mathbf{I}$  is an  $M \times M$  unit matrix and  $\mathbf{Z}$  is an  $M \times M$  matrix with entries given by Eq. (5.23).  $\mathbf{v}_3$ ,  $\mathbf{v}_4$ ,  $\mathbf{i}_3$  and  $\mathbf{i}_4$  contain total voltages and total currents at the input ports of the MSA array (see Fig. 5.5). The network relations, Eq. (5.21) and Eq. (5.22), can

be written as follows [8]

$$\begin{bmatrix} \frac{1}{2}(v_1 - Z_0 i_1) \\ \frac{1}{2}(v_3 - Z_0 i_3) \end{bmatrix} = \begin{bmatrix} s_{1,1} & s_{1,3} \\ s_{3,1} & s_{3,3} \end{bmatrix} \begin{bmatrix} \frac{1}{2}(v_1 + Z_0 i_1) \\ \frac{1}{2}(v_3 + Z_0 i_3) \end{bmatrix}, \quad (5.25)$$

$$\begin{bmatrix} \frac{1}{2}(v_2 - Z_0 i_2) \\ \frac{1}{2}(v_4 - Z_0 i_4) \end{bmatrix} = \begin{bmatrix} s_{2,2} & s_{2,4} \\ s_{4,2} & s_{4,4} \end{bmatrix} \begin{bmatrix} \frac{1}{2}(v_2 + Z_0 i_2) \\ \frac{1}{2}(v_4 + Z_0 i_4) \end{bmatrix}. \quad (5.26)$$

After substitution of  $i_2$  by 0 in Eq. (5.26) and having solved  $v_1$  and  $v_2$  in terms of  $i_1$ , we obtain [5]

$$z_{1,1} = \frac{Z_{1,1}}{Z_0} = \frac{1 + s_{1,1}}{1 - s_{1,1}} - \frac{1}{2(1 - s_{1,1})^2} s_{1,3} Z (I - S_0^{(2)}) Z^t E s_{3,1}, \quad (5.27)$$

$$z_{2,1} = \frac{Z_{2,1}}{Z_0} = \frac{1}{(1 - s_{1,1})(1 - s_{2,2})} s_{2,4} Z^t E s_{3,1}, \quad (5.28)$$

where

$$\begin{aligned} E &= [I - X]^{-1}, \quad X = \frac{1}{4}(I - S_0^{(1)})Z(I - S_0^{(2)})Z^t, \\ S_0^{(2)} &= \frac{1}{1 - s_{2,2}} s_{4,2} s_{2,4} + s_{4,4}, \\ S_0^{(1)} &= \frac{1}{1 - s_{1,1}} s_{3,1} s_{1,3} + s_{3,3}. \end{aligned} \quad (5.29)$$

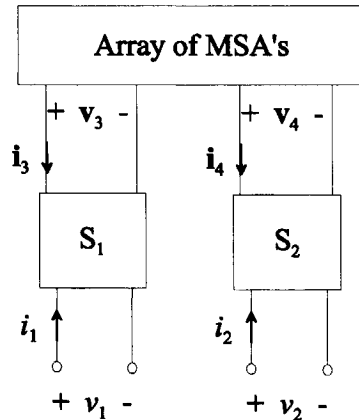


Figure 5.5: Voltage and current descriptions.

Eq. (5.27) and Eq. (5.28) represent the self and mutual impedance between the two antennas in terms of the radiating, receiving and scattering properties of each antenna in free space. If the two antennas are identical and reciprocal, we have

$$Z_{\text{array}} = \begin{bmatrix} Z_{1,1} & Z_{2,1} \\ Z_{2,1} & Z_{1,1} \end{bmatrix}. \tag{5.30}$$

The normalized self and mutual impedances can be approximated by the following series

$$z_{1,1} = \frac{1 + s_{1,1}}{1 - s_{1,1}} - \frac{1}{2(1 - s_{1,1})^2} s_{1,3} Z (I - S_0^{(2)}) Z^t (I + X + X^2 + \dots) s_{3,1}, \tag{5.31}$$

$$z_{2,1} = \frac{1}{(1 - s_{1,1})(1 - s_{2,2})} s_{2,4} Z^t (I + X + X^2 + \dots) s_{3,1}, \tag{5.32}$$

where we have used  $E = (I - X)^{-1} = (I + X + X^2 + \dots)$ . The successive terms in the series in Eq. (5.31) and Eq. (5.32) correspond to successive multiple reflections between antenna (1) and antenna (2). Note that the first term in the second series depends only on the transmit properties of antenna (1) and the receive properties of antenna (2). If we neglect the terms related to multiple reflections between antenna (1) and antenna (2) in Eq.(5.32), we obtain for the mutual impedance [5][7]

$$\begin{aligned} z_{2,1} &\approx \frac{1}{(1 - s_{1,1})(1 - s_{2,2})} s_{2,4} Z^t s_{3,1}, \\ &= \frac{1}{(1 - s_{1,1})(1 - s_{2,2}) \eta_0} \lim_{r \rightarrow \infty} r^2 \int_{\varphi=0}^{2\pi} \int_{\Gamma} \mathbf{E}_1(r, \theta, \varphi) \cdot \mathbf{E}_2^*(r, \theta, \varphi) \exp(-j\mathbf{k} \cdot \mathbf{D}) \sin \theta d\theta d\varphi, \end{aligned} \tag{5.33}$$

where  $\mathbf{E}_1(r, \theta, \varphi)$  and  $\mathbf{E}_2(r, \theta, \varphi)$  are the electric far fields of antenna (1) and antenna (2), respectively. The obtained final expression of the normalized mutual impedance is similar to the expressions published by Kerns [9] and Yaghjian [10].

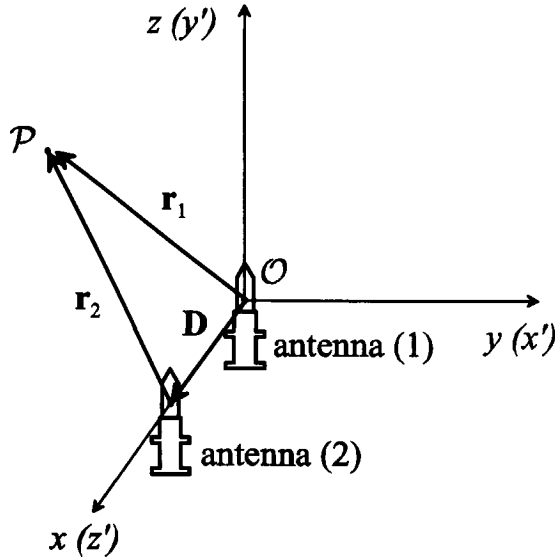


Figure 5.6: Array geometry and coordinate systems.

### 5.3.3 The embedded patterns of an array of two dielectric rod antennas

Here, we will consider the canonical problem of an array of two identical dielectric rod antennas as shown in Fig. 5.6. The electric far field radiated by antenna (1) and antenna (2) can be written respectively as

$$\mathbf{E}_1(r, \theta, \varphi) = b_3 \sqrt{\frac{\eta_0}{2\pi}} \sqrt{G_1(\theta, \varphi)} \frac{\exp(-jk_0 r_1)}{r_1} \mathbf{e}, \quad (5.34)$$

$$\mathbf{E}_2(r, \theta, \varphi) = b_4 \sqrt{\frac{\eta_0}{2\pi}} \sqrt{G_2(\theta, \varphi)} \frac{\exp(-jk_0 r_2)}{r_2} \mathbf{e}, \quad (5.35)$$

where  $G_{1,2}(\theta, \varphi)$  is a function representing the antenna gain, while  $\mathbf{e}$  is a vector denoting the antenna polarization. These quantities are found using the numerical method described in Chapter 4.  $b_3$  and  $b_4$  are complex constants yet to be determined. The

total electric far field radiated by the array is given by

$$\mathbf{E}(r, \theta, \varphi) = \sqrt{\frac{\eta_0}{2\pi}} \left( b_3 \sqrt{G_1(\theta, \varphi)} \frac{\exp(-jk_0 r_1)}{r_1} + b_4 \sqrt{G_2(\theta, \varphi)} \frac{\exp(-jk_0 r_2)}{r_2} \right) \mathbf{e}.$$

The coefficients  $b_3$  and  $b_4$  are related to the amplitudes of incoming waves  $a_1$  and  $a_2$  at the local ports of antenna (1) and antenna (2), respectively, as follows

$$\begin{bmatrix} b_3 \\ b_4 \end{bmatrix} = \begin{bmatrix} s_{3,1} & s_{3,2} \\ s_{3,2} & s_{3,1} \end{bmatrix} \begin{bmatrix} a_1 \\ a_2 \end{bmatrix}. \quad (5.36)$$

We should note that we have assumed that the dielectric rod antenna radiates a single mode, i.e. the mutual coupling will affect only the antenna current amplitude and not the distribution. The embedded pattern of antenna (1) can be found when antenna (1) is excited by  $a_1$  and antenna (2) is terminated in a matched load ( $a_2 = 0$ ). We have then  $b_3 = s_{3,1}a_1$  and  $b_4 = s_{3,2}a_1$ . The generalized Ohm's Law for this case becomes

$$\begin{bmatrix} v \\ -Z_0 i_2 \end{bmatrix} = \begin{bmatrix} Z_{1,1} & Z_{1,2} \\ Z_{2,1} & Z_{2,2} \end{bmatrix} \begin{bmatrix} i_1 \\ i_2 \end{bmatrix}, \quad (5.37)$$

where  $i_1$  and  $i_2$  are proportional to the current distribution of antenna (1) and antenna (2), respectively. The ratio  $s_{3,2}/s_{3,1}$ , which is a measure of the amount of pattern degradation due to mutual coupling, can be determined from Eq. (5.37) as

$$s_{3,2}/s_{3,1} \sim \frac{i_2}{i_1} = \frac{-Z_{2,1}}{Z_{2,2} + Z_0} = -\frac{z_{2,1}}{2}, \quad (5.38)$$

where the normalized mutual impedance  $z_{2,1}$  is given by Eq. (5.19). Appendix D contains the numerical evaluation of the integral in the complex plane for a dielectric rod antenna. At this stage, the array pattern, including mutual coupling effects, can be calculated for any set of excitations. Although the study was done for an array of two dielectric rod antennas (the canonical problem), the obtained model can easily be extended to arrays with more elements.

## 5.4 Experimental and numerical results

In this section we analyze the mutual coupling in an array of two dielectric rod antennas using the technique described in the previous sections. After completing the design of a single antenna element using the steps described in Chapter 4, we constructed an array of two identical elements. The antennas are designed to provide a linearly polarized, broad pattern at a central frequency 3.3GHz. A special antenna mounting interface was required for the DUCAT positioning system for making array measurements. The mounting platform allows us to vary the inter-element spacing about the range (5.0cm–14.0cm). The lower bound is reached when the antennas' metallic flanges are in contact. Mutual coupling measurements are sensitive to the external environment, and it is a condition of the technique that a reflection-free or at least very low-scattering situation exists. For this reason the measurements were repeated independently at the ESTEC Compact Antenna Test Range (CATR) to confirm the results, see Fig. 5.7.

The coupling ratio ( $s_{3,2}/s_{3,1}$ ), which is a measure of the amount of pattern degradation due to mutual coupling, was computed for different inter-element spacings ( $\mathbf{D} = d\mathbf{i}_z$ ). The results are indicated in Fig. 5.8. As expected, the larger  $d$ , the lower the coupling ratio and  $\lim_{d \rightarrow \infty} s_{3,2}/s_{3,1} = 0$ . Hence, the embedded pattern approaches the isolated pattern for an increasing inter-element spacing.

Although the embedded patterns were computed for different inter-element spacings, we here give the results only for two cases:  $d = 0.77\lambda$  and  $d = 0.55\lambda$ . Since a single dielectric rod antenna has a Gain of  $\approx 9.5$  dBi at the frequency that is considered, the two dielectric rod antennas are highly coupled at such inter-element spacings, i.e. their equivalent aperture distributions are strongly overlapping.

The computed and measured embedded patterns for an array of two dielectric rod antennas at an inter-element spacing  $0.77\lambda$  are given in Fig. 5.9 for antenna (1)

and in Fig. 5.10 for antenna (2). It is clearly seen that both embedded patterns are asymmetrical with respect to the  $z$ -axis, they are broader than the isolated pattern (see Fig. 4.11, Gain-loss  $\approx 1$  dB) and as might intuitively be expected, are the mirror image of each other. The embedded patterns were measured by exciting one antenna and terminating the other antenna in a matched load. When both antennas are excited ( $a_1 \neq 0$  and  $a_2 \neq 0$ ), the array pattern will be a superposition of the two embedded patterns multiplied by the excitation coefficients  $a_1$  and  $a_2$ . Fig. 5.11 shows the measured and computed array pattern when the array elements are unequally excited in amplitude and phase ( $a_1/a_2 = -6.4$  dB ( $-12.2^\circ$ )). The results of the case where the array elements are equally excited are given in Fig. 5.12 (Gain-increase  $\approx 2.5$  dB). The computed and measured embedded element pattern for an array of two dielectric rod antennas at an inter-element spacing of  $0.55\lambda$  is given in Fig. 5.13 (Gain-loss  $\approx 1.5$  dB), while the array pattern that results when both elements are equally excited is shown in Fig. 5.14. From the results we see that even at this very small inter-element spacing the agreement between theory and experiment is still good. Discrepancies between the model and the experiment results are due to the multiple reflections between the two antennas. The multiple reflections, which are neglected in the present model, become more significant as the inter-element spacing is decreased.

The inter-port coupling between the two dielectric rod antennas was measured and the results are given in Fig. 5.15. Although there is a strong interaction in terms of pattern degradation, the inter-port coupling has been found to remain small in all cases. This may be explained if one recalls that the dimensions of the dielectric rod were chosen carefully to preferentially excite a quasi single mode in the forward propagation direction. When the antenna is used in a coupled environment, most of the coupled energy will eventually be transferred to this forward mode and less energy will be coupled to the back-traveling mode.



The model assumes only coupling between fields which propagate to the far zone; any present reactive coupling is not taken into account. However, in the case of dielectric rod antennas the reactive coupling may be neglected. This is because the reactive field is confined to a region very near to the dielectric slab and decays rapidly with distance.

## 5.5 Conclusions

In this chapter the Minimum Scattering Antenna (MSA) theory was applied to predict the effect of mutual coupling between two identical dielectric rod antennas. To the author's knowledge this is the first time such a technique has been applied with success to dielectric rod antennas. Although dielectric rod antennas do not belong to the class of MSAs, we have found that even when the multiple scattering between the two antenna elements is neglected, one can still approximate the free-space coupling between dielectric rod antennas by a coupling between the radiation modes of two coupled MSAs. This resulted in an expression for the mutual impedance which involves only the radiation pattern of a single dielectric rod antenna when isolated in free space.

A coupling ratio was introduced to represent the amount of pattern degradation due to the mutual coupling. The embedded patterns can be obtained by using the coupling ratio and standard array theory. Note that in this approach the power conservation law is enforced inherently, which is not the case when standard array theory is used where a normalization factor must be introduced. A number of examples were treated and a comparison with measurement results was provided. The presented examples include different inter-element spacings and different array excitations (symmetrical and asymmetrical). A very good agreement was observed between theory and experiment, even for asymmetrical excited arrays and arrays having relatively small separation distances.

The inter-port coupling between two dielectric rod antennas was measured for different configurations. Although there is a strong interaction in terms of pattern degradation, it was found that the inter-port coupling remains small ( $< -25$  dB) in all cases considered.

The accuracy of the model presented depends on the inter-element spacing. It was found that for moderate inter-element spacing, down to  $0.55\lambda$ , the presented model predicted the mutual coupling between two dielectric rod antenna well. In cases where multiple reflections between the array elements are strong, the approximations made are no longer valid and a different approach must be sought. In the case of finite arrays of dielectric rod antennas, one can still use the numerical method described in the previous chapter to analyze the mutual coupling. Such a method takes into account all electromagnetic scattering between the array elements, provided that the computational requirements are available.

This chapter has shown that the dielectric rod antenna design that was optimized in the previous chapter is a very good candidate for array applications where both high-gain elements and small inter-element spacings are required. Since the embedded patterns are linearly dependent on the isolated element pattern and the inter-port coupling is very low, one can design an appropriate network which can compensate for the mutual coupling effects or at least make use of it in a beneficial way. This will be demonstrated in the next chapter.

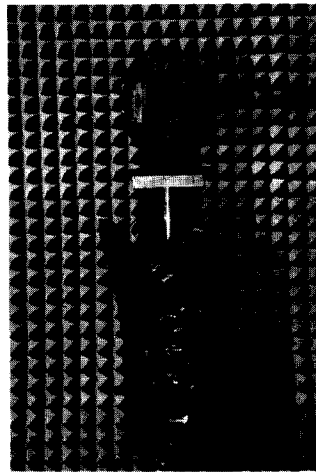
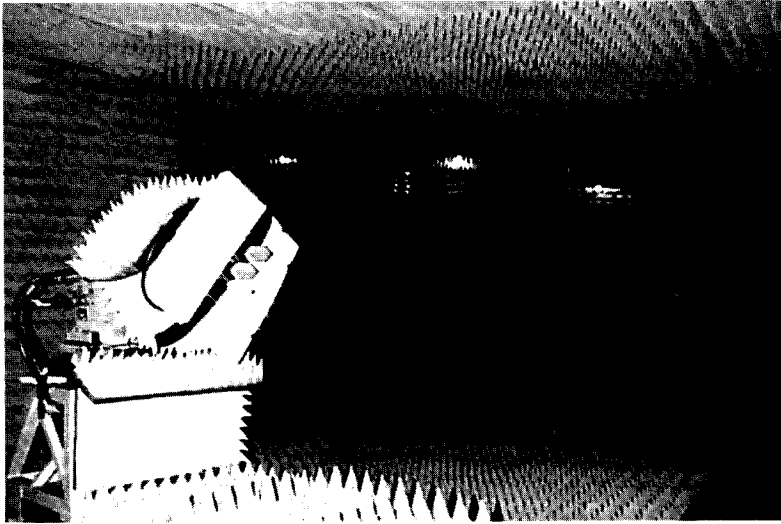


Figure 5.7: Array of two dielectric rod antennas ready for measurements. Top: in ESA-ESTEC CATR. Bottom: in DUCAT.

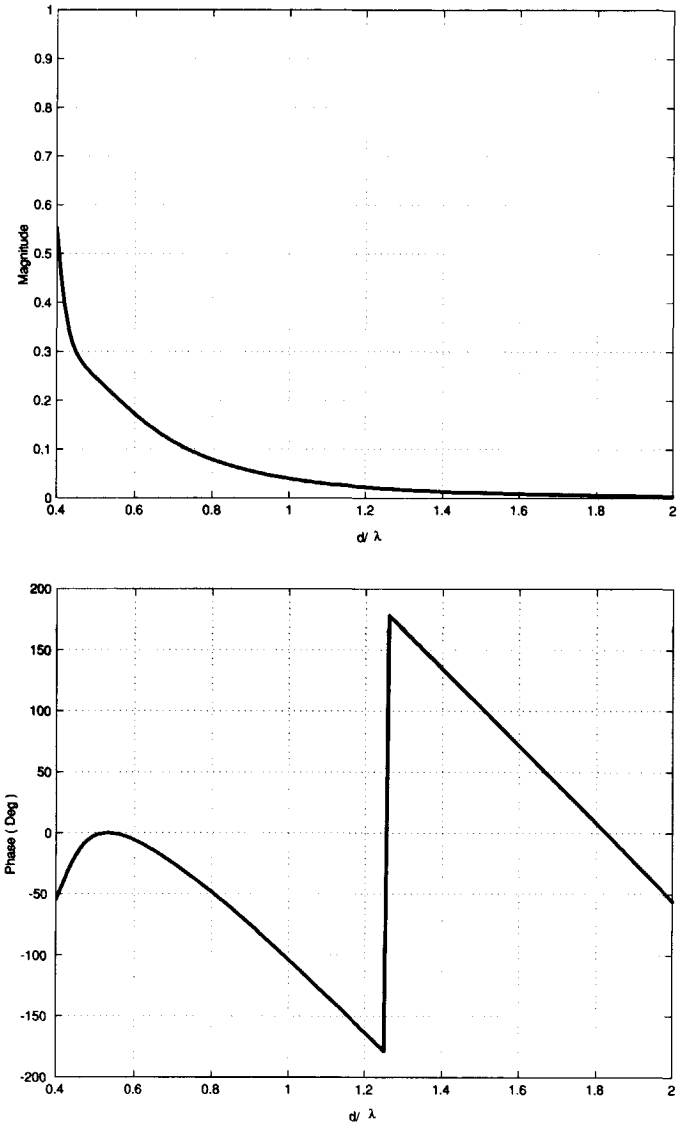


Figure 5.8: Amplitude and phase of the coupling ratio ( $s_{3,2}/s_{3,1}$ ) versus inter-element spacing.

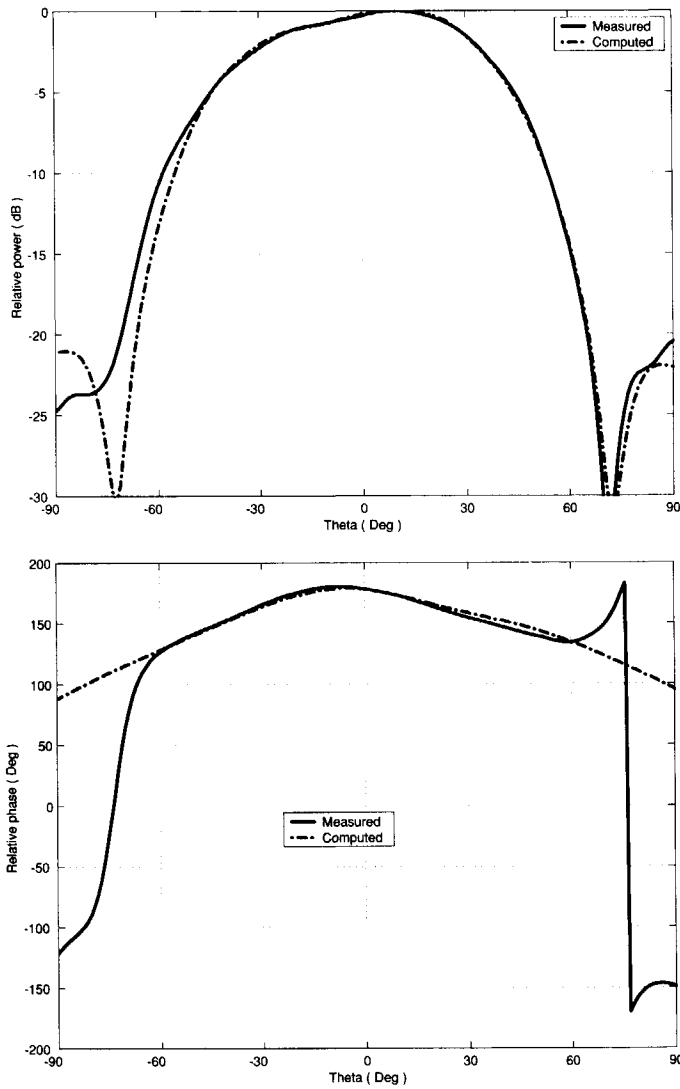


Figure 5.9: Computed and measured far-field patterns for an array of two dielectric rod antennas: Antenna (1) excited and antenna (2) resistively terminated ( $d = 0.77\lambda$ , frequency = 3.3 GHz).

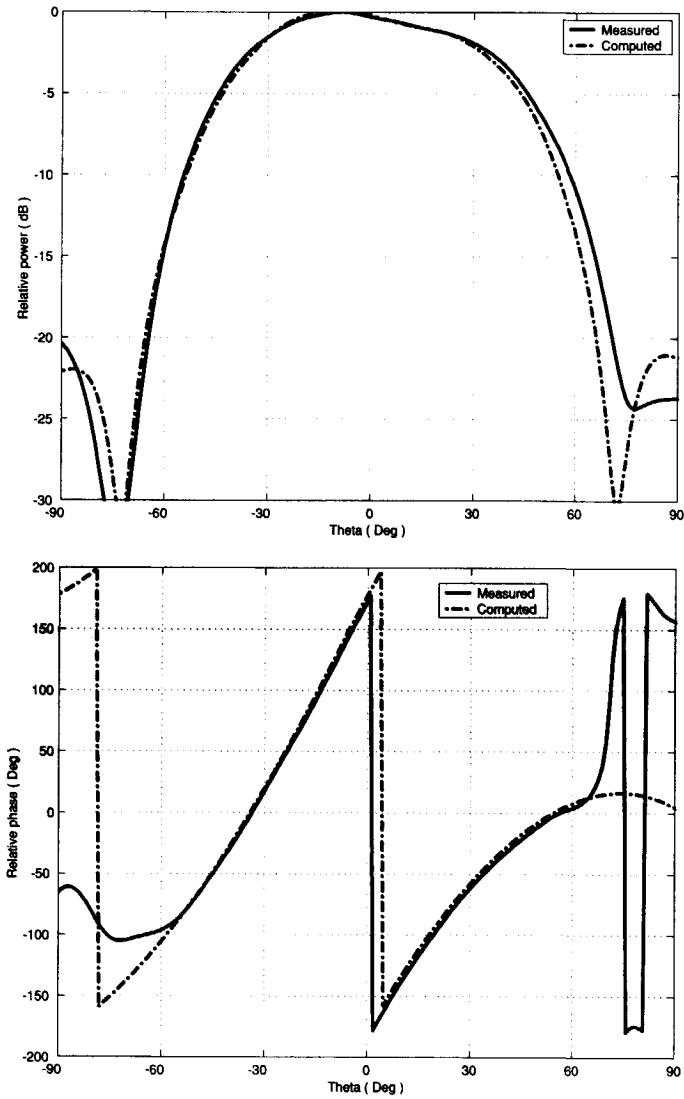


Figure 5.10: Computed and measured far-field patterns for an array of two dielectric rod antennas: Antenna (2) excited and antenna (1) resistively terminated ( $d = 0.77\lambda$ , frequency = 3.3 GHz).

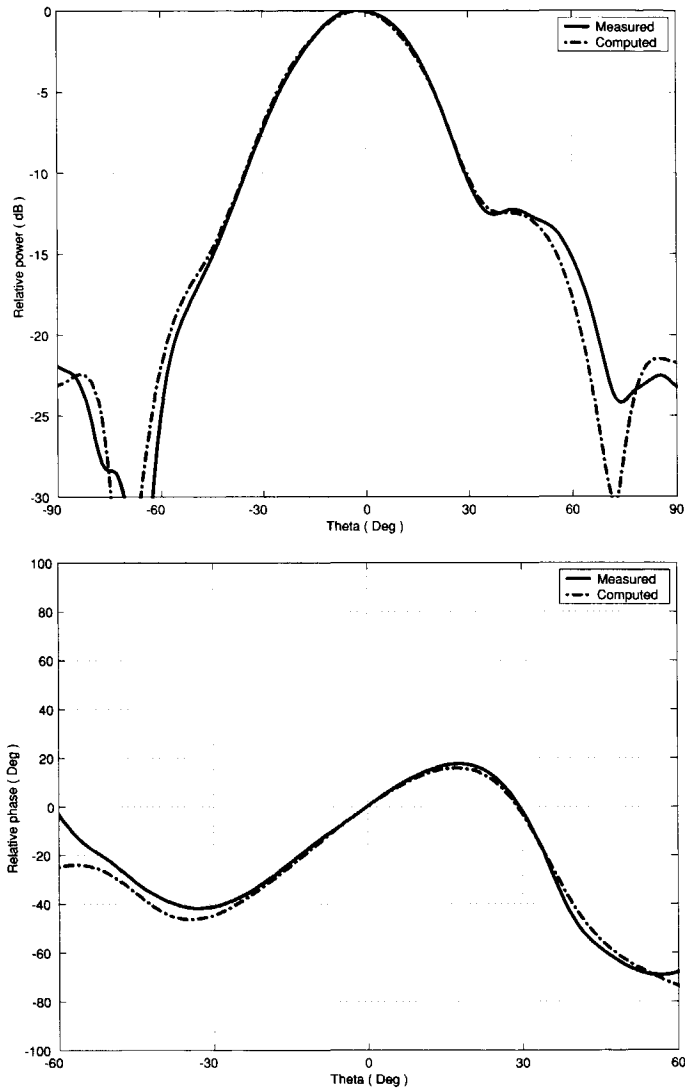


Figure 5.11: Computed and measured far-field patterns for an array of two dielectric rod antennas unequally excited in phase and amplitude ( $d = 0.77\lambda$ , frequency = 3.3 GHz,  $a_1/a_2 = -6.4$  dB ( $-12.2^\circ$ )).

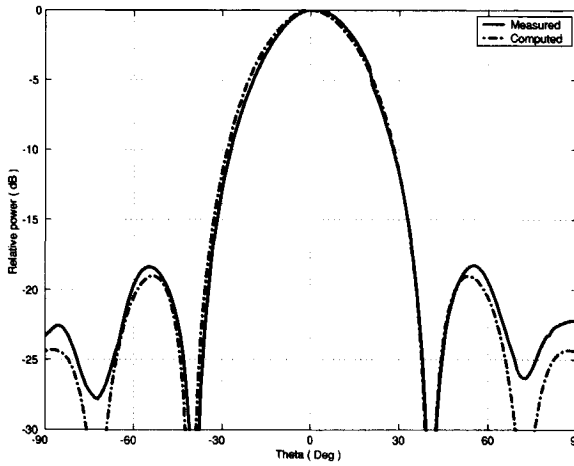


Figure 5.12: Computed and measured far-field patterns for an array of two dielectric rod antennas equally excited in phase and amplitude ( $d = 0.77\lambda$ , frequency = 3.3 GHz,  $a_1/a_2 = 1$ ).

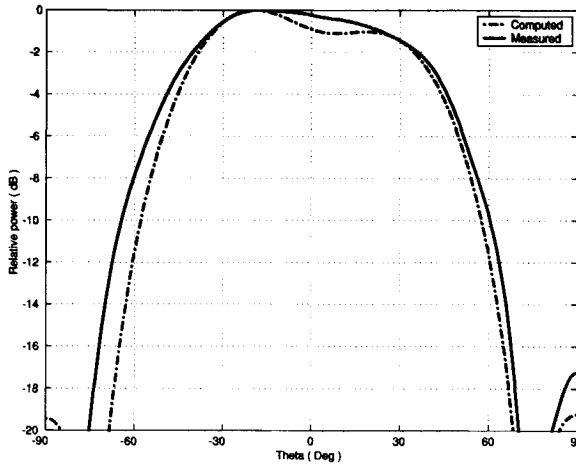


Figure 5.13: Computed and measured far-field patterns for an array of two dielectric rod antennas: Antenna (2) excited and antenna (1) resistively terminated ( $d = 0.55\lambda$ , frequency = 3.3 GHz).



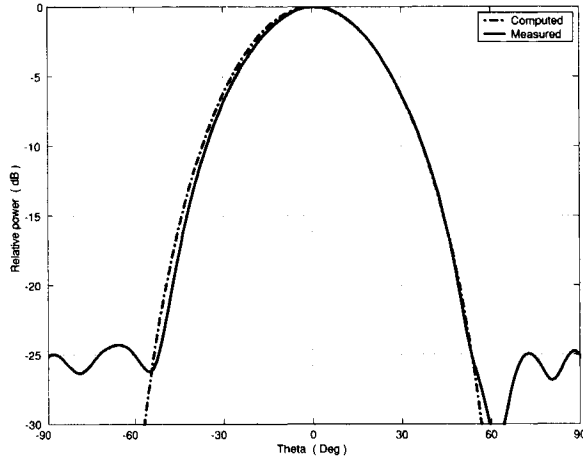


Figure 5.14: Computed and measured far-field patterns for an array of two dielectric rod antennas equally excited in phase and amplitude ( $d = 0.55\lambda$ , frequency = 3.3 GHz,  $a_1/a_2 = 1$ ).

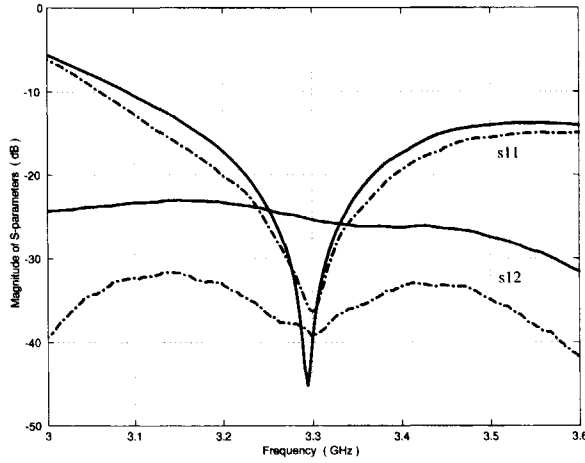


Figure 5.15: Measured inter-port coupling between two dielectric rod antennas versus frequency for two different inter-element spacings ( $-$  :  $d = 0.55\lambda$ ,  $-.-$  :  $d = 0.77\lambda$ ).



## References

- [1] Y.T. Lo and S.W. Lee, "*Antenna Handbook*", Van Nostrand Reinhold company, New York 1988.
- [2] C.A. Balanis, "*Antenna Theory; Analysis and Design*", second edition, John Wiley & Sons INC., 1982.
- [3] D.F. Kelley and W.L. Stutzman, "*Array Antenna Pattern Modeling Methods that Include Mutual Coupling Effects*", IEEE Trans. Antennas Propagat., vol. AP-41, pp. 1625-1632, 1993.
- [4] W.K. Kahn, "*Minimum Scattering Antennas*", IEEE Trans. Antennas Propagat., vol. AP-13, pp. 671, 1965.
- [5] W. Wasykiwskyj, "*Theory of Mutual Coupling Among Minimum Scattering Antennas*", IEEE Trans. Antennas Propagat., vol. AP-18, pp. 204, 1970.
- [6] J.B. Andersen, "*Coupling Between Minimum Scattering Antennas*", IEEE Trans. Antennas Propagat., vol. AP-22 pp. 832, 1974.
- [7] W. Wasykiwskyj and W.K. Kahn, "*Scattering Properties and Mutual Coupling of Antennas with Prescribed Radiation Pattern*", IEEE Trans. Antennas Propagat., vol. AP-18 pp. 741-752, 1970.
- [8] P.A. Rizzi, "*Microwave Engineering, Passive Circuits*", Prentice-Hall, Inc., 1988.

- [9] D.M. Kerns, "*Plane-Wave Scattering-Matrix Theory of Antennas and Antenna-Antenna Interactions*", National Bureau of Standards (US), Monograph 162, June 1981.
- [10] A.D. Yaghjian, "*Efficient Computation of Antenna Coupling and Fields within the Near-Field Region*", IEEE Trans. Antennas Propagat., vol. AP-30, pp. 113-128, 1982.
- [11] A.C. Ludwig, "*Mutual Coupling, Gain and Directivity of an Array of two Identical Antennas*", IEEE Trans. Antennas Propagat., pp. 837-841, November 1976.
- [12] R.L. Lewis, "*Spherical-Wave Source-Scattering Matrix Analysis of Coupled Antennas; a General System two-Port Solution*", IEEE Trans. Antennas Propagat., vol. AP-35, pp. 1375-1380, 1987.
- [13] A.L. Cullen and O. Ozkan, "*Coupled Parallel Rectangular Dielectric Waveguides*", PROC. IEE, vol. 122, No. 6, pp. 593-599, June 1975.
- [14] M.D. Abouzahra and L. Lewin, "*Coupling of Degenerate Modes on Curved Dielectric Slab Sections and Application to Directional Couplers*", IEEE Trans. MTT-28, No. 10, pp. 1096-1101, October 1980.
- [15] H. Cory, C.G. Parini and A.D. Oliver, "*Longitudinal Coupling Between Elements in a Disc-on-Rod Antenna Array*", Electronics Letters, vol. 21, No. 3, pp. 112-113, 31<sup>st</sup> January 1985.
- [16] J. Luzwick and R.F. Harrington, "*Mutual Coupling Analysis in a Finite Planar Rectangular Waveguide Antenna Array*", Electromagnetics 2:25-42, 1982.
- [17] Q. Balzano and T.B. Dowling, "*Mutual Coupling Analysis of Arrays of Apertures on Cones*", IEEE Trans. Antennas Propagat., pp. 92-97, January 1974.

# Chapter 6

## Multiple-beam reflector antenna using a dielectric rod array

### 6.1 Introduction

At the Delft University of Technology a new Transportable Atmospheric Radar (TARA) has been designed and constructed [1]. The project was financed by the Netherlands Technology Foundation (STW). The TARA antenna system consists of two separate reflector antennas with parabolic shape: one used for transmitting and the other for receiving. Each antenna system has multiple beams pointing at different directions (i.e.  $0^\circ$ ,  $15^\circ$  in both the horizontal and the vertical plane). The beams are switched electronically to measure three-dimensional wind fields.

Reflector antennas are widely used in communication and radar systems because of their low cost, low weight, and high reliability when compared to lens or phased-array systems. Most reflectors are parabolic, with a single focal point (focus). A plane wave received from the bore-sight direction is reflected by the parabolic surface and focused at the focal point. By reciprocity, a transmitted wave emanating from a feed located at the focus will be collimated by the reflector into a highly directive beam. A good

review on the theory of reflector antennas can be found in [2].

In a reflector antenna, beam switching can be achieved by using a feed positioned at a distance out of the focus (off-focus). However, the beam generated by a reflector antenna with a source located off-focus is very broad (low gain) and has high side lobes. Thus, the obtained beam is not of practical use. This performance deterioration can be substantially reduced if more than one feed element is simultaneously employed. The resulting feed array creates the required amplitude and phase distribution across the reflector surface, which produces a well-shaped beam at a given pointing angle in the far-field zone. Hence, the parameters to be optimized are the location, geometry and individual excitation of the array elements.

The location of the feed array, the number of elements and the inter-element spacing are obtained by considering the reflector antenna system in the receive situation. A plane wave arriving from a known angular direction is then assumed to be incident on the reflector surface, and the Physical Optics (PO) technique is used to construct the field distribution (amplitude and phase) that is created in the focal region. The array geometry and location are found by inspecting the focal fields; by looking for regions with high energy density.

The array excitations are obtained by considering the reflector antenna system (array and reflector) in the transmit situation. Each array element is excited separately and the individual gains are computed at the required pointing angle using PO. The results are combined and the array excitations are adjusted to achieve a maximum total gain. In the optimization process, aspects related to mutual coupling, losses in the Beam-Forming Network (BFN) and aperture blockage caused by struts and feed housing are very crucial. It are these factors that really determine the overall performance and they must be included in the optimization procedure for an accurate antenna design.

In this chapter, a design procedure is provided for reflector antennas fed by a finite

array of dielectric rod antennas. The method proposed makes use of the electromagnetic models developed in the previous chapters. It takes into account mutual coupling between the dielectric rods and blockage due to the feed housing and struts, which are required for mechanical stability and mounting purposes. The method was applied to design the novel feed system of TARA. The goal of the feed design in TARA was to maximize the gain and decrease the side-lobe level of the beams at the different pointing angles. The novelty aspect is the use of high-gain miniaturized rods packed closely together to achieve full sampling of the focal field distribution in the receive case and to improve the scanned beams patterns in the transmit case.

This chapter is organized as follows: in section 2, the reflector antenna is considered in the receive mode and the Physical Optics technique is used to construct the field distribution in the focal region and to determine the array geometry. In section 3, the computation of the far-field pattern of a reflector antenna fed by an array of dielectric rods is described (transmit case). Then the optimization of the array excitation vector for maximal directive gain, including mismatches and mutual coupling, is treated. In section 4, a hybrid Physical Optics-Moment Method is presented for analyzing the blockage caused by struts and feed housing. In section 5, the design method is applied to the feed system of TARA. Finally, some concluding remarks on the design procedure are given.

## **6.2 Reflector antenna in receive case: Focal plane analysis**

In this section the Physical Optics (PO) technique is used to compute the fields in the focal region of a parabolic reflector antenna when receiving a plane wave from an arbitrary direction. The general problem geometry and coordinate system used

throughout this section are shown in Fig. 6.1. The reflector surface has a diameter  $D$ , a focal distance  $F$  and is assumed to be perfectly conducting.

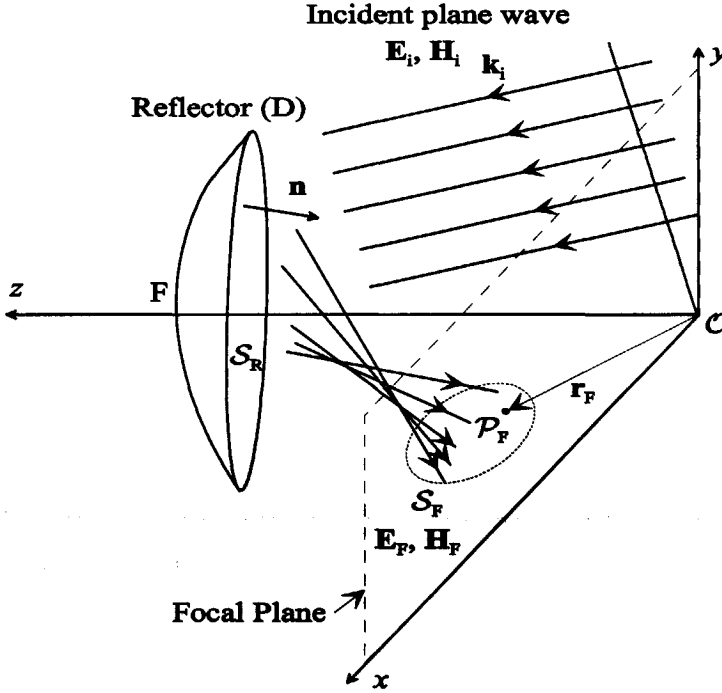


Figure 6.1: General geometry of a reflector antenna illuminated by a plane wave.

### 6.2.1 Computation of the focal fields

Consider a reflector antenna in the receive mode. A plane wave ( $\mathbf{E}_i, \mathbf{H}_i$ ) is assumed incident on the reflector surface from a fixed direction  $\mathbf{k}_i$  as shown in Fig. 6.1. A plane wave propagating in free space may be represented as follows

$$\mathbf{E}_i = \mathbf{e}_i \exp(-j\mathbf{k}_i \cdot \mathbf{r}), \quad (6.1)$$

$$\mathbf{H}_i = \frac{1}{\omega\mu_0} \mathbf{k}_i \times \mathbf{e}_i \exp(-j\mathbf{k}_i \cdot \mathbf{r}), \quad (6.2)$$



where  $\mathbf{e}_i$  is a unit vector defining the polarization of the plane wave.

When the plane wave reaches the conducting reflector surface, it induces an electric current distribution  $\mathbf{J}_S$ . The induced electric current density excites the scattered field. When the transverse dimensions of the reflector, i.e. the radii of curvature of the reflector surface and the radii of curvature of the incident wave front, are all much larger than several wavelengths, then the Physical Optics technique can be used. The Physical Optics approximation to the induced electric current density  $\mathbf{J}_S$  is given by

$$\mathbf{J}_S \approx 2\mathbf{n} \times \mathbf{H}_i, \quad (6.3)$$

where  $\mathbf{n}$  is the unit outward normal at the reflector illuminated side  $S_R$  and  $\mathbf{H}_i$  is the incident plane wave magnetic field. Note that the PO current exists only on the illuminated side of the reflector. Hence, the diffracted field at the reflector edge is not taken into account.

Using the Green's representation for the electromagnetic field, Eq. (2.56) and Eq. (2.57), we can express the electric field in free space at any point  $\mathcal{P}_F$  located on the focal plane (see Fig. 6.1) as

$$\mathbf{E}_F(\mathbf{r}_F) = -j\omega\mu_0 \int_{S_R} [(1+p(1+p))\mathbf{J}_S - (\mathbf{J}_S \cdot \hat{\mathbf{i}}_R)\hat{\mathbf{i}}_R(1+3p(1+p))] G dA, \quad (6.4)$$

$$p = \frac{1}{jk_0 R}, \quad G = \frac{\exp(-jk_0 R)}{4\pi R}, \quad (6.5)$$

$$\mathbf{R} = \mathbf{r}_F - \mathbf{r}_R, \quad \hat{\mathbf{i}}_R = \frac{\mathbf{R}}{R},$$

where  $\mathbf{r}_R$  and  $\mathbf{r}_F$  are position vectors denoting a point on the reflector surface  $S_R$  (illuminated side) and a point on the focal plane, respectively. Note that the focal plane is located in the near-field zone of the reflector antenna. Computation of the field at a single point in the focal region involves an integration over the entire reflector surface. Construction of the focal field means repeating the integration for a large number of points. This may require a large computational time. One can use simple ray tracing, i.e. based on Snell's law for reflection, in order to select a particular region

and then use Eq. (6.4) to accurately determine the power and phase distribution in that region. This reduces the computational time significantly. Although the study done here was for a single plane-wave incidence, one can easily extend it to a general source by expressing the incident field as a superposition of plane waves with different amplitudes, directions and polarizations.

### 6.2.2 Near-field matching condition

Now we proceed with the synthesis of the primary source, which will create, when transmitting, a beam in a direction opposite to the direction of incidence of the plane wave. The electromagnetic field created in the focal plane in the receive case is denoted by  $\mathbf{E}_F$  and  $\mathbf{H}_F$ , while  $\mathbf{E}_p$  and  $\mathbf{H}_p$  represent the unknown electromagnetic field which will be present at the same plane when the primary source is transmitting. Furthermore, let  $\mathcal{S}_F$  be the part of the focal plane with the highest power density in the receive situation. The primary fields  $\mathbf{E}_p$  and  $\mathbf{H}_p$  must be matched to the focal region fields  $\mathbf{E}_F$  and  $\mathbf{H}_F$  to guarantee maximal power transfer from the transmitting primary source into the angular direction of the plane wave. The matching is performed across the surface  $\mathcal{S}_F$ . This condition is represented mathematically by the power transmission coefficient  $\eta$  defined as [2, p. 68]

$$\eta = \frac{1}{16P_F P_p} \left| \int_{\mathcal{S}_F} (\mathbf{E}_F \times \mathbf{H}_p + \mathbf{H}_F \times \mathbf{E}_p) \cdot d\mathbf{A} \right|^2, \quad (6.6)$$

where  $P_F$  and  $P_p$  are the total powers contained in the focal fields and primary source fields, respectively. They are defined by

$$P_F = \frac{1}{2} \operatorname{Re} \int_{\mathcal{S}_F} \mathbf{E}_F \times \mathbf{H}_F^* \cdot d\mathbf{A}, \quad P_p = \frac{1}{2} \operatorname{Re} \int_{\mathcal{S}_F} \mathbf{E}_p \times \mathbf{H}_p^* \cdot d\mathbf{A}. \quad (6.7)$$

The power transmission coefficient  $\eta$ , Eq. (6.6), represents the efficiency of the primary source and must be maximized. In the ideal case, i.e. perfect matching, it will become

one. At this stage, Eq. (6.6) can be used to synthesize the primary source using a set of elementary sources. However, this procedure is very difficult because it requires complete knowledge of the near field of the elementary sources, including their mutual coupling. A different approach, which takes into account mutual coupling and requires only the far field of the elementary sources, will be presented in the next section.

### 6.3 Reflector antenna in transmit case: Array synthesis

In this section the dielectric rod antenna is chosen as the elementary source and the array synthesis is performed based only on far-field patterns. First we derive an expression for the far-field pattern (secondary pattern) of a reflector antenna fed by an array of dielectric rod antennas (see Fig. 6.2). Then, the secondary pattern due to each rod is computed separately and the results are combined to maximize the directivity at a given angular direction. The effects due to mutual coupling between the dielectric rod antennas are included.

#### 6.3.1 Secondary pattern of reflectors fed by a dielectric rod array

Consider the problem of Fig. 6.2. A reflector antenna is illuminated by an array of  $N$  dielectric rod antennas. Each individual dielectric rod produces an electromagnetic field ( $\mathbf{E}_i, \mathbf{H}_i$ ) incident on the reflector surface  $\mathcal{S}_R$  which may be represented by

$$\mathbf{E}_i = \sqrt{\frac{\eta_0}{2\pi}} \sqrt{G_i(\mathbf{r})} c_i \mathbf{e}_i \frac{\exp(-jk_0 R_i)}{R_i}, \quad (6.8)$$

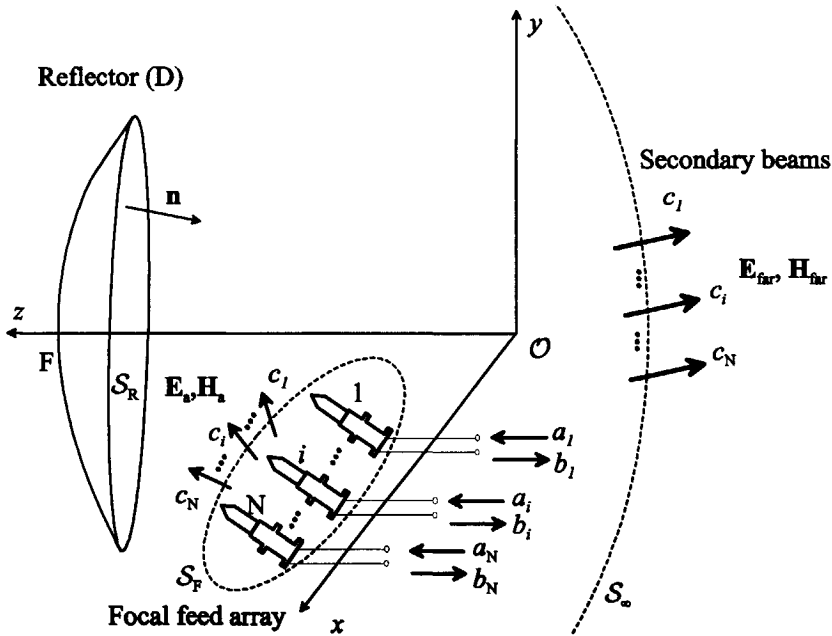


Figure 6.2: Reflector antenna fed by an array of dielectric rods located in the focal region.

$$\mathbf{H}_i = \sqrt{\frac{1}{2\pi\eta_0}} \sqrt{G_i(\mathbf{r})} c_i [\mathbf{R}_i \times \mathbf{e}_i] \frac{\exp(-jk_0 R_i)}{R_i}, \quad (6.9)$$

where  $\mathbf{r}$  is the position vector of a point  $\mathcal{P}$  on the reflector surface.  $\mathbf{e}_i$ ,  $G_i$  and  $\mathbf{r}_i$  are respectively the polarization vector, the directive gain pattern and the position vector of the dielectric rod antenna with index  $i$ . These quantities are numerically determined using the electromagnetic model developed in Chapter 4.  $\mathbf{R}_i$  is defined in Fig. 6.3. The complex coefficients  $c_i$  ( $i = 1, \dots, N$ ) are related to the array excitation vector  $\mathbf{a}$  by

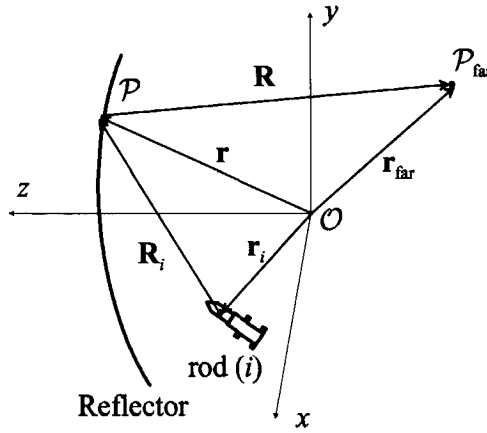


Figure 6.3: Definition of position vectors.

$$\mathbf{c} = S_{\beta,\alpha} \mathbf{a} = \begin{bmatrix} c_1 \\ \vdots \\ c_N \end{bmatrix} = \begin{bmatrix} t_{1,1} & \cdots & t_{1,N} \\ \vdots & \ddots & \vdots \\ t_{N,1} & \cdots & t_{N,N} \end{bmatrix} \begin{bmatrix} a_1 \\ \vdots \\ a_N \end{bmatrix}. \quad (6.10)$$

Furthermore we have

$$\mathbf{b} = S_{\alpha,\alpha} \mathbf{a} = \begin{bmatrix} b_1 \\ \vdots \\ b_N \end{bmatrix} = \begin{bmatrix} s_{1,1} & \cdots & s_{1,N} \\ \vdots & \ddots & \vdots \\ s_{N,1} & \cdots & s_{N,N} \end{bmatrix} \begin{bmatrix} a_1 \\ \vdots \\ a_N \end{bmatrix}, \quad (6.11)$$

where we have used the general scattering matrix representation of the dielectric rod antenna developed in chapter 5. The transmission matrix  $S_{\beta,\alpha}$  and reflection matrix  $S_{\alpha,\alpha}$  represent the mutual coupling and mismatches in the array environment. The induced electric current density on the reflector's illuminated side is obtained using the PO approximation. We have

$$\mathbf{J}_S(\mathbf{r}) \approx \sum_{i=1}^N c_i \mathbf{J}_i(\mathbf{r}), \quad (6.12)$$

$$\mathbf{J}_i(\mathbf{r}) = \sqrt{\frac{2}{\pi\eta_0}} \sqrt{G_i(\mathbf{r})} [\mathbf{n} \times (\mathbf{R}_i \times \mathbf{e}_i)] \frac{\exp(-jk_0 R_i)}{R_i},$$

The secondary pattern in the far-field zone can be obtained from Eq. (6.4) after using the well-known far-field approximations. The result for the electric far-field is

$$\mathbf{E}_{\text{far}}(\mathbf{r}_{\text{far}}) = -j \frac{\omega \mu_0 \exp(-jk_0 r_{\text{far}})}{4\pi r_{\text{far}}} \sum_{i=1}^N c_i \int_{S_R} [\mathbf{J}_i - (\mathbf{J}_i \cdot \hat{\mathbf{r}}_{\text{far}}) \hat{\mathbf{r}}_{\text{far}}] \exp(jk_0 \mathbf{r} \cdot \hat{\mathbf{r}}_{\text{far}}) dA, \quad (6.13)$$

where  $\hat{\mathbf{r}}_{\text{far}} = \mathbf{r}_{\text{far}}/r_{\text{far}}$  and the vector  $\mathbf{r}_{\text{far}}$  is defined in Fig. 6.3. Eq. (6.13) may be written in general as

$$\mathbf{E}_{\text{far}}(\theta, \varphi) = \sqrt{\frac{\eta_0}{2\pi}} \frac{\exp(-jk_0 r_{\text{far}})}{r_{\text{far}}} \mathbf{e}^{\text{far}}(\theta, \varphi) \sum_{i=1}^N c_i \sqrt{G_i^{\text{far}}(\theta, \varphi)} \exp(j\Psi_i^{\text{far}}(\theta, \varphi)), \quad (6.14)$$

where  $\mathbf{e}^{\text{far}}(\theta, \varphi)$  is a vector denoting the wave polarization.  $G_i^{\text{far}}(\theta, \varphi)$  and  $\Psi_i^{\text{far}}(\theta, \varphi)$  are, respectively, the gain and phase patterns due to each individual dielectric rod computed in the far field. They can be found in Eq. (6.13).

### 6.3.2 Far-field conjugate matching including mutual coupling

For any array excitation vector  $\mathbf{a}$ , the vector  $\mathbf{c}$  is first calculated using Eq. (6.10). Then the far-field pattern, including mutual coupling, mismatches and the reflecting surface, is simply given by Eq. (6.14). Note that the far-field gain and phase patterns,  $G_i^{\text{far}}(\theta, \varphi)$  and  $\Psi_i^{\text{far}}(\theta, \varphi)$ , depend only on the individual rod locations. The array geometry (rod locations) is found by inspecting the power and phase distribution in the focal region. One should search for high power density regions. They are found using the method described in the previous section. Once the array geometry is known, only optimization of the excitation vector  $\mathbf{a}$  is still required.

An important performance index for optimizing array antennas is the directive gain  $G(\theta, \varphi)$ . The directive gain is defined as the ratio of the radiation intensity (radiated power per solid angle) in the direction of the main beam to the total power accepted by the antenna  $P_a$  [3, p. 1-25]

$$G(\theta, \varphi) = \frac{2\pi r_{\text{far}}^2 \mathbf{E}_{\text{far}}(\theta, \varphi) \cdot \mathbf{E}_{\text{far}}^*(\theta, \varphi)}{\eta_0 P_a}. \quad (6.15)$$

where  $P_a = \mathbf{a}^+ \mathbf{a} - \mathbf{b}^+ \mathbf{b}$ . The optimum excitation vector  $\tilde{\mathbf{a}}$  is found after maximizing Eq. (6.15) for a given pointing angle  $(\theta_s, \varphi_s)$ . After substituting Eq. (6.14) into Eq. (6.15) we obtain

$$G(\theta_s, \varphi_s) = \frac{\mathbf{c}^+ \mathbf{g} \mathbf{g}^+ \mathbf{c}}{\mathbf{a}^+ \mathbf{a} - \mathbf{b}^+ \mathbf{b}}, \quad (6.16)$$

where the superscript  $+$  means the transpose and conjugate of the vector. The vector  $\mathbf{g}$  is constructed as follows

$$\mathbf{g} = \left[ \sqrt{G_1^{\text{far}}(\theta_s, \varphi_s)} \exp(-j\Psi_1^{\text{far}}(\theta_s, \varphi_s)) \quad \cdots \quad \sqrt{G_N^{\text{far}}(\theta_s, \varphi_s)} \exp(-j\Psi_N^{\text{far}}(\theta_s, \varphi_s)) \right]^t. \quad (6.17)$$

Eq. (6.16) can also be expressed only in terms of the vector  $\mathbf{a}$ . We obtain

$$G(\theta_s, \varphi_s) = \frac{\mathbf{a}^+ \mathbf{S}_{\beta, \alpha}^+ \mathbf{g} \mathbf{g}^+ \mathbf{S}_{\beta, \alpha} \mathbf{a}}{\mathbf{a}^+ [\mathbf{I} - \mathbf{S}_{\alpha, \alpha}^+ \mathbf{S}_{\alpha, \alpha}] \mathbf{a}} = \frac{\mathbf{a}^+ \mathbf{A} \mathbf{a}}{\mathbf{a}^+ \mathbf{B} \mathbf{a}}, \quad (6.18)$$

$$\mathbf{A} = \mathbf{f} \mathbf{f}^+, \quad \mathbf{f} = \mathbf{S}_{\beta, \alpha}^+ \mathbf{g}, \quad \mathbf{B} = [\mathbf{I} - \mathbf{S}_{\alpha, \alpha}^+ \mathbf{S}_{\alpha, \alpha}]. \quad (6.19)$$

The matrices  $\mathbf{A}$  and  $\mathbf{B}$  are both Hermitian, i.e.  $\mathbf{A}^+ = \mathbf{A}$  and  $\mathbf{B}^+ = \mathbf{B}$ . Furthermore, the matrix  $\mathbf{B}$  is positive definite, i.e.  $\forall \mathbf{a} \neq \mathbf{0} \Rightarrow \mathbf{a}^+ \mathbf{B} \mathbf{a} > 0$ . Hence the optimization problem reduces to the determination of the vector  $\mathbf{a}$  such that Eq. (6.18) is maximized. Since Eq. (6.18) is a ratio of two Hermitian forms with the second form being positive definite we can use the following theorem from linear algebra [4, p. 322]

*Theorem: Let a function  $G$  of a vector  $\mathbf{a}$  be defined as*

$$G = \frac{\mathbf{a}^+ \mathbf{A} \mathbf{a}}{\mathbf{a}^+ \mathbf{B} \mathbf{a}}$$

*where  $\mathbf{A}$  and  $\mathbf{B}$  are both Hermitian and  $\mathbf{B}$  is positive definite. Then*

1. *The eigenvalues  $\lambda_N \geq \cdots \geq \lambda_1$  of the "regular pencil"  $\det(\mathbf{A} - \lambda \mathbf{B}) = 0$  are real-valued.*
2. *The eigenvalues represent the bounds of the function  $G(\mathbf{a})$ ;  $\lambda_N \geq G(\mathbf{a}) \geq \lambda_1$ .*

A very useful corollary, proven in [5], makes the optimization problem very simple and is repeated here for completeness

*Corollary: If the matrix A can be written as  $A = \mathbf{f}\mathbf{f}^+$  then*

1. *The largest and only nonzero eigenvalue of the "regular pencil",  $A - \lambda B$ , is  $\max(\lambda) = \mathbf{f}^+ B^{-1} \mathbf{f}$ .*
2. *The eigenvector corresponding to  $\max(\lambda)$  is  $\tilde{\mathbf{a}} = B^{-1} \mathbf{f}$ .*

In the case of maximization of the directive gain  $G$  given by Eq. (6.18), we obtain

$$\max_{\mathbf{a}=\tilde{\mathbf{a}}} (G) = \mathbf{g}^+ S_{\beta,\alpha} \left[ \mathbf{I} - S_{\alpha,\alpha}^+ S_{\alpha,\alpha} \right]^{-1} S_{\beta,\alpha}^+ \mathbf{g}, \quad (6.20)$$

$$\tilde{\mathbf{a}} = \left[ \mathbf{I} - S_{\alpha,\alpha}^+ S_{\alpha,\alpha} \right]^{-1} S_{\beta,\alpha}^+ \mathbf{g}. \quad (6.21)$$

Eq. (6.21) represents the optimum array excitation vector for a given array geometry, frequency, and pointing angle. It includes the effect of mutual coupling and mismatches in the array environment. The interactions between the reflecting surface and the feeding array, known as aperture blockage, will cause a further gain drop and must be included in the model. This can be done when constructing the vector  $\mathbf{g}$ . A method for computing aperture blockage caused by feed housing and struts, which are required for mechanical stability and mounting purposes, is presented in the next section.

## 6.4 Analysis of feeds and struts blockage in reflector antennas

### 6.4.1 Introduction

Nowadays antennas have strict requirements for low side lobes and low cross polarization. This is why offset reflector antennas are preferable compared to symmetrical



ones because the latter suffer from high side lobes caused by the blockage of the struts supporting the feed system. However, symmetrical reflectors are structurally simpler, more compact and cheaper to manufacture. It is therefore important to analyze the effects of strut blockage in order to reduce it.

When the blocking structure interacts with the wave that is leaving the reflector and with the wave emanating from the feed it leads to gain loss and increases the side lobes and cross polarization. The amount of beam degradation depends strongly on the cross-sectional shape (circular, triangular, rectangular), size, geometry (quadrupod, tripod), and orientation of the struts. The disadvantages caused by the obstruction of the aperture by the feed struts can be partially overcome by carefully dimensioning those parameters.

Studies on the evaluation of the scattering from struts and their effects on the radiation performance of reflector antennas have been reported by a number of researchers using different techniques. The shadow method [6], the induced field ratio method [7], equivalent current technique [8], and experimentally based methods [9] have all been employed to investigate the effects of blockage in reflector antennas. However those techniques are either approximate and/or limited only to some basic geometry or symmetrical feeding.

In this section, a hybrid Physical Optics-Moment Method is used for an efficient and accurate analysis of the radiation from reflector antennas having a perfectly conducting struts of arbitrary shape and off-axis feeds.

#### 6.4.2 Problem description and method of solution

The Method of Moments (MoM) represents a suitable procedure for dealing with electromagnetic scattering from arbitrary shaped metallic bodies in the lower frequency range. However, with increasing frequency or size of the body, both the computation time and the memory requirements exceed available computer capacities. Due to the

electrically large nature of reflector antennas, their rigorous analysis using the method of moments requires enormous computer resources. The numerical tool most used for the analysis of reflector antennas is the Physical Optics technique (PO). Therefore a hybrid method combining Physical Optics with the MoM is suitable for the analysis of large reflector antennas with metallic struts of arbitrary shape.

Let us consider the reflector surface to be the PO region and the metallic struts to be the MoM region. The total scattered field at an observation point  $\mathcal{P}$  in free space can be obtained by a superposition of partial fields in the following manner

$$\mathbf{E}(\mathbf{r}) = \mathbf{E}_a(\mathbf{r}) + \mathbf{E}_r(\mathbf{r}) + \mathbf{E}_s(\mathbf{r}), \quad (6.22)$$

where the first term represents the total field generated by the focal array and is given by

$$\mathbf{E}_a(\mathbf{r}) = \sum_{i=1}^N \mathbf{E}_i(\mathbf{r}), \quad (6.23)$$

$N$  is the total number of feed elements and  $\mathbf{E}_i$  is given by Eq. (6.8). The assumption was made that the primary source (focal array) is not affected by the field scattered from the reflector and the blocking structure. The second term of Eq. (6.22) represents the field scattered by the reflector in the presence of aperture blockage and is computed using PO. We have

$$\mathbf{E}_r(\mathbf{r}) = - \int_{\mathcal{S}_R} \left( j\omega\mu_0 G(\mathbf{r}, \mathbf{r}') \mathbf{J}_S^{\text{PO}}(\mathbf{r}') - \frac{1}{j\omega\epsilon_0} \nabla'_S \cdot \mathbf{J}_S^{\text{PO}}(\mathbf{r}') \nabla G(\mathbf{r}, \mathbf{r}') \right) dA', \quad (6.24)$$

Finally, the last term of Eq. (6.22) denotes contributions from the metallic blocking structure and is given by

$$\mathbf{E}_s(\mathbf{r}) = - \int_{\mathcal{S}_S} \left( j\omega\mu_0 G(\mathbf{r}, \mathbf{r}') \mathbf{J}_S^{\text{MoM}}(\mathbf{r}') - \frac{1}{j\omega\epsilon_0} \nabla'_S \cdot \mathbf{J}_S^{\text{MoM}}(\mathbf{r}') \nabla G(\mathbf{r}, \mathbf{r}') \right) dA', \quad (6.25)$$

where  $\mathcal{S}_S$  is the surface enclosing the metallic blocking structure. The remaining symbols were defined in Chapter 3. The electric current density  $\mathbf{J}_S^{\text{PO}}$  is given by the

PO approximation as

$$\mathbf{J}_S^{\text{PO}}(\mathbf{r}) \approx 2\mathbf{n} \times (\mathbf{H}_n(\mathbf{r}) + \mathbf{H}_s(\mathbf{r})), \quad \forall \mathbf{r} \in \mathcal{S}_R \quad (6.26)$$

$$\mathbf{H}_a(\mathbf{r}) = \sum_{i=1}^{\text{NF}} \mathbf{H}_i(\mathbf{r}),$$

where  $\mathbf{H}_i$  is given by Eq. (6.9). Since the electromagnetic problem addressed here is a large-scale problem, we assume in the remaining of this section that the first term of Eq. (6.26) is dominant. This means that multiple scattering between struts and reflector is not taken into account. Hence, Eq. (6.26) is approximated by

$$\mathbf{J}_S^{\text{PO}}(\mathbf{r}) \approx 2\mathbf{n} \times \mathbf{H}_a(\mathbf{r}), \quad \forall \mathbf{r} \in \mathcal{S}_R \quad (6.27)$$

The unknown electric current density  $\mathbf{J}_S^{\text{MoM}}$  is found after enforcing the following boundary condition

$$\mathbf{n} \times \mathbf{E}_s(\mathbf{r}) = -\mathbf{n} \times (\mathbf{E}_a(\mathbf{r}) + \mathbf{E}_r(\mathbf{r})), \quad \forall \mathbf{r} \in \mathcal{S}_S \quad (6.28)$$

Eq. (6.28) is solved using the MoM and following the same procedure described in Chapter 3. As a result, the obtained MoM matrix is identical to the matrix  $\mathbf{Z}^{\text{c-c}}$  defined in Eq. (B.7) (see Appendix B). Hence we can use the same computer code.

## 6.5 The design procedure applied to the feed system of TARA

### 6.5.1 Introduction

At the Delft University of Technology, different radar systems with reflector antennas have been developed. One of the larger systems is the S-band Delft Atmospheric Research Radar (DARR) [10], which is used for atmospheric profiling. DARR is a permanent system constructed in an urbanized coastal area and is located on the top

of the electrical engineering building at Delft University of Technology (DUT). As atmospheric conditions depend on the geographical situation, measurements carried out at different locations could give extra information on the atmosphere. Therefore, at the Delft University of Technology a new Transportable Atmospheric RADar (TARA) has been designed and constructed [1]. The project was financed by the Netherlands Technology Foundation (STW) under grant No. Del.44-3311. In this section, we apply the procedure described in the previous sections to design the novel feed system of TARA.

### **6.5.2 TARA antenna requirements**

The TARA system is a Frequency Modulated Continuous Wave (FM-CW) radar designed to work at S-band. The system will have high gain and therefore large antennas which should remain transportable. Two separate reflector antennas, one for transmit and one for receive, are used to satisfy the strong isolation usually required in FM-CW radars. Each reflector is of parabolic shape with a diameter  $D=3\text{m}$  and a focal distance  $F=1.535\text{m}$ . The diameter is a trade-off between transportability and narrow beam (high gain), while the focal distance is a trade-off between mechanical stability and low cross-polarization. The antenna system of TARA is capable of forming multiple beams pointing at different directions (i.e.  $0^\circ$ ,  $15^\circ$  in both the horizontal and the vertical plane). The beams are switched electronically to measure three-dimensional wind fields. This is achieved by exciting the parabolic reflector by a feed located at the focus and two small arrays located off-focus. The feed located at the focus is dually polarized to allow for full polarimetric measurements while the offset feeds are linearly polarized. All the feed elements used in TARA are identical dielectric rod antennas, the design of which is described in Chapter 4. The fact that TARA must be transportable adds more constraints to the size and mechanical stability of the whole antenna system; see Table 6.1 for a list of the TARA antenna specifications.

Table 6.1: TARA antenna specifications

Centre frequency	3.2975Ghz	$\lambda = 9,1 \text{ cm}$
Reflector diameter (D)	3m	$33\lambda$
Focal distance (F)	1.535m	F/D= 0.51
Number of beams	3	$0^\circ$ and $15^\circ$ in two orthogonal planes
Gain	> 37dBi	All beams
Beam width	< $3^\circ$	All beams
Cross polarization	< -30dB	Average value
1 <sup>st</sup> side-lobe level	< -25dB	All beams
90 <sup>o</sup> side-lobe level	< -80dB	All beams

### 6.5.3 Central feed design

The first configuration treated here is a parabolic reflector with a dielectric rod antenna located at the focus. The procedure described in Chapter 4 (section 4.4) is used to design a dielectric rod antenna with a gain of 9.5 dBi at centre frequency. Furthermore, the design must provide an edge taper, i.e. power drop at the reflector edge, of -10dB. This guarantees an optimum illumination [11, p. 814] of the reflector surface and reduces the spillover (energy which does not reach the reflector) and diffraction occurring at the reflector edge. The optimized dielectric rod (see Fig. 4.5 and Table 4.1 in Chapter 4) is integrated in a metallic housing and is mechanically supported by four very thin cylindrical struts (cross-dimensions  $0.25\lambda$ ). For stability purposes, the struts are connected to the back of the reflector system. This configuration has minimal aperture blockage and is used to validate the theoretical model. All measurements and computational results presented here were obtained with the TARA configuration with the parameters listed in Table 6.1. The experiments were carried out at the IRCR far-field outdoor range [12]. Fig. 6.4 shows the computed and measured H-plane far-field pattern of the TARA antenna system with a dielectric rod antenna at the focus.

The computed pattern in Fig. 6.4 was obtained using PO without considering the blockage. From the measurements it is clear that the aperture blockage by the four struts and feed housing causes an increase of the level of the near side lobes and that it fills in the nulls of the radiation pattern.

Table 6.2: Summary of the results obtained for the minimum blockage configurations

	Pointing angle	Directive gain	1 <sup>st</sup> side-lobe level	3-dB beam width
Computed (PO without blockage)	0°	39.4dBi	-25dB	2.0°
	13.7°	37.3dBi	-8.4dB	2.6°
Measured (minimum blockage)	0°	38.8dBi	-22dB	2.0°
	13.4°	36.4dBi	-8.4dB	2.5°

The second configuration analyzed is a parabolic reflector antenna with a dielectric rod located off-focus. This configuration is obtained from the previous configuration by changing the length of only two of the four struts, i.e. making one shorter and lengthening the other. It was then possible to put the dielectric rod off-focus at location  $\mathbf{r} = 0.41\mathbf{i}_z$  and to direct it toward the reflector centre (tilt angle 14.9°). The computed and measured far-field patterns for the off-focus configuration are given in Fig. 6.5. As expected, a significant beam degradation is observed (very high side lobes). If the requirements are to be satisfied, more elements are indeed required. A comparison of the computed and measured results for the two antenna configurations is provided in Table 6.2.

#### 6.5.4 Dielectric rod array design for the 15° pointing angle

In this part we focus on the design of the 15° feed array. Let a plane wave, linearly polarized in the  $y$ -direction, be incident on the TARA reflector. The field distribution

in the focal region is computed and the results for the electric field  $y$ -component are drawn in Fig. 6.6. The power distributions along two orthogonal lines crossing the point with maximum field intensity are shown in Fig. 6.7. The phase distributions along the same two lines are given in Fig. 6.8 and Fig. 6.9. Any primary source having a power distribution identical to that of Fig. 6.7 and a phase distribution conjugate to that of Fig. 6.8 and Fig. 6.9 will create a well-shaped beam at  $15^\circ$  in the far-field zone. If the size of the primary source is finite, then the formed beam will have side lobes.

When a large array of elements is used as primary source, many elements will have very low excitations since the field intensity is non-uniformly distributed. The large number of elements increases the aperture blockage and the complexity of the beam-forming network (resulting in more losses, high costs and calibration problems). The result is a feed design with a very poor efficiency. A trade-off between all these factors is made by considering only the region with the highest power density. This region of elliptical shape is called the focal spot.

The cross-dimensions of the focal spot depend on the scan angle. The larger the scan angle, the larger the spot. Hence, the size of the array depends on the cross-dimensions of the focal spot. In the case of  $15^\circ$ , the cross-dimensions are approximately ( $\approx 0.8 \times 0.6\lambda(3\text{dB})$  and  $1.5 \times 1.1\lambda(10\text{dB})$ ). Hence, a design consisting of two dielectric rod antennas with unequal complex amplitudes is sufficient to form a beam at  $15^\circ$  (*design step 1*). Subsequently, Eq. (6.20) is used to tune the array inter-element spacing until the required directive gain at  $15^\circ$  is achieved (*design step 2*). For each inter-element spacing the mutual coupling matrix is calculated using the method of Chapter 5 (Eq. 5.35). In the case of TARA, an array of two dielectric rod antennas separated by  $0.77\lambda$  is required (see Table 6.3). The array excitations follow directly from Eq. (6.21) (*design step 3*). A plot of the directive gain versus power ratio and phase difference between the two elements is presented in Fig. 6.10. The maximum

directive gain, including mutual coupling, is reached at a power ratio of  $-6.5\text{dB}$  and a phase difference of  $1^\circ$ . According to Fig. 6.10, the directive gain depends strongly on the power ratio and not on the phase difference. Hence, by varying the phase difference one may change the radiation pattern at different angles without seriously affecting the maximum directive gain at  $15^\circ$ . This is demonstrated in Fig. 6.11 where the phase difference is used to lower the first side-lobe level. The data for the TARA  $15^\circ$  final array design is given in Table 6.3.

Table 6.3: The TARA dielectric rod array design data

	Location ( m )	Coefficient
Feed (1)	(0.39, 0.0, $-0.035$ )	$-6.5\text{dB}(-13^\circ)$
Feed (2)	(0.46, 0.0, $-0.035$ )	$0.0\text{dB}(0^\circ)$

### 6.5.5 Analysis of struts and housing blockage in TARA

Since TARA is transportable and has to operate under different weather conditions it has a bulkier feed supporting structure (see Fig. 6.12). This supporting structure is used to mount the three feed systems of TARA and guarantees mechanical stability even under severe weather conditions (wind force 6). However, the electrical performance of the antenna system may be degraded due to aperture blockage. To quantify the blockage effects caused by such a large metallic structure we used a hybrid PO/MoM technique. Only first-order scattering was considered. The whole antenna system was discretized using triangular patches ( $NTR_{\text{reflector}} = 5888$ ,  $NTR_{\text{strut}} = 3831$ ). To approximate blockage due to the feed housing, each feed system was replaced by a metallic cylinder occupying the same volume (see Fig. 6.12). Given the large size of the electromagnetic problem encountered here (memory  $> 257\text{MB}$ , CPU time  $> 24$  h), the code had to be migrated to the Cray-J90se parallel computer system of the Delft University of Technology.



Table 6.4: Summary of the results obtained for the TARA 15° beam

	Pointing angle	Directive gain	1 <sup>st</sup> side-lobe level	3-dB beam width
Computed	14.98°	37.2dBi	-18dB	2.73°
Measured	15.4°	37.0dBi	-20.5dB	2.78°

Fig. 6.13 shows the computed and measured far-field patterns including blockage and mutual coupling for the case when feed (1) is excited and feed (2) is terminated in a matched load. The results for the case when feed (2) is excited and feed (1) is terminated in a matched load are given in Fig. 6.14. Both results are combined to obtain the total far-field pattern for the scanned beam. The different contributions from individual blocking structures are given separately in Fig. 6.15. Note that Fig. 6.15 provides the antenna engineer with a lot of insight into which blocking part causes the most pattern degradation at a certain angular region. The measured and computed total far-field pattern for the scanned beam, including mutual coupling and blockage, are given in Fig. 6.16. A good agreement is observed between the theory and the measurements. A summary of the performance of the TARA 15° beam is listed in Table 6.4. The feed designs presented here are currently integrated in the operational transportable atmospheric radar TARA. A picture of the final antenna system of TARA and the TARA radar can be found in Fig. 6.17 and Fig. 6.18, respectively.

## 6.6 Conclusions

In this chapter, a technique was presented for the synthesis and analysis of finite arrays of miniaturized dielectric rods that is used to improve the scan capabilities of multiple-beam reflector antennas. The synthesis method includes mutual coupling

and mismatches in the array environment and permits an accurate determination of the array geometry, location and excitations.

The location, geometry and size of the feed array is obtained from the knowledge of the field distribution in the focal region of the reflector system. The focal region fields are accurately constructed by illuminating the reflector by a plane wave and by computing the reflected field using the Physical Optics method.

A novel array design based on miniaturized dielectric rod antennas was used to achieve a better sampling of the field distribution in the focal region in the receive situation and to improve the radiation pattern in the transmit situation.

Once the array geometry is determined, computation of the far field due to each dielectric rod separately is performed. Next, an analytical expression is used to find the array excitations that maximize the directive gain at a given angular direction. This method first compensates for the mutual coupling matrix and then performs a conjugate matching to the computed individual patterns. The obtained complex array excitations give the best possible gain achievable for a fixed array geometry. Further tuning of the phase of the individual elements permits a lowering of the near side lobe levels without seriously diminishing the maximum directive gain.

In the design of feed arrays for reflector antennas, the aperture blockage caused by the struts and the feed housing is very crucial. These cause a gain drop and an increase in the level of the near side lobes. A numerical method that combines Physical Optics and Method of Moment was used to analyze the aperture blockage caused by large metallic structures of arbitrary shape positioned in front of a large reflector antenna system. The scattered field from different blocking metallic parts can be computed separately and the results may be used to design supporting structures which are both mechanically stable and at the same time electrically "invisible" in some angular regions.

The synthesis method was applied with success to design and analyze the novel

feed system of the transportable atmospheric radar (TARA) which was designed at the Delft University of Technology. The blockage caused by the metallic struts and feed housing in the TARA antenna system was analyzed. Measurements were performed at the IRCTR far-field outdoor range. A good agreement between theory and experiment was observed. The feed designs resulting from this work have now been integrated in the operational transportable atmospheric radar TARA.

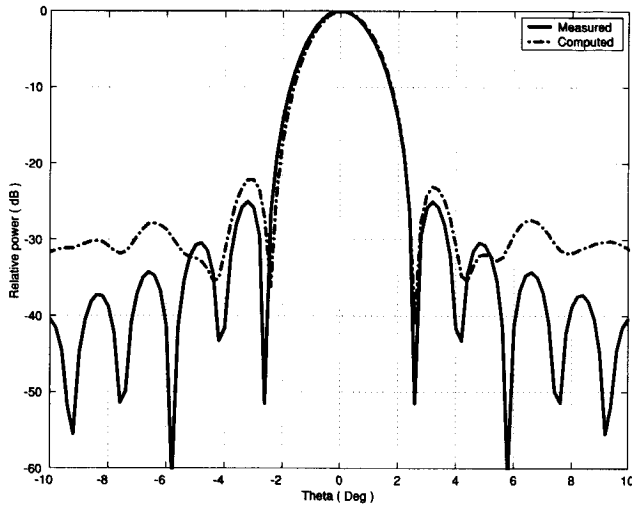


Figure 6.4: Far-field pattern of the TARA antenna system with feed at focus (frequency 3.3 GHz, minimal blockage setup).

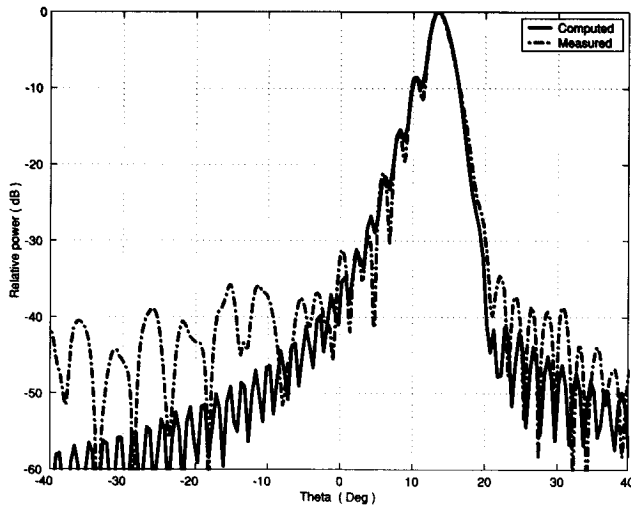


Figure 6.5: Far-field pattern of the TARA antenna system with single feed off-focus (frequency 3.3 GHz, minimal blockage setup).

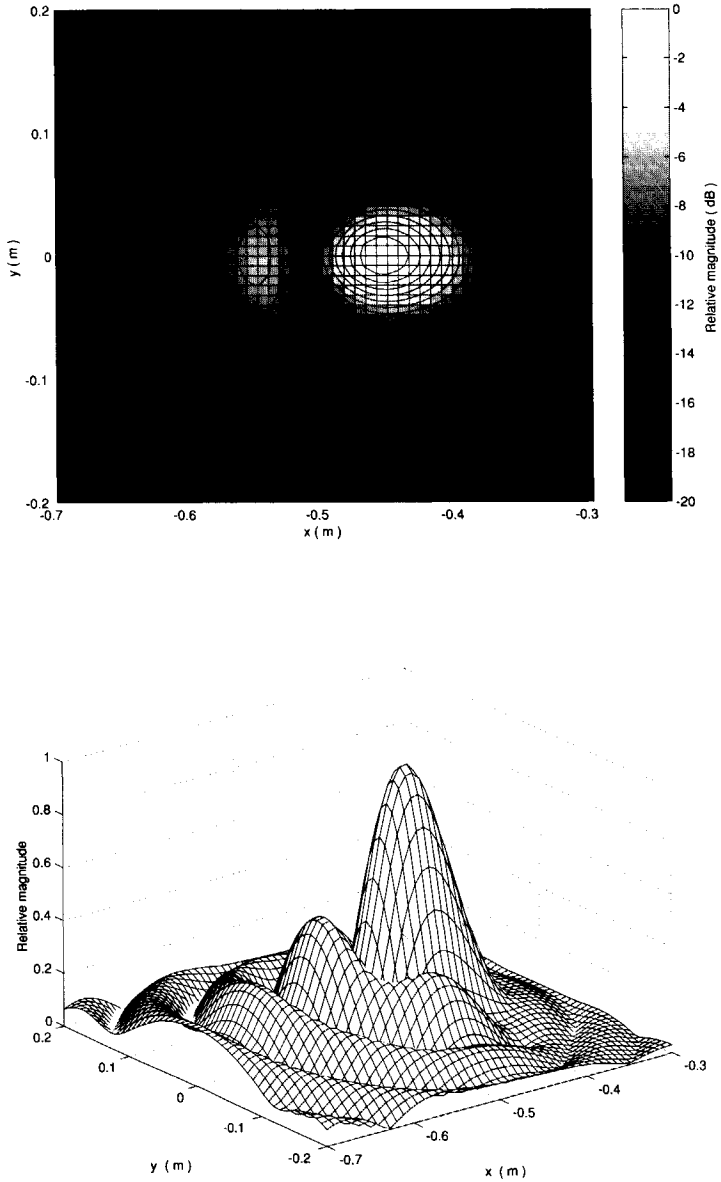


Figure 6.6: Field distribution in the focal region for  $15^\circ$  plane-wave incidence.

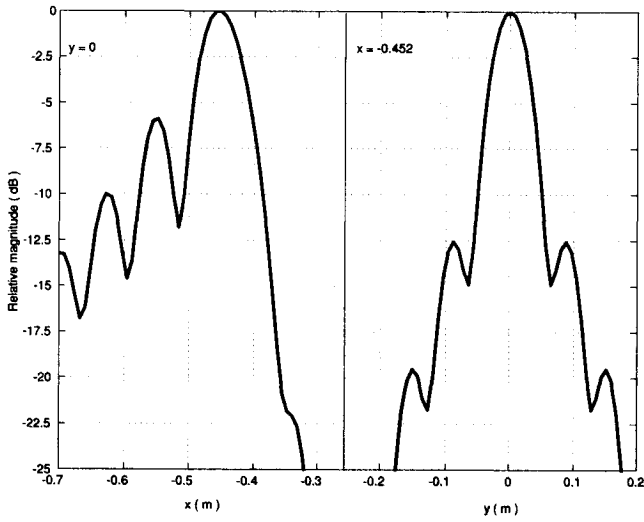


Figure 6.7: Power distribution along two orthogonal lines crossing the maximum of the focal spot.

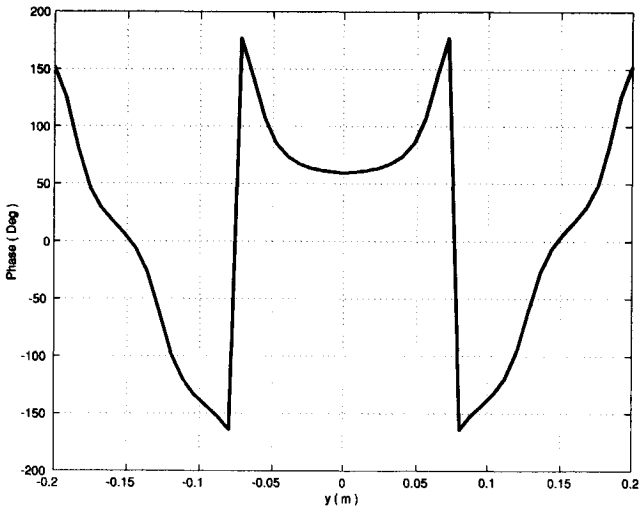


Figure 6.8: Phase distribution along the  $y$ -axis.

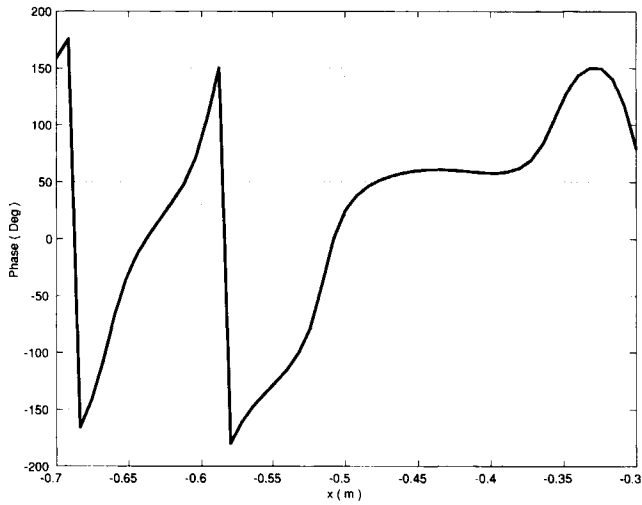


Figure 6.9: Phase distribution along the  $x$ -axis.

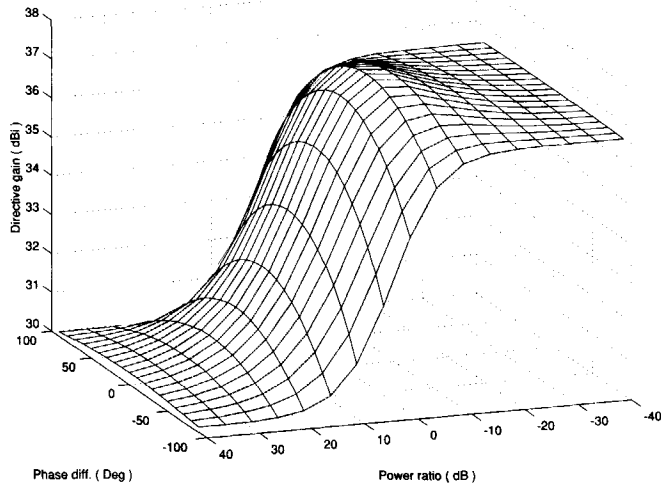


Figure 6.10: The optimum directive gain versus power ratio and phase difference between two dielectric rod antennas in the focal spot.

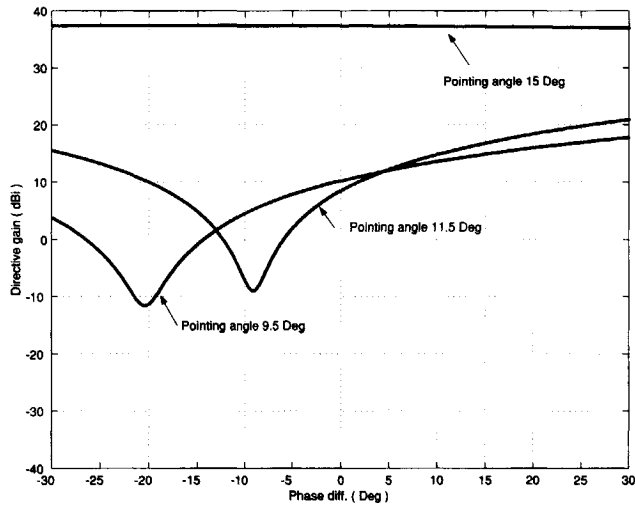


Figure 6.11: Directive gain versus phase difference between the two dielectric rod antennas for different pointing angles.

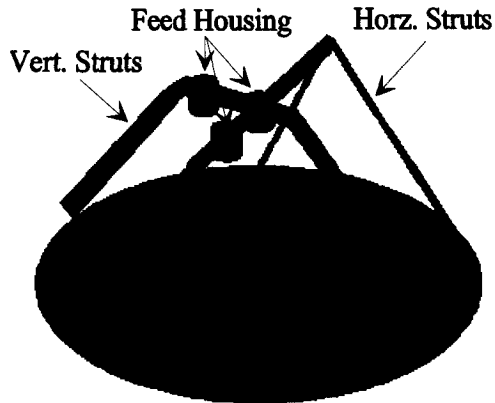


Figure 6.12: Discretized geometry used for blockage calculations.



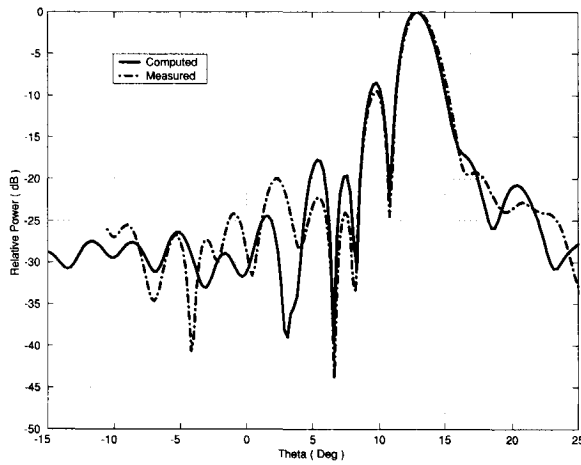


Figure 6.13: Far-field pattern of the TARA reflector antenna when Feed (1) is excited and Feed (2) is terminated in a matched load (Mutual coupling and blockage included).

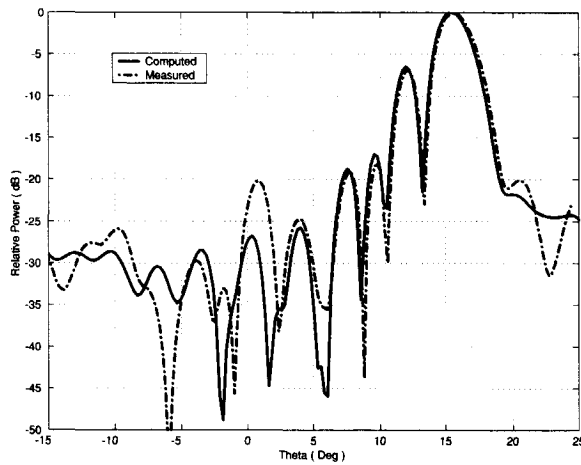


Figure 6.14: Far-field pattern of the TARA reflector antenna when Feed (2) is excited and Feed (1) is terminated in a matched load (Mutual coupling and blockage included).

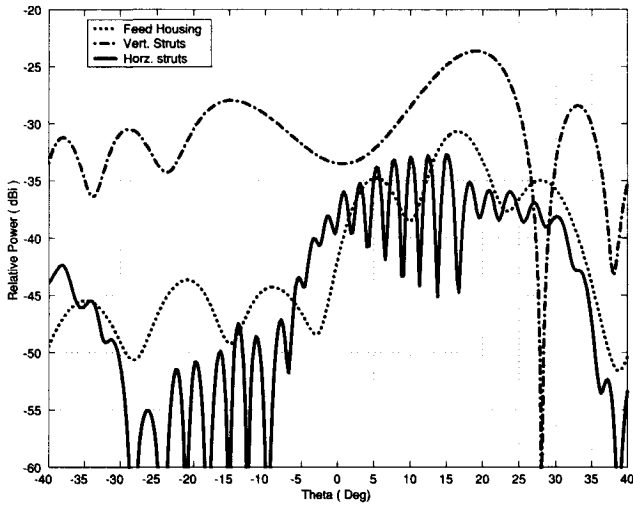


Figure 6.15: Contributions to the far-field due to individual blocking structures.

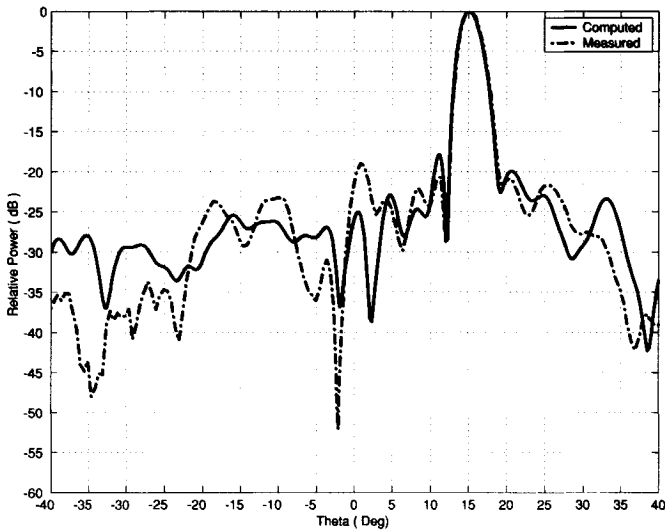


Figure 6.16: The TARA 15° scanned beam including mutual coupling and blockage.

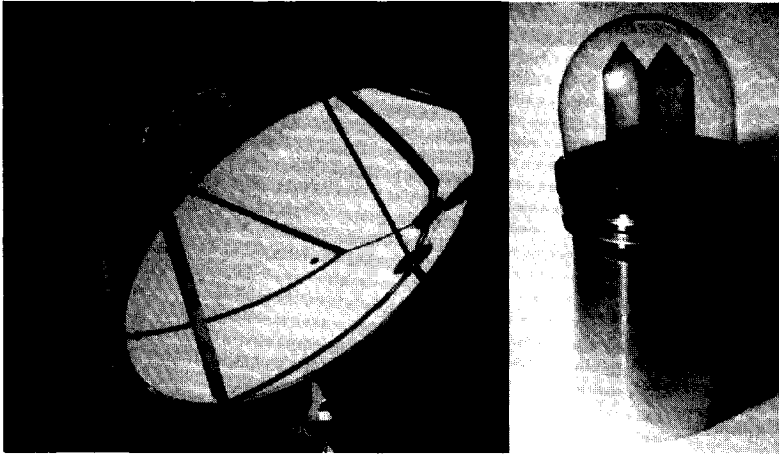


Figure 6.17: Left: The TARA antenna system. Right: The offset focal plane array.



Figure 6.18: The Transportable Atmospheric Radar (TARA).



## References

- [1] S. Heijnen and L.P. Ligthart, "*TARA: Transportable Atmospheric Radar*", European Microwave Conf. Proc., pp. 61, October 1998, The Netherlands.
- [2] A.W. Love, "*Reflector Antennas*", IEEE Press 1978.
- [3] Y.T.Lo and S.W. Lee, "*Antenna Handbook*", Van Nostrand Reinhol Company, New York 1988.
- [4] F.R. Gantmacher, "*The Theory of Matrices*", vol. I, Chelsea Publishing Company, New York, 1959.
- [5] D.K. Cheng, "*Optimization Techniques for Antenna Arrays*", Proceedings of the IEEE, vol 59, No. 12, pp. 1664-1674, December 1971.
- [6] V. Hombach and H. Thielen, "*Shadow Method for Estimating the Strut Influence in Paraboloidal Antennas*", Electronics Letters, vol. 20, No. 19, pp. 792-793, 13<sup>th</sup> September 1984.
- [7] P.S. Kildal, E. Olsen and J.A. Aas, "*Losses, Sidelobes, and Cross-Polarization Caused by Feed-Support Struts in Reflector Antennas: Design Curves*", IEEE AP-36, pp. 182-190, February 1988.

- 
- [8] L.C. Silva and L.M.D. Henriques, "Analysis of Scattering by Cylindrical Struts of Arbitrary Cross Section", Electronics Letters, vol. 21, No. 1, pp. 42-44, 3<sup>th</sup> January 1985.
- [9] K.M. Keen, "A Measurement Technique for Modeling the Effects of Feed Support Struts on Large Reflector Antennas", IEEE Trans. Antennas and Propagat., vol. AP-28, pp. 562-564, July 1980.
- [10] L.P. Ligthart and L.R. Nieuwkerk, "Studies of Precipitation Processes in the Troposphere Using an FM-CW Radar", Journal of Atmospheric and Oceanic Technology, Vol. 6, No. 5, pp. 798-808, October 1989.
- [11] C.A. Balanis, "Antenna Theory, Analysis and Design", John Wiley & Sons Inc., New York 1982.
- [12] P. Aubry, P. Hakkaart, J.H. Zijderveld and L.P. Ligthart, "Implementation of an Outdoor Far-Field Measurement System at IRCTR", Proc. 28th European Microwave Conf., vol. 2, pp. 549-552, Amsterdam 1998, The Netherlands.

# Chapter 7

## Conclusions and discussion

### 7.1 Discussion of research

In this dissertation, a complete and accurate design and analysis procedure is provided for multiple-beam reflector antennas using arrays of dielectric rods. It is demonstrated that the miniaturized dielectric rod antenna is a good reflector feed-array element because it can produce a relatively high gain although it has a small cross section so that feed elements can be packed closely together. This makes it possible to design arrays with an inter-element spacing in the order of half a wavelength without a serious degradation of the array performances. Aspects related to the miniaturization process, the radiation mechanism and the electromagnetic model of a single dielectric rod antenna and the analysis of the mutual coupling for arrays with very small inter-element spacing are all addressed in this work. The array of miniaturized dielectric rod antennas is employed to improve the off-axis beam switching capabilities of conventional reflector antennas. The novel hybrid reflector array-feed design permits a full sampling of the focal field distribution in the receive case and significantly improves the scanned beam patterns in the transmit case. The feed-array synthesis method adopted in this research takes into account mutual coupling between the dielectric rods, losses in the

beam-forming network and blockage due to the metallic feed housing and the struts which are required for mechanical stability and mounting purposes.

*In Chapter 2*, a formulation is presented for the aperture admittance and the far-field radiation pattern for highly miniaturized dielectric-filled waveguide antennas mounted on an infinite ground plane. The generalized scattering matrix approach is used to model the antenna's internal structure (i.e. discontinuities and matching devices). Sequential scattering mechanisms are taken into account by using a numerically stable direct cascading process, involving scattering matrices only. A variational expression for the aperture admittance is developed that uses reaction integrals and spectral-field representations. A novel expression for the aperture admittance, including higher-order excitations and their mutual interactions, is derived. The radiation mechanism of highly miniaturized apertures is studied thoroughly and new results are given. Different means of increasing the radiation efficiency are presented and the advantages and disadvantages are discussed. Measurements were performed on different antenna configurations and the good agreement between theory and experiment demonstrates the accuracy of the model.

*Chapter 3* is devoted to the development of a 3-D diagnostic and design tool for analyzing and improving the radiation characteristics of dielectric-filled waveguide antennas. The obtained code enabled the detailed design and further refinement of the outer metallic profile of the waveguide antenna. Using the equivalence principle and boundary conditions a set of integral equations is obtained with surface electric and magnetic currents as the unknowns. These coupled integral equations are solved by the MoM to yield the surface currents, from which the radiation pattern is calculated. The electromagnetic field inside the waveguide is represented by means of the waveguide modal decomposition derived in Chapter 2. The electric current density is expanded in terms of vector rooftop basis functions defined over triangular patches. The magnetic current density is expanded using transversal waveguide modal func-



tions defined over the aperture. The code was implemented on a massively parallel computer system (CRAY J90se) supported by the Delft University of Technology. A number of numerical examples are presented and results are given in the form of induced currents distribution and far-field patterns. The presented results indicate that an antenna design that is improved with respect to gain, side lobes, cross polarization and back lobe can be obtained by optimizing the external corrugation profile on the metallic structure around the waveguide. A single dielectric filled waveguide antenna was then built and tested. The excellent agreement between simulated and measured antenna performances (pattern and reflection coefficient) demonstrate the accuracy and robustness of the formulation.

*In Chapter 4*, a rigorous technique based on a hybrid-iterative MoM is proposed for analyzing dielectric rod antennas with arbitrary 3-D shape. The method takes into account the launcher (waveguide feed) and can handle arbitrary shaped dielectric bodies. When one wants to optimize dielectric rod antennas, many control parameters must be taken into account, and often these conflict. The present numerical code allows the investigation of their effects. In general any "geometry" can be numerically analyzed and optimized. However, it should be stressed for completeness that the computational cost of the method is high for complex structures and with the present formulation the method would be limited to very large computer platforms. Further work on techniques that speed up the computational scheme should be done. Three different antenna geometries were investigated: a uniform dielectric section with terminal tapering, a cut-wedge configuration, and a wedge configuration. The results indicate that by properly shaping the dielectric body, improvements can be achieved in side-lobe level and cross-polar performance. The general design procedure of dielectric rod antennas is reviewed and a detailed description is given for an optimized prototype operating at S-band. The prototype was constructed and the experimental data were used to validate the numerical code. Excellent agreement is observed

between the proposed model and the experimental data.

*In Chapter 5*, the Minimum Scattering Antenna (MSA) theory is used to predict the effect of mutual coupling between two identical dielectric rod antennas. To the author's knowledge this is the first time such a technique has been applied with success to dielectric rod antennas. Although dielectric rod antennas do not belong to the class of MSAs, we have found that by neglecting the multiple scattering between the two antenna elements one can still approximate the free-space coupling between dielectric rod antennas by a coupling between two MSAs. This resulted in an expression for the mutual impedance which involves only the radiation pattern of a single dielectric rod antenna when isolated in free space. A number of examples were treated and a comparison with measurement results was provided. The presented examples include different inter-element spacings and different array excitations (symmetrical and asymmetrical). A good agreement was observed between theory and experiment, even for asymmetrical excited arrays and arrays having small separation distances. In cases where multiple reflections between the array elements are strong, the approximations made are no longer valid and a different approach must be sought. In the case of finite arrays of dielectric rod antennas, one can use the numerical method developed in Chapter 4 to analyze the mutual coupling effects accurately.

*In Chapter 6*, a technique was presented for the synthesis and analysis of finite arrays of miniaturized dielectric rod antennas that are used to improve the scan capabilities of multiple-beam reflector antennas. The synthesis method includes mutual coupling in the array environment and permits an accurate determination of the array geometry, location and excitations. A novel array design based on miniaturized dielectric rod antennas was used to achieve a better sampling of the field distribution in the focal region in the receive situation and to improve the radiation pattern in the transmit situation. An analytical expression was used to find the array excitations which maximize the directive gain at a given angular direction. This method first

compensates for the mutual coupling matrix and then performs a conjugate matching to the far field from each array element. The obtained complex array excitations give the best possible gain achievable for a fixed array geometry. Further tuning of the phase of the individual elements permits a lowering of the near side lobe levels without seriously diminishing the maximum directive gain. In the design of feed arrays for reflector antennas, aperture blockage caused by struts and feed housing is very crucial. The blockage causes a gain drop and an increase in the level of the near side lobes. A numerical method based on a combination of Physical Optics and Method of Moment was used to analyze the aperture blockage caused by large metallic structures of arbitrary shape positioned in front of a large reflector antenna system. The scattered field from different blocking metallic parts can be computed separately and the results may be used to design supporting structures which are both mechanically stable and at the same time electrically "invisible" in some angular space regions.

## 7.2 Main conclusions

- The electromagnetic models and the array synthesis method presented in this dissertation were applied with success in the design and analysis of the novel feed system of the transportable atmospheric radar (TARA), which was realized at full scale at the Delft University and is at the moment fully operational.
- The design procedures and the techniques used to model a single miniaturized dielectric rod antenna and an antenna in an array environment have been described in detail.
- A miniaturized dielectric rod antenna design with exceptionally good low input loss, high gain and low mutual coupling levels has been realized.
- It is believed that the miniaturized dielectric rod antenna, the physics of which

was discussed in this work, is a very good candidate for a wide variety of array applications.

### 7.3 Implications of research

In this section recommendations are made for future research. They concern two main subjects:

The Hybrid surface/volume MoM method is a robust flexible electromagnetic analysis tool suitable for many applications, like antenna-design, simulation of ground-penetrating radar scenarios, development of antennas for mobile telecommunications, ...etc. Because of the large area of application of such a technique, further work is recommended especially on improving the efficiency of the implementation of the method, development of a machine-user interface, and making it commercially available.

The miniaturized dielectric rod antenna is a good candidate for many applications: smart arrays for mobile telecommunications, polarimetric feed systems for satellite antennas, radars for air safety (bird detection), ...etc. Additional studies are needed on the theoretical and experimental characterization of the dielectric rod antenna behaviour, especially at the high frequencies (millimeter-waves). Investigations should be carried out on antenna matching, the use of different excitation methods and the use of different materials.

Finally, this Ph.D. study has contributed to the realization of a unique transportable FM-CW radar with a sophisticated antenna system. The antennas developed in this thesis allow accurate polarimetric measurements of meteorological targets and 3-D wind profiles. This permits further research on the physics of the atmosphere. The TARA system is currently involved in a joint European remote sensing project. Measurement campaigns are planned for the next 5-10 years.

# Appendix A

## Expressions for admittance integral and matching condition

### A.1 Derivation of scattering matrix of general step

In this section, the scattering matrix  $S$  of a general step discontinuity is derived. First, we write the linear system of Eq. (2.17) as follows

$$\begin{aligned}\mathbf{a}_1 + V^T \mathbf{a}_2 &= \mathbf{b}_1 + V^T \mathbf{b}_2, \\ V \mathbf{a}_1 - \mathbf{a}_2 &= -V \mathbf{b}_1 + \mathbf{b}_2,\end{aligned}\tag{A.1}$$

where  $\mathbf{a}_1 = \begin{bmatrix} a^{1,TE} \\ a^{1,TM} \end{bmatrix}$ ,  $\mathbf{a}_2 = \begin{bmatrix} a^{2,TE} \\ a^{2,TM} \end{bmatrix}$ ,  $\mathbf{b}_1 = \begin{bmatrix} b^{1,TE} \\ b^{1,TM} \end{bmatrix}$  and  $\mathbf{b}_2 = \begin{bmatrix} b^{2,TE} \\ b^{2,TM} \end{bmatrix}$ . The S-matrix representation of a linear network is defined by

$$\begin{aligned}\mathbf{b}_1 &= S_{11} \mathbf{a}_1 + S_{12} \mathbf{a}_2, \\ \mathbf{b}_2 &= S_{21} \mathbf{a}_1 + S_{22} \mathbf{a}_2,\end{aligned}\tag{A.2}$$

where  $\mathbf{a}_1$  and  $\mathbf{a}_2$  contain the amplitudes of incident waves at port 1 and port 2 respectively and  $\mathbf{b}_1$  and  $\mathbf{b}_2$  contain the amplitudes of outgoing waves at port 1 and port 2

respectively. The sub-matrices  $S_{11}$  and  $S_{21}$  can be found after solving Eq. (A.1) for the case  $\mathbf{a}_2 = 0$ ; we then have

$$\begin{aligned}\mathbf{a}_1 &= \mathbf{b}_1 + \mathbf{V}^T \mathbf{b}_2, \\ \mathbf{V} \mathbf{a}_1 &= -\mathbf{V} \mathbf{b}_1 + \mathbf{b}_2,\end{aligned}\tag{A.3}$$

Solving for  $\mathbf{b}_2$  yields

$$\mathbf{b}_2 = \mathbf{V} [\mathbf{a}_1 + \mathbf{b}_1] = \mathbf{V} [\mathbf{I} + \mathbf{S}_{11}] \mathbf{a}_1,\tag{A.4}$$

where we have used the relation ( $\mathbf{b}_1 = -\mathbf{S}_{11} \mathbf{a}_1$  when  $\mathbf{a}_2 = 0$ ). Eq. (A.4), when inserted into Eq. (A.3), gives

$$\mathbf{a}_1 = \mathbf{b}_1 + \mathbf{V}^T \mathbf{V} [\mathbf{a}_1 + \mathbf{b}_1] \implies \mathbf{b}_1 = [\mathbf{I} + \mathbf{V}^T \mathbf{V}]^{-1} [\mathbf{I} - \mathbf{V}^T \mathbf{V}] \mathbf{a}_1.\tag{A.5}$$

Hence,

$$\begin{aligned}\mathbf{S}_{11} &= [\mathbf{I} + \mathbf{V}^T \mathbf{V}]^{-1} [\mathbf{I} - \mathbf{V}^T \mathbf{V}], \\ \mathbf{S}_{21} &= \mathbf{V} [\mathbf{I} + \mathbf{S}_{11}].\end{aligned}\tag{A.6}$$

The sub-matrices  $\mathbf{S}_{12}$  and  $\mathbf{S}_{22}$  can be found in a similar manner to  $\mathbf{S}_{11}$  and  $\mathbf{S}_{21}$  by letting  $\mathbf{a}_1 = 0$  and solving Eq. (A.1). We obtain

$$\begin{aligned}\mathbf{S}_{12} &= \mathbf{S}_{21}^T, \\ \mathbf{S}_{22} &= \mathbf{V} \mathbf{S}_{12} - \mathbf{I}.\end{aligned}\tag{A.7}$$

## A.2 Evaluation of the mutual admittance integral

This appendix deals with aspects related to the evaluation of the following integral

$$Y_{m,n} = -j^{m+n} nm \int_{-\infty}^{\infty} \int_{-\infty}^{\infty} \frac{2ab(k^2 - k_x^2) \sin^2(k_y \frac{b}{2}) \cos^2(k_x \frac{a}{2})}{\omega \mu k_z (k_y \frac{b}{2})^2 [(n\pi)^2 - (k_x a)^2] [(m\pi)^2 - (k_x a)^2]} dk_x dk_y.\tag{A.8}$$

This integral plays an essential role in the computation of the aperture admittance as formulated in Chapter 2. If we apply Parseval's theorem and let

$$\tilde{F}_1(k_x, k_y) = \frac{4\pi^2}{k_z},\tag{A.9}$$

$$\tilde{F}_2^{m,n}(k_x, k_y) = -j^{m+n}nm \frac{2ab(k^2 - k_x^2) \sin^2(k_y \frac{b}{2}) \cos^2(k_x \frac{a}{2})}{\omega\mu (k_y \frac{b}{2})^2 [(n\pi)^2 - (k_x a)^2] [(m\pi)^2 - (k_x a)^2]}, \tag{A.10}$$

then we obtain

$$Y_{m,n} = \frac{1}{4\pi^2} \int_{-\infty}^{\infty} \int_{-\infty}^{\infty} \tilde{F}_1(k_x, k_y) \tilde{F}_2^{m,n}(k_x, k_y) dk_x dk_y = \int_{-\infty}^{\infty} \int_{-\infty}^{\infty} f_1(x, y) f_2^{m,n}(x, y) dx dy, \tag{A.11}$$

where  $f_1(x, y)$ , and  $f_2^{m,n}(x, y)$  are the inverse Fourier transform of  $\tilde{F}_1(k_x, k_y)$ , and  $\tilde{F}_2^{m,n}(k_x, k_y)$ , respectively. The first function can be evaluated directly after application of the stationary phase point method

$$f_1(x, y) = 2\pi j \frac{\exp(-jk_0 \sqrt{x^2 + y^2})}{\sqrt{x^2 + y^2}}. \tag{A.12}$$

Before computing the second function  $f_2^{m,n}$ , we define two new functions  $f^{m,n}(x)$  and  $g(y)$  as follows

$$f_2^{m,n}(x, y) = \frac{2a}{\pi^2 b \omega \mu} g(y) f^{m,n}(x), \tag{A.13}$$

where

$$g(y) = \int_{-\infty}^{\infty} \frac{\sin^2(k_y b/2)}{k_y^2} \exp(-jk_y y) dk_y, \tag{A.14}$$

and

$$f^{m,n}(x) = \int_{-\infty}^{\infty} \frac{-j^{m+n}nm(k^2 - k_x^2) \cos^2(k_x \frac{a}{2})}{[(n\pi)^2 - (k_x a)^2] [(m\pi)^2 - (k_x a)^2]} \exp(-jk_x x) dk_x, \tag{A.15}$$

The function  $g(y)$  can be written in terms of complex exponential functions only

$$g(y) = - \int_{-\infty}^{\infty} \frac{\exp(jk_y (b - y)) + \exp(-jk_y (b + y)) - 2 \exp(-jk_y y)}{4k_y^2} dk_y. \tag{A.16}$$

This integration is carried out in the complex  $k_y$  plane. The exponential functions should remain finite; this implies conditions on the integration path in the complex plane. The double singularity at zero is avoided during the integration. By using the Cauchy's theorem, we get the following result

$$g(y) = \frac{\pi}{2} (b - |y|), \quad |y| < b. \tag{A.17}$$

Similar we find for  $f^{m,n}(x)$

$$f^{m,n}(x) = \begin{cases} \frac{-j^{n+m}}{2\pi^2 a(n^2-m^2)} \left( \left[ k_0^2 - \left( \frac{m\pi}{a} \right)^2 \right] n \sin \frac{m\pi|x|}{a} - \left[ k_0^2 - \left( \frac{n\pi}{a} \right)^2 \right] m \sin \frac{n\pi|x|}{a} \right) \\ |x| < a, n \neq m, \text{ and } n, m \text{ odd} \\ \frac{1}{4\pi^2 a n} \left( \frac{1}{\pi} \left[ k_0^2 + \left( \frac{n\pi}{a} \right)^2 \right] \sin \frac{n\pi|x|}{a} + \frac{n}{a} \left[ k_0^2 - \left( \frac{n\pi}{a} \right)^2 \right] (a - |x|) \cos \frac{n\pi|x|}{a} \right) \\ |x| < a, n = m, \text{ and } n, m \text{ odd} \end{cases} \quad (\text{A.18})$$

After replacing Eq. (A.12), Eq. (A.17) and Eq. (A.18) into Eq. (A.11) we finally get

$$Y_{m,n} = j \frac{2a}{b\omega\mu} \int_{-b}^b \int_{-a}^a (b - |y|) f^{m,n}(|x|) \frac{\exp(-jk_0\sqrt{x^2+y^2})}{\sqrt{x^2+y^2}} dx dy. \quad (\text{A.19})$$

Since the kernel of Eq. (A.19) is an even function with respect to  $x$  and  $y$ , it can be simplified further. We obtain

$$Y_{m,n} = j \frac{8a}{b\omega\mu} \int_0^b \int_0^a (b - y) f^{m,n}(x) \frac{\exp(-jk_0\sqrt{x^2+y^2})}{\sqrt{x^2+y^2}} dx dy. \quad (\text{A.20})$$

This integral can be evaluated numerically using standard quadrature rules.

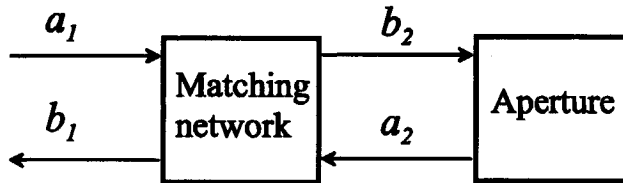


Figure A.1: Radiating aperture and matching network.

### A.3 Aperture matching condition

The aim of this subsection is to derive a matching condition for dielectric filled waveguide antennas. Let  $S$  denote the scattering matrix of a lossless two-port matching network. We may write



$$\begin{aligned} b_1 &= S_{11}a_1 + S_{12}a_2, \\ b_2 &= S_{21}a_1 + S_{22}a_2. \end{aligned} \quad (\text{A.21})$$

Making use of the diagram of Fig. A.1, we can express the aperture reflection coefficient as

$$\Gamma = \frac{a_2}{b_2}. \quad (\text{A.22})$$

The matching network is assumed to be located far enough from the aperture discontinuity. The higher-order modes, excited at the aperture, will be sufficiently attenuated when they reach the matching device and one can simply use 2-port network representations. The reflection coefficient at the input of the matching device is given by

$$\frac{b_1}{a_1} = S_{11} + S_{12} \frac{a_2}{a_1}, \quad (\text{A.23})$$

substituting Eq. (A.22) into the second part of Eq. (A.21), yields

$$\Gamma b_2 = a_2 = \Gamma (S_{21}a_1 + S_{22}a_2),$$

and hence

$$\frac{a_2}{a_1} = \frac{\Gamma S_{21}}{1 - \Gamma S_{22}}, \quad (\text{A.24})$$

When this result is used in Eq. (A.23), we obtain

$$\frac{b_1}{a_1} = S_{11} + \frac{\Gamma S_{21} S_{12}}{1 - \Gamma S_{22}} = \frac{S_{11} - \Gamma (S_{11} S_{22} - S_{12} S_{21})}{1 - \Gamma S_{22}}. \quad (\text{A.25})$$

Since the matching device is represented by a symmetric lossless two-port network, the following properties are valid

$$\begin{aligned} |S_{11}| &= |S_{22}|, \\ S_{12} &= S_{21}, \\ S_{11} S_{12}^* + S_{12} S_{22}^* &= 0, \\ |S_{12}| &= \sqrt{1 - |S_{11}|^2}. \end{aligned} \quad (\text{A.26})$$

Before we can derive the matching condition, we need to prove an indispensable expression. This is done using the properties mentioned above.

$$\begin{aligned}
 (S_{11}S_{22} - S_{12}S_{21}) S_{22}^* &= S_{11} |S_{11}|^2 - S_{12} (S_{12}S_{22}^*), \\
 &= S_{11} |S_{11}|^2 + S_{12} (S_{11}S_{12}^*), \\
 &= S_{11} (|S_{11}|^2 + |S_{12}|^2), \\
 &= S_{11} (|S_{11}|^2 + (1 - |S_{11}|^2)), \\
 &= S_{11}.
 \end{aligned} \tag{A.27}$$

By applying this equality to the input reflection coefficient, given by Eq. (A.25), we obtain

$$\frac{b_1}{a_1} = \det[S] \frac{S_{22}^* - \Gamma}{1 - \Gamma S_{22}}, \tag{A.28}$$

where  $\det[S] = (S_{11}S_{22} - S_{12}S_{21})$ .

It is obvious that Eq. (A.28) is zero when the following condition is fulfilled:

$$S_{22}^* = \Gamma. \tag{A.29}$$

## Appendix B

# Derivation of the MOM matrix for aperture on 3-D metallic body

### B.1 Entries of the sub-matrix $\mathbf{Z}^{c-c}$

The entries of the sub-matrix  $\mathbf{Z}^{c-c}$  are found after evaluation of the following expression

$$j\omega \langle \mathbf{f}_m, \mathbf{A} \rangle_{T\mathcal{R}_m^\pm} + \langle \mathbf{f}_m, \nabla \phi_e \rangle_{T\mathcal{R}_m^\pm} = \sum_n^N Z_{m,n}^{c-c} I_n, \quad m = 1, \dots, N \quad (\text{B.1})$$

substituting the basis functions  $\mathbf{f}_m$  by their expressions and taking the inner product gives

$$\begin{aligned} j\omega \langle \mathbf{f}_m, \mathbf{A} \rangle_{T\mathcal{R}_m^\pm} &= j\omega l_m \left\{ \frac{1}{2S_m^+} \int_{T\mathcal{R}_m^+} \mathbf{A}(\mathbf{r}') \cdot \boldsymbol{\rho}_m^+ dA' + \frac{1}{2S_m^-} \int_{T\mathcal{R}_m^-} \mathbf{A}(\mathbf{r}') \cdot \boldsymbol{\rho}_m^- dA' \right\}, \\ &\approx j\omega l_m \left\{ \frac{1}{2S_m^+} \mathbf{A}(\mathbf{r}_m^{c,+}) \cdot \boldsymbol{\rho}_m^{c,+} \int_{T\mathcal{R}_m^+} dA' + \frac{1}{2S_m^-} \mathbf{A}(\mathbf{r}_m^{c,-}) \cdot \boldsymbol{\rho}_m^{c,-} \int_{T\mathcal{R}_m^-} dA' \right\}, \\ &\approx j\omega l_m \left[ \frac{1}{2} \mathbf{A}(\mathbf{r}_m^{c,+}) \cdot \boldsymbol{\rho}_m^{c,+} + \frac{1}{2} \mathbf{A}(\mathbf{r}_m^{c,-}) \cdot \boldsymbol{\rho}_m^{c,-} \right], \quad m = 1, \dots, N \end{aligned} \quad (\text{B.2})$$

**208 B. Derivation of the MOM matrix for aperture on 3-D metallic body**

$$\begin{aligned}
 \langle \mathbf{f}_m, \nabla \phi_e \rangle_{\mathcal{TR}_m^\pm} &= \int_{\mathcal{TR}_m} \nabla \phi_e(\mathbf{r}') \cdot \mathbf{f}_m(\mathbf{r}') dA' = \int_{\mathcal{TR}_m} \nabla \cdot (\phi_e \mathbf{f}_m) dA' - \int_{\mathcal{TR}_m} \phi_e (\nabla \cdot \mathbf{f}_m) dA', \\
 &= - \int_{\mathcal{TR}_m} \phi_e (\nabla \cdot \mathbf{f}_m) dA' = -l_m \left\{ \frac{1}{\mathcal{S}_m^\pm} \int_{\mathcal{TR}_m^\pm} \phi_e(\mathbf{r}') dA' - \frac{1}{\mathcal{S}_m^-} \int_{\mathcal{TR}_m^-} \phi_e(\mathbf{r}') dA' \right\}, \\
 &\approx l_m [\phi_e(\mathbf{r}_m^{c,-}) - \phi_e(\mathbf{r}_m^{c,+})], \quad m = 1, \dots, N
 \end{aligned} \tag{B.3}$$

The vector potential  $\mathbf{A}$  is given by

$$\begin{aligned}
 \mathbf{A}(\mathbf{r}_m^{c,\pm}) &= \mu_0 \int_S \mathbf{J}_S(\mathbf{r}') G(\mathbf{r}_m^{c,\pm}, \mathbf{r}') dA', \\
 &\approx \mu_0 \sum_n^N \left( \int_{\mathcal{TR}_n} \mathbf{f}_n G dA' \right) I_n = \sum_n^N \mathbf{A}_{m,n}^\pm I_n, \quad m = 1, \dots, N
 \end{aligned} \tag{B.4}$$

The scalar potential  $\phi_e$  is given by

$$\begin{aligned}
 \phi_e(\mathbf{r}_m^{c,\pm}) &= -\frac{1}{j\omega\epsilon_0} \int_S (\nabla' \cdot \mathbf{J}_S(\mathbf{r}')) G(\mathbf{r}_m^{c,\pm}, \mathbf{r}') dA', \\
 &\approx -\frac{1}{j\omega\epsilon_0} \sum_n^N \left( \int_{\mathcal{TR}_n} (\nabla' \cdot \mathbf{f}_n) G dA' \right) I_n = \sum_n^N \phi_{m,n}^\pm I_n, \quad m = 1, \dots, N
 \end{aligned} \tag{B.5}$$

where

$$\begin{aligned}
 G(\mathbf{r}_m^{c,\pm}, \mathbf{r}') &= \frac{\exp(-jk_0 |\mathbf{r}_m^{c,\pm} - \mathbf{r}'|)}{4\pi |\mathbf{r}_m^{c,\pm} - \mathbf{r}'|}, \quad \mathbf{A}_{m,n}^\pm = \mu_0 \int_{\mathcal{TR}_n} \mathbf{f}_n(\mathbf{r}') \frac{\exp(-jk_0 |\mathbf{r}_m^{c,\pm} - \mathbf{r}'|)}{4\pi |\mathbf{r}_m^{c,\pm} - \mathbf{r}'|} dA', \\
 \phi_{m,n}^\pm &= -\frac{1}{4\pi j\omega\epsilon_0} \int_{\mathcal{TR}_n} (\nabla' \cdot \mathbf{f}_n(\mathbf{r}')) \frac{\exp(-jk_0 |\mathbf{r}_m^{c,\pm} - \mathbf{r}'|)}{|\mathbf{r}_m^{c,\pm} - \mathbf{r}'|} dA'.
 \end{aligned} \tag{B.6}$$

Finally we obtain for the entries of the sub-matrix  $Z^{c-c}$  with size  $[N \times N]$

$$Z_{m,n}^{c-c} = l_m \left[ \frac{j\omega}{2} (\mathbf{A}_{m,n}^+ \cdot \boldsymbol{\rho}_m^{c,+} + \mathbf{A}_{m,n}^- \cdot \boldsymbol{\rho}_m^{c,-}) + \phi_{m,n}^- - \phi_{m,n}^+ \right], \quad m, n = 1, \dots, N \tag{B.7}$$

The integrals over  $\mathcal{TR}_n^\pm$  can be evaluated numerically using standard quadrature schemes.

## B.2 Entries of the sub-matrix $\mathbf{Z}^{c-a}$

The entries of the sub-matrix  $\mathbf{Z}^{c-a}$  are found after evaluation of the following expression

$$\langle \mathbf{f}_m, \mathbf{E}_{\text{ap}} \rangle_{\mathcal{S}} = \sum_l^{\text{NTE}} Z_{m,n}^{c-a,\text{TE}} (V_l^{\text{TE}} + V_l^{i,\text{TE}}) + \sum_l^{\text{NTM}} Z_{m,n}^{c-a,\text{TM}} (V_l^{\text{TM}} + V_l^{i,\text{TM}}), \quad m = 1, \dots, N \quad (\text{B.8})$$

where

$$\mathbf{E}_{\text{ap}} = -\frac{1}{\epsilon_0} \nabla \times \mathbf{F} - \frac{1}{2} \mathbf{n} \times \mathbf{K}_{\mathcal{S}}(\mathbf{r}), \quad (\text{B.9})$$

we may write

$$\langle \mathbf{f}_m, \mathbf{E}_{\text{ap}} \rangle_{\mathcal{S}} \approx \frac{l_m}{2} [\mathbf{E}_{\text{ap}}(\mathbf{r}_m^{c,+}) \cdot \boldsymbol{\rho}_m^{c,+} + \mathbf{E}_{\text{ap}}(\mathbf{r}_m^{c,-}) \cdot \boldsymbol{\rho}_m^{c,-}], \quad (\text{B.10})$$

and

$$\mathbf{E}_{\text{ap}}(\mathbf{r}_m^{c,\pm}) = - \int_{\mathcal{S}_{\text{ap}}} \nabla G(\mathbf{r}', \mathbf{r}_m^{c,\pm}) \times \mathbf{K}_{\mathcal{S}}(\mathbf{r}') dA' - \frac{1}{2} \mathbf{n} \times \mathbf{K}_{\mathcal{S}}(\mathbf{r}_m^{c,\pm}). \quad (\text{B.11})$$

Using the following properties

$$\nabla G(\mathbf{r}', \mathbf{r}_m^{c,\pm}) = -(jk_0 + \frac{1}{R_m^\pm}) \frac{\exp(-jk_0 R_m^\pm)}{R_m^\pm} \hat{\mathbf{i}}_{R_m^\pm}, \quad R_m^\pm = |\mathbf{r}_m^{c,\pm} - \mathbf{r}'|, \quad \hat{\mathbf{i}}_{R_m^\pm} = \frac{\mathbf{r}_m^{c,\pm} - \mathbf{r}'}{R_m^\pm}, \quad (\text{B.12})$$

results

$$\mathbf{E}_{\text{ap}}(\mathbf{r}_m^{c,\pm}) = \int_{\mathcal{S}_{\text{ap}}} (jk_0 + \frac{1}{R_m^\pm}) \frac{\exp(-jk_0 R_m^\pm)}{4\pi R_m^\pm} \hat{\mathbf{i}}_{R_m^\pm} \times \mathbf{K}_{\mathcal{S}}(\mathbf{r}') dA' - \frac{1}{2} \mathbf{n} \times \mathbf{K}_{\mathcal{S}}(\mathbf{r}_m^{c,\pm}). \quad (\text{B.13})$$

The magnetic current density is defined as

$$\mathbf{K}_{\mathcal{S}}(\mathbf{r}) = \sum_l^{\text{NTE}} \mathbf{g}_l^{\text{TE}}(\mathbf{r}) (V_l^{\text{TE}} + V_l^{i,\text{TE}}) + \sum_l^{\text{NTM}} \mathbf{g}_l^{\text{TM}}(\mathbf{r}) (V_l^{\text{TM}} + V_l^{i,\text{TM}}), \quad (\text{B.14})$$

where

$$V_l^{\text{TE;TM}} = \frac{b_l^{\text{TE;TM}}}{\sqrt{Y_l^{\text{TE;TM}}}}, \quad V_l^{i,\text{TE;TM}} = \frac{a_l^{\text{TE;TM}}}{\sqrt{Y_l^{\text{TE;TM}}}}, \quad \mathbf{g}_l^{\text{TE;TM}}(\mathbf{r}) = -\mathbf{n} \times \mathbf{e}_l^{\text{TE;TM}}(\mathbf{r}). \quad (\text{B.15})$$

After substituting Eq. (B.14) into Eq. (B.13) we obtain

$$\mathbf{E}_{\text{ap}}(\mathbf{r}_m^{c,\pm}) = \sum_l^{\text{NTE}} \mathbf{F}_{m,l}^{\pm,\text{TE}} (V_l^{\text{TE}} + V_l^{i,\text{TE}}) + \sum_l^{\text{NTM}} \mathbf{F}_{m,l}^{\pm,\text{TM}} (V_l^{\text{TM}} + V_l^{i,\text{TM}}), \quad (\text{B.16})$$

## 210 B. Derivation of the MOM matrix for aperture on 3-D metallic body

where

$$\mathbf{F}_{m,l}^{\pm, \text{TE}; \text{TM}} = \int_{S_{\text{ap}}} (jk_0 + \frac{1}{R_m^{\pm}}) \frac{\exp(-jk_0 R_m^{\pm})}{4\pi R_m^{\pm}} \hat{\mathbf{i}}_{R_m^{\pm}} \times \mathbf{g}_l^{\text{TE}; \text{TM}}(\mathbf{r}') dA' - \frac{1}{2} \mathbf{n} \times \mathbf{g}_l^{\text{TE}; \text{TM}}(\mathbf{r}_m^{c,\pm}). \quad (\text{B.17})$$

The entries of the sub-matrices  $Z^{c-a, \text{TE}}$  and  $Z^{c-a, \text{TM}}$  are found using Eqs. (B.8) and (B.16)

$$\begin{aligned} Z_{m,l}^{c-a, \text{TE}} &= \frac{lm}{2} \left[ \mathbf{F}_{m,l}^{+, \text{TE}} \cdot \boldsymbol{\rho}_m^{c,+} + \mathbf{F}_{m,l}^{-, \text{TE}} \cdot \boldsymbol{\rho}_m^{c,-} \right], \\ Z_{m,l}^{c-a, \text{TM}} &= \frac{lm}{2} \left[ \mathbf{F}_{m,l}^{+, \text{TM}} \cdot \boldsymbol{\rho}_m^{c,+} + \mathbf{F}_{m,l}^{-, \text{TM}} \cdot \boldsymbol{\rho}_m^{c,-} \right]. \end{aligned} \quad (\text{B.18})$$

Finally the sub-matrix  $Z^{c-a}$  is given by

$$Z^{c-a} = \begin{bmatrix} Z^{c-a, \text{TE}} & Z^{c-a, \text{TM}} \end{bmatrix}. \quad (\text{B.19})$$

Note that the size of  $Z^{c-a}$  is  $[N \times (\text{NTE} + \text{NTM})]$ .

### B.3 Entries of the sub-matrix $Z^{a-a}$

The entries of the sub-matrix  $Z^{a-a}$  are found using the following expression

$$\begin{aligned} \langle \mathbf{g}_m^{\text{TE}}, \mathbf{H}_{\text{wg}} \rangle_{S_{\text{ap}}} &= \int_{S_{\text{ap}}} \mathbf{g}_m^{\text{TE}}(\mathbf{r}) \cdot \mathbf{H}_{\text{wg}}(\mathbf{r}) dA, \quad m = 1, \dots, \text{NTE} \\ \langle \mathbf{g}_m^{\text{TM}}, \mathbf{H}_{\text{wg}} \rangle_{S_{\text{ap}}} &= \int_{S_{\text{ap}}} \mathbf{g}_m^{\text{TM}}(\mathbf{r}) \cdot \mathbf{H}_{\text{wg}}(\mathbf{r}) dA, \quad m = 1, \dots, \text{NTM} \end{aligned} \quad (\text{B.20})$$

The magnetic field  $\mathbf{H}_{\text{wg}}$  is given by

$$\mathbf{H}_{\text{wg}}(\mathbf{r}) = \sum_l^{\text{NTE}} \mathbf{g}_l^{\text{TE}}(\mathbf{r}) Y_l^{\text{TE}} (V_l^{\text{TE}} - V_l^{i, \text{TE}}) + \sum_l^{\text{NTM}} \mathbf{g}_l^{\text{TM}}(\mathbf{r}) Y_l^{\text{TM}} (V_l^{\text{TM}} - V_l^{i, \text{TM}}) \quad (\text{B.21})$$

After putting Eq. (B.21) into Eq. (B.20) and applying the orthogonality of the wave-guide modal functions we obtain

$$\begin{aligned} \langle \mathbf{g}_m^{\text{TE}}, \mathbf{H}_{\text{wg}} \rangle_{S_{\text{ap}}} &= \sum_l^{\text{NTE}} \delta_{m,l} Y_l^{\text{TE}} (V_l^{\text{TE}} - V_l^{i, \text{TE}}), \quad m = 1, \dots, \text{NTE} \\ \langle \mathbf{g}_m^{\text{TM}}, \mathbf{H}_{\text{wg}} \rangle_{S_{\text{ap}}} &= \sum_l^{\text{NTM}} \delta_{m,l} Y_l^{\text{TM}} (V_l^{\text{TM}} - V_l^{i, \text{TM}}), \quad m = 1, \dots, \text{NTM} \end{aligned} \quad (\text{B.22})$$

where  $\delta_{m,l} = 1$  if  $m = l$  and zero otherwise. From Eq. (B.22) we derive the sub-matrix  $Z^{a-a}$

$$Z^{a-a} = \begin{bmatrix} Z^{a-a,TE} & 0 \\ 0 & Z^{a-a,TM} \end{bmatrix} \tag{B.23}$$

where

$$\begin{aligned} Z_{m,l}^{a-a,TE} &= \delta_{m,l} Y_l^{TE} \\ Z_{m,l}^{a-a,TM} &= \delta_{m,l} Y_l^{TM} \end{aligned} \tag{B.24}$$

The sub-matrix  $Z^{a-a}$  is a square matrix with dimensions  $[(NTE+NTM) \times (NTE+NTM)]$ .

### B.4 Entries of the sub-matrix $Z^{a-c}$

The entries of the sub-matrix  $Z^{a-c}$  can be derived from

$$\begin{aligned} \langle \mathbf{g}_m^{TE}, \mathbf{J}_S \times \mathbf{n} \rangle_{S_{ap}} &= \int_{S_{ap}} \mathbf{g}_m^{TE}(\mathbf{r}) \cdot (\mathbf{J}_S(\mathbf{r}) \times \mathbf{n}) dA, \quad m = 1, \dots, NTE \\ \langle \mathbf{g}_m^{TM}, \mathbf{J}_S \times \mathbf{n} \rangle_{S_{ap}} &= \int_{S_{ap}} \mathbf{g}_m^{TM}(\mathbf{r}) \cdot (\mathbf{J}_S(\mathbf{r}) \times \mathbf{n}) dA, \quad m = 1, \dots, NTM \end{aligned} \tag{B.25}$$

where

$$\mathbf{J}_S(\mathbf{r}) = \sum_n^N \mathbf{f}_n(\mathbf{r}) I_n. \tag{B.26}$$

Putting Eq. (B.26) into Eq. (B.25) results in

$$\begin{aligned} \langle \mathbf{g}_m^{TE}, \mathbf{J}_S \times \mathbf{n} \rangle_{S_{ap}} &= \sum_n^N \left( \int_{S_{ap}} \mathbf{g}_m^{TE}(\mathbf{r}) \cdot (\mathbf{f}_n(\mathbf{r}) \times \mathbf{n}) dA \right) I_n, \quad m = 1, \dots, NTE \\ \langle \mathbf{g}_m^{TM}, \mathbf{J}_S \times \mathbf{n} \rangle_{S_{ap}} &= \sum_n^N \left( \int_{S_{ap}} \mathbf{g}_m^{TM}(\mathbf{r}) \cdot (\mathbf{f}_n(\mathbf{r}) \times \mathbf{n}) dA \right) I_n, \quad m = 1, \dots, NTM \end{aligned} \tag{B.27}$$

The sub-matrix  $Z^{a-c}$  is found to be

$$Z^{a-c} = \begin{bmatrix} Z^{a-c,TE} \\ Z^{a-c,TM} \end{bmatrix} \tag{B.28}$$

## 212 B. Derivation of the MOM matrix for aperture on 3-D metallic body

where

$$\begin{aligned} Z_{m,n}^{\text{a-c,TE}} &= \int_{\hat{S}_{\text{ap}}} \mathbf{g}_m^{\text{TE}}(\mathbf{r}) \cdot (\mathbf{f}_n(\mathbf{r}) \times \mathbf{n}) dA, \\ Z_{m,n}^{\text{a-c,TM}} &= \int_{\hat{S}_{\text{ap}}} \mathbf{g}_m^{\text{TM}}(\mathbf{r}) \cdot (\mathbf{f}_n(\mathbf{r}) \times \mathbf{n}) dA. \end{aligned} \tag{B.29}$$

The sub-matrix  $Z^{\text{a-c}}$  has dimensions  $[(\text{NTE}+\text{NTM}) \times \text{N}]$ .



## Appendix C

# Derivation of MoM matrix for dielectric rod antenna problem

This appendix is devoted to the numerical evaluation of the set of coupled integral equations derived in Chapter 4

$$\begin{aligned}
 -j\omega\mu_0 \int_{\mathcal{V}_{\text{diel}}} \mathbf{J}_V G dV' + \frac{1}{j\omega\epsilon_0} \int_{\mathcal{V}_{\text{diel}}} \nabla' \cdot \mathbf{J}_V \nabla G dV' - \int_S (j\omega\mu_0 G \mathbf{J}_S - \frac{1}{j\omega\epsilon_0} \nabla'_S \cdot \mathbf{J}_S \nabla G) dA' \\
 - \int_{\mathcal{S}_{\text{ap}}} \nabla \times G \mathbf{K}_S dA' = \mathbf{J}_V / (j\omega\kappa\hat{\epsilon}), \quad \mathbf{r} \in \mathcal{V}_{\text{diel}}
 \end{aligned} \tag{C.1}$$

$$\begin{aligned}
 -j\omega\mu_0 \mathbf{n} \times \int_{\mathcal{V}_{\text{diel}}} \mathbf{J}_V G dV' + \frac{1}{j\omega\epsilon_0} \mathbf{n} \times \int_{\mathcal{V}_{\text{diel}}} \nabla' \cdot \mathbf{J}_V \nabla G dV' \\
 - \mathbf{n} \times \int_S (j\omega\mu_0 G \mathbf{J}_S - \frac{1}{j\omega\epsilon_0} \nabla'_S \cdot \mathbf{J}_S \nabla G) dA' - \mathbf{n} \times \int_{\mathcal{S}_{\text{ap}}} \nabla \times G \mathbf{K}_S dA' \\
 = -\frac{1}{2} \mathbf{K}_S \chi_S, \quad \mathbf{r} \in \mathcal{S}
 \end{aligned} \tag{C.2}$$

$$\mathbf{n} \times \mathbf{H}_{\text{wg}} = \mathbf{J}_S, \quad \mathbf{r} \in \mathcal{S}_{\text{ap}} \tag{C.3}$$

## C.1 The discretized form of the integral equations

The electric surface current density  $\mathbf{J}_S$  is approximated using RWG's basis functions  $\mathbf{f}_n$ , defined over triangular patches, and is given by the following expansion

$$\mathbf{J}_S(\mathbf{r}) \approx \sum_n^{N_f} I_n \mathbf{f}_n(\mathbf{r}), \quad \mathbf{r} \in \mathcal{S} \quad (\text{C.4})$$

where  $\mathbf{f}_n$  is defined in Eq. (3.27). The magnetic surface current density  $\mathbf{K}_S$  is related to the field inside the waveguide, in Eq. (3.6), as

$$\mathbf{K}_S(\mathbf{r}) \approx \sum_n^{N_g} (V_n + V_n^i) \mathbf{g}_n(\mathbf{r}), \quad \mathbf{r} \in \mathcal{S}_{\text{ap}} \quad (\text{C.5})$$

where  $V_n = a_n^{\text{TE;TM}} / \sqrt{Y_n^{\text{TE;TM}}}$ ,  $V_n^i = b_n^{\text{TE;TM}} / \sqrt{Y_n^{\text{TE;TM}}}$ , and  $\mathbf{g}_n(\mathbf{r}) = -\mathbf{n} \times \mathbf{e}_n^{\text{TE;TM}}(\mathbf{r})$  if  $\mathbf{r} \in \mathcal{S}_{\text{ap}}$  and zero otherwise. Note that the summation in Eq. (C.5) is taken over both the TE and TM modes and that each value of the subscript  $n$  corresponds to a waveguide modal function with mode index  $(k, l)$ . The volume electric current density  $\mathbf{J}_V$  can be obtained from the expansion of the electric flux density  $\mathbf{D}$  into vectorial basis functions,  $\mathbf{d}_n$ , defined over a pair of tetrahedra, as

$$\mathbf{J}_V(\mathbf{r}) = j\omega\kappa(\mathbf{r})\mathbf{D}(\mathbf{r}) = j\omega\kappa(\mathbf{r}) \sum_n^{N_d} D_n \mathbf{d}_n(\mathbf{r}), \quad \mathbf{r} \in \mathcal{V}_{\text{diel}} \quad (\text{C.6})$$

Replacing each current density, in Eq. (A.1-3), by its discretized form results in

$$\sum_n^{N_d} D_n [\mathbf{E}_n^d(\mathbf{r}) - \mathbf{d}_n(\mathbf{r})/\hat{\epsilon}] = \sum_n^{N_f} I_n \mathbf{E}_n^f(\mathbf{r}) + \sum_n^{N_g} (V_n + V_n^i) \mathbf{E}_n^g(\mathbf{r}), \quad \forall \mathbf{r} \in \mathcal{V}_{\text{diel}} \quad (\text{C.7})$$

$$\mathbf{n} \times \sum_n^{N_d} D_n \mathbf{E}_n^d(\mathbf{r}) = \mathbf{n} \times \sum_n^{N_f} I_n \mathbf{E}_n^f(\mathbf{r}) + \sum_n^{N_g} (V_n + V_n^i) \left[ \mathbf{n} \times \mathbf{E}_n^g(\mathbf{r}) - \frac{1}{2} \mathbf{g}_n(\mathbf{r}) \right], \quad \forall \mathbf{r} \in \mathcal{S} \quad (\text{C.8})$$

$$\mathbf{n} \times \sum_n^{N_g} (V_n - V_n^i) Y_n \mathbf{g}_n(\mathbf{r}) = \sum_n^{N_f} I_n \mathbf{f}_n(\mathbf{r}), \quad \forall \mathbf{r} \in \mathcal{S}_{\text{ap}} \quad (\text{C.9})$$

where

$$\mathbf{E}_n^d(\mathbf{r}) = \omega^2 \mu_0 \int_{\mathcal{V}_{\text{diel}}} \kappa(\mathbf{r}') \mathbf{d}_n(\mathbf{r}') G dV' + \frac{1}{\epsilon_0} \int_{\mathcal{V}_{\text{diel}}} \nabla' \cdot [\kappa(\mathbf{r}') \mathbf{d}_n(\mathbf{r}')] \nabla G dV', \quad (\text{C.10})$$

$$\mathbf{E}_n^f(\mathbf{r}) = \int_S \left( j\omega\mu_0 G \mathbf{f}_n(\mathbf{r}') - \frac{1}{j\omega\epsilon_0} \nabla'_S \cdot \mathbf{f}_n(\mathbf{r}') \nabla G \right) dA', \quad (\text{C.11})$$

$$\mathbf{E}_n^g(\mathbf{r}) = \int_{S_{\text{sp}}} \nabla \times G \mathbf{g}_n(\mathbf{r}') dA'. \quad (\text{C.12})$$

The MoM matrix is obtained after multiplying Eq. (C.7), Eq. (C.8) and Eq. (C.9) by  $\mathbf{d}_m$ ,  $\mathbf{f}_m$ , and  $\mathbf{g}_m$ , respectively and integrating the resulting products over the individual sub-domains. We get

$$\sum_n^{N_d} D_n \langle \mathbf{d}_m, \mathbf{E}_n^d - \mathbf{d}_n / \hat{\epsilon} \rangle_{V_{\text{diel}}} = \sum_n^{N_f} I_n \langle \mathbf{d}_m, \mathbf{E}_n^f \rangle_{V_{\text{diel}}} + \sum_n^{N_g} (V_n + V_n^i) \langle \mathbf{d}_m, \mathbf{E}_n^g \rangle_{V_{\text{diel}}}, \quad \forall m = 1, \dots, N_d \quad (\text{C.13})$$

$$\sum_n^{N_d} D_n \langle \mathbf{f}_m, \mathbf{E}_n^d \rangle_S = \sum_n^{N_f} I_n \langle \mathbf{f}_m, \mathbf{E}_n^f \rangle_S + \sum_n^{N_g} (V_n + V_n^i) \langle \mathbf{f}_m, \mathbf{E}_n^g + \frac{1}{2} \mathbf{n} \times \mathbf{g}_n \rangle_S, \quad \forall m = 1, \dots, N_f \quad (\text{C.14})$$

$$\sum_n^{N_g} (V_n - V_n^i) Y_n \langle \mathbf{g}_m, \mathbf{g}_n \rangle_{S_{\text{sp}}} = \sum_n^{N_f} I_n \langle \mathbf{g}_m, \mathbf{f}_n \times \mathbf{n} \rangle_{S_{\text{sp}}}, \quad \forall m = 1, \dots, N_g \quad (\text{C.15})$$

or in matrix form

$$\begin{bmatrix} Z^{d-d} & Z^{d-f} & Z^{d-g} \\ Z^{f-d} & Z^{f-f} & Z^{f-g} \\ 0 & Z^{g-f} & Z^{g-g} \end{bmatrix} \begin{bmatrix} \mathbf{D} \\ \mathbf{I} \\ \mathbf{V} \end{bmatrix} = \begin{bmatrix} -Z^{d-g} \\ -Z^{f-g} \\ Z^{g-g} \end{bmatrix} \mathbf{V}^i \quad (\text{C.16})$$

$$\mathbf{D} = \begin{bmatrix} D_1 & \dots & D_{N_d} \end{bmatrix}^T, \quad \mathbf{I} = \begin{bmatrix} I_1 & \dots & I_{N_f} \end{bmatrix}^T, \quad \mathbf{V} = \begin{bmatrix} V_1 & \dots & V_{N_g} \end{bmatrix}^T, \quad \mathbf{V}^i = \begin{bmatrix} V_1^i & \dots & V_{N_g}^i \end{bmatrix}^T \quad (\text{C.17})$$

The total number of unknowns equals  $(N_d + N_f + N_g)$ .

## C.2 Entries of the sub-matrix $Z^{d-d}$

The entries of the sub-matrix  $Z^{d-d}$  are found after evaluation of the following expression

$$Z_{m,n}^{d-d} = \langle \mathbf{d}_m, \mathbf{E}_n^d \rangle_{\mathcal{V}_{\text{diel}}} - \langle \mathbf{d}_m, \mathbf{d}_n / \hat{\epsilon} \rangle_{\mathcal{V}_{\text{diel}}}, \quad \forall m, n = 1, \dots, N_d \quad (\text{C.18})$$

The second part of the term in Eq. (C.18) can be evaluated analytically as

$$\langle \mathbf{d}_m, \mathbf{d}_n / \hat{\epsilon} \rangle_{\mathcal{V}_{\text{diel}}} = \frac{1}{\hat{\epsilon}_n^+} \int_{\mathcal{T}_m^+} \mathbf{d}_m(\mathbf{r}) \cdot \mathbf{d}_n(\mathbf{r}) dV + \frac{1}{\hat{\epsilon}_n^-} \int_{\mathcal{T}_m^-} \mathbf{d}_m(\mathbf{r}) \cdot \mathbf{d}_n(\mathbf{r}) dV \quad (\text{C.19})$$

In Eq. (C.19), if  $\mathcal{T}_m^+ \neq \mathcal{T}_n^\pm$  then the first integral is zero and if  $\mathcal{T}_m^- \neq \mathcal{T}_n^\pm$  then the second integral equals zero. In all other cases, both integrals can be evaluated by utilizing normalized volume coordinates (Ref. Chapter 4, [14] [15]),

$$\langle \mathbf{d}_m, \mathbf{d}_n / \hat{\epsilon} \rangle_{\mathcal{V}_{\text{diel}}} = \frac{1}{\hat{\epsilon}_n^+} \frac{S_m S_n}{9 \mathcal{V}_m^+ \mathcal{V}_n^\pm} \int_{\mathcal{T}_m^+} \boldsymbol{\rho}_m^+ \cdot \boldsymbol{\rho}_n^\pm dV + \frac{1}{\hat{\epsilon}_n^-} \frac{S_m S_n}{9 \mathcal{V}_m^- \mathcal{V}_n^\pm} \int_{\mathcal{T}_m^-} \boldsymbol{\rho}_m^- \cdot \boldsymbol{\rho}_n^\pm dV \quad (\text{C.20})$$

The vector  $\boldsymbol{\rho}_m^\pm$  can be written as  $\pm (\mathbf{r} - \mathbf{r}_m^{i,\pm})$ , where  $\mathbf{r}_m^{i,\pm}$  is the position vector of the free vertex in  $\mathcal{T}_m^\pm$  opposite to the face associated with the basis function with index  $m$ . In the numerical evaluation of Eq. (C.20) the following rule may be used

$$\begin{aligned} \int_{\mathcal{T}_q} \boldsymbol{\rho}_m^\pm \cdot \boldsymbol{\rho}_n^\pm dV &= (\pm)_n (\pm)_m \int_{\mathcal{T}_q} (\mathbf{r} - \mathbf{r}_m^{i,\pm}) \cdot (\mathbf{r} - \mathbf{r}_n^{j,\pm}) dV \\ &= (\pm)_n (\pm)_m \mathcal{V}_q \left[ \frac{9}{5} |\mathbf{r}^{\text{cq}}|^2 - (\mathbf{r}_m^{i,\pm} + \mathbf{r}_n^{j,\pm}) \cdot \mathbf{r}^{\text{cq}} + (\mathbf{r}_m^{i,\pm} \cdot \mathbf{r}_n^{j,\pm}) - \frac{1}{10} \sum_{i=1}^4 \mathbf{r}_i \cdot \sum_{j=i+1}^4 \mathbf{r}_j \right] \end{aligned} \quad (\text{C.21})$$

where  $\mathbf{r}^{\text{cq}} = \frac{1}{4} \sum_{i=1}^4 \mathbf{r}_i$  is the vector position of the centroid of  $\mathcal{T}_q$  and  $\mathbf{r}_i$  ( $i = 1, \dots, 4$ ) are vector positions of the vertices of  $\mathcal{T}_q$ .

In order to evaluate the first term in Eq. (C.18), we write it as follows

$$\langle \mathbf{d}_m, \mathbf{E}_n^d \rangle_{\mathcal{V}_{\text{diel}}} = \langle \mathbf{d}_m, \mathbf{A}_n^d \rangle_{\mathcal{V}_{\text{diel}}} - \langle \mathbf{d}_m, \nabla \phi_n^d \rangle_{\mathcal{V}_{\text{diel}}} \quad (\text{C.22})$$

First, we evaluate the expression  $\langle \mathbf{d}_m, \mathbf{A}_n^d \rangle_{\mathcal{V}_{\text{diel}}}$

$$\begin{aligned} \langle \mathbf{d}_m, \mathbf{A}_n^d \rangle_{\mathcal{V}_{\text{diel}}} &= \frac{S_m}{3 \mathcal{V}_m^+} \int_{\mathcal{T}_m^+} \boldsymbol{\rho}_m^+ \cdot \mathbf{A}_n^d(\mathbf{r}) dV + \frac{S_m}{3 \mathcal{V}_m^-} \int_{\mathcal{T}_m^-} \boldsymbol{\rho}_m^- \cdot \mathbf{A}_n^d(\mathbf{r}) dV \\ &\approx \frac{S_m}{3} \left[ \boldsymbol{\rho}_m^{c,+} \cdot \mathbf{A}_n^d(\mathbf{r}_m^{c,+}) + \boldsymbol{\rho}_m^{c,-} \cdot \mathbf{A}_n^d(\mathbf{r}_m^{c,-}) \right] \end{aligned} \quad (\text{C.23})$$

where  $\rho_m^{c,\pm} = \pm (\mathbf{r}_m^{c,\pm} - \mathbf{r}_m^{i,\pm})$  and  $\mathbf{r}_m^{c,\pm}$  denotes the vector position of the centroid of  $\mathcal{T}_m^\pm$ . The vector  $\mathbf{A}_n^d(\mathbf{r}_m^{c,\pm})$  is defined as

$$\begin{aligned} \mathbf{A}_n^d(\mathbf{r}_m^{c,\pm}) &= \mathbf{A}_n^{d,+}(\mathbf{r}_m^{c,\pm}) + \mathbf{A}_n^{d,-}(\mathbf{r}_m^{c,\pm}) \\ \mathbf{A}_n^{d,\pm}(\mathbf{r}_m^{c,\pm}) &= \omega^2 \mu_0 \frac{\mathcal{S}_n}{12\pi\nu_n^\pm} \kappa(\mathbf{r}_n^{c,\pm}) \int_{\mathcal{T}_n^\pm} \rho_n^\pm \exp(-jk_0 R_m^\pm) / R_m^\pm dV' \\ R_m^\pm &= |\mathbf{r}' - \mathbf{r}_m^{c,\pm}|, \quad \rho_n^\pm = \pm (\mathbf{r}' - \mathbf{r}_n^{i,\pm}) \end{aligned} \quad (\text{C.24})$$

Next, we evaluate the expression  $\langle \mathbf{d}_m, \nabla \phi_n^d \rangle_{\mathcal{V}_{\text{diel}}}$

$$\begin{aligned} \langle \mathbf{d}_m, \nabla \phi_n^d \rangle_{\mathcal{V}_{\text{diel}}} &= \int_{\mathcal{V}_{\text{diel}}} \mathbf{d}_m \cdot \nabla \phi_n^d dV = \int_{\mathcal{V}_{\text{diel}}} [\nabla \cdot \mathbf{d}_m \phi_n^d - \phi_n^d \nabla \cdot \mathbf{d}_m] dV \\ &= \int_{\mathcal{S}_{\text{diel}}} \phi_n^d \mathbf{d}_m \cdot \mathbf{n} dA - \int_{\mathcal{V}_{\text{diel}}} \phi_n^d \nabla \cdot \mathbf{d}_m dV \end{aligned} \quad (\text{C.25})$$

where  $\mathcal{S}_{\text{diel}}$  is the boundary of  $\mathcal{V}_{\text{diel}}$ . Eq. (C.25) can be further simplified as

$$\langle \mathbf{d}_m, \nabla \phi_n^d \rangle_{\mathcal{V}_{\text{diel}}} \approx \begin{cases} \mathcal{S}_m [\phi_n^d(\mathbf{r}_m^{c,-}) - \phi_n^d(\mathbf{r}_m^{c,+})], & \text{if } \mathcal{T}_m^+ \text{ and } \mathcal{T}_m^- \in \mathcal{V}_{\text{diel}} \\ (\pm)_m \mathcal{S}_m [\phi_n^d(\mathbf{r}_m^{c,\pm} \pm \frac{1}{3}\rho_m^{c,\pm}) - \phi_n^d(\mathbf{r}_m^{c,\pm})] & \text{if } \mathcal{T}_m^+ \text{ or } \mathcal{T}_m^- \notin \mathcal{V}_{\text{diel}} \end{cases} \quad (\text{C.26})$$

where we have used the property ( $\mathbf{d}_m \cdot \mathbf{n} = 1$ ) and all the integrals have been approximated by their value at the centroid. The vector  $\mathbf{r}_m^{c,\pm} \pm \frac{1}{3}\rho_m^{c,\pm}$  represents the vector position of the centroid of the face associated with basis function  $\mathbf{d}_m$  and located on  $\mathcal{S}_{\text{diel}}$ . The scalar  $\phi_n^d(\mathbf{r})$  equals

$$\begin{aligned} \phi_n^d(\mathbf{r}) &= -\frac{1}{4\pi\epsilon_0} \int_{\mathcal{V}_{\text{diel}}} \nabla' \cdot [\kappa(\mathbf{r}') \mathbf{d}_n(\mathbf{r}')] \exp(-jk_0 R) / R dV' \\ &= -\frac{1}{4\pi\epsilon_0} \int_{\mathcal{V}_{\text{diel}}} [\mathbf{d}_n(\mathbf{r}') \cdot \nabla' \kappa(\mathbf{r}') + \kappa(\mathbf{r}') \nabla' \cdot \mathbf{d}_n(\mathbf{r}')] \exp(-jk_0 R) / R dV' \\ &= \phi_n^{d,+}(\mathbf{r}) + \phi_n^{d,-}(\mathbf{r}), \end{aligned} \quad (\text{C.27})$$

$$\phi_n^{d,\pm}(\mathbf{r}) = \mp \frac{\mathcal{S}_n \kappa_n^\pm}{4\pi\epsilon_0 \mathcal{V}_n^\pm} \int_{\mathcal{T}_n^\pm} \exp(-jk_0 R) / R dV' \pm \frac{\kappa_n^\pm}{4\pi\epsilon_0} \int_{\mathcal{S}_n} \exp(-jk_0 R) / R dA' \quad (\text{C.28})$$

where  $R = |\mathbf{r}' - \mathbf{r}|$  and  $\kappa_n^\pm$  is the value of  $\kappa(\mathbf{r})$  inside  $\mathcal{T}_n^\pm$ . In Eq. (C.28) the first part represents the contribution from the induced volume charge densities while the second

term represents the contribution from induced surface charge distributions. Note that in a homogeneous medium the total volume charge densities must be zero.

### C.3 Entries of the sub-matrix $Z^{d-f}$

The elements of the matrix  $Z^{d-f}$  are given by

$$\begin{aligned} Z_{m,n}^{d-f} &= -\langle \mathbf{d}_m, \mathbf{E}_n^f \rangle_{\mathcal{V}_{\text{diel}}}, \\ &\approx -\frac{S_m}{3} \left[ \rho_m^{c,+} \cdot \mathbf{E}_n^f(\mathbf{r}_m^{c,+}) + \rho_m^{c,-} \cdot \mathbf{E}_n^f(\mathbf{r}_m^{c,-}) \right], \end{aligned} \quad (\text{C.29})$$

$\forall m = 1, \dots, N_d, \forall n = 1, \dots, N_f$

where

$$\begin{aligned} \mathbf{E}_n^f(\mathbf{r}_m^{c,\pm}) &= \mathbf{E}_n^{f,+}(\mathbf{r}_m^{c,\pm}) + \mathbf{E}_n^{f,-}(\mathbf{r}_m^{c,\pm}) \quad (\text{C.30}) \\ \mathbf{E}_n^{f,\pm}(\mathbf{r}_m^{c,\pm}) &= \frac{I_n}{S_n^\pm} \left[ \frac{1}{2} j\omega\mu_0 \int_{S_n} \rho_n^\pm G dA' - \frac{1}{j\omega\epsilon_0} \pm \int_{S_n} \nabla G dA' \right] \\ R_m^\pm &= |\mathbf{r}_m^{c,\pm} - \mathbf{r}'|, \hat{\mathbf{i}}_{R_m^\pm} = \mathbf{R}_m^\pm / R_m^\pm \\ G &= \exp(-jk_0 R_m^\pm) / (4\pi R_m^\pm), \nabla G = -\left( jk_0 + \frac{1}{R_m^\pm} \right) G \hat{\mathbf{i}}_{R_m^\pm} \end{aligned} \quad (\text{C.31})$$

$S_n$  represents the surface of a triangular patch on  $S$ .

### C.4 Entries of the sub-matrix $Z^{d-g}$

The elements of the matrix  $Z^{d-g}$  are given by

$$\begin{aligned} Z_{m,n}^{d-g} &= -\langle \mathbf{d}_m, \mathbf{E}_n^g \rangle_{\mathcal{V}_{\text{diel}}}, \\ &\approx -\frac{S_m}{3} \left[ \rho_m^{c,+} \cdot \mathbf{E}_n^g(\mathbf{r}_m^{c,+}) + \rho_m^{c,-} \cdot \mathbf{E}_n^g(\mathbf{r}_m^{c,-}) \right], \end{aligned} \quad (\text{C.32})$$

$\forall m = 1, \dots, N_d, \forall n = 1, \dots, N_g$

where

$$\begin{aligned} \mathbf{E}_n^g(\mathbf{r}_m^{c,\pm}) &= \mathbf{E}_n^{g,+}(\mathbf{r}_m^{c,\pm}) + \mathbf{E}_n^{g,-}(\mathbf{r}_m^{c,\pm}) \quad (\text{C.33}) \\ \mathbf{E}_n^{g,\pm}(\mathbf{r}_m^{c,\pm}) &= \int_{S_{\text{ap}}} \nabla \times G(\mathbf{r}', \mathbf{r}_m^{c,\pm}) \mathbf{g}_n(\mathbf{r}') dA' = \int_{S_{\text{ap}}} \nabla G(\mathbf{r}', \mathbf{r}_m^{c,\pm}) \times \mathbf{g}_n(\mathbf{r}') dA' \end{aligned} \quad (\text{C.34})$$

The integration is taken over the waveguide aperture surface  $S_{\text{ap}}$ .

## C.5 Entries of the sub-matrix $Z^{f-d}$

The elements of the matrix  $Z^{f-d}$  can be obtained from

$$\begin{aligned} Z_{m,n}^{f-d} &= \langle \mathbf{f}_m, \mathbf{E}_n^d \rangle_{\mathcal{S}}, \\ &\approx \frac{L_m}{2} \left[ \boldsymbol{\rho}_m^{c,+} \cdot \mathbf{E}_n^d(\mathbf{r}_m^{c,+}) + \boldsymbol{\rho}_m^{c,-} \cdot \mathbf{E}_n^d(\mathbf{r}_m^{c,-}) \right], \end{aligned} \quad (\text{C.35})$$

$$\forall m = 1, \dots, N_f, \forall n = 1, \dots, N_d$$

$$\mathbf{E}_n^d(\mathbf{r}_m^{c,\pm}) = \mathbf{E}_n^{d,+}(\mathbf{r}_m^{c,\pm}) + \mathbf{E}_n^{d,-}(\mathbf{r}_m^{c,\pm}) \quad (\text{C.36})$$

where

$$\begin{aligned} \mathbf{E}_n^{d,\pm}(\mathbf{r}_m^{c,\pm}) &= \omega^2 \mu_0 \frac{S_n}{12\pi v_n^{\pm}} \kappa(\mathbf{r}_n^{c,\pm}) \int_{\mathcal{I}_n^{\pm}} \boldsymbol{\rho}_n^{\pm} \exp(-jk_0 R_m^{\pm}) / R_m^{\pm} dV' \\ &+ \frac{1}{\epsilon_0} \left[ \pm \frac{S_n \kappa_n^{\pm}}{v_n^{\pm}} \int_{\mathcal{I}_n^{\pm}} \nabla \mathbf{G}(\mathbf{r}', \mathbf{r}_m^{c,\pm}) dV' \mp \kappa_n^{\pm} \int_{\mathcal{S}_n} \nabla \mathbf{G}(\mathbf{r}', \mathbf{r}_m^{c,\pm}) dA' \right] \end{aligned} \quad (\text{C.37})$$





## Appendix D

# Numerical evaluation of the mutual impedance

This appendix is devoted to the numerical evaluation of the mutual impedance between two dielectric rod antennas. The array geometry and coordinate systems are given in Fig. 5.6. The gain function of a single dielectric rod antenna can be well fitted by

$$G(\theta) = \sum_{i=0}^N g_i \cos^{2i}(\theta), \quad (\text{D.1})$$

where  $g_i$  ( $i = 0, 1, \dots, N$ ) are constants. The gain function is defined in the coordinate system  $(\mathbf{i}_x, \mathbf{i}_y, \mathbf{i}_z)$  with spherical coordinates  $(r, \theta, \varphi)$ . For computational convenience we express the gain function in the coordinate system  $(\mathbf{i}_{x'}, \mathbf{i}_{y'}, \mathbf{i}_{z'})$  with spherical coordinates  $(r, \alpha, \varphi')$ . After a coordinate rotation (see Fig. 5.6) we obtain

$$G(\alpha, \varphi') = \sum_{i=0}^N g_i (\sin \alpha \sin \varphi')^{2i}. \quad (\text{D.2})$$

The mutual impedance is given by

$$\begin{aligned} z_{2,1} &= \frac{1}{2\pi} \int_0^\pi \int_\Gamma G(\alpha, \varphi') \exp(-j\mathbf{k} \cdot \mathbf{D}) \sin \alpha d\alpha d\varphi', \\ &= \frac{1}{2\pi} \sum_{i=0}^N g_i \int_0^\pi \int_\Gamma (\sin \alpha \sin \varphi')^{2i} \exp(-jk_0 \cos \alpha d) \sin \alpha d\alpha d\varphi', \\ &= \frac{1}{2\pi} \sum_{i=0}^N g_i \left[ \int_0^\pi (\sin \varphi')^{2i} d\varphi' \right] \left[ \int_\Gamma (\sin \alpha)^{2i+1} \exp(-jk_0 \cos \alpha d) d\alpha \right], \end{aligned} \quad (\text{D.3})$$

where we have used  $\mathbf{D} = d\mathbf{i}_z$ . The integral over  $d\varphi'$  can be evaluated analytically and is given by

$$\int_0^\pi (\sin \varphi')^{2i} d\varphi' = \sqrt{\pi} \frac{\Gamma(i + \frac{1}{2})}{\Gamma(i + 1)}, \quad (\text{D.4})$$

where  $\Gamma(x)$  is the gamma function with argument  $x$ . The integration along the  $\Gamma$  path in the complex plane must be taken as follows

$$\int_\Gamma (\ ) d\alpha = \int_0^{\frac{\pi}{2}} (\ ) d\alpha + \int_{\frac{\pi}{2}+0j}^{\frac{\pi}{2}+\infty j} (\ ) d\alpha. \quad (\text{D.5})$$

Let

$$Z_1^i = \int_0^{\frac{\pi}{2}} (\sin \alpha)^{2i+1} \exp(-jk_0 \cos \alpha d) d\alpha, \quad Z_2^i = \int_{\frac{\pi}{2}+0j}^{\frac{\pi}{2}+\infty j} (\sin \alpha)^{2i+1} \exp(-jk_0 \cos \alpha d) d\alpha. \quad (\text{D.6})$$

After applying a change of integration variable  $t = \cos \alpha$  we obtain

$$Z_1^i = \int_0^1 (1-t^2)^i \exp(-jk_0 dt) dt, \quad Z_2^i = j \int_0^\infty (1+t^2)^i \exp(-k_0 dt) dt. \quad (\text{D.7})$$

Finally we have

$$z_{2,1} = \frac{1}{2} \sum_{i=0}^N g_i \frac{\Gamma(i + \frac{1}{2})}{\sqrt{\pi} \Gamma(i + 1)} [Z_1^i + Z_2^i].$$

The remaining integrations can be evaluated numerically using standard quadrature rules.

# Appendix E

## List of symbols and acronyms

CATR	Compact Antenna Test Range
DARR	Delft Atmospheric Research Radar
DUCAT	Delft University Chamber for Antenna Tests
ESA	European Space Agency
IRCTR	International Research Centre for Telecommunications- transmission and Radar
MSA	Minimum Scattering Antenna
STW	Netherlands Technology Foundation
TARA	Transportable Atmospheric RAdar
TE	Transverse Electric
TM	Transverse Magnetic
TTT	Telecommunication and Teleobservation Technology
VSWR	Voltage Standing Wave Ratio

$j$	$j^2 = -1$
$\omega$	Angular frequency
$f_c$	Cut-off frequency
$(i_x, i_y, i_z)$	Cartesian coordinates system
$\mathbf{r}, \mathbf{r}'$	Position vectors
$r, \theta, \varphi$	Spherical coordinates
$\mathbf{k} = k_x \mathbf{i}_x + k_y \mathbf{i}_y + k_z \mathbf{i}_z$	Propagation vector
$a, b$	Rectangular waveguide cross-section dimensions
$\mathbf{n}$	Unit normal
$\epsilon$	Electric permittivity
$\hat{\epsilon}$	Complex electric permittivity
$\mu$	Magnetic permeability
$\sigma$	Conductivity
$\kappa$	Contrast function
$\rho$	Charge density
$G(\mathbf{r}, \mathbf{r}')$	Green's function
$S, \mathcal{W}$	Closed Surfaces
$\partial W$	Boundary of surface $W$
$\mathcal{V}$	Volume
$\Pi$	Hertzian vector potential
$\mathbf{A}$	Electric vector potential
$\mathbf{F}$	Magnetic vector potential
$\mathbf{E}(x, y, z)$	Electric field
$\mathbf{D}(x, y, z)$	Electric flux density
$\mathbf{H}(x, y, z)$	Magnetic field
$\mathbf{E}_{wg}$	Electric field inside the waveguide
$\mathbf{H}_{wg}$	Magnetic field inside the waveguide
$\tilde{\mathbf{E}}(k_x, k_y, k_z), \tilde{\mathbf{H}}(k_x, k_y, k_z)$	Electric and magnetic field in spectral domain

$\mathbf{J}_S$	Surface electric current density
$\mathbf{J}_V$	Volume electric current density
$\mathbf{K}_S$	Surface magnetic current density
$\mathbf{f}_n(\mathbf{r})$	Expansion function for electric current density
$\mathbf{d}_n(\mathbf{r})$	Expansion function for flux density
$\mathbf{g}_n(\mathbf{r})$	Expansion function for magnetic current density
$\mathbf{e}_{m,n}^{\text{TE;TM}}(x, y)$	Transverse modal field distribution
$A_{m,n}^{-,c;h}$	Wave traveling in $-z$ direction
$A_{m,n}^{+,c;h}$	Wave traveling in $+z$ direction
$a_{m,n}$	Amplitude of incident wave
$b_{m,n}$	Amplitude of reflected wave
$Y_{m,n}^{\text{TE;TM}}$	Admittance of mode $(m, n)$
$\gamma_{m,n}$	Propagation constant of mode $(m, n)$
$G(\theta, \varphi)$	Antenna gain function
$P(\theta, \varphi)$	Antenna power pattern
$y_{\text{ap}}$	Aperture admittance
$\Gamma$	Reflection coefficient of the fundamental mode
$\mathbf{S}$	Scattering matrix
$\mathbf{Z}$	Impedance matrix
$\mathbf{I}$	Unit matrix
$\mathbf{L}(n)$	Vector at iteration $n$
$\Gamma(x)$	Gamma function with argument $x$
$+$	Complex conjugate and transpose
$*$	Complex conjugate
$\prime$	Transpose
PV	Principal value
$\mathcal{TR}$	Triangle
$\mathcal{T}$	Tetrahedral



# Acknowledgments

I am very grateful to all the people who have helped me in various ways during my research. Particularly, I would like to thank my promoters Prof. L.P. Ligthart for encouraging me to start this work, for creating a very stimulating environment and for teaching me all I know about antennas, and Prof. T. Birand (working at the Middle East Technical University, Ankara) for his guidance and valuable advice.

The work in this thesis has been carried out at the International Research Centre for Telecommunication transmission and Radar at the Delft University of Technology. I wish to thank all the nice members of this great institute, particularly S.H. Heijnen, A. Heldring, I.L. Morrow, and Prof. A. Yarovoy. I also would like to thank P. Aubry and J.H. Zijderveld for doing the measurements involved in this dissertation. I am especially indebted to my colleague and very close friend D.P. Tran for all the scientific and philosophical discussions we had during the nights and the weekends we spent together in our office.

During my Ph.D. research, hardware had to be constructed. For that I would like to thank the members of the mechanical workshop of the Delft University of Technology. Especially, I would like to mention Bas van Eijk and Ruud van Weijk, who put a lot of effort in the construction of the feeds.

I am grateful to the members of the Laboratory of Electromagnetic Research of the Delft University of Technology for their help during my research. In particular, I wish to thank Dr. G. Mur for his constructive comments and for the many hours

spent on helping me to finish this thesis.

The cooperation with colleagues from the Middle East Technical University in Ankara was very fruitful and enlightening. I would like to thank T. Ciloglu, G. Dural and Prof. A. Hizal for productive discussions and for the nice time I spent in Ankara.

I wish to express my gratitude to A. Roederer and A.J.M. Polegre of the European Space Agency for the valuable discussions, the tools provided, and for giving me the opportunity to do measurements at the Compact Antenna Test Range.

I am very grateful to my father, Chrif Moumen, for his help and encouragement and for giving me the opportunities to find my own way in life. Last, but not least I want to thank the most important women in my life, my mother Zohra and my wife Mariam, for their support, encouragement, care and patience.

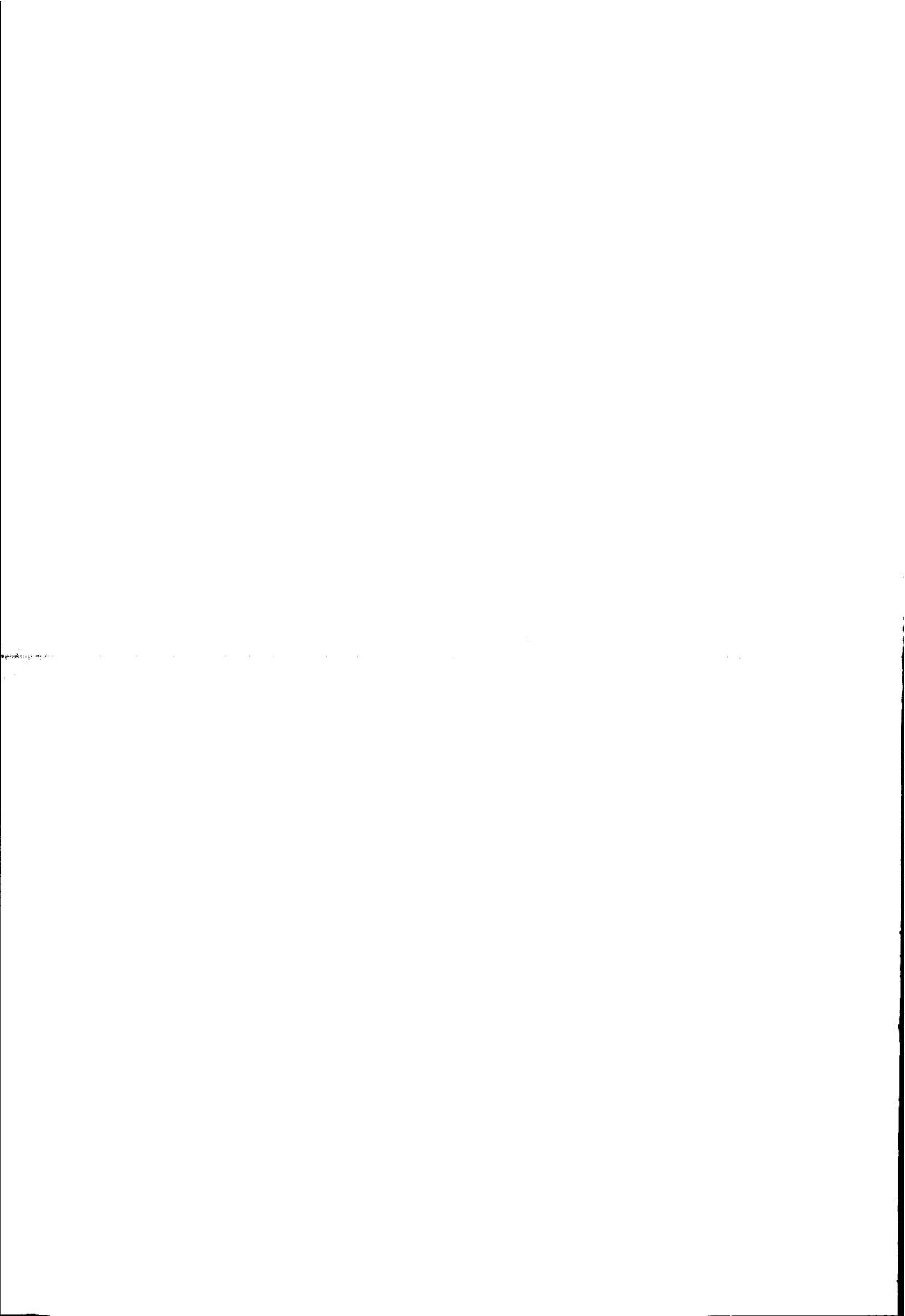
*January 2001*

*Abderrahim Moumen*



## Samenvatting (Summary in Dutch)

In dit proefschrift wordt een volledige en nauwkeurige ontwerp en analyse procedure voor multibundel reflectorantennes behandeld waarbij kleine arrays van geminiaturiseerde diëlectrische staafantennes gebruikt worden. Het is aangetoond dat deze staafantennes goed functioneren als reflector belichters omdat ze met relatief kleine elementen toch een hoge gain kunnen genereren. Doordat ze zo klein zijn kunnen individuele elementen dicht op elkaar geplaatst worden waardoor het array compact wordt (weinig blokkering) en een verbeterde offset bundel geeft (verbeterde resolutie). Verschillende aspecten die samenhangen met het miniaturiseringsproces alsmede met het stralingsmechanisme en het elektromagnetisch model van een enkele diëlectrische staafantenne worden behandeld. Ook de mutuele koppeling voor kleine interelement afstanden is bestudeerd. Dit heeft geresulteerd in het ontwerp en de bouw van een geminiaturiseerde diëlectrische staaf antenne array met lage reflectie coëfficiënt, hoge bundelingsfaktor en lage mutuele koppeling. De arraysynthese die in dit proefschrift behandelt wordt houdt rekening met effecten als mutuele koppeling, blokkering ten gevolge van behuizing en arrayondersteuning en verliezen in het bundelvormend netwerk. Het ontworpen belichter systeem is toegepast in de transporteerbare atmosfeer radar (TARA) die door het Internationale Research Centre for Telecommunications-transmission and Radar (IRCTR) van de Technische Universiteit Delft ontwikkeld en gebouwd is, en momenteel volledig operationeel is.



## Author publications

1. A. Moumen and L.P. Ligthart, "*Radiation Pattern and Aperture Admittance of Dielectric Filled Waveguides with Rectangular Cross Section Using the Mode Matching Technique*", in 28<sup>th</sup> European Microwave Conference, pp. 587-592, October 1998.
2. A. Moumen, T. Birand, A. Roederer, and L.P. Ligthart, "*Application of the MSAs Theory to Investigate The Coupling Between Two Dielectric Rod Antennas*", 10<sup>th</sup> International Symposium on Antennas JINA, pp. 310-313, Nice France, November 1998.
3. A. Moumen and L.P. Ligthart; "*Design of a Focal Plane Dielectric Rod Array for Feeding a Multiple Beam Reflector Antenna*", IEEE-AP International Symposium Digest, Vol. 2, pp. 1152-1155, Orlando Florida, July 1999.
4. A. Moumen and L.P. Ligthart; "*Radiation from a Dielectric Filled Waveguide Terminated by a Finite Metallic Flange of Arbitrary Shape*", in 29<sup>th</sup> European Microwave Conference, pp. 331-334, October 1999.
5. A. Moumen and L.P. Ligthart, "*Rigorous Analysis of Dielectric Rod Antennas of Arbitrary Shape Using A Hybrid-Iterative Technique*", AP-2000, CDROM No. 75, Davos Switzerland, April 2000.
6. A. Moumen and L.P. Ligthart, "*Feed Design for Axial Symmetric and Non-Axial*

- Symmetric Antennas with Low Sidelobes*", IRCTR and ESA-ESTEC joined mini-symposium on development of low sidelobe antennas, October 1999.
7. A. Moumen and L.P. Ligthart, "A Hybrid Physical Optics-Moment Method for Reflector Antennas with Complex Struts Geometry and Off-Axis Feeding", IEEE-AP International Symposium Digest, AP vol. 2, p. 830, Salt Lake City Utah, July 2000.
  8. A. Moumen and L.P. Ligthart, "Synthesis of a Dielectric Rod Array for a Multiple Beam Reflector Antenna", IEEE-AP International Symposium Digest, AP vol. 4, p. 1914, Salt Lake City Utah, July 2000.
  9. A. Moumen, T. Birand, and L.P. Ligthart, "Experimental Design of A Dielectric Rod Antenna for a Multiple Beam Array Fed Reflector System", submitted to IEEE Trans. Antennas. Propagat.
  10. I.L. Morrow, A. Moumen and P. van Genderen, "Measurement and Modelling of Transient TEM Horn Antennas", IEEE-AP International Symposium Digest, Salt Lake City Utah, URSI vol., p. 345, July 2000.
  11. A. Moumen and L.P. Ligthart, "Miniaturized Dielectric Rod Antennas: A Good Candidate for Array Applications", Int. Symp. Antennas for Radar Earth Observation (AEO2000), IRCTR, Delft University of Technology, 8<sup>th</sup> June 2000.
  12. A. Buke, A. Moumen, I. L. Morrow and L. P. Ligthart, "Optimized Dual-Polarized Aperture-Coupled Patch Antenna", Microwave and Optical Technology Letters, vol. 27, No. 4, November 20 2000.

# Curriculum vitae

Abderrahim Moumen was born in Oujda, Morocco, on January 21, 1973. He received the Baccalaureate certificate in Electronics from the Moulay Youssef High School in Tangier, Morocco, in June 1990.

In August 1990 Abderrahim attended the Dutch School of languages in the Netherlands where he received the Dutch certificate in languages. Upon completion he enrolled with Delft University of Technology and read for the degree of M.Sc. in Electrical Engineering. Abderrahim performed his graduation work under the supervision of Prof. L.P. Ligthart in the Telecommunication and Teleobservation Technology (TTT) department on the subject of analysis and design of novel scannable reflector antenna systems for remote sensing applications

After graduating in July 1996, he joined the Delft University of Technology as an assistant professor trainee within the International Research Centre for Telecommunication transmission and Radar (IRCTR). Here, he conducted the research resulting in the present dissertation.

